Multi-Objective, Multiphasic and Multi-Step Self-Optimising Continuous Flow Systems

Adam D. Clayton

Submitted in accordance with the requirements for the degree of Doctor of Philosophy

School of Chemical and Process Engineering

February 2020

The candidate confirms that the work submitted is his/her own, except where work which has formed part of jointly-authored publications has been included. The contribution of the candidate and the other authors to this work has been explicitly indicated below. The candidate confirms that appropriate credit has been given within the thesis where reference has been made to the work of others.

The work in Chapter 1 has appeared in: **A. D. Clayton**, J. A. Manson, C. J. Taylor, T. W. Chamberlain, B. A. Taylor, G. Clemens and R. A. Bourne, *React. Chem. Eng.*, **2019**, 4, 1545-1554. ADC, JAM and CJT were responsible for preparation of the review. The contribution from other authors was project supervision (TWC, BAT, GC, RAB).

The work in Chapter 2 has appeared in: A. M. Schweidtmann, **A. D. Clayton**, N. Holmes, E. Bradford, R. A. Bourne and A. A. Lapkin, *Chem. Eng. J.*, **2018**, 352, 277-282. ADC was responsible for carrying out all experimentation for one of the case studies, improving the optimisation program and data analysis including modelling and simulations. The contribution from other authors was writing the optimisation algorithm (AMS, EB, AAL), experimentation for a second case study (NH) and project supervision (RAB, AAL).

The work in Chapter 3 has appeared in: **A. D. Clayton**, A. M. Schweidtmann, G. Clemens, J. A. Manson, C. J. Taylor, C. G. Niño, T. W. Chamberlain, N. Kapur, A. J. Blacker, A. A. Lapkin and R. A. Bourne, *Chem. Eng. J.*, **2020**, 384, 123340. ADC was responsible for carrying out all experimentation, data modelling and simulations. The contribution from other authors was coding support (AMS, JAM, CJT), reactor construction (CGN) and project supervision (GC, TWC, NK, AJB, AAL, RAB).

The work in Chapter 4 has appeared in: J. A. Manson, **A. D. Clayton**, C. G. Niño, R. Labes, T. W. Chamberlain, A. J. Blacker, N. Kapur and R. A. Bourne, *CHIMIA*, **2019**, 73, 817-822. ADC was responsible for carry out reactor characterisation and all subsequent experimentation. The contribution from other authors was writing the optimisation algorithm (JAM), construction of the LED light array (CGN), preparation of the manuscript for publication (RL) and project supervision (TWC, AJB, NK, RAB).

The work in Chapter 5 has appeared in: **A. D. Clayton**, L. A. Power, W. Reynolds, C. Ainsworth, D. R. J. Hose, M. F. Jones, T. W. Chamberlain, A. J. Blacker and R. A. Bourne, *J. Flow. Chem.*, **2020**, 10, 199-206. ADC was responsible for carrying

out all optimisation experiments, data modelling, reactor characterisation and improving the optimisation program. The contribution from other authors was pKa determination (LP), characterisation of the membrane-based separator (WR) and project supervision (CA, DRJH, MFJ, TWC, AJB, RAB).

“The best time to plant a tree was 25 years ago. The second best time to plant a tree is today.” – Eliud Kipchoge

Acknowledgements

I would firstly like to thank my supervisor Richard Bourne for the opportunity to work on such an exciting and multidisciplinary project. Although initially overwhelmed by the coding and chemical engineering aspects of the project, Rich has a unique way of making you realise that any goal can be achieved with enough determination – a lesson I will not quickly forget. Also, despite becoming increasingly busy whilst climbing the academic ladder, Rich always found time to help with my own early career development by presenting me with new and exciting opportunities. I would also like to thank my co-supervisors John Blacker and Nik Kapur, whose combined industrial knowledge proved to be invaluable throughout the project.

I would like to thank all of the great people I have had the pleasure of collaborating with throughout this project. The team at AstraZeneca (Graeme, Brian, Niall, Anne, Ali, Martin, Caroline, David) who made me feel welcome and taught me so much throughout my three month placement in Macclesfield. The co-authors of published work, with special mentions for Artur Schweidtmann, Jamie Manson and Alexei Lapkin whose coding experience was crucial to the success of the work, and Thomas Chamberlain whose meticulous eye for detail was particularly useful when preparing manuscripts. All present and past members of the iPRD, especially Nicholas Holmes and Alistair Baker who always made time to help train me at the start of the project. Everyone else who made the University of Leeds a great place to work over the last few years: Connor, Calum, Ollie, Holly, Ricardo, Ilias, Chris, Luke, Brendan, Mike, Mary, Lisa, Will, Becky, Tom, Rosie, Sam, Christiane, Nisha.

Thank you to all of my family, in particular my parents David and Linda Clayton. Their continual (and sometimes relentless!) encouragement for me to pursue higher education from a young age still remains one of the biggest contributors to my motivation.

Finally and foremost I would like to thank my loving wife Laura Clayton. The support you provide on a daily basis accumulates to the biggest reason I am able to undertake projects like these. We are a great team and none of this would be possible without you.

Abstract

Continuous flow chemistry is currently a vibrant area of research, offering many advantages over traditional batch chemistry. These include: enhanced heat and mass transfer, access to a wider range of reaction conditions, safer use of hazardous reagents, telescoping of multi-step reactions and readily accessible photochemistry. As such, there has been an increase in the adoption of continuous flow processes towards the synthesis of active pharmaceutical ingredients (APIs) in recent years.

Advances in the automation of laboratory equipment has transformed the way in which routine experimentation is performed, with the digitisation of research and development (R&D) greatly reducing waste in terms of human and material resources. Self-optimising systems combine algorithms, automated control and process analytics for the feedback optimisation of continuous flow reactions. This provides efficient exploration of multi-dimensional experimental space, and accelerates the identification of optimum conditions. Therefore, this technology directly aligns with the drive towards more sustainable process development in the pharmaceutical industry. Yet the uptake of these systems by industrial R&D departments remains relatively low, suggesting that the capabilities of the current technology are still limited.

The work in this thesis aims to improve existing self-optimisation technologies, to further bridge the gap between academic and industrial research. This includes introducing multi-objective optimisation algorithms and applying them towards the synthesis of APIs, developing a new multiphasic CSTR cascade reactor with photochemical capabilities and including downstream work-up operations in the optimisation of multi-step processes.

Table of Contents

List of Figures

List of Schemes

List of Tables

List of Abbreviations

1°	Primary
2°	Secondary
3°	Tertiary
A	Pre-exponential factor
Ac	Acetyl
Act	Actinometric compound
AD	Alzheimer's disease
API	Active pharmaceutical ingredient
Aq	Aqueous
Aβ	Amyloid β
BA	Benzylamine
BACE1	β-site amyloid precursor protein cleaving enzyme 1
Bn	Benzyl
Boc	*tert*-Butyloxycarbonyl
bp	Boiling point
BS	Batch sequential
BS-TSEMO	Batch-sequential Thompson sampling efficient multi-objective
Bu	Butyl
CCF	Face centred composite
cm	Centimetre
CPU	Central processing unit
CSTR	Continuous stirred tank reactor
d	Doublet
DABO	Diethanolamine boronic ester
DCM	Dichloromethane
DIBAL	Diisobutylaluminium hydride
DIPEA	Diisopropylethylamine
DLS	Dynamic light scattering
DMSO	Dimethyl sulfoxide
DoE	Design of experiments
E_a	Activation energy
EIM-EGO	Expected improvement matrix efficient global optimisation
Equiv	Equivalents
Et	Ethyl

FFD	Full factorial design
g	Gram
GA	Genetic algorithm
GC	Gas chromatography
GP	Gaussian process
GPC	Gel permeation chromatography
h	Hour
HAT	Hydrogen abstraction transfer
hept	Heptet
Hex	Hexyl
HPLC	High performance liquid chromatography
Hz	Hertz
I	High throughput experimentation
ID	Inner diameter
Imp	Impurity
i-Pr	Isopropyl
IR	Infrared
ISC	Intersystem crossing
J	Coupling constant
k	Rate constant
K	Kelvin
kg	Kilogram
L	Litre
LC	Liquid chromatography
LCA	Life cycle assessment
LED	Light emitting diode
LHC	Latin hypercube
LLE	Liquid-liquid extraction
m	Metre or multiplet
mCPBA	meta-Chloroperoxybenzoic acid
Me	Methyl
Mes	Mesylate
MFC	Mass flow controller
MHz	Megahertz
min	Minute
MINLP	Mixed integer nonlinear programming

mL	Millilitre
MLR	Multiple linear regression
mmol	Millimoles
MOAL	Multi-objective active learner
mol	Moles
MOOA	Multi-objective optimisation algorithm
MS	Mass spectrometry
MΩ	Megohm
n	Number of moles
NBA	*o*-Nitrobenzaldehyde
NMP	*N*-Methyl-2-pyrrolidone
NMR	Nuclear magnetic resonance
NMSIM	Nelder-Mead simplex
ns	Nanosecond
NSGA	Non-dominated-sort genetic algorithm
OD	Outer diameter
ODE	Ordinary differential equation
Org	Organic
OVAT	One-variable-at-a-time
P	Pressure
ParEGO	Pareto efficient global optimisation
PAT	Process analytical technologies
PFR	Plug flow reactor
Ph	Phenyl
PK	Paal-Knorr
PlatEMO	Platform for evolutionary multi-objective optimisation
PRESS	Predictive error sum of squares
PS	Photosensitiser
PSI	Pounds per square inch
PTFE	Polytetrafluoroethylene
R	Gas constant
R&D	Research and development
RME	Reaction mass efficiency
RSS	Residual sum of squares
RTD	Residence time distribution
s	Second or singlet

sc	Supercritical
SD	Standard deviation
SM	Starting material
SMSIM	Super modified simplex
S_NAr	Nucleophilic aromatic substitution
SNOBFIT	Stable noisy optimisation by branch and fit
solv	Solvent
STY	Space-time yield
T	Temperature
t	Triplet
T/p	Temperature and pressure
TBADT	Tetra-*n*-butylammonium decatungstate
TBAF	Tetra-*n*-butylammonium fluoride
TBS	*tert*-Butyldimethylsilyl
Temp	Temperature
tert	Tertiary
TFA	Trifluoroacetic acid
THF	Tetrahydrofuran
TMB	Trimethoxybenzene
TMS	Trimethylsilane
tR	Residence time
t_{res}	Residence time
TSEMO	Thompson sampling efficient multi-objective
TSS	Total sum of squares
uPLC	Ultra performance liquid chromatography
UV-Vis	Ultra-violet visible
V	Volume
VdV	Van de Vusse
µL	Microlitre
µm	Micrometre
µs	Microsecond
ν	Volumetric flow rate

Chapter 1 Introduction

1.1 Ideal and Non-Ideal Reactor Types

In chemical engineering, ideal models are applied to reactors to simplify predictions of reactor performance. Three common ideal reactor types include: batch reactor, plug flow reactor (PFR) and continuous stirred tank reactor (CSTR). Each of these can be classified based on their reactant concentration profiles with respect to time and space (Figure 1). Batch reactors operate under transient state, where the composition of the reaction mixture changes with respect to time. In contrast, the PFR and CSTR are both continuous reactors. Hence, after an initial transient period, they operate under steady state, where the composition of the reaction mixture is constant with respect to time.[1]

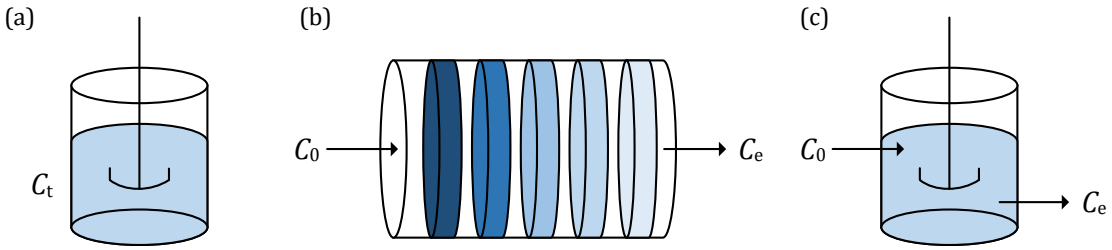

Figure 1. Concentration profiles of three ideal reactor types: (a) batch reactor; (b) plug flow reactor (PFR); (c) continuous stirred tank reactor (CSTR). C_t = [reactant] at time t, C_0 = initial [reactant], C_e = [reactant] in the effluent.

Both the batch reactor and CSTR are assumed to have perfect mixing, which results in a uniform composition throughout the entire reactor. As such, the effluent from a CSTR has the same composition as the mixture within the reactor. For a PFR, where the reaction mixture flows through a tube, there is no mixing in the axial direction giving rise to an infinite number of discrete reaction plugs. The composition of the reaction plugs are the same at a given length along the reactor, however, their composition varies as a function of distance travelled. As the distance travelled increases, the concentration of reactants decreases, resulting in the formation of a concentration gradient along the tube.[2]

The residence time distribution (RTD) of a flow reactor is defined as the distribution of times which molecules spend within the reactor. Determining the RTD reveals information regarding mixing and flow patterns within a reactor. Therefore, the RTD of real reactors can be compared to their corresponding ideal

model to troubleshoot for potential problems, as well as determine the reactor performance for reactions with known kinetics.

The residence time distribution function, $E(t)$, is a probability distribution function which describes the amount of time a molecule could spend within the reactor. Hence, the area under the curve for a plot of $E(t)$ against time, t, is unity (E curve) [Eq (1)].[3] The value of $E(t)dt$ is equal to the fraction of molecules that spend time t inside the reactor. This is known as the cumulative distribution function, $F(t)$, and is obtained by integrating the area under the E curve between the limits t and 0 [Eq (2)].[4]

$$\int_0^\infty E(t)\, dt = 1 \tag{1}$$

$$\int_0^t E(t)\, dt = F(t) \tag{2}$$

As $E(t)$ is a probability distribution function, the mean residence time, t_m, is equal to the first moment of the function *i.e*. the total area under the curve for a plot of $tE(t)$ against t [Eq (3)]. Similarly, the variation around the mean, σ^2, is given by the second moment of the function [Eq (4)].[3] It is standard practice to use the values of t_m and σ^2 when comparing reactors.

$$t_m = \int_0^\infty tE(t)\, dt \tag{3}$$

$$\sigma^2 = \int_0^\infty (t - t_m)^2 E(t)\, dt \tag{4}$$

The RTD for an ideal PFR and CSTR can be derived (Figure 2). In the instance of an ideal PFR with no axial mixing, all molecules will spend an equal amount of time within the reactor ($\sigma^2 = 0$). The RTD is a spike of infinite height and zero width, as defined by the Dirac Delta function [Eq (5)]. For an ideal single CSTR with perfect mixing, not all molecules spend an equal amount of time within the reactor ($\sigma^2 > 0$). Instead, there is an exponential decay in $E(t)$ with time [Eq (6)].[1] τ is the space time, calculated by dividing the reactor volume, V, by the volumetric flow rate, ν ($\tau = V/\nu$).

$$E(t) = \delta(t - \tau) \quad (5)$$

$$E(t) = \frac{1}{\tau} e^{-t/\tau} \quad (6)$$

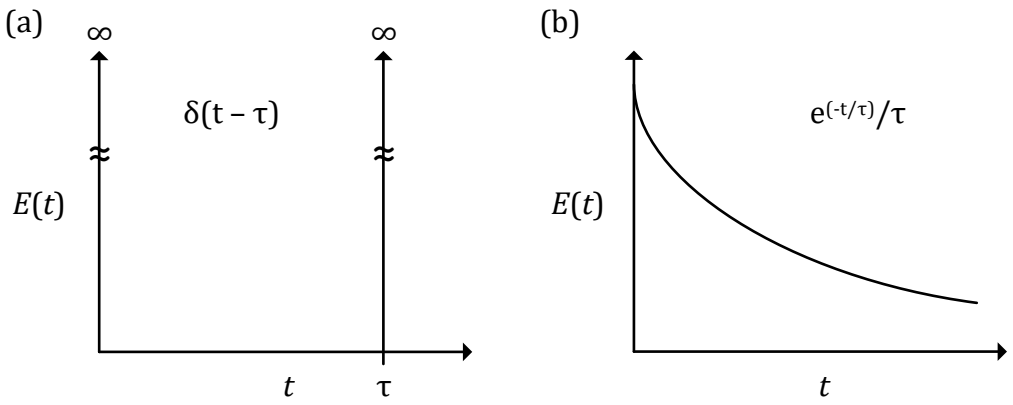

Figure 2. RTD profiles for ideal reactors: (a) PFR: spike of infinite height and zero width; (b) single CSTR: exponential decay of $E(t)$ with increasing time.

In reality the RTDs of reactors will deviate from their ideal models, for example, some axial dispersion will be observed in a tubular reactor. This is caused by frictional forces between the walls of the reactor and the fluid resulting in a non-uniform velocity profile (Figure 3). This is known as Taylor dispersion, and results in a bell-shaped RTD in contrast to the spike expected from the PFR model. The extent of dispersion is dependent on the channel dimensions, where narrower channels reduce the extent of dispersion.[5, 6]

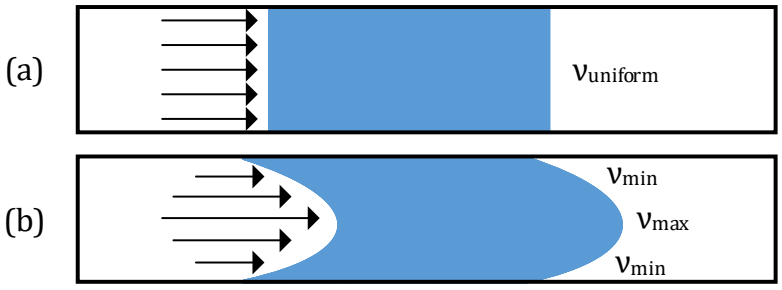

Figure 3. Flow through a tube: (a) ideal plug flow where there is no axial dispersion; (b) Taylor dispersion caused by a non-uniform flow velocity, and resulting in a parabolic profile.

Other discrepancies from the ideal models can occur as a result of reactor failures, including bypassing and dead volume (Figure 4). Bypassing is where some material passes straight through the reactor, and dead volume refers to a volume in the reactor where material becomes stagnant. For a bypassing system, ν of the

non-bypassing material is lower than that expected. Hence, the residence time observed is greater than τ. For a PFR, this would be shown by a RTD with two spikes: one close to the origin for the bypassing material and a second at a time greater than τ. For a CSTR, this results in a slower exponential decay of $E(t)$. For a system with a dead volume, the V of the reactor is less that that expected. Hence, the residence time observed is lower than τ. For a PFR, this would be shown by a RTD with a spike at a time less than τ. For a CSTR, this results in a faster exponential decay of $E(t)$.[3]

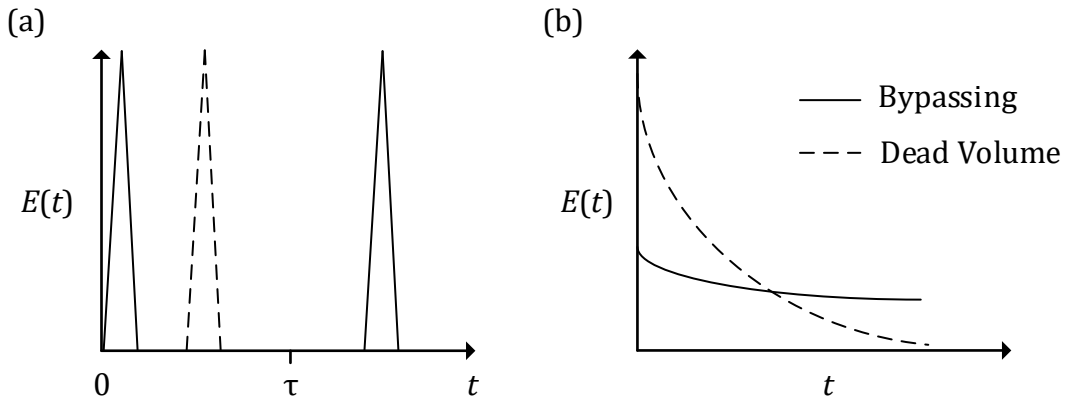

Figure 4. RTD profiles for reactors deviating from ideality: (a) PFR: bypassing – two spikes, one observed at $t > \tau$; dead volume – one spike observed at $t < \tau$; (b) CSTR: bypassing – slower exponential decay of $E(t)$; dead volume – faster exponential decay of $E(t)$.

The PFR and CSTR models highlight an important difference in terms of reactor efficiency. For reactions with an order greater than 0, the rate of reaction decreases as the conversion increases, as a result of a decreasing reactant concentration. In the PFR, the reactant concentration decreases gradually along the length of the reactor; whereas in the CSTR, the reactant concentration drops immediately to a lower value as a result of perfect mixing. Thus, the average rate of reaction for a PFR is higher than a CSTR, and a higher conversion will be achieved for reactors of the same volume. However, a stepwise drop in concentration for a mixed flow reactor can be achieved by using a number, n, of equal volume CSTRs in series, where the volume of each CSTR = V/n. This stepwise drop in concentration indicates that increasing n brings the behaviour of the system closer to that of a PFR, evident in both the concentration and RTD profiles (Figure 5).[7]

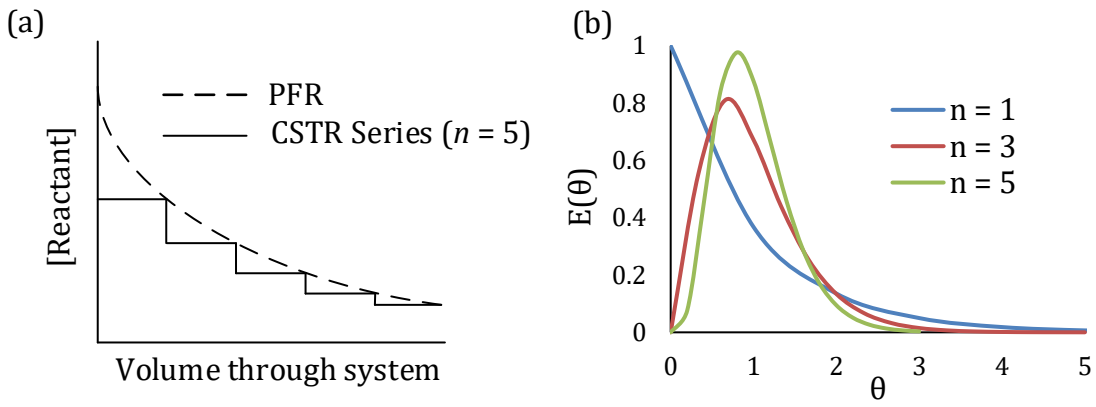

Figure 5. Convergence in behaviour of a CSTR cascade to PFR with increasing *n*: (a) concentration profile: stepwise decrease in reactant concentration along the length of the reactor; (b) RTD: profile becomes sharper with increasing *n*. E(Θ) = normalised distribution function, Θ = normalised residence time.

1.2 Advantages of Flow Chemistry

1.2.1 Diffusion, Mixing and Mass Transfer

The extent of mixing within a reactor influences the conversion and selectivity of reactions. The flow pattern of fluids can be defined by the Reynolds number (*Re*), and calculated according to [Eq (7)], where ρ = density, ν = velocity, D = diameter and μ = viscosity. For example, flow in a tube can be characterised as laminar (*Re* < 2000), transitional (2000 < *Re* < 3000) and turbulent (*Re* > 3000).[8] Turbulent flow has chaotic changes in flow velocity which creates effective mixing between the fluid layers. In contrast, laminar flow has a constant flow velocity resulting in no disruption between the parallel fluid layers. Therefore, mixing in the laminar regime is dependent on the rate of diffusion. Laboratory-scale flow reactors generally operate under the laminar regime due to a combination of low flow rates and small dimensions. Segregated mixing regimes are observed in conventional batch reactors, where turbulent regimes occur in close proximity to the stirrer and laminar regimes occur towards the walls of the vessel.[9] As tubular flow reactors inherently have a higher surface area to volume ratio compared to batch reactors, the rate of diffusion, and therefore the rate of mixing, is significantly higher.

$$Re = \frac{\rho v D}{\mu} \tag{7}$$

For reactions with consecutive steps, the Damköhler number (Da) can be used to describe reaction selectivity. The Damköhler number defines the ratio of the rate of reaction to rate of diffusion [Eq (8)], where k = rate constant, C_0 = initial concentration, n = order of reaction, d_t = diameter of tube and D = diffusion coefficient. Therefore, if $Da < 1$, greater than 95% homogeneity is achieved before the reaction takes place. However, if $Da > 1$, the reaction is diffusion limited resulting in the formation of concentration gradients.[10]

$$Da = \frac{kC_0^{n-1}d_t^2}{4D} \tag{8}$$

Consider a reaction with a competitive consecutive side-reaction (S1 + S2 → P1 and P1 + S2 → P2). When $Da > 1$, S1 and S2 react before the reaction mixture is fully homogeneous. This results in a localised concentration of P1 forming, which can react with S2 to form significant amounts of P2 (Figure 6). This is a phenomenon known as 'mixing-disguised selectivity'.[11] Flow reactors can be used to eliminate these concentration gradients due to their enhanced mixing properties, making them well suited for very fast reactions.[12]

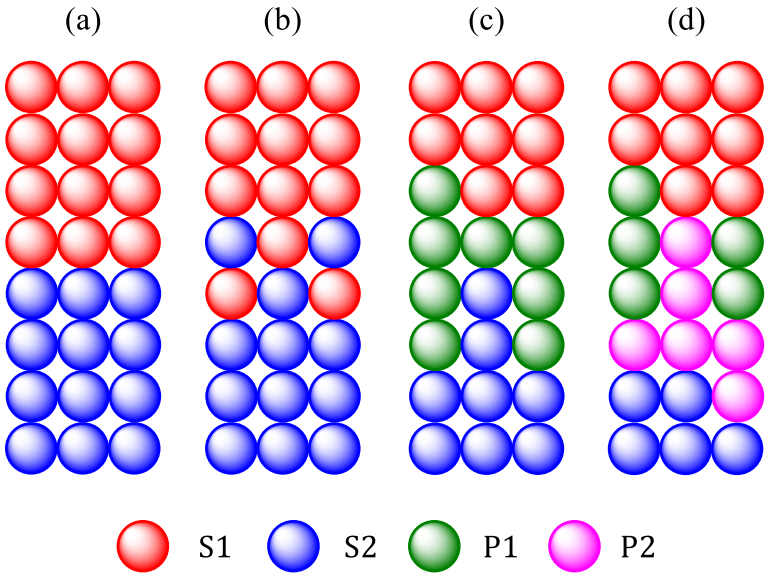

Figure 6. Graphical representation of a reaction with a competitive consecutive side-reaction where $Da > 1$: (a) reactants S1 and S2 prior to mixing; (b) incomplete mixing of reactants S1 and S2 before the reaction starts; (c) localised concentration of desired product P1; (d) S2 reacts with P1 to form significant amounts of P2.

Many chemical reactions involve a combination of multiple phases (gas, liquid and solid), particularly in industry where high concentrations are utilised to reduce the use of solvents. In these systems, efficient mixing is crucial to maximise the

interfacial area between the phases and ensure a high rate of mass transfer. Hence, flow reactors generally perform better than batch reactors for multiphasic reactions. One of the major challenges for performing flow chemistry in microreactors is processing solids which can clog the channels. To circumvent this, solid reagents can be encapsulated in a column to create a packed-bed reactor. This enables heterogeneous catalysed reactions to be conducted in flow, and removes the need to separate the catalyst downstream.[13] However, the reagents often require immobilisation on solid supports to prevent leaching, and the precipitation of solid by-products still remains problematic.

For gas-liquid and liquid-liquid reactions, slug flow is most commonly observed in microfluidic reactors (Figure 7). Slug flow is achieved by mixing in a tee-piece, which creates a build-up of pressure behind one of the perpendicular phases, resulting in droplet formation.[14] The transverse interfaces between the slugs provide a high surface area to volume ratio, and therefore an enhanced rate of mass transfer. Furthermore, formation of a thin film of gas along the walls of the tube creates Taylor recirculation patterns in the liquid phase. This increases the rate of mass transfer by minimising the concentration gradients within the slugs.[15]

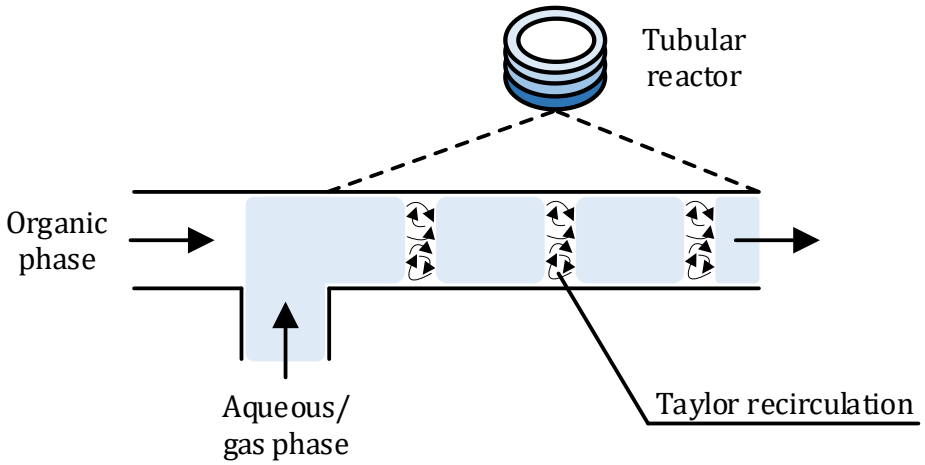

Figure 7. Slug flow commonly observed in a microreactor under liquid-liquid or gas-liquid biphasic conditions.

1.2.2 Enhanced Heat Transfer

Flow reactors have superior heat transfer compared to batch reactors due to a higher surface area to volume ratio. This provides rapid dissipation of heat generated during exothermic reactions, enabling: better temperature control, safer scale-up and a reduced use of energy intensive cryogenic conditions.[16] Furthermore,

reaction selectivity is increased by preventing side-reactions or decomposition of thermally unstable products from occurring. Given this, flow reactors have been utilised for aromatic nitration reactions owing to a strong exotherm and tendency for poor regioselectivity.[17] For example, the nitration of 2-isopropoxybenzaldehyde **1.1** with fuming HNO_3 to form **1.2** was investigated (Scheme 1). On kilogram scale in batch, the heat evolved from the reaction resulted in a poor regioselectivity (**1.2**:**1.3**, 40:60) and isolated yield (30%). Optimisation of this procedure in a microreactor gave an improved regioselectivity (**1.2**:**1.3**, 87:13) and yield (65%), as the enhanced heat transfer prevented the formation of a significant temperature gradient within the reactor.[18]

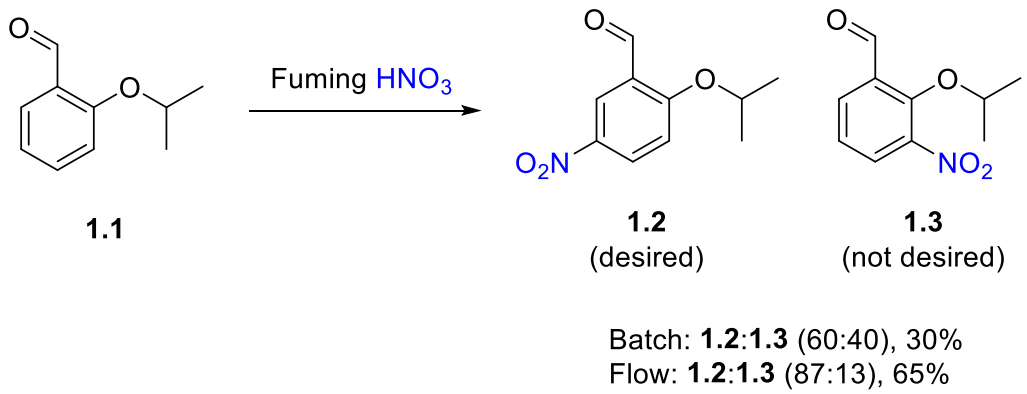

Scheme 1. Nitration of 2-isopropoxybenzaldehyde **1.1** to form desired regioisomer **1.2** and undesired by-product **1.3**. The flow process compared favourably to batch, with a higher regioselectivity and isolated yield, due to rapid dissipation of the exotherm.

1.2.3 Greater Control of Reaction Conditions

The residence time defines the length of time a molecule spends within a reactor. For flow reactors, the residence time can be precisely controlled by adjusting the length of the reactor and the flow rates. This, coupled with better control over mixing and temperature, enables chemical reactions that cannot be achieved in batch.[19, 20] These properties have contributed towards the drive in ideal synthesis by offering protecting-group-free synthesis. For example, it was shown that organolithium transformations could be achieved on ketone bearing aromatics using a microreactor, mitigating the need for wasteful protection and deprotection steps (Scheme 2).[21] Initially, *in situ* generated *o*-pentanoyl-substituted phenyllithium **1.5** was trapped using methanol as an electrophile. At a 3 s residence time, only a 30% yield of **1.6** was achieved due to undesired dimerisation of **1.5** to

give **1.7** in 70% yield. A reduction in residence time to 0.003 s resolved the reactions and afforded **1.6** in a 90% yield. Hence, the high-resolution reaction time control offered by flow reactors enables transformations that better align with sustainable chemistry.

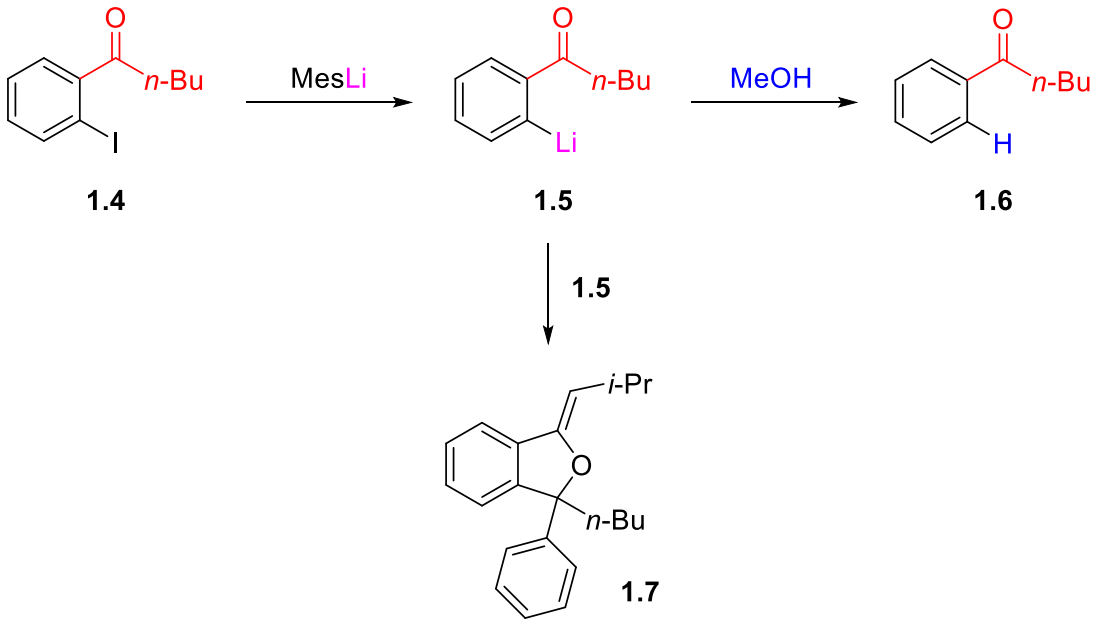

Scheme 2. Lithiation of aryl iodide **1.4** with MesLi yielding *o*-pentanoyl-substituted phenyllithium **1.5**, followed by quenching with methanol to produce protonated product **1.6**. Dimerisation of **1.5** forms undesired by-product **1.7**.

1.2.4 High T/p Reactors and Safer Use of Hazardous Reagents

Increasing the temperature of a reaction increases the rate of reaction, as defined by the Arrhenius equation. Therefore, in cases where selectivity is not reduced at higher temperatures, the simplest and cheapest way to increase productivity is to increase the reaction temperature.[22] However, batch reactions are often limited to the boiling point of the solvent, as high-pressure batch reactors in manufacturing are large and expensive. In contrast, the pressure and temperature of continuous flow reactors can be safely manipulated above atmospheric conditions. This often results in a reduction in reaction time and reactor size, thereby offering significant benefits in terms of process intensification.[23]

A key consideration during process development is the safety of the reagents used and/or intermediates generated during a reaction. Under continuous flow operation, only small amounts of the chemical species are exposed to the reaction conditions at any given time. This mitigates the risks linked with the accumulation of hazardous intermediates, and enables hazardous reagents to be used in

combination with high-temperature/high-pressure conditions.[24] For example, the use of a silicon carbide microreactor allowed the development of a rapid Wolff-Kishner reduction (Scheme 3a).[25] The use of flow conditions removed the risks associated with build-up of explosive hydrazine gas in the headspace of the reactor. Similarly, explosive hydrazoic acid gas was generated *in situ* to achieve a 100% atom economical synthesis of tetrazoles (Scheme 3b).[26] Furthermore, the use of high T/p conditions reduced the reaction time from 24 h in batch to 10 min in flow.[27]

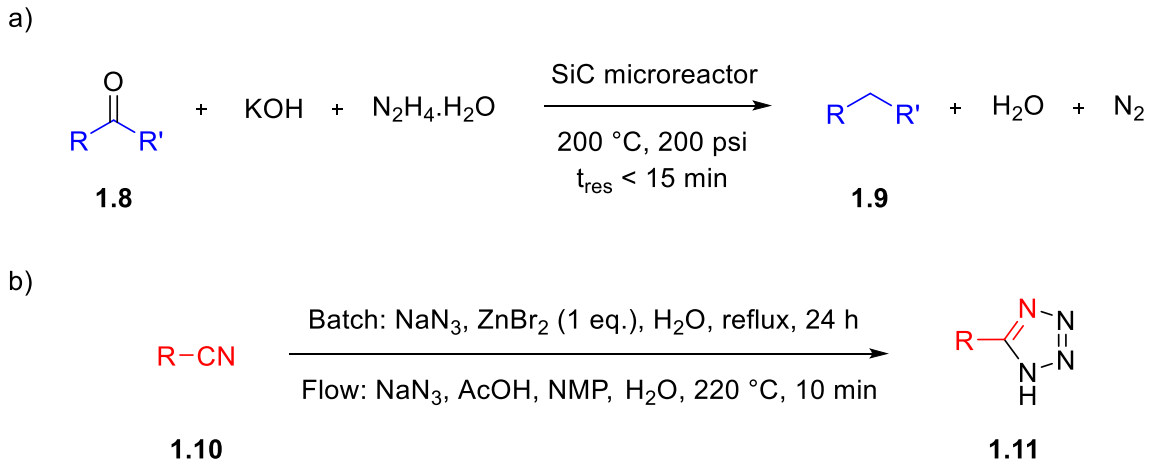

Scheme 3. Examples of processes benefitting from high T/p conditions and improved safety in flow: (a) Wolff-Kishner reduction using hydrazine; (b) synthesis of tetrazoles using NaN_3 generated *in situ*.

1.3 Automation of Continuous Flow Systems

1.3.1 Analysis and Screening

The automation of laboratory equipment, such as chromatography autosamplers, removes the need for chemists to conduct repetitive and laborious tasks, providing them more time to focus on research-based challenges.[28] Flow chemistry is particularly well-suited for automated analysis, as in-line and on-line process analytical technologies (PAT) can be integrated at multiple points along the reactor.[29] This removes the need for sample preparation, and thus generates large amounts of real-time data which is more representative of reactor performance and reaction composition. Furthermore, unstable intermediates can be detected which helps provide greater mechanistic understanding.[30] The advantages and

disadvantages of the analytical techniques commonly used in organic chemistry are highlighted in Table 1.

Table 1. Advantages and disadvantages of the different analytical techniques used commonly in organic chemistry. IR = infrared; UV-Vis = Ultraviolet-Visible; NMR = nuclear magnetic resonance; HPLC = high performance liquid chromatography; GC = gas chromatography; MS = mass spectrometry.

	Analytical Technique					
Properties	**IR**	**UV-Vis**	**NMR**	**HPLC**	**GC**	**MS**
Structural information	✓	✗	✓	✗	✗	✓
Quantitative	✓	✓	✓	✓	✓	✓
Short analysis time	✓	✓	✓	✗	✗	✓
Short method development	✓	✓	✓	✗	✗	✓
Simple calibration (no cross-validation)	✗	✗	✓	✓	✓	✗
Easy data analysis for complex mixtures	✗	✗	✗	✓	✓	✗

High-throughput experimentation (HTE) is where large numbers of experiments are conducted in parallel, enabling rapid screening of substrates and conditions for reaction discovery and optimisation. The miniaturisation of HTE is desirable to ensure its applicability towards highly functionalised compounds. Nanomole-scale HTE utilising biological-assay well plates to evaluate 1536 reactions in 2.5 hours was achieved.[31] However, these plate-based approaches suffer from limitations such as the use of non-volatile solvents and ambient temperatures to avoid evaporation. The development of a nanomole-scale flow system circumvented these limitations, whilst maintaining a high throughput of >1500 reactions per 24 hours.[32] This was achieved by the use of a liquid handler to create 5 μL reaction slugs containing two reactants, catalyst, ligand and base (1 μL each). These slugs were introduced to the desired reaction solvent, where diffusion created a homogeneous 500 μL reaction slug. Notably, this approach enabled the screening of solvents as a discrete variable in flow, without the need to make all combinations of reagent stock solutions.[33] The analysis time was minimised by using two ultra performance liquid chromatography-mass spectrometry (uPLC-MS) instruments in parallel, such that when one instrument was performing analysis, the other was waiting for the next reaction slug (Figure 8).

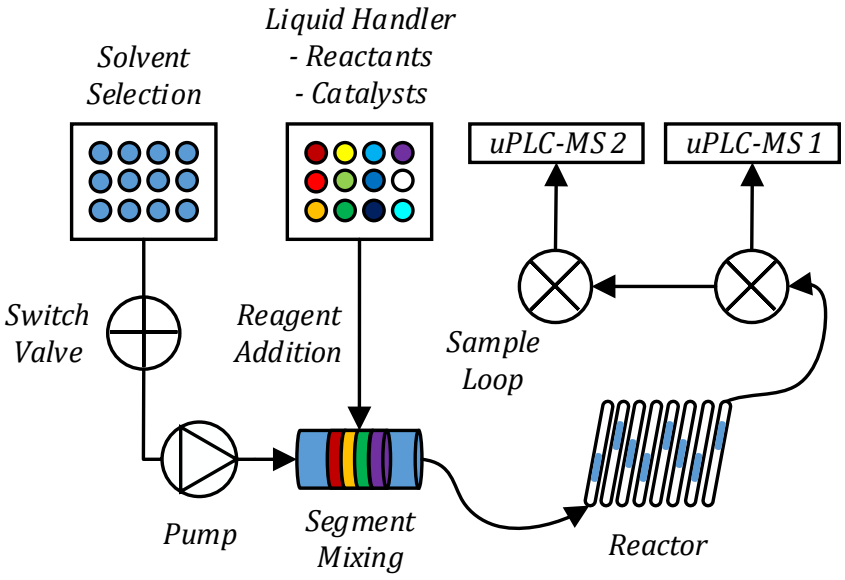

Figure 8. Nanomole-scale flow system for high throughput screening of discrete variables.

1.3.2 Process Control

The ability to maintain steady state operation by controlling process variables, such as pump flow rates, is crucial for consistent product quality and safety. This can be achieved by creating a feedback loop, where changes to the process variables are made dependant on the real-time interpretation of responses from integrated PAT. An example of this includes the controlled dosing of reagents into a segmented flow stream, as developed by Ley *et al.*[34] This was demonstrated on a reduction crotylation sequence of ester **1.12** (Scheme 4). The formation and dispersion of intermediate aldehyde **1.13** from DIBAL reduction of ester **1.12** was monitored using in-line IR. This enabled the flow rate of boronate **1.14** to be controlled, such that a 1:1 stoichiometry of **1.13** and **1.14** was accurately maintained over a stream of varying concentration. Therefore, this method avoided wasting the expensive chiral boronate **1.14**, and provided a safeguard against upstream equipment failure.

Similarly, feedback loops can be used to control work-up unit operations for continuous purification processing. In terms of gravity-based separation, a 'computer-vision' approach was adopted where inlet and outlet pump flow rates were controlled by monitoring the level of the solvent interface.[35] In other work, in-line pH monitoring was used to control the addition of NaOH for quenching of a Boc deprotection under aqueous HCl conditions.[36]

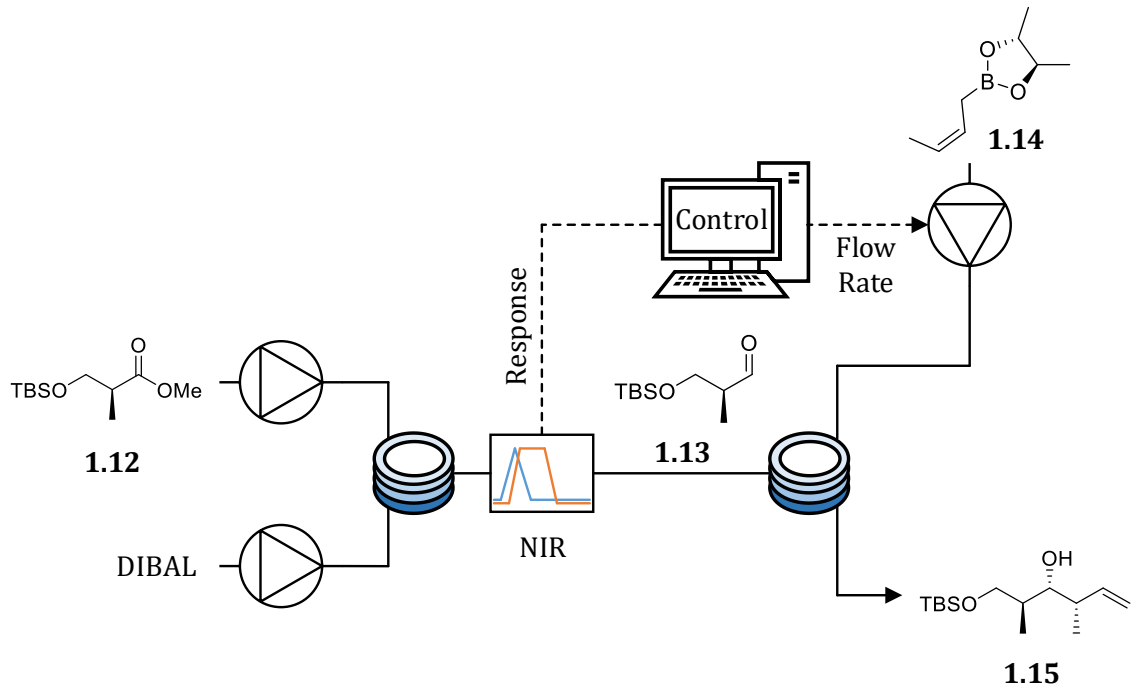

Scheme 4. Diastereoselective reduction crotylation sequence of ester **1.12** to alcohol **1.15**. Accurate dosing of the chiral boronate **1.14** in a 1:1 stoichiometry with aldehyde intermediate **1.13** was achieved using in-line IR monitoring.

1.3.3 Optimisation

1.3.3.1 One-Variable-at-a-Time

Autosampling of reaction mixtures in flow enables a series of predefined experiments to be conducted in an automated fashion. This is useful for screening reaction conditions during optimisation studies. One strategy is one-variable-at-a-time (OVAT) optimisation, where only one variable is changed per experiment. This is represented in Figure 9 for a two-variable optimisation. Initially, variable ***Y*** is held fixed at y_i whilst variable ***X*** is varied along the line ***A*** to ***B***, identifying point ***C*** as the best result. Variable ***X*** is then held fixed at x_i whilst variable ***Y*** is varied along the line ***D*** to ***E***, identifying point ☆ as the optimum for the reaction. However, this approach suffers from two major drawbacks: (i) failure to account for the effect of interactions between the variables; (ii) exploration of a very limited region of experimental space. Therefore, OVAT optimisation risks failing to locate the optimum for response surfaces similar to that shown in Figure 9, as the absence of information regarding variable interactions prevents efficient exploration of the entire experimental space.[37]

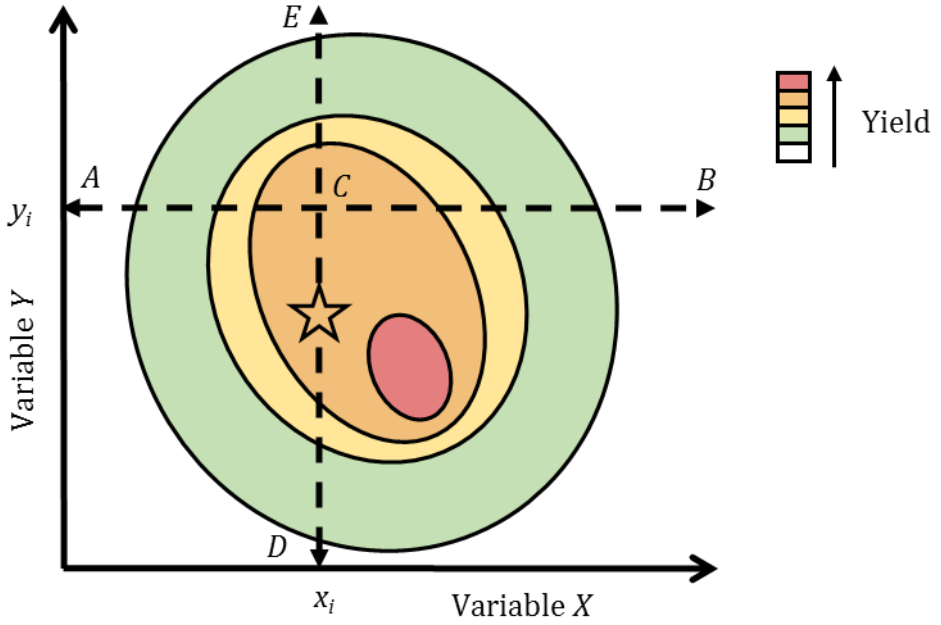

Figure 9. An example of a two-variable OVAT optimisation. ☆ = optimum.

This approach was utilised to optimise a Sonogashira reaction for the synthesis of a matrix metalloproteinase inhibitor in flow.[38] The use of automated flow experiments resulted in a combined optimisation and 100 g scale production time of just 50 hours. However, the Sonogashira reaction represents a complex catalytic process requiring a palladium catalyst and copper co-catalyst. Hence, there is a high risk that the true optimum was not located due to unidentified synergistic effects between the continuous variables and catalytic species.

1.3.3.2 Design of Experiments

Design of experiments (DoE) is a statistical optimisation approach. A series of predefined experiments are conducted, with the aim of identifying the effect of each individual (main) factor and the effect of synergistic and antagonistic interactions between the factors. This enables polynomial modelling of a response surface for the defined experimental space and prediction of the global optimum.

Full factorial designs (FFD) are used to screen the factors that are assumed to have a significant effect on the response, by determining the coefficient for each main and interaction term. Each factor is assigned a discrete level and experiments are conducted at all possible combinations of these levels across all factors. In addition, experiments are conducted in replicate at the centre-point conditions to give a measure of repeatability. The number of experiments required, N, is given by [Eq (9)], where n = number of levels, k = number of factors and m = number of

centre-point replicates. Hence, for a 2-level 3-factor FFD with upper and lower levels +1 and -1 respectively, the experimental space is defined by a cube with experiments at each vertex (Figure 10).[39]

$$N = n^k + m \tag{9}$$

2-level 3-factor FFD
$2^3 + 3 = 11$ exp

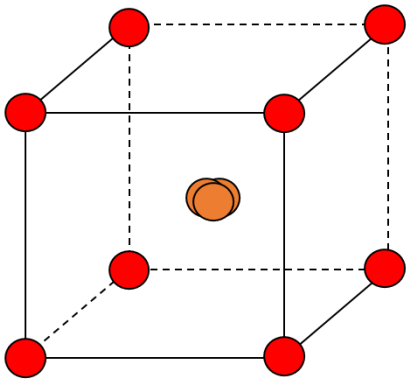

Exp	X_1	X_2	X_3
1	+1	+1	+1
2	-1	+1	+1
3	+1	-1	+1
4	-1	-1	+1
5	+1	+1	-1
6	-1	+1	-1
7	+1	-1	-1
8	-1	-1	-1
9	0	0	0
10	0	0	0
11	0	0	0

$$Y = b_0 + b_1X_1 + b_2X_2 + b_3X_3 + b_{12}X_1X_2 + b_{13}X_1X_3 + b_{23}X_2X_3 + b_{123}X_1X_2X_3$$

Figure 10. A 2-level 3-factor FFD with 3 centre-point replicates. The design requires 11 experiments to determine the coefficients, *b*, of the main and interaction terms. 2^k factorial experiments = red circles, centre-point experiments = orange circles.

When processes have long reaction times and/or involve high value reagents it is important to keep the number of experiments required to a minimum. The coefficients of the main and interaction terms can be determined by conducting an initial FFD screening. When a factor is found to have no significant effect on the response, it can be excluded from any subsequent optimisation studies, thus reducing the overall number of experiments required. However, the number of experiments for the initial FFD increases exponentially with an increase in the number of factors. Hence, when the number of factors is high, the use of an FFD can be impractical.

In these cases, fractional factorial designs can be used, which confound main effects and/or interaction terms to reduce the number of experiments. This approach utilises the sparsity-of-effects principle, which states that a system is dominated by main effects and low-order interactions. Therefore, confounding

high-order interactions with main effects will have a negligible effect on model accuracy. An important property of the design is the resolution, which defines the ability to separate main effects and low-order interactions. The extent of confounding for resolution III, IV and V designs are summarised in Table 2. The number of experiments required, and expression notation, for a fractional factorial design is given by [Eq (10)], where n = number of levels, k = number of factors and p = number of generators (design settings).[40, 41]

$$N = n^{k-p} \tag{10}$$

Table 2. Extent of confounding for different resolution fractional factorial designs.

Resolution	Extent of Confounding
III	Main effects confounded with two-factor interactions.
IV	Main effects not confounded with two-factor interactions; two-factor interactions confounded with two-factor interactions.
V	Main effects not confounded with ≤ three-factor interactions; two-factor interaction not confounded with two-factor interactions; three-factor interactions confounded with two-factor interactions.

For example, a 2^{4-1} fractional factorial design was used to optimise the reaction variables for the synthesis of active pharmaceutical ingredient (API) AZD0530 **1.18** (Scheme 5).[42] The variables studied were: equivalents of base (*A*), equivalents of water (*B*), temperature (*C*) and equivalents of alcohol **1.17** (*D*). The design was constructed using the generator $I = ABCD$, which implies $D = ABC$. A 3-factor FFD was produced for *A*, *B* and *C*, which was used to construct the levels of *D* based on $D = ABC$. This resulted in a resolution IV design, as indicated by the number of letters in the generator. Hence, each main effect was confounded with a three-factor interaction ($A = BCD$, $B = ACD$, $C = ABD$, $D = ABC$) and each two-factor interaction was confounded with another two-factor interaction ($AB = CD$, $AC = BD$, $AD = BC$). This enabled the main effects of the four factors to be studied in half the number of experiments compared to a 2^4 FFD.

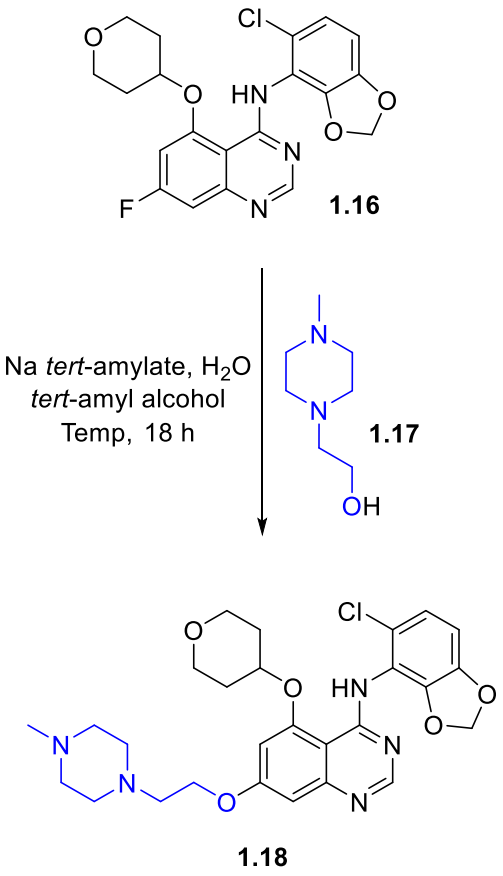

Exp	*A*	*B*	*C*	*D = ABC*
1	+1	+1	+1	+1
2	-1	+1	+1	-1
3	+1	-1	+1	-1
4	-1	-1	+1	+1
5	+1	+1	-1	-1
6	-1	+1	-1	+1
7	+1	-1	-1	+1
8	-1	-1	-1	-1
9	0	0	0	0
10	0	0	0	0

Scheme 5. A 2-level fractional factorial design (resolution IV) with 2 centre-points used to optimise the reaction variables for the synthesis of AZD0530 **1.18**.

In some cases, the response surface may have a significant degree of curvature. Therefore, accurate model predictions cannot be made using a factorial design, which assumes a linear relationship between each factor, *X*, and the response, *Y*. The inclusion of centre-point replicates provides a useful indication for the presence of curvature, as a bad fit would be observed if the relationship was non-linear. If curvature is detected, an optimisation design is required to characterise the square terms. 2-level full factorial designs can readily be extended to central composite optimisation designs by the inclusion of axial points, which are defined by [(±α, 0, 0), (0, ±α, 0), (0, 0, ±α)] for a 3-factor optimisation. The face centred composite (CCF, α = 1, Figure 11) design is best suited for the optimisation of chemical reactions, as the parameter limits are usually dictated by the experimental limits of the equipment, making α > 1 infeasible. The number of experiments required for a CCF design is given by [Eq (11)].[39] An alternative to central composite optimisation designs is the Box-Behnken, which is discussed in more detail in Chapter 3.

$$N = 2^k + 2k + m \tag{11}$$

3-factor CCF
$2^3 + (2\times3) + 3 = 17$ exp

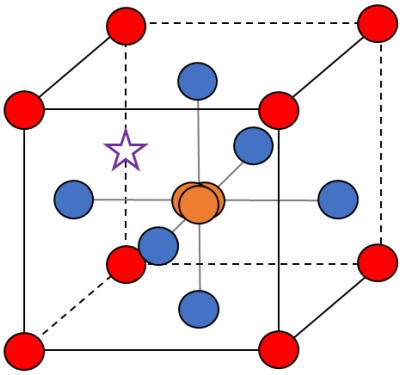

Exp	X_1	X_2	X_3
1-8	FFD		
9	+1	0	0
10	-1	0	0
11	0	+1	0
12	0	-1	0
13	0	0	+1
14	0	0	-1
15	0	0	0
16	0	0	0
17	0	0	0

$$Y = b_0 + b_1X_1 + b_2X_2 + b_3X_3 + b_{12}X_1X_2 + b_{13}X_1X_3 + b_{23}X_2X_3 + b_{123}X_1X_2X_3 + b_{11}X_1^2 + b_{22}X_2^2 + b_{33}X_3^2$$

Figure 11. A 3-factor CCF design with 3 centre-points. The design requires 17 experiments to determine the coefficients, *b*, of the main, interaction and square terms. 2^k factorial experiments = red circles, centre-point experiments = orange circles, axial experiments = blue circles, optimum = ☆.

1.3.3.3 Self-Optimisation

Self-optimisation is an algorithmic optimisation approach using a computer controlled reactor platform. The combination of a flow reactor, system controlled in/on-line analytical tools and an optimisation algorithm creates a feedback loop, where the reaction conditions (pump flow rates and temperature) are changed within predefined parameter limits based on the results of previous experiments (Figure 12).[43] This process is carried out iteratively until convergence on the optimum is achieved, or an alternative termination criterion is satisfied. One advantage of this approach is that black-box feedback optimisation algorithms do not require *a priori* information, as experimental data is modelled to determine subsequent experiments. In this way, intelligent analysis of the experimental space reduces the number of experiments required, providing a faster, cheaper and 'greener' method for reaction optimisation. Furthermore, autonomous real-time interpretation of data closes the experimental loop, enabling minimal human intervention during the entire optimisation process.[44, 45]

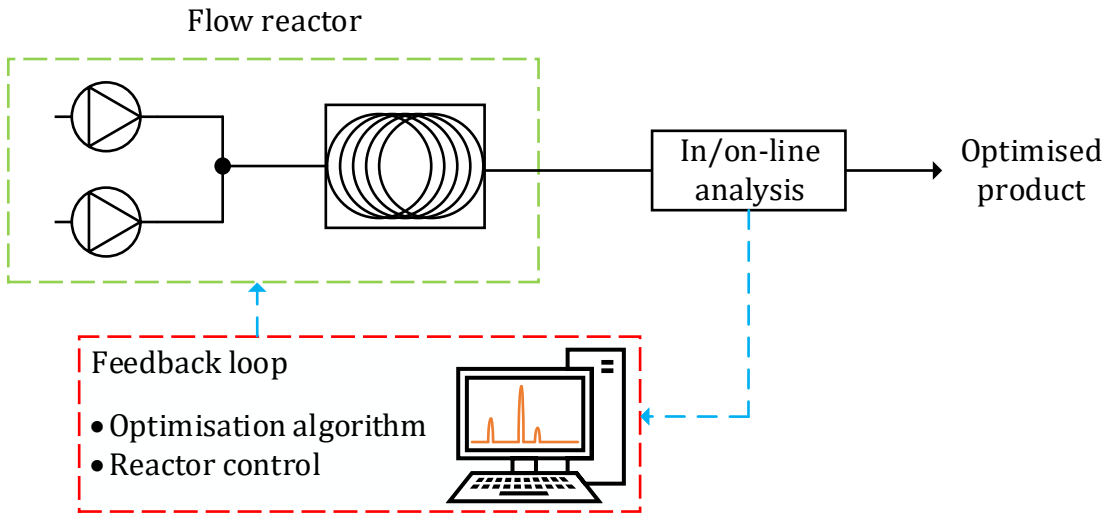

Figure 12. Schematic of a self-optimising continuous flow reactor.

All reported uses of self-optimisation between the 1st of January 2007 and the 28th of February 2019 are summarised in Table 3. Inspection of Table 3 reveals that most reported cases have optimised reactions using relatively simple substrates, with only three reports describing the use of self-optimisation towards API or natural product synthesis.[46-48] This indicates that an increase in experimental efficiency is required to enable the optimisation of reactions involving high-value reagents. Rather, research has predominantly focused on the development and application of PAT, with examples covering all of the major analytical tools used in organic synthetic chemistry (HPLC, GC, IR, NMR, MS). Furthermore, studies have thus far been limited to the optimisation of continuous variables (residence time, temperature, equivalents), with only one reported example including discrete variables (solvent, catalyst, ligand).[49] This has been partly due to the complexity of the set-up required for a droplet-flow approach. Also, investigations have only been concerned with single-step reaction optimisation, overlooking the optimisation of work-up unit operations and complex multi-step processes.

The majority of the algorithms used can be categorised as either local search or global search. The choice of algorithm is an integral part of a self-optimising system, as it controls the experimental efficiency and the nature of the results obtained.[50] Therefore, algorithm development will play a key role in solving many of the limitations highlighted above.

Table 3. A summary of all reported applications of self-optimisation between 01/01/2007 and 28/02/2019. LC = liquid chromatography; DLS = dynamic light scattering; GPC = gel permeation chromatography; SNOBFIT = stable noisy optimisation by branch and fit; NMSIM = Nelder-Mead simplex; SMSIM = super modified simplex; MOAL = multi-objective active learner; TSEMO = Thompson sampling efficient multi-objective; MINLP = mixed integer nonlinear programming.

Year	Reaction(s)	Analysis	Algorithm	Ref
2007	Synthesis of CdSe nanoparticles	Fluorescence spectroscopy	SNOBFIT	51
2010	Synthesis of CdSe nanoparticles	Fluorescence spectroscopy	NMSIM	52
2010	Heck-Matsuda cross-coupling of 4-chlorobenzotrifluoride and 2,3-dihydrofuran	HPLC	NMSIM	53
2010	Knoevenagel condensation between *p*-anisaldehyde and malononitrile; oxidation of benzyl alcohol to benzaldehyde	HPLC	NMSIM; gradient-based; SNOBFIT	54
2011	Dehydration of ethanol over γ-alumina in $scCO_2$; methylation of 1-pentanol with DMC over a γ-alumina catalyst in $scCO_2$	GC	SMSIM	55
2011	Methylation of 1-pentanol with DMC and MeOH over a γ-alumina catalyst in $scCO_2$	GC	SMSIM	56
2012	Paal-Knorr reaction between 2,5-hexandione and ethanolamine	IR	Gradient-based	57
2012	Methylation of 1-pentanol with DMC over a γ-alumina catalyst in $scCO_2$	GC	SMSIM	58
2013	Solvent-free methylation of 1-pentanol with DMC over a γ-alumina catalyst	IR	SMSIM; SNOBFIT	59
2015	Catalytic reaction of aniline with DMC in toluene and $scCO_2$	GC	SMSIM	60
2015	Imine formation by reaction of benzaldehyde and benzylamine	NMR	NMSIM	61
2015	Mono-alkylation of *trans*-1,2-diaminocyclohexane with 4-methoxybenzyl chloride	LC/MS	Feedback DoE	62
2015	Emulsion copolymerisation	DLS; GC	MOAL	63
2016	Methylation of methyl nicotinate with aqueous methylamine	MS	SNOBFIT	64
2016	Final step in the synthesis of EGFR kinase inhibitor AZD9291	HPLC	SNOBFIT	46

2016	Heck-Matsuda cross-coupling of *cis*-2-buten-1,4-diol and 4-chlorobenzene diazonium tetrafluoroborate	GC/MS	NMSIM	65
2016	Suzuki-Miyaura cross-coupling (4 reactions)	HPLC	Feedback DoE	49
2016	Hydration of 3-cyanopyridine over MnO_2; Appel reaction of 1-phenylethanol forming (1-bromoethyl)benzene	MS; IR	Complex Simplex	66
2017	Synthesis of *o*-xylenyl C_{60} adducts	HPLC	SNOBFIT	67
2018	Claisen-Schmidt condensation between acetone and benzaldehyde	HPLC	SNOBFIT	68
2018	S_NAr reaction between 2,4-difluoronitrobenzene and morpholine; *N*-alkylation of α-methylbenzylamine with benzyl bromide	HPLC	TSEMO	69
2018	Steps towards the synthesis of carpanone	HPLC; NMR	NMSIM	47
2018	Buchwald-Hartwig amination; Horner-Wadsworth-Emmons olefination; reductive amination; Suzuki-Miyaura cross-coupling; S_NAr; photoredox; ketene generation and [2+2] cycloaddition	HPLC	SNOBFIT	70
2018	Suzuki-Miyaura cross-coupling of 3-chloropyridine and 2-fluoropyridine-3-boronic acid pinacol ester	HPLC	MINLP 1; MINLP 2	71
2018	Steps towards the synthesis of lidocaine; steps towards the synthesis of bupropion	IR	NMSIM	48
2018	Semihydrogenation of 2-methyl-3-butyn-2-ol to 2-methyl-3-buten-2-ol	GC	SNOBFIT	72
2018	Photoredox iridium-nickel dual-catalysed decarboxylative arylation cross-coupling of Cbz-Pro-OH and various aryl halides	HPLC	Feedback DoE	73
2018	[2+2] photocyclisation reaction between benzophenone and furan	IR	NMSIM	74
2019	Thermal RAFT polymerisation of *n*-butyl acrylate	GPC	Not stated	75

1.4 Algorithms for the Self-Optimisation of Chemical Reactions

1.4.1 Local Search

The basic simplex approach is a local optimisation method first introduced by Spendley *et al.* in 1962.[76] The simplex is a convex polyhedron with $n + 1$ vertices, where n is the number of variables and each vertex represents a function evaluation. The initial simplex can either be user-defined or random, and moves across the predefined experimental space through a series of successive reflections. The vertex corresponding to the worst result is reflected through the centroid of the other points, and is replaced with a new function evaluation. This process is carried out iteratively until an optimum is identified (Figure 13). The disadvantage of this approach is that the size of the initial simplex dictates the efficiency with which the experimental space is explored.

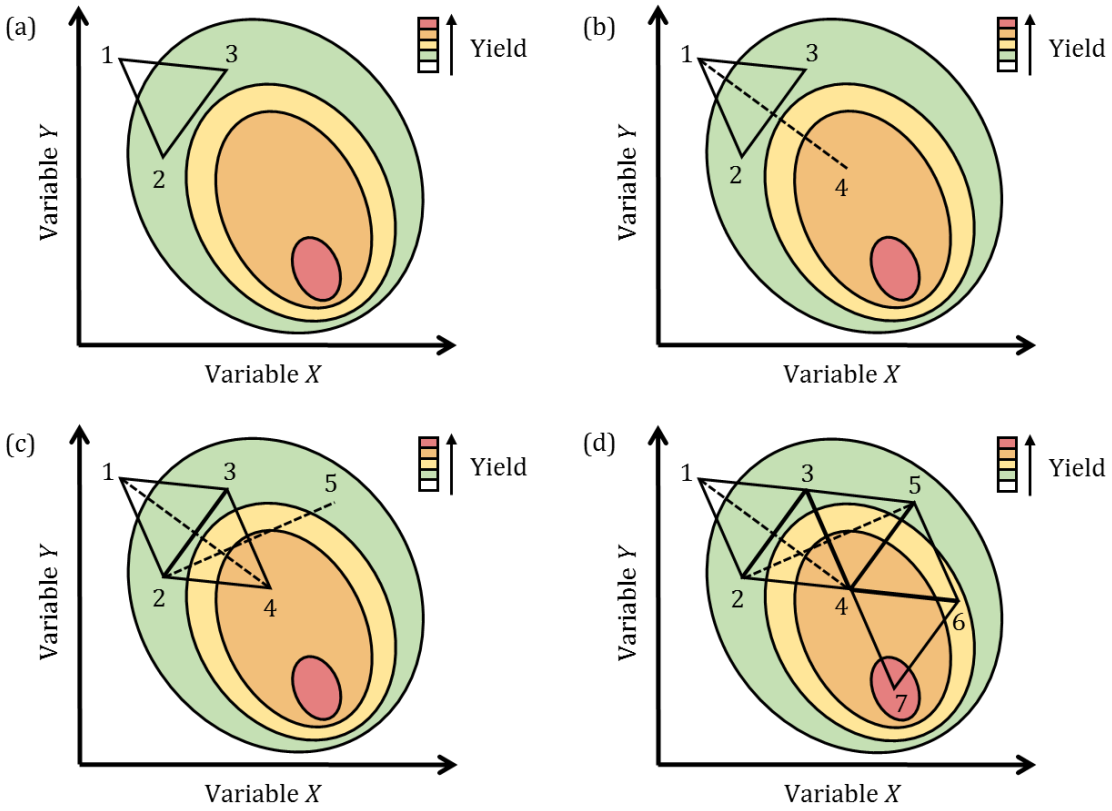

Figure 13. Graphical representation of a 2-variable basic simplex optimisation: (a) initial polyhedron with $n + 1$ vertices is generated; (b) the worst result **1** is reflected through the centroid of the other vertices **2** & **3**, and replaced with new function evaluation **4**; (c) the worst result **2** in the updated simplex is reflected through the centroid of the other vertices **3** & **4**, and replaced with new function evaluation **5**; (d) the process is repeated iteratively until convergence on a local optimum **7**.

The Nelder-Mead simplex (NMSIM) was later reported as a less rigid improvement on the basic simplex.[77] This approach introduced additional geometrical transformations, including: inside contraction, multiple contraction, outside contraction, reflection and expansion (Figure 14). This enables the simplex to adapt itself to the local landscape, and contract in the neighbourhood of the optimum. The coefficients for these transformations are fixed at values that were found to be suitable for a wide range of optimisation problems.

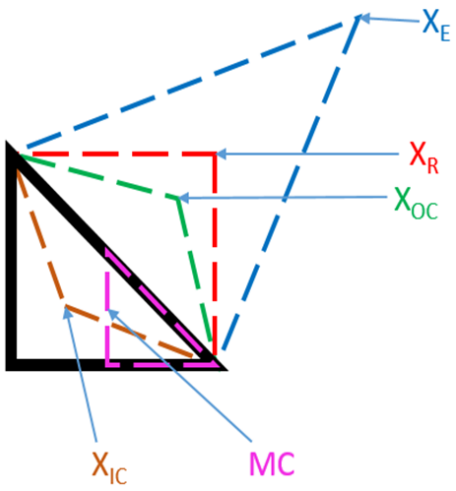

Figure 14. Geometric transformations of the Nelder-Mead simplex: inside contraction (X_{IC}); multiple contraction (MC); outside contraction (X_{OC}); reflection (X_R); expansion (X_E).

To further increase the adaptability of the simplex method, Routh *et al.* proposed modifications to allow the coefficients of the geometric transformations to change during the optimisation based on the local landscape.[78] A graphical representation of an expansion in the super modified simplex (SMSIM) approach is shown in Figure 15. In contrast to NMSIM, an experiment is conducted at both the centroid **P** and reflected **R** vertices of the initial simplex **WNB**. A second order polynomial is then fit through points **WPR** and extrapolated to determine the optimum expansion distance to vertex **E**. Similarly, when an expansion is not expected to improve the response, the polynomial model can predict the optimum contraction distance. Hence, SMSIM is a faster optimisation method compared to NMSIM, as it is better able to elongate along steep gradients in the local landscape.

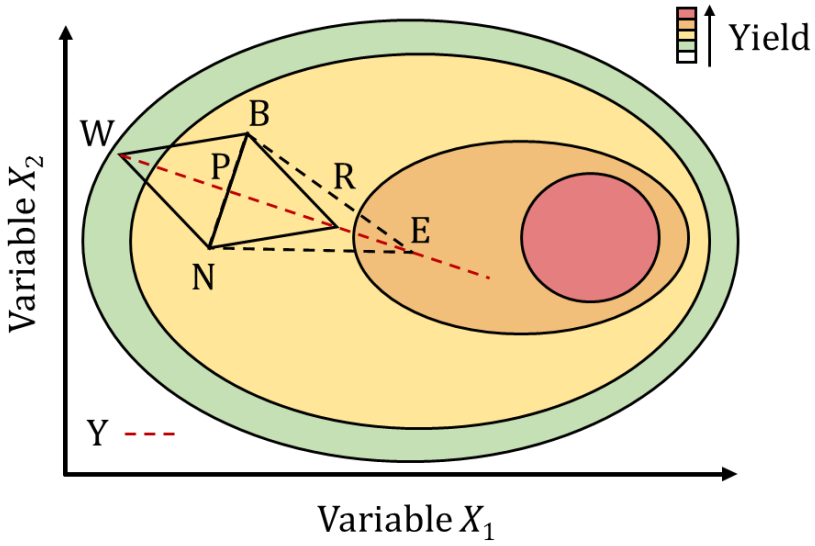

Figure 15. Graphical representation of a SMSIM geometrical transformation for a 2-variable problem. The worst result **W** is reflected through the centroid **P** of the best **B** and next best **N** vertices, and a function evaluation carried out at reflected point **R**. An additional function evaluation is conducted at **P**, and a second order polynomial at **WPR** used to predict the optimum expansion coefficient along the line **Y**. The next experiment is conducted at vertex **E**.

Gradient-based methods, such as steepest descent (or steepest ascent for maximisation problems),[41] are another form of local optimisation technique. The steepest ascent method is initialised by a 2^k FFD design centred on a random point. A polynomial model is fit to the local landscape and subsequent experiments conducted along the trajectory of steepest ascent. When an experiment gives a worse response than the previous experiment, a new 2^k FFD is conducted around the current best point. The new model is used to identify if the optimum has been passed or if a change of direction is required (Figure 16).

Modifications of the steepest descent algorithm include conjugate gradient[79] and Armijo conjugate gradient.[80] The conjugate gradient algorithm utilises a weighted sum of the last search direction and the direction calculated from the steepest descent method to determine the new trajectory. This prevents large changes in search direction, and thus avoids erratic paths across difficult terrain. The Armijo conjugate gradient algorithm increases the efficiency of the search by varying the step size along the trajectory. This reduces the number of experiments required compared to when a fixed step size is used, particularly in cases where the initial point is far from the local optimum.

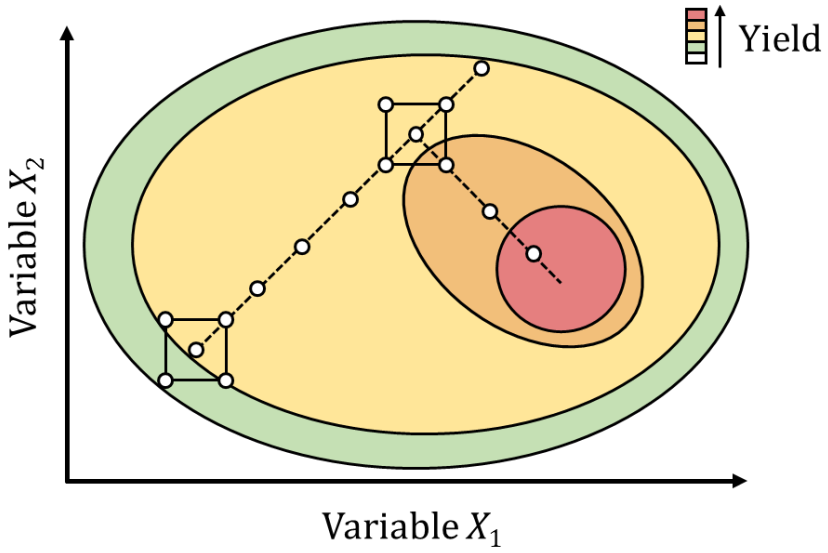

Figure 16. Graphical representation of the steepest ascent method. An initial 2^k FFD is performed, followed by experiments along the trajectory of steepest ascent to the optimum.

1.4.2 Global Search

Global search algorithms are designed to efficiently locate the global optimum of more complex response surfaces. In these cases, local search methods can become trapped on local optima and thus yield an overall sub-optimal result. One solution to this is to run a local optimiser multiple times at uniformly distributed initial points throughout the experimental space. However, this approach requires many iterations, and is therefore unsuitable for expensive-to-evaluate problems such as the experimental optimisation of chemical reactions.

Genetic algorithms (GA) are stochastic optimisers which follow the theory of evolution in nature. Every iteration of the algorithm is comprised of a fixed-size population containing individuals, where an individual is an experiment in the context of reaction optimisation. Each experiment in the population is evaluated and the experiments which give the best response are selected to form the new population (Figure 17). The new population is formed via two different mechanisms: (i) reaction variables from different experiments are interchanged (crossover); (ii) a single variable of an experiment is randomly changed (mutation).[81] Combination of a GA with a HTE platform enabled the optimisation of a catalyst, cocatalyst and ligand combination for the oxidation of methane.[82] However, this optimisation required 384 experiments, which reflects the large population size required for GA.

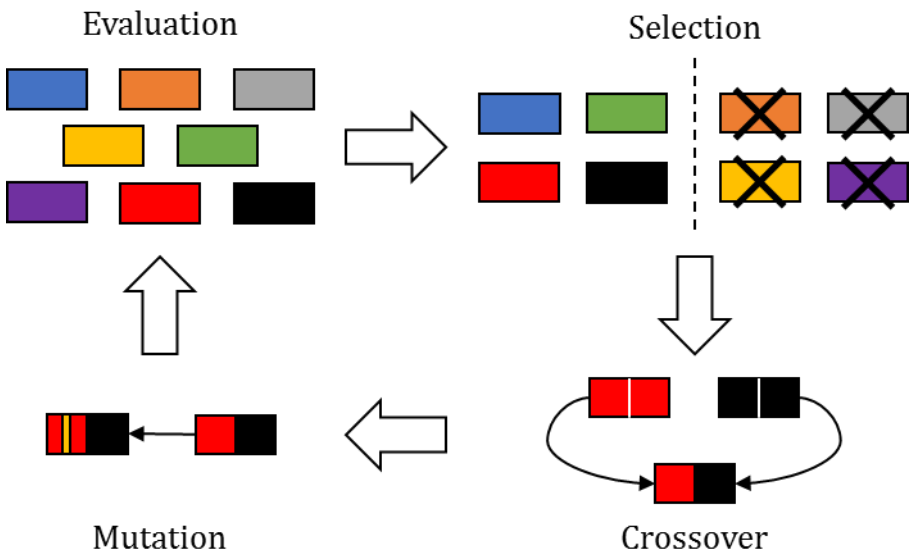

Figure 17. Diagram showing the iterative process of a genetic algorithm (GA). The population is evaluated and the best experiments selected to undergo crossover and mutation to produce the next population for evaluation.

SNOBFIT is currently the only single objective global optimisation algorithm which has been used in self-optimisation.[83] It is a derivative-free optimiser, which means it does not require any gradient information regarding the objectives response surface. The algorithm builds local polynomial surrogate models in subsections of the experimental space. Surrogate models are models of the process variables to an objective function built using the current data, which can be optimised *in silico* as a cheaper alternative to conducting experiments.[84] SNOBFIT uses these surrogate models to exploit areas of high interest (class 1, 2 & 3 experiments). In addition, experimental space vacant of data is continually explored (class 4 & 5 experiments) to ensure the global optimum is identified (Figure 18). The five classifications of experiments are highlighted below:

- Class 1: The minimum point predicted from the local polynomial model around the current best point.
- Class 2: The minimum points predicted from polynomial models that are local to other points.
- Class 3: The minimum points predicted from polynomial models that are nonlocal to other points.
- Class 4: Points in currently unexplored regions of experimental space. The probability of exploring this space is set by the user.
- Class 5: Random points generated to fill the experimental space.

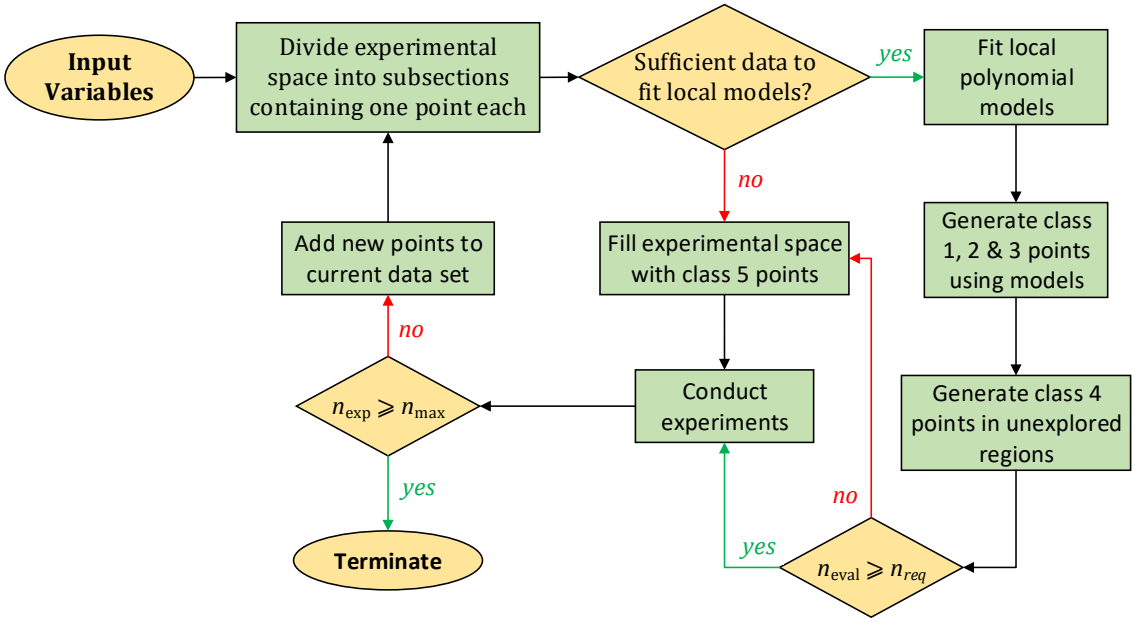

Figure 18. Flow diagram for a SNOBFIT optimisation. n_{exp} = total number of experiments conducted, n_{max} = maximum number of experiments allowed, n_{eval} = number of function evaluations in the current call, n_{req} = number of experiments required for one call.

Bayesian optimisation is a category of derivative-free global optimisation methods which use surrogate models to optimise expensive-to-evaluate functions.[85] The surrogate models are often in the form of a Gaussian process (GP), which defines a distribution over all possible functions that are consistent with the observed data [Eq (12)]. Hence, a GP can be specified by a mean function m [Eq (13)] and a covariance function k [Eq (14)], where y is the observation of a function f, $\mathbf{x}$ and $\mathbf{x'}$ are input vectors and $\mathbb{E}_f$ is the expectation over the function.[86] Initially, the unknown objective function is treated as a random function overlaid with our prior beliefs about the system. The covariance function (or kernel) is a measure of similarity between the inputs, and is used to determine the confidence intervals over the mean function. The kernel includes a signal variance hyperparameter (algorithm setting) which can be tuned to handle noisy optimisations.

As data is collected, the prior is updated to form the posterior distribution. The posterior distribution is used to construct an acquisition function, which utilises the trade-off between exploration and exploitation to determine the next evaluation point (Figure 19).[87] For a maximisation problem, the acquisition function is high when the mean function is high (exploitation) and/or the uncertainty is high (exploration). Therefore, experiments generally focus on reducing uncertainty in the most lucrative regions. However, the hyperparameter which controls the

trade-off between exploration and exploitation can be set to favour one of these characteristics. Alternatively, the trade-off can be inherent in some acquisition functions, such as Thompson sampling.[88]

$$y\,(\mathbf{x}) \sim GP\left(m(\mathbf{x}), k(\mathbf{x}, \mathbf{x}')\right) \tag{12}$$

$$m(\mathbf{x}) \coloneqq \mathbb{E}_f[f(\mathbf{x})] \tag{13}$$

$$k(\mathbf{x}, \mathbf{x}') \coloneqq \mathbb{E}_f\left[\left(y(\mathbf{x}) - m(\mathbf{x})\right)\left(y(\mathbf{x}') - m(\mathbf{x}')\right)\right] \tag{14}$$

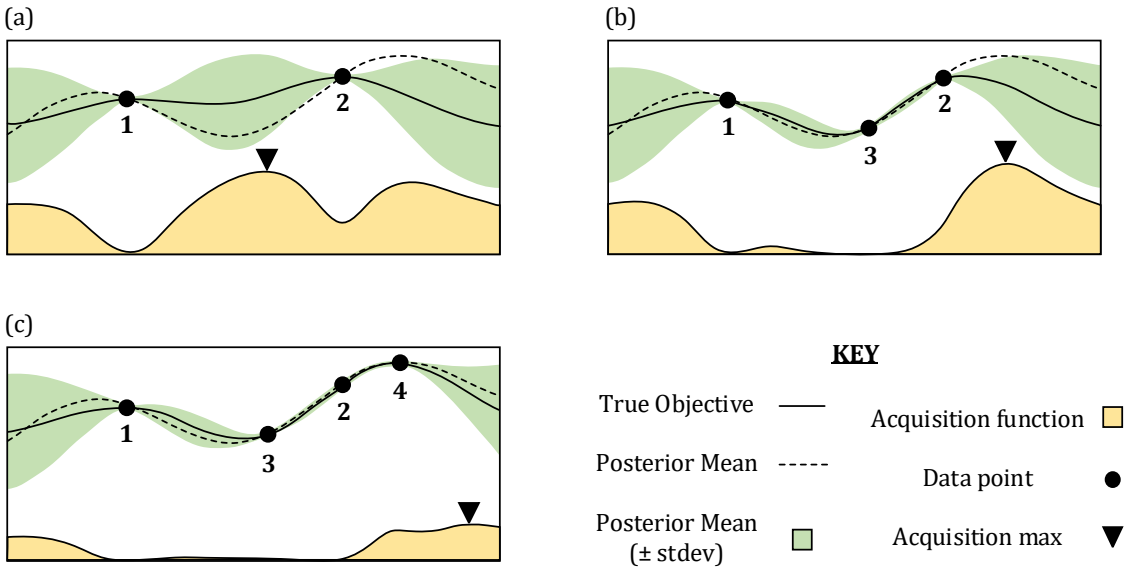

Figure 19. Bayesian optimisation approach for maximisation of a single objective. The posterior mean and acquisition function are updated after each new data point, *N*, is obtained: (a) *N* = 2; (b) *N* = 3; (c) *N* = 4. Subsequent experiments are conducted at the maximum of the acquisition function, which corresponds to a trade-off between exploration and exploitation.

1.5 Project Aims

Progress in automated feedback optimisation has provided an efficient tool towards achieving the goal of accelerated reaction development. Intelligent exploration of multivariate experimental space by state-of-the-art algorithms has significantly reduced the time and labour intensity required for reaction optimisation. Furthermore, the integration of a variety of different in/on-line PAT with flow reactors has expanded the scope of self-optimising systems to a wide range of chemistries. However, there are still a very limited number of reports for the application of this technology towards complex pharmaceutically relevant

processes, suggesting that further developments are required to align with the interests of industry. Examples of such developments which are addressed in this work are outlined below:

- More efficient algorithms – The algorithms used have largely been limited to single objective optimisations. However, multiple process metrics must be simultaneously considered to achieve both an economically and environmentally viable process.
- Multiphasic chemistry – The majority of lab-scale flow reactions involve homogeneous solutions. However, many industrially relevant processes involve a combination of phases, and can require relatively long residence times which are difficult to achieve in microreactors.
- Multi-step processes – Current examples of self-optimisation have been limited to a single reaction step. However, API syntheses represent more complex multi-step sequences which include work-up unit operations.

Chapter 2 introduces the concept of machine learning multi-objective optimisation algorithms, and their application towards self-optimising continuous flow reactors. Two conflicting objectives were simultaneously optimised for an exemplar reaction, and the trade-off between them identified in a practical number of experiments. In addition, the problem of minimising product impurities is included, which has not been addressed in previous self-optimisations.

Chapter 3 focuses on the optimisation of a pharmaceutically relevant process for the synthesis of API Lanabecestat. A combination of DoE and multi-objective optimisation was utilised to optimise a Sonogashira cross-coupling reaction, where the benefits associated with multi-objective optimisation of discrete steps in multi-step route design were realised. In addition, a new methodology for the *in silico* comparison of multi-objective algorithm performance was created to enable self-optimising platforms to remain up-to-date with state-of-the-art technology.

Chapter 4 describes the development of a photochemical miniature CSTR cascade reactor for multiphasic reactions. The mixing properties and absorbed photon flux density of the reactor were characterised via RTD profiling and actinometry respectively, showing increased performance compared to batch reactors. A self-optimisation approach, utilising a new optimal response surface

mapping algorithm, enabled the improvement of continuous flow conditions for the site-selective aerobic oxidation of C(sp^3)-H bonds.

Chapter 5 investigates the use of self-optimising systems for complex multi-step reaction and work-up processes. Initially, an optimisation platform for in-line liquid-liquid separation of structurally similar impurities was developed, and the approach utilised to optimise a tandem reaction-extraction process. This was further extended to the simultaneous optimisation of a biphasic two-step process with respect to three objectives, significantly reducing the time required for process development.

Chapter 2 Multi-Objective Self-Optimisation of Continuous Flow Reactors

2.1 Introduction

The majority of algorithms used for the self-optimisation of continuous flow reactors in the last decade were designed to minimise or maximise a single objective function. However, when developing a process it is important to consider multiple economic and environmental process metrics.[58] Commonly employed process metrics and their equations are displayed in Table 4.

The % yield [Eq (15)] is a ubiquitous metric used by chemists during reaction optimisation and is widely considered very useful for evaluating reaction efficiency. However, by itself the % yield fails to adequately account for productivity and downstream processing costs. For example, a high yield could be obtained by using a large excess of reagents over a prolonged period of time, thus resulting in a costly work-up procedure and low productivity respectively. Rather, the % yield, purity [Eq (16)] and space-time yield (STY) all need to be considered for a more complete economic analysis, where the STY [Eq (17)] is expressed as the mass of product produced per unit volume per unit of time.[89] Nevertheless, none of these metrics by themselves or in combination are sufficient for driving the development of sustainable processes.

Atom economy [Eq (18)] was introduced as an easily accessible metric for synthetic chemists to assess waste generation. This metric considers how much of the starting materials are incorporated into the desired product, but ignores key factors such as the molar excess of reactants and the use of solvents and reagents.[90] Because of this, two other metrics were proposed to give better measures of environmental impact: E-factor (or mass intensity) and reaction mass efficiency (RME). The E-factor [Eq (19)] is the ratio of the total mass of waste to the mass of the desired product, where the total mass of waste includes everything used within the process such as reactants, reagents, solvents and catalysts.[91] In contrast, the RME [Eq (20)] is a combination of yield, atom economy and molar excess. An analysis of these metrics across 28 different chemistries led to the conclusion that the RME is probably the most useful metric for evaluating how 'green' a process is.[92]

Table 4. Metrics for evaluating the economic and environmental impact of a chemical process. m = mass, V = volume of reactor, t_{res} = residence time, MW = molecular weight, SM = starting material.

Process Metric	Equation	
% Yield	$\frac{m_{product} \times 100}{Expected\ m_{product}}$	(15)
% Purity	$\frac{m_{product} \times 100}{m_{mixture}}$	(16)
Space-time yield (STY)	$\frac{m_{product}}{V \times t_{res}}$	(17)
Atom Economy	$\frac{MW_{product}}{\sum_{i=1}^{n} MW_{SM}(i)}$	(18)
E-Factor	$\frac{m_{waste}}{m_{product}}$	(19)
Reaction Mass Efficiency (RME)	$\frac{MW_{product} \times yield}{MW_{SM1} + (MW_{SM2} \times equiv_{SM2})}$	(20)

The process metrics outlined above are frequently conflicting, which means that the optimum for each metric is located in a different region of experimental space. One approach to this problem is to conduct multiple single objective optimisations to identify the optimum for each metric. This one-objective-at-a-time approach was used to optimise the yield, throughput and cost for a Heck-Matsuda reaction using a modified NMSIM algorithm (Scheme 6).[65] Notably, optimising for the different criteria gave significantly different values of performance with respect to % yield. However, this approach does not consider the objectives simultaneously, and therefore fails to identify a satisfactory compromise between the conflicting performance criteria.

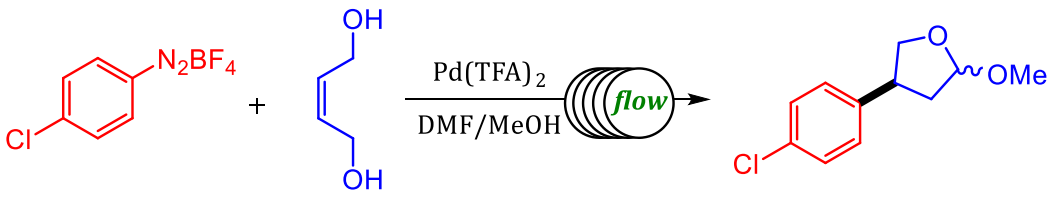

2.01 **2.02** **2.03**

Optimisation 1: **Yield = 92%.**
Optimsation 2: **Throughput = 427.1 mg/h**, Yield = 67%.
Optimisation 3: **Cost = 8.51 €/g**, Yield = 77%.

Scheme 6. Heck-Matsuda reaction optimised for yield, throughput and cost.

In a separate study, a poor 42% conversion was observed for a Paal-Knorr reaction which had been optimised for productivity (Scheme 7a).[57] In contrast to the one-objective-at-a-time approach, a penalty function was introduced to penalise conversions of less than 85%. This method successfully identified a compromise between the objectives where the conversion increased to 81% at the cost of a 31% decrease in productivity. Nevertheless, the authors concluded that an *a priori* economic analysis of the process would be required to determine the desired weighting on the objectives before conducting a final optimisation. Similarly, Fitzpatrick *et al.* combined throughput, conversion and consumption into a single objective function [Eq (21)] during optimisation of an Appel reaction (Scheme 7b), where τ = residence time, z = [**2.08**], p = [PPh_3O], s = [**2.07**], x = CBr_4 equiv. and y = PPh_3 equiv.[66] However, the *a priori* determination of adequate weightings for each term proved difficult, and initially led to skewed results. These examples highlight some major problems with the scalarisation of multiple objectives: (i) quantitative *a priori* knowledge is needed to adequately specify objective weightings, thus requiring additional experiments; (ii) minor changes to the weightings can result in significant changes to the solution achieved; (iii) only one optimal result is obtained, which is dependent on the chosen objective function and does not reveal the complete trade-off between conflicting performance criteria.

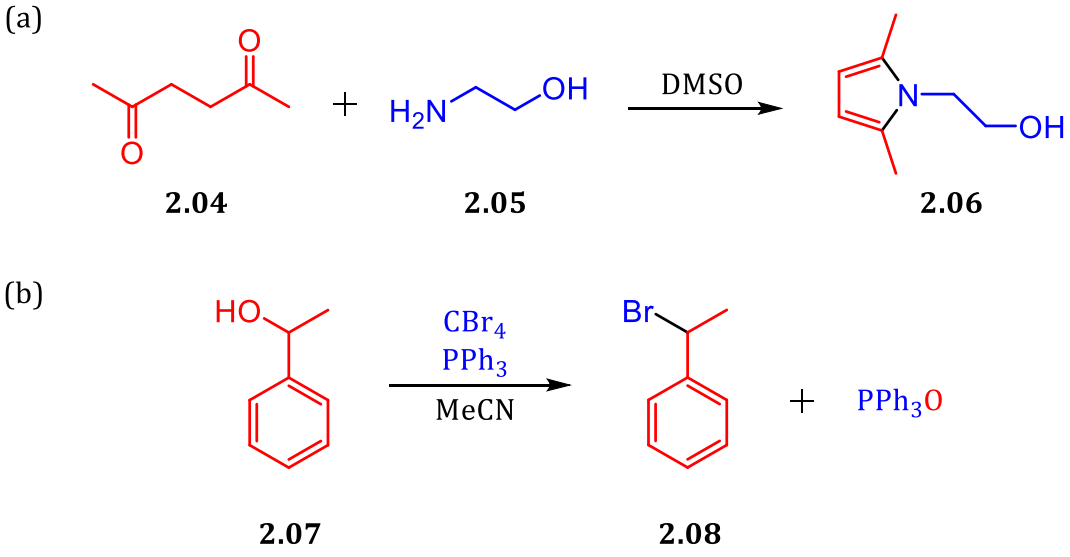

Scheme 7. Reactions optimised via the scalarisation of multiple objectives: (a) Paal-Knorr reaction optimised for throughput and conversion using a penalty function; (b) Appel reaction optimised for throughput, conversion and consumption using a weighted function [Eq (21)].

$$f(\ldots) = 0.25\left(\underbrace{\frac{1}{\tau} + z}_{\text{Throughput}}\right) + \underbrace{\frac{16p}{s + 0.25(x+y)}}_{\text{Conversion}} \quad \begin{matrix}\text{Conversion} \\ \text{Consumption}\end{matrix} \tag{21}$$

The true solution to a multi-objective optimisation problem is a set of non-dominated solutions known as the Pareto front (Figure 20), where a non-dominated solution is one which cannot be improved without having a detrimental effect on the other. Hence, a multi-objective maximisation problem where variable vector $\mathbf{x} = \{x_1,\ldots,x_n\}$ is formulated as follows. In objective space $\mathbf{X}$, find variable vector $\mathbf{x}^*$ which maximises K objective functions $z(\mathbf{x}^*) = \{z_1(\mathbf{x}^*),\ldots,z_K(\mathbf{x}^*)\}$, where objective space $\mathbf{X}$ is restricted by bounds on the variables. A feasible solution $\boldsymbol{a}$ dominates another feasible solution $\boldsymbol{b}$ ($\boldsymbol{a} \succ \boldsymbol{b}$) when $z_i(\boldsymbol{a}) \geq z_i(\boldsymbol{b})$ for $i = 1,\ldots,K$ and $z_j(\boldsymbol{a}) > z_j(\boldsymbol{b})$ for at least one objective j.[93] In contrast to scalarisation, the identification of a set of solutions and presentation of a front enables *a posteriori* decisions to be made regarding the desired optimum based on knowledge of the complete trade-off.

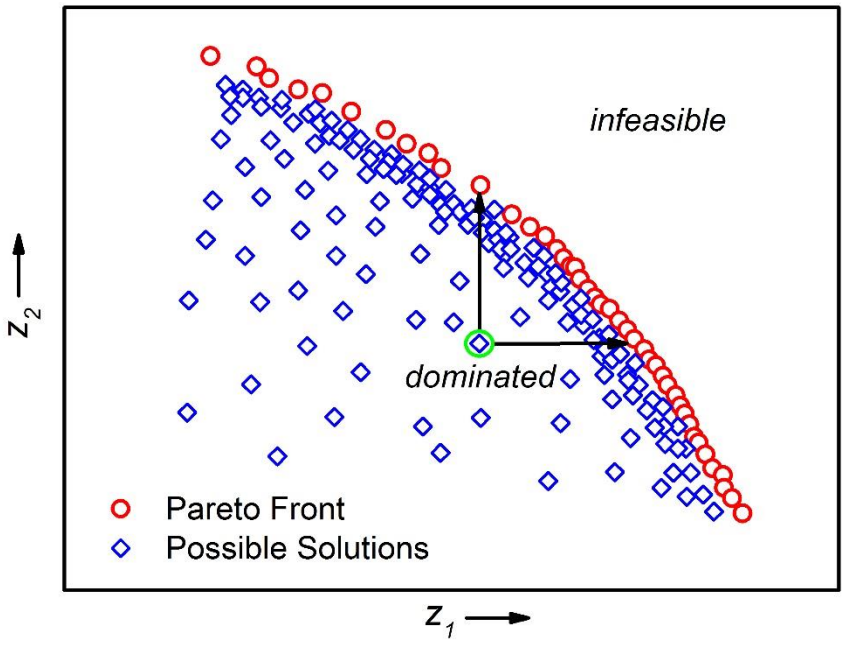

Figure 20. An example of a system with two conflicting maximisation performance criteria z_1 and z_2. It is infeasible to find the utopian point where both z_1 and z_2 are at their optimal values. The points on the Pareto front are non-dominated solutions, as z_1 or z_2 cannot be improved without having a detrimental effect on the other.

The genetic algorithms discussed in Chapter 1 can readily be modified to handle multi-objective optimisation problems, the most widely used of which is the fast non-dominated-sort genetic algorithm (NSGA-II).[94] NSGA ranks the population using Pareto dominance, where solutions on local fronts closer to the Pareto front are ranked better i.e. lower. Notably, NSGA-II penalises solutions near dense sections of the Pareto front to ensure a diverse Pareto front is obtained (rank = number of dominating solutions + 1). For example, in Figure 21a solution ***i*** is dominated by solutions ***c***, ***d*** and ***e*** so is given a rank of 4, whereas solutions ***f***, ***g*** and ***h*** are only dominated by one solution so are given a rank of 2. Furthermore, NSGA-II is an elitist algorithm, which means it will always select solutions with the better ranks for crossover and mutation to create the next generation. If two solutions have the same rank, then diversity is prioritised and the solution with the higher crowding distance is selected. The crowding distance is calculated by averaging the side length of a cuboid with a perimeter defined by the solutions nearest non-dominated neighbours as vertices (Figure 21b).

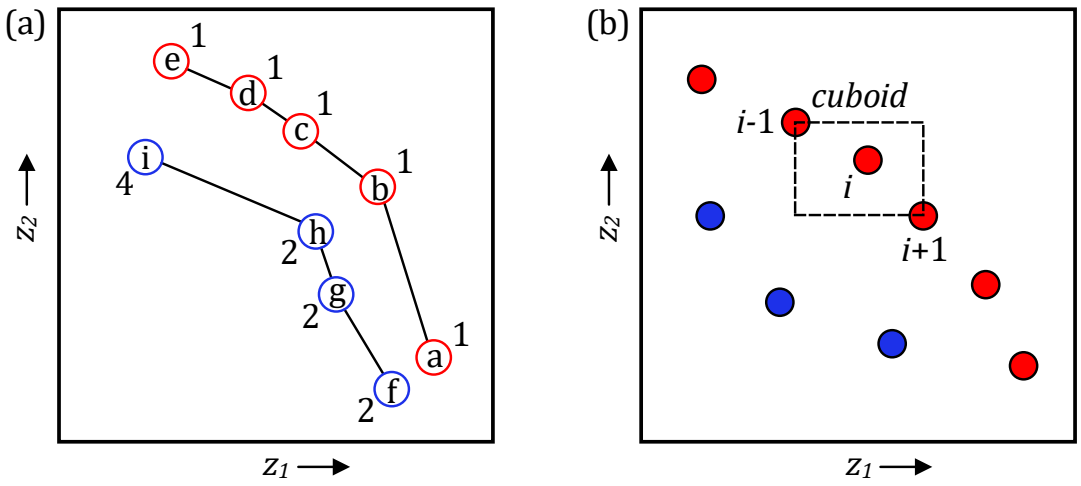

Figure 21. Graphical representations of adaptations to the NSGA algorithm to ensure a diverse front is identified: (a) ranking system; (b) crowding distance.

Most problems of interest in chemistry represent expensive-to-evaluate functions, particularly in the pharmaceutical industry where the focus is on low-volume, high-value products. Although NSGA-II is capable of solving multi-objective problems, the population size, and therefore total number of evaluations required, are too large to be practical for self-optimisation. Hence, a machine learning algorithm called multi-objective active learner (MOAL) was designed for expensive-to-evaluate multi-target optimisation tasks.[95] The algorithm was successfully applied to the optimisation of an emulsion polymerisation recipe

with 14 input variables, simultaneously targeting a conversion of ≥99% and particle diameter of 100 ± 1 nm.[63] Similarly, the Thompson sampling efficient multi-objective optimisation (TSEMO) algorithm was recently reported to converge on the Pareto front within a small budget of evaluations, and compared favourably against other Bayesian multi-objective optimisers for *in silico* test problems.[96]

2.2 Thompson Sampling Efficient Multi-Objective Algorithm

The Thompson Sampling Efficient Multi-Objective (TSEMO) algorithm follows a Bayesian optimisation framework, employing GPs as surrogates and Thompson sampling as a heuristic to exploit the trade-off between exploration and exploitation. A multi-objective genetic algorithm is used to evaluate randomly selected functions from the GPs, and experiments suggested which aim to improve the hypervolume of the Pareto front. The algorithm is represented graphically in Figure 22.

A Latin hypercube (LHC) space-filling design is used to initialise the algorithm. The LHC design splits the experimental space into an *N*-by-*N* grid, where *N* is equal to the number of samples. Experiments are then conducted such that no experiment is in the same row or column as another, thus ensuring that a good spread of samples across all possible values is achieved.[97] GP surrogate models are then fit to each objective. In this case, the GPs are distributions over 4000 possible functions that are consistent with the LHC data. A sample from the 4000 possible functions are selected at random, and the multi-objective NSGA-II algorithm used to identify their Pareto fronts *in silico*. This generates a candidate set of experiments, which are ranked based on their predicted hypervolume improvement (Figure 23). The hypervolume is defined as the volume between the current non-dominated front and a reference point (anti-utopian point). Experiments corresponding to the largest hypervolume improvement are conducted, thus ensuring convergence on a well distributed Pareto front.[98] The GPs are updated with the results of the experiments, and the process repeated iteratively. The trade-off between exploration and exploitation desired in Bayesian optimisation is inherently accounted for by the randomness of sampling from the GPs.

It is desirable in self-optimisation to conduct more than one experiment per iteration (batch-sequential), as this reduces the overall time spent waiting for analysis. The performance of the TSEMO algorithm was found to be very similar

when implementing one or four experiments per iteration.[96] Therefore, all experimental work herein was conducted using four experiments per iteration.

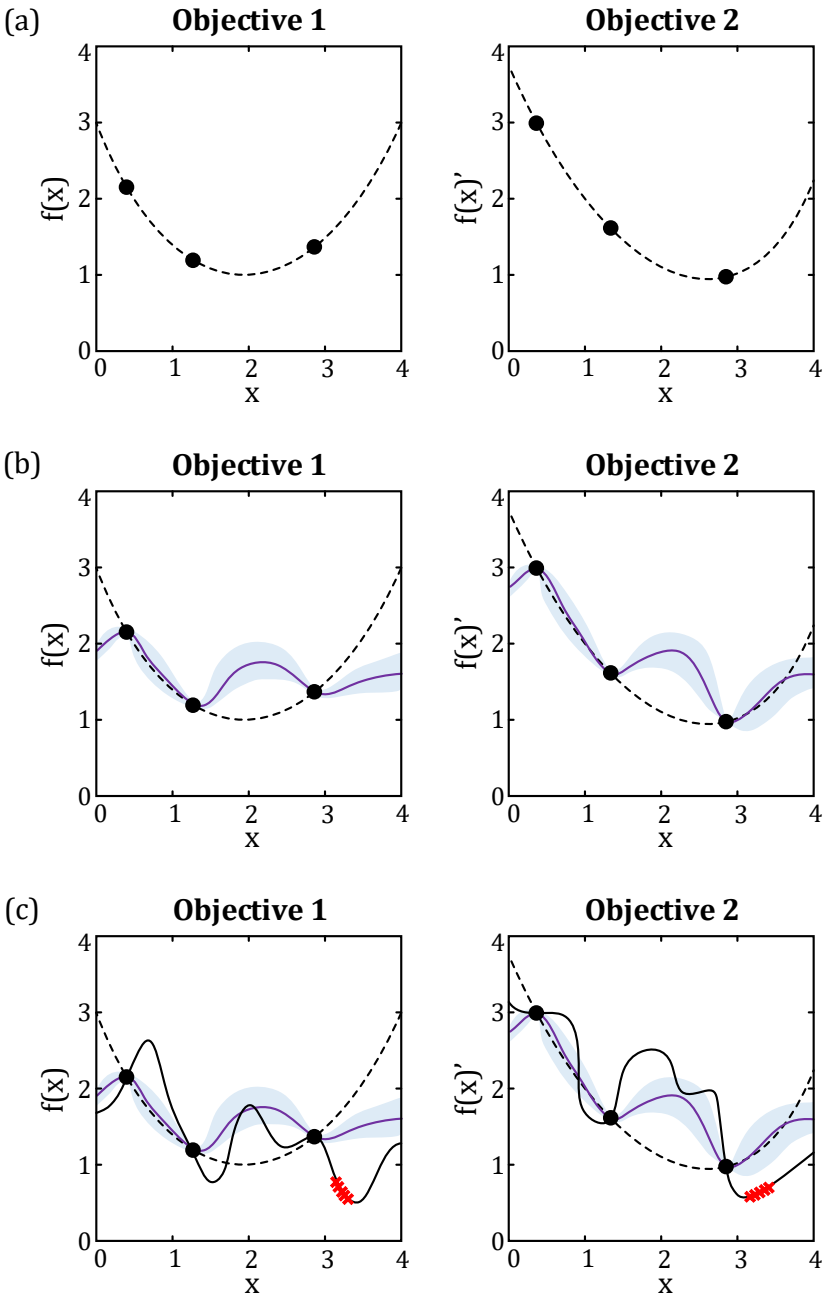

Figure 22. Different stages of the TSEMO algorithm for the minimisation of two-objectives, f(x) and f(x)', with a single variable, x: (a) initial dataset collected; (b) GP model fit to the current data for both objectives; (c) Pareto front of a randomly selected function determined using NSGA-II. Objective = ---, data point = •, mean = —, function = —, Pareto front of sampled function = ×, confidence interval = shaded area.

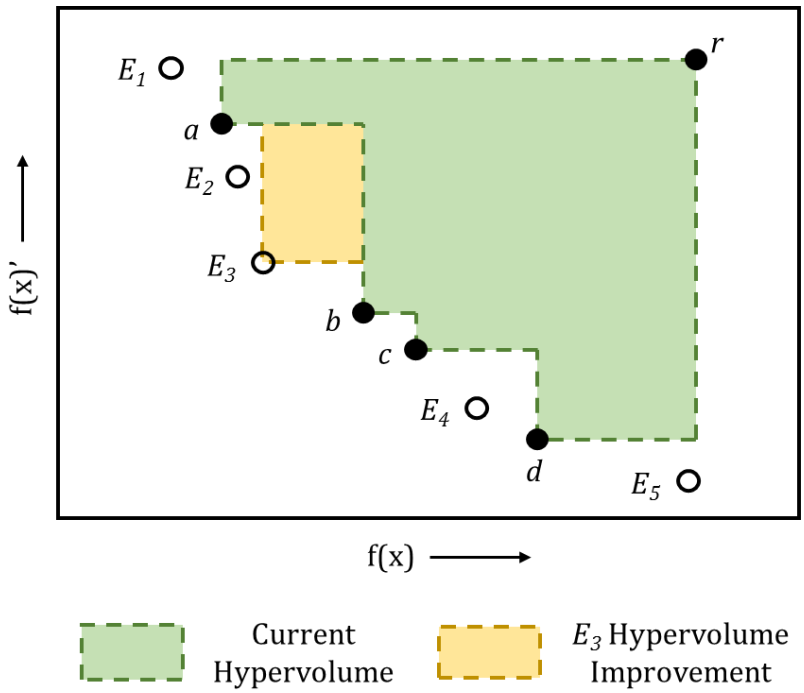

Figure 23. Hypervolume plot showing the process used to select experiments from the candidate set, E_i. The current hypervolume is the volume between the non-dominated front (*a*, *b*, *c*, *d*) and a reference point, *r*. In this case, E_3 is selected as it offers the largest predicted hypervolume improvement.

2.3 *N*-Benzylation of Primary Amines

In 2006 the most frequently used reactions in the pharmaceutical industry belonged to the 'heteroatom alkylation and arylation' category, 57% of which involved *N*-substitution.[99] However, the direct alkylation of primary amines with alkyl halides is prone to significant by-product formation via overreaction. This is due to the nucleophilicity of the nitrogen atom increasing with an increasing number of alkyl substituents: tertiary (3°) > secondary (2°) > primary (1°).[100] Hence, the *N*-benzylation of α-methylbenzylamine **2.09** with benzyl bromide **2.10** was selected as a suitably challenging case study to test the TSEMO algorithm (Scheme 8). The reaction forms the desired 2° amine **2.11** and undesired 3° amine **2.12** as a by-product. The formation of the corresponding quaternary ammonium salt was suppressed by using diisopropylethylamine (DIPEA) as the base for the reaction.[101]

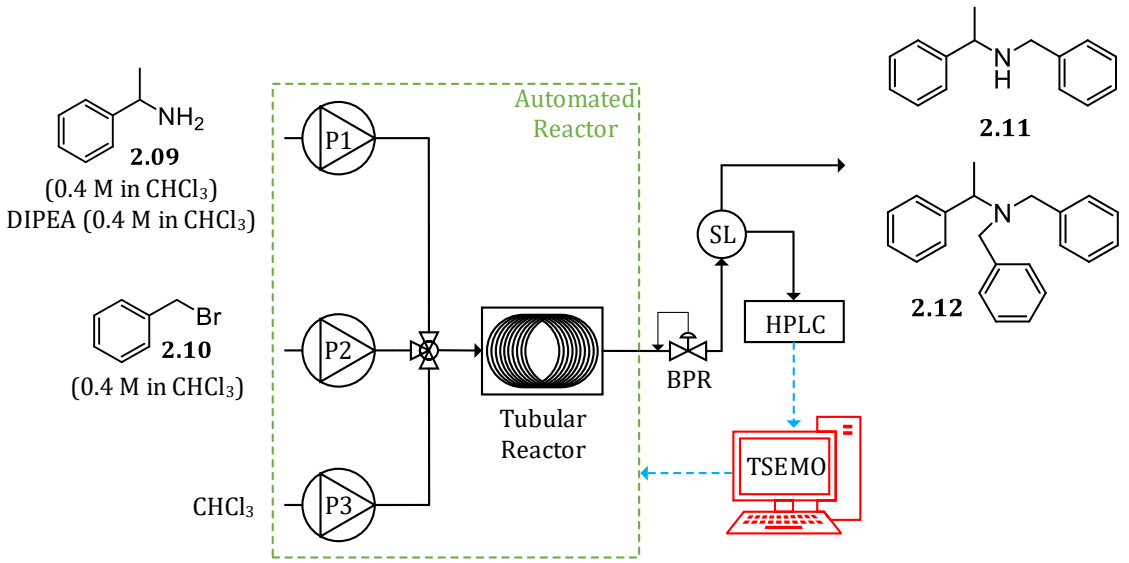

Scheme 8. Schematic of the automated flow reactor used to optimise the *N*-benzylation of α-methylbenzylamine **2.09**. P = pump, BPR = back-pressure regulator, SL = sample loop. See experimental for more details.

The optimisation was initially formulated according to [Eq (22)]. To find operating conditions that were both economically viable and environmentally friendly, we aimed to maximise the STY [Eq (17)] and minimise the E-factor [Eq (19)] respectively. As TSEMO is a minimisation algorithm, the negative of the response was input to achieve objective maximisation. The objectives were natural log-transformed, as this has been shown to better fit response surfaces in cases where there is a limited amount of data.[102] Due to the natural log-transformation, the algorithm favours a natural log-spaced Pareto front. The optimisation was conducted with respect to four variables: P1 flow rate, P2:P1 ratio, P3:P1 ratio and temperature.

$$minimise[-\ln(STY), \ln(E-Factor)] \quad (22)$$

subject to:

$$P1/mL\ min^{-1} \in [0.2, 0.4]$$

$$P2{:}P1 \in [0.5, 3.0]$$

$$P3{:}P1 \in [0.25, 1.0]$$

$$Temperature/°C \in [50, 140]$$

The objectives were selected based on prior beliefs that the STY and E-factor would be conflicting performance criteria. It was hypothesised that the STY would favour higher equivalents of **2.10** and shorter residence times (high P2:P1 and P1 flow rate), whereas the E-factor would favour lower equivalents of **2.10** and longer

residence times (low P2:P1 and P1 flow rate). Rather, it was found that the STY and E-factor are complimentary performance criteria with the same optimum set of conditions. Furthermore, the relationship between the objectives at any point in the experimental space could be defined by the curve shown in Figure 24. This reflected the nature of the competitive consecutive reaction system, where milder conditions limit the conversion of **2.09** and harsher conditions promote the formation of **2.12**.

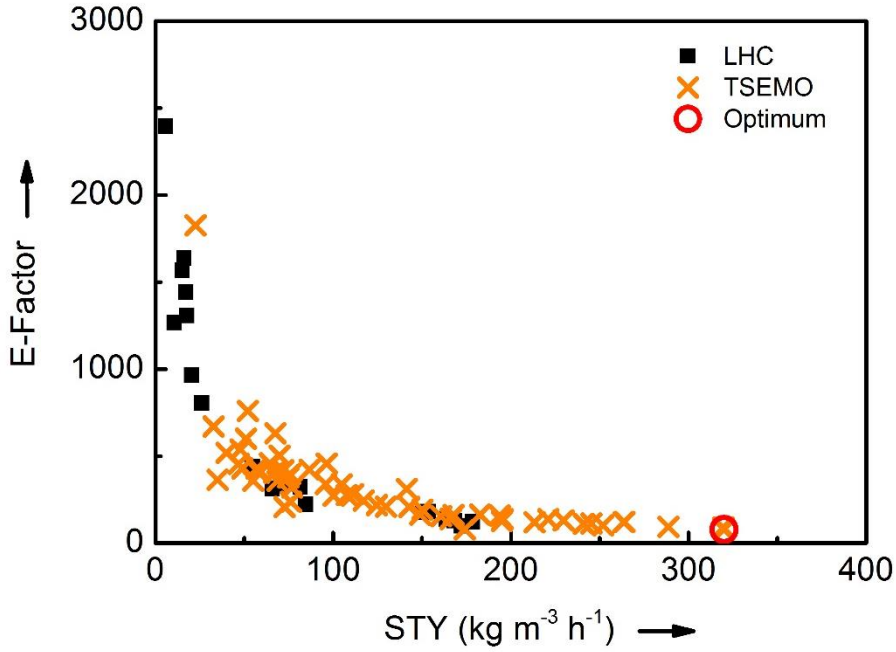

Figure 24. Results for the optimisation of the *N*-benzylation reaction with respect to STY and E-factor. The initial LHC size was 20. The TSEMO algorithm conducted 58 additional experiments, locating a single optimum.

These initial results highlighted the selection of conflicting performance criteria without *a priori* information as a significant challenge. To overcome this, a pause was introduced in the algorithm after the initial LHC experiments. This would enable polynomial models of the current data to be constructed, and the response surfaces for different metrics of interest to be evaluated. The experimental space was updated to focus on regions of greater interest based on the previous results:

updated limits:

$$\text{P1/mL min}^{-1} \in [0.2, 0.4]$$

$$\text{P2:P1} \in [1.0, 5.0]$$

$$\text{P3:P1} \in [0.5, 1.0]$$

$$\text{Temperature/°C} \in [110, 150]$$

As the majority of dead-time is spent waiting for the reactor to cool down, the 20 LHC experiments were conducted in ascending order with respect to

temperature. The results were used to model polynomial response surfaces for different metrics using multiple linear regression (MLR), with the aim of identifying two conflicting performance criteria. When all main, interaction and square terms were included, the model was saturated and defined according to [Eq (23)], where Y is the response, b_i are the coefficients and X_i are the input variables (X_1 = P1, X_2 = P2:P1, X_3 = P3:P1, X_4 = Temp).

$$f = b_0 + b_1X_1 + b_2X_2 + b_3X_3 + b_4X_4 + b_{12}X_1X_2 + b_{13}X_1X_3 + b_{14}X_1X_4 + b_{23}X_2X_3 + b_{24}X_2X_4 + b_{34}X_3X_4 + b_{11}X_1^2 + b_{22}X_2^2 + b_{33}X_3^2 + b_{44}X_4^2 \quad (23)$$

The quality of the model was assessed using R^2 and Q^2 as validation metrics. The results of the experiments (n = 20) are defined by vector $y = [y_1,\ldots,y_n]$ with a mean of $\bar{y}$ and corresponding vector $f = [f_1,\ldots,f_n]$ for predicted values. R^2 measures the proportion of variance in the data which is explained by the model. It is calculated according to [Eq (24)], where the residual sum of squares (*RSS*) [Eq (25)] is divided by the total sum of squares (*TSS*) [Eq (26)]. The RSS and TSS are the sum of the squared difference between the observed response y_i and the predicted response f_i or the mean of the observed response $\bar{y}$ respectively. Therefore, the closer R^2 is to 1 the better the fit of the model to the experimental data.

$$R^2 = 1 - \frac{RSS}{TSS}, \qquad 0 \leq R^2 \leq 1 \quad (24)$$

$$RSS = \sum_{i=1}^{n} (y_i - f_i)^2 \quad (25)$$

$$TSS = \sum_{i=1}^{n} (y_i - \bar{y})^2 \quad (26)$$

Q^2 measures the ability of the model to make accurate predictions and is calculated according to [Eq (27)], where the predictive error sum of squares (*PRESS*) [Eq (28)] is divided by the TSS. The PRESS is the sum of squared difference between the observed response y_i and the predicted response $f_{i/i}$ when the i-th sample is omitted from the training data. Therefore, the closer Q^2 is to 1 the better the predictive ability of the model.

$$Q^2 = 1 - \frac{PRESS}{TSS}, \qquad Q^2 \leq 1 \tag{27}$$

$$PRESS = \sum_{i=1}^{n} \left(y_i - f_{i/i}\right)^2 \tag{28}$$

The goodness of fit for the STY and % impurity (% yield of **2.12**) saturated models were excellent, with R^2 values of 0.9941 and 0.9964 respectively. Therefore, a series of modifications were made which focused on improving the models predictive ability. Initially, the shape of the response distributions were assessed to determine if a transformation was required to achieve a normal distribution. A normal distribution is favoured as it fits many natural phenomena. This is explained by the central limit theorem, which states that when a large number of random samples are taken from a population, the distribution of the means of those samples will converge to a normal distribution. Histograms of the responses showed that the % impurity distribution was positively skewed (Figure 25a). This was rectified by use of a logit transformation according to [Eq (29)], where $\hat{y}$ is the transformed response.[40]

$$\hat{y}_i = \log_{10}\left(\frac{y_i - 0}{100 - y_i}\right) \tag{29}$$

The models were further refined by removing any insignificant main, interaction or square terms from the saturated models.[39] As each term was removed, the models were refit which adjusted the confidence intervals of the coefficients. Hence, each term was removed one at a time in order of relevance to the response. For the % impurity, this process reduced the number of terms from 14 to 9 (Figure 25b).

Normal probability plots are used as a diagnostic tool for regression models to identify potential outliers. They are plots of the normal probability against deleted studentised residuals. The deleted studentised residuals were calculated as follows: (i) delete each response one at a time; (ii) refit the model with the remaining *n*-1 responses; (iii) compare the observed response with the predicted response; (iv) divide the deleted residuals by its estimated standard deviation. Therefore, the deleted studentised residuals provide a measure of how influential a data point is. Responses with deleted studentised residuals that are beyond ±4 standard deviations from the mean are identified as outliers, and should be re-evaluated or

removed (Figure 25c). In this case, the normal probability plots for the refined models of STY and % impurity were linear, indicating normally distributed noise. Furthermore, no outliers were detected for either model.

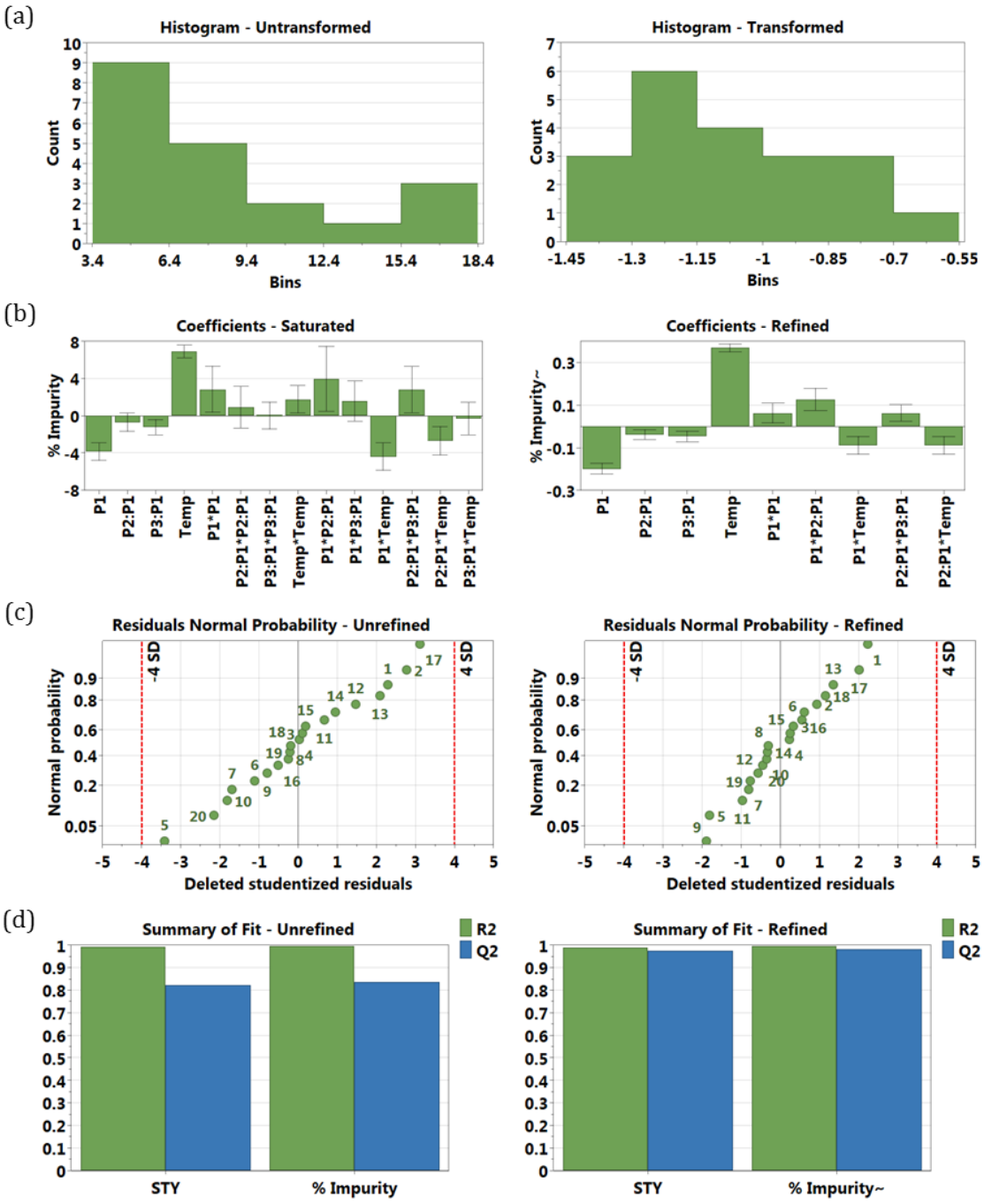

Figure 25. Statistics for modelling of the 20 LHC experiments: (a) histograms comparing response distribution for untransformed and logit transformed models of % impurity; (b) coefficient plots comparing saturated and unsaturated models of % impurity; (c) residuals normal probability plots comparing the unrefined and refined models of % impurity; (d) summary of fit plots comparing the unrefined and refined models of STY and % impurity.

The model refinement process outlined above significantly improved the predictive ability of the STY and % impurity models, as highlighted by an increase in Q^2 (Figure 25d). Response surfaces for a variety of metrics from Table 4 were constructed using this method, and compared to identify two conflicting performance criteria. The STY and % impurity were identified as suitably conflicting objectives based on their 4D contour plots shown in Figure 26 and Figure 27 respectively.

Under all conditions, maximising the STY favours high temperatures and low P3:P1 ratios, whereas minimising % impurity favours low temperatures and high P3:P1 ratios. For example, the predicted optimum conditions for STY were: P1 = 0.40 mL min^{-1}; P2:P1 = 1.19; P3:P1 = 0.50; temperature = 148.7 °C. In contrast, the predicted optimum conditions for % impurity were: P1 = 0.40 mL min^{-1}; P2:P1 = 1.19; P3:P1 = 0.97; temperature = 111.8 °C. In addition, the factor θ_i contributions for each model are displayed in Table 5, where a higher value corresponds to a greater contribution to the response. The temperature had the greatest effect on both objectives, which suggested it would be the dominant factor in the conflicting relationship. Therefore, the optimisation was reformulated according to [Eq (30)], and the TSEMO algorithm initiated using the 20 LHC experiments as the initial dataset.

$$minimise[-\ln(STY), \ln(\%\ impurity)] \tag{30}$$

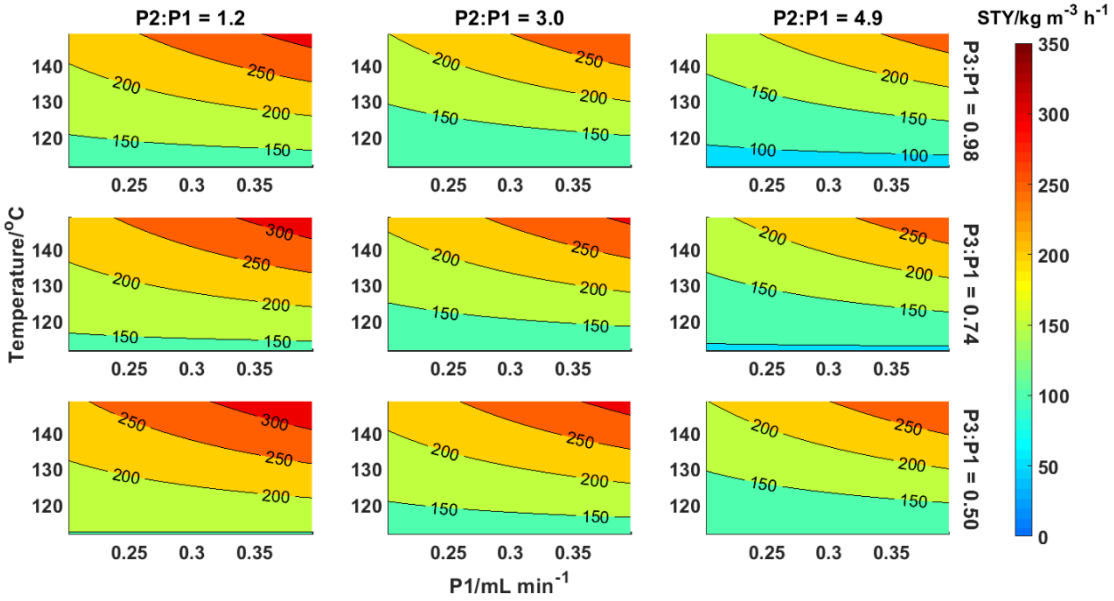

Figure 26. 4D response contour plots of STY.

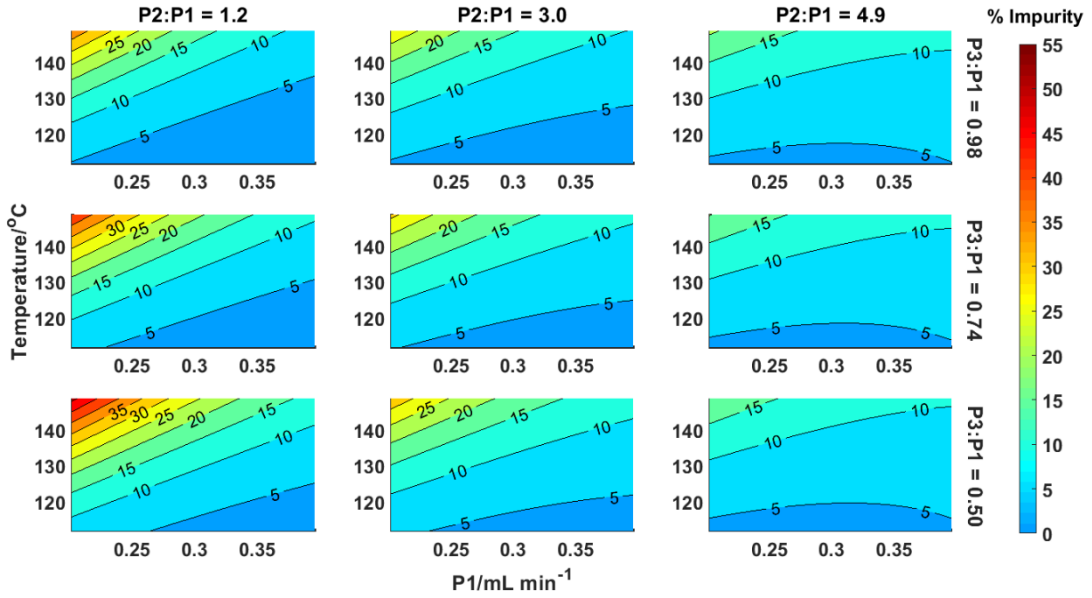

Figure 27. 4D response contour plots of % impurity.

Table 5. Factor contributions for the STY and % impurity polynomial models, where a higher value corresponds to a greater contribution to the response. θ_i = factor.

Variable	Poly 1 (STY)	Poly 2 (% impurity)
θ_{P1}	27.83	13.51
$\theta_{P2:P1}$	11.93	28.85
$\theta_{P3:P1}$	5.84	13.26
θ_{Temp}	54.40	44.39

The TSEMO algorithm conducted an additional 58 experiments, 20 of which formed a dense Pareto front (Figure 28). The optimal STY was 331 kg m^{-3} h^{-1} with an impurity yield of 10.0%. Conversely, the optimal impurity yield was 2.2% with a STY of 142 kg m^{-3} h^{-1}. Therefore, the objective space highlighted the inherent trade-off between the objectives, and thus validated the prediction made from the polynomial models. Reaction profiles for the STY and % impurity are displayed in Figure 29 and Figure 30 respectively. The trends in the reaction profiles were also in good agreement with the LHC model-based predictions for both objectives. For example, the results showed that the STY could initially be increased whilst having a relatively small effect on the % impurity. This corresponded to increasing the concentration at the lower temperature limits. Any further increase in STY required increasing the temperature, which resulted in a substantial increase in % impurity.

The multi-objective optimisation of the *N*-benzylation reaction successfully identified the target trade-off curve.[69] However, it should be noted that although the TSEMO algorithm searches globally, it is a stochastic method and therefore cannot guarantee identification of the global Pareto front within a limited number of experiments. One of the main advantages of identifying the Pareto front is that the information can be used for process design. For example, it could be beneficial in this case to accept higher impurities if the higher STY offsets the additional downstream purification costs. In contrast, single objective optimisation methods used thus far only identify one solution, and provide no information regarding the shape of the Pareto front. Furthermore, the optimum solution identified for one objective could still be dominated by the Pareto front. For example, Figure 28 highlights several points with a low % impurity and different STY. A single objective optimisation with respect to % impurity cannot differentiate between these points, whereas this approach can identify points which improve the STY without having a detrimental effect on the % impurity.

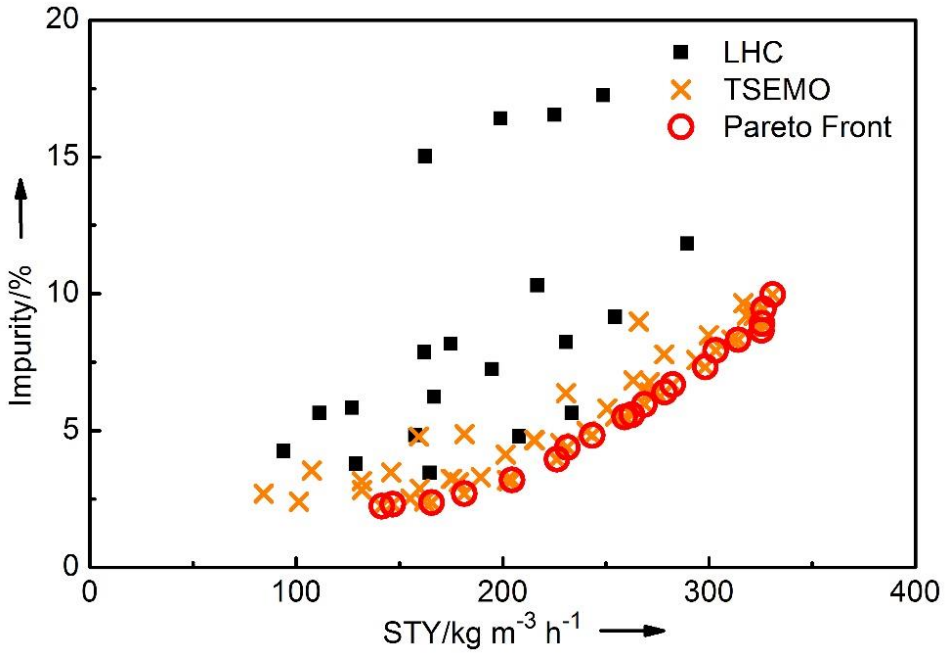

Figure 28. Results for the optimisation of the *N*-benzylation reaction with respect to STY and % impurity. The initial LHC size was 20. The TSEMO algorithm conducted 58 additional experiments, 20 of which formed a dense Pareto front highlighting the trade-off between the objectives.

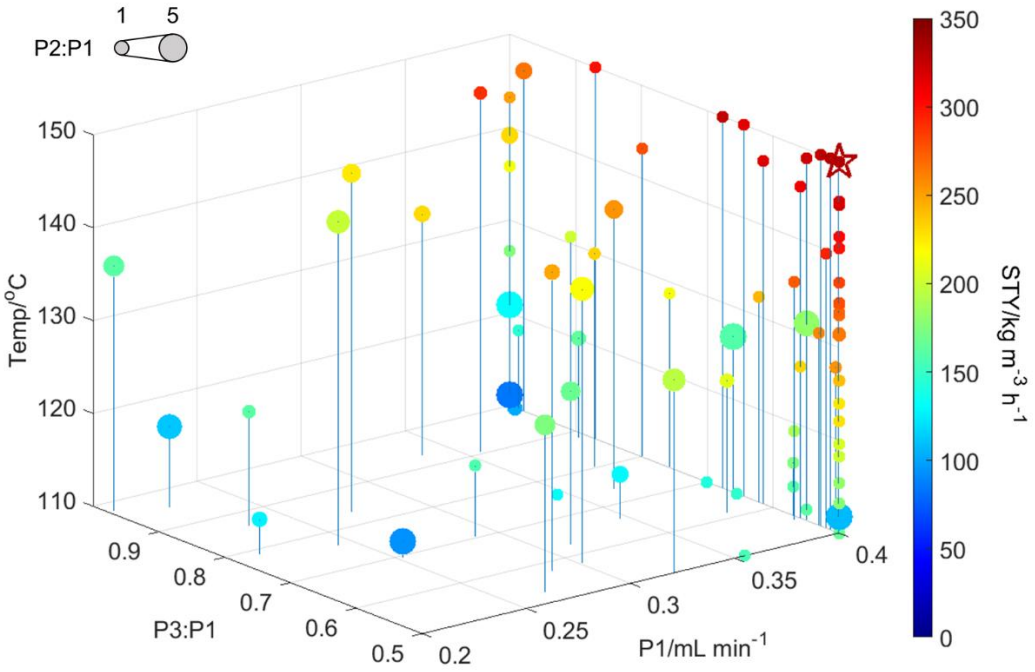

Figure 29. STY results for experiments performed during the multi-objective optimisation. ☆ = maximum STY.

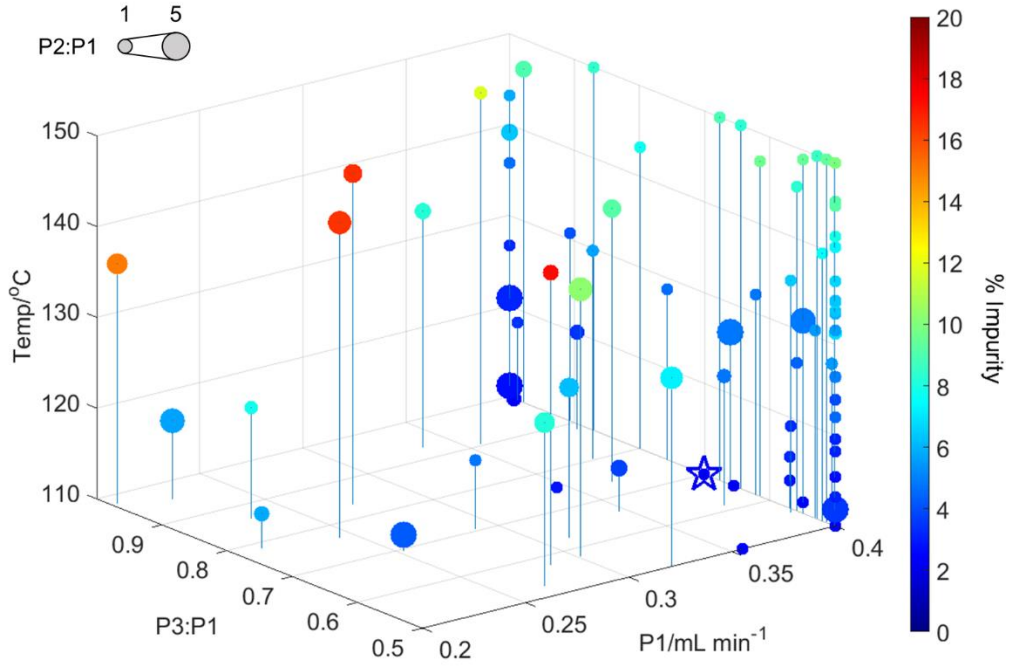

Figure 30. % impurity results for the experiments performed during the multi-objective optimisation. ☆ = minimum % impurity.

The GPs constructed during each iteration of the TSEMO algorithm include hyperparameters, which provide qualitative information regarding factor θ_i contributions for each objective (Table 6). In this case, lower values correspond to a greater contribution to the objective. This is referred to as automatic relevance determination, which is a useful tool for identifying important variables amongst large multidimensional datasets, where visual techniques are difficult.[86] The hyperparameters show that temperature is the most relevant variable for both objectives. This is consistent with the Pareto optimal points, where temperature is the dominant variable in describing the trade-off between STY and % impurity. In addition, the GPs provide a hyperparameter σ_n^2 which defines the noise of the system. The low values observed reflected the experimental robustness of the automated self-optimising flow platform, which enabled the generation of precise GP models.

Table 6. Hyperparameters for the STY and % impurity GP models, where a lower value corresponds to a greater contribution to the response. θ_i = factor, $\boldsymbol{\sigma_n^2}$ = noise.

Variable	GP 1 (STY)	GP 2 (% impurity)
θ_{P1}	13.14	4.20
$\theta_{P2:P1}$	11.45	5.53
$\theta_{P3:P1}$	20.62	18.11
θ_{Temp}	7.50	3.28
σ_n^2	4.02×10^{-5}	6.14×10^{-6}

It was hypothesised that models of the initial 20 LHC experiments could be sufficient to predict the global Pareto front without any additional experimentation. This would lead to a significant reduction in the time and materials required for multi-objective optimisation of a chemical system. Ranking of the factor contributions in order of importance revealed discrepancies between the LHC polynomial models and complete GP models. As a result, both polynomial and GP models of the initial 20 LHC experiments were tested to see which provided the best fit with the experimentally determined Pareto front. Each model was evaluated *in silico* using 58 iterations of the TSEMO algorithm, with one experiment per iteration. The results showed that the polynomial model provided a better prediction of the Pareto front compared to the GP model (Figure 31).

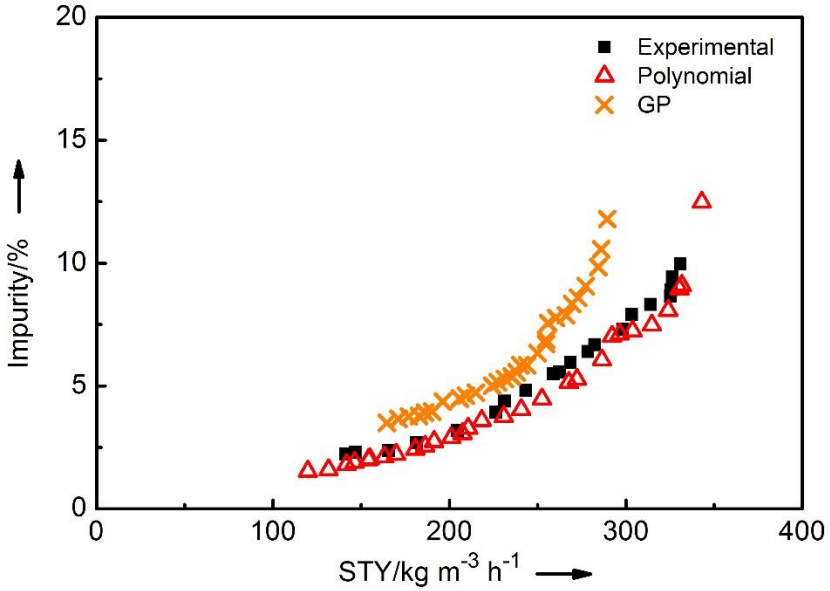

Figure 31. Comparison between the experimentally determined Pareto front and the predicted Pareto fronts from the polynomial and GP models after 20 LHC experiments. The models were evaluated using 58 iterations of the TSEMO algorithm, with one experiment per iteration.

The polynomial model was further scrutinised by predicting the response for each objective at the conditions corresponding to the experimentally determined Pareto optimal solutions. Figure 32 displays the results in ascending order with respect to STY, and includes error bars for the model predictions which define the 95% confidence intervals. The models accurately predict the STY at values less than or equal to 300 kg m^{-3} h^{-1}, and the % impurity at values less than or equal to 8%. However, the models were significantly less accurate at higher objective values, particularly for the % impurity, where experimental data points were outside the 95% confidence intervals. This was likely caused by overfitting the model to the 20 LHC data points, where extra terms were included in the model as a result of residual noise associated with the experimental system.

In summary, the polynomial models were useful for the identification of conflicting performance criteria. In addition, they were satisfactory for providing an initial indication of the global Pareto front shape, and outcompeted the GP models extracted from the TSEMO algorithm. However, model predictions were not accurate in all regions of the experimental space. Therefore, it would be advised that the Pareto front should be located experimentally, including cases where the models are of high quality according to statistical diagnostics.

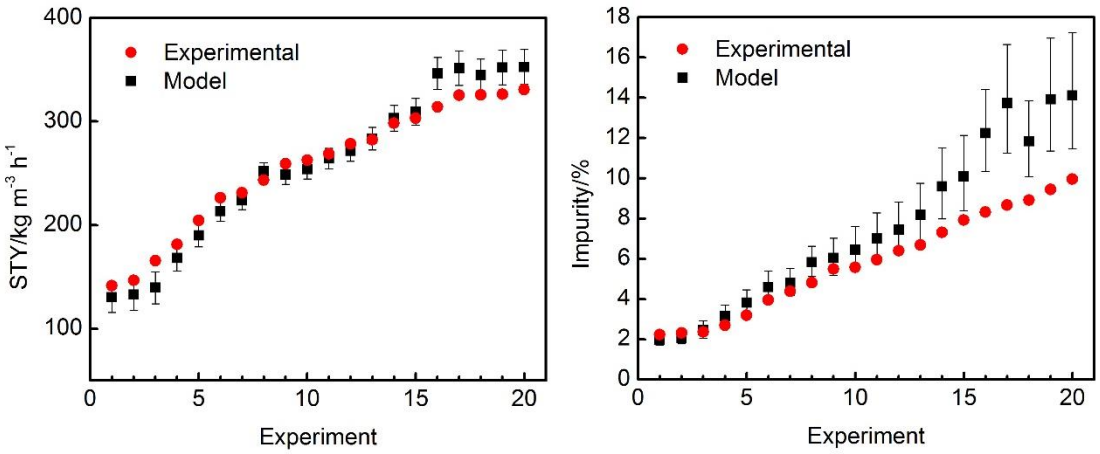

Figure 32. Comparison between Pareto front solutions determined experimentally and predicted from the corresponding conditions using the LHC polynomial models. The results are displayed in ascending order with respect to STY. Error bars = 95% confidence intervals of the model.

2.4 Conclusions

The task of optimising chemical reactions is highly challenging as multiple relevant process metrics need to be considered. However, scalarisation approaches used in previous work have suffered from the identification of sub-optimal compromises.[57, 66] In this work, a multi-objective optimisation algorithm has been applied to the self-optimisation of an *N*-benzylation reaction.[69, 96] The proposed set-up simultaneously optimised conflicting economic (STY) and environmental (impurity profile) objectives with respect to four variables. In addition, the problem of identifying conflicting performance criteria without *a priori* knowledge was overcome via empirical polynomial modelling of the initial dataset. The trade-off curve between the objectives was identified in a total of 78 experiments, providing significantly more information per experiment compared to previous single objective optimisations. The problem of minimising product impurities had not been addressed in previous self-optimisations, but is a scenario of particular importance in the pharmaceutical industry. This example demonstrated how identification of the Pareto front reveals essential information required for process design. Furthermore, the use of GPs provided additional knowledge regarding the relevance of the variables for each objective. We envisage that the developed approach will become a *de facto* method for reaction optimisation, as it aligns with the drive towards more sustainable process development.

Chapter 3 API Process Development: A Multi-Objective Pareto Front Optimisation Approach

3.1 Introduction

Currently the pharmaceutical industry is dominated by batch manufacturing, owing to a combination of existing infrastructure and the requirement for flexible multipurpose reactors. However, continuous processing was highlighted as the most important green engineering research area by the Roundtable in 2011.[103] This was driven by factors such as lower production costs, increased quality from steady-state operation and increased process safety. As such, numerous examples of end-to-end API syntheses utilising batch-flow hybrid or continuous flow set-ups have been reported in recent years (Figure 33).[104-109] Therefore, the ability to efficiently optimise these processes is of growing importance with respect to creating affordable treatments for a wide range of diseases.

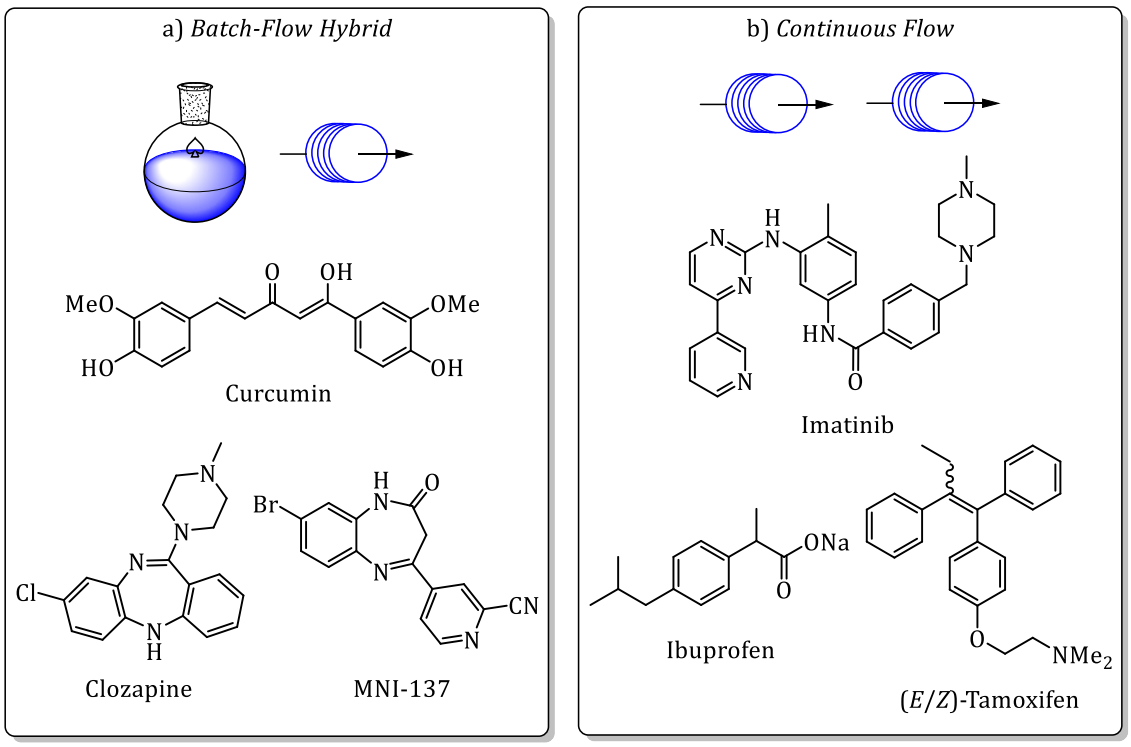

Figure 33. Examples of APIs synthesised using flow chemistry: (a) batch-flow hybrid set-ups; (b) end-to-end flow synthesis.

Alzheimer's disease (AD) is a chronic neurodegenerative disease which effects 5.4 million people in America. This is projected to grow to 13.8 million by 2050 owing to an ageing population. Furthermore, there is currently no cure for AD, with pharmacological treatments focusing on improving symptoms.[110] It is hypothesised that AD is caused by β-site amyloid precursor protein cleaving enzyme 1 (BACE1) generating neurotoxic amyloid β (Aβ) fragments. As a result, BACE1 inhibitor drugs have been developed with the goal of reducing Aβ concentrations in the brain.[111] Notably, amidine- and guanidine-containing heterocycles were identified to form a strong hydrogen-bonding network with the active site of BACE1.[112] For example, AstraZeneca and Eli Lilly co-developed lanabecestat **3.01** (AZD3293), which entered phase III clinical trials in 2016.[113] The drug was shown to have desirable properties, including: (i) high gastrointestinal and blood-brain barrier permeability; (ii) slow off-rate kinetics; (iii) prolonged suppression of Aβ in plasma and cerebrospinal fluid; (iv) equivalent bioavailability in tablet and oral solution.[114-116]

The retrosynthetic analysis of lanabecestat **3.01** and it's key 3-propyne-pyridine moiety **3.03** are shown in Scheme 9. The final step of the synthesis involves a palladium-catalysed Suzuki cross-coupling reaction between aryl bromide **3.02** and boronic acid **3.03**. The boronic acid of 3-propyne-pyridine moiety **3.03** is installed via a tandem lithiation-borylation sequence from the corresponding aryl bromide **3.04**. A palladium-catalysed Sonogashira cross-coupling reaction between commercially available 3,5-diboromopyridine **3.05** and TMS-propyne **3.06** initiates the synthetic sequence.

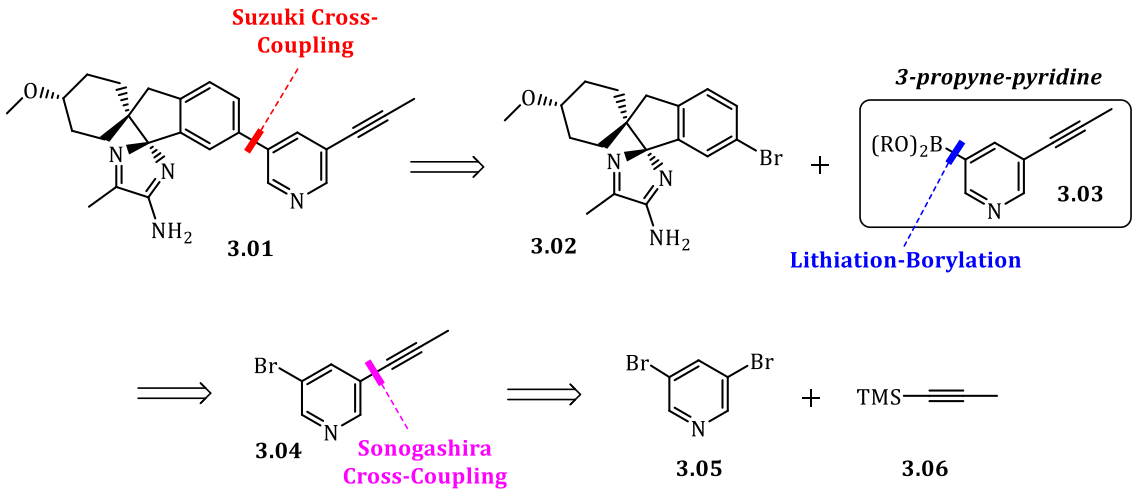

Scheme 9. Retrosynthetic analysis of lanabecestat **3.01** and it's key 3-propyne-pyridine moiety.

This method was used for kilogram-scale batch manufacturing of lanabecestat **3.01**.[117, 118] The process conditions for the synthesis of the 3-propyne-pyridine moiety are shown in Scheme 10. Initially, a Sonogashira cross-coupling reaction between 3,5-dibromopyridine **3.05** and TMS-propyne **3.06** yielded a mixture of desired mono-alkyne **3.04** and undesired bis-alkyne **3.07**. Use of TMS-propyne **3.06** as a surrogate for propyne gas required the addition of TBAF as a desilylating agent. In addition, a relatively long reaction time and high copper co-catalyst loading were required. Subsequent lithiation-borylation using *n*-HexLi and triisopropyl boronate under cryogenic conditions afforded boronic acid **3.03**, which was converted to a diethanolamine boronic ester (DABO) **3.08** by reaction with diethanolamine. The resultant DABO **3.08** was shown to be more air-stable than the parent boronic acid **3.03**, and could be used directly in the following Suzuki cross-coupling reaction.[118]

This process is a prime example of where transitioning from batch to continuous flow has the potential to be advantageous. For example: (i) access to higher temperatures to increase the rate of reaction could allow a reduction in the copper co-catalyst loading; (ii) safer use of explosive propyne gas would remove the need for the expensive TMS-propyne surrogate and TBAF additive; (iii) greater control over reaction time and mixing could improve product ratios; (iv) enhanced heat transfer could enable the rapid lithiation-borylation step to be performed under less energy-intensive cryogenic conditions. Therefore, process characteristics such as atom economy and cost have the potential to be significantly improved.

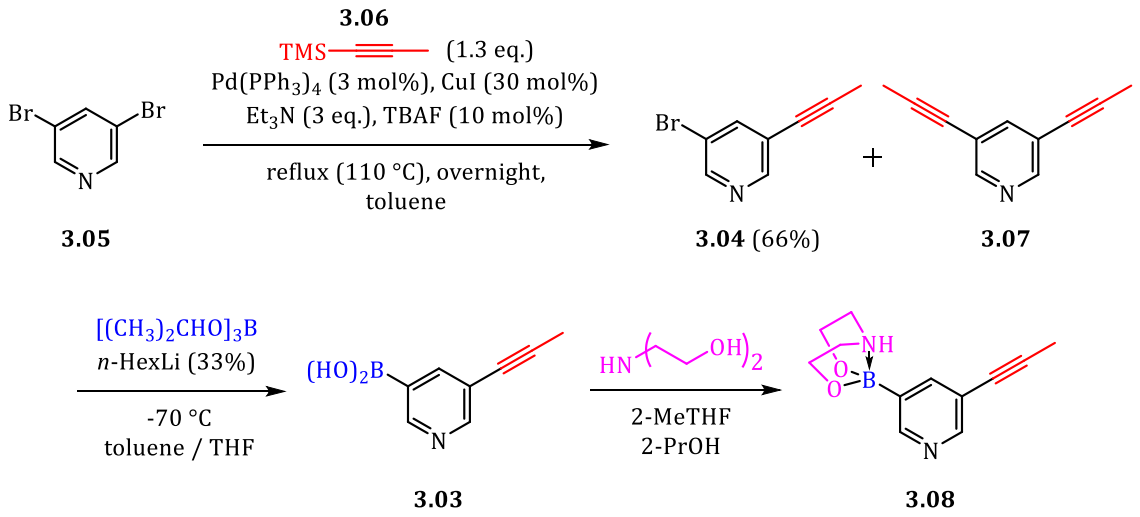

Scheme 10. Batch synthesis of the 3-propyne-pyridine moiety starting from 3,5-dibromopyridine **3.05**.

The Sonogashira reaction is a synthetic tool used to construct sp^2-sp carbon-carbon bonds between aryl halides and terminal alkynes. Hence, it is extensively used to synthesise arylalkynes which are ubiquitous scaffolds in APIs. Traditionally, the reaction requires a palladium catalyst and a copper co-catalyst (Scheme 11). The active Pd(0) catalyst is generated *in situ* via ligand dissociation or reduction from a suitable precatalyst. Initially, oxidative addition of R^1-X to Pd(0) occurs, where the rate is higher for substrates with a reduced electron density on the C-X bond. Meanwhile, the Cu(I) salt coordinates to the terminal alkyne substrate to form a π-alkyne-Cu complex, which increases the acidity of the acetylenic proton. This enables abstraction of the acetylenic proton in the presence of base, forming a copper acetylide. Transmetallation from the copper acetylide to the Pd(II) complex generates a palladium acetylide, which undergoes *cis*/*trans* isomerisation and reductive elimination to afford the arylalkyne and regenerated Pd(0) catalyst.[119] Herein, this chapter focuses on the development and optimisation of a continuous flow Sonogashira reaction towards the synthesis of lanabecestat **3.01**.

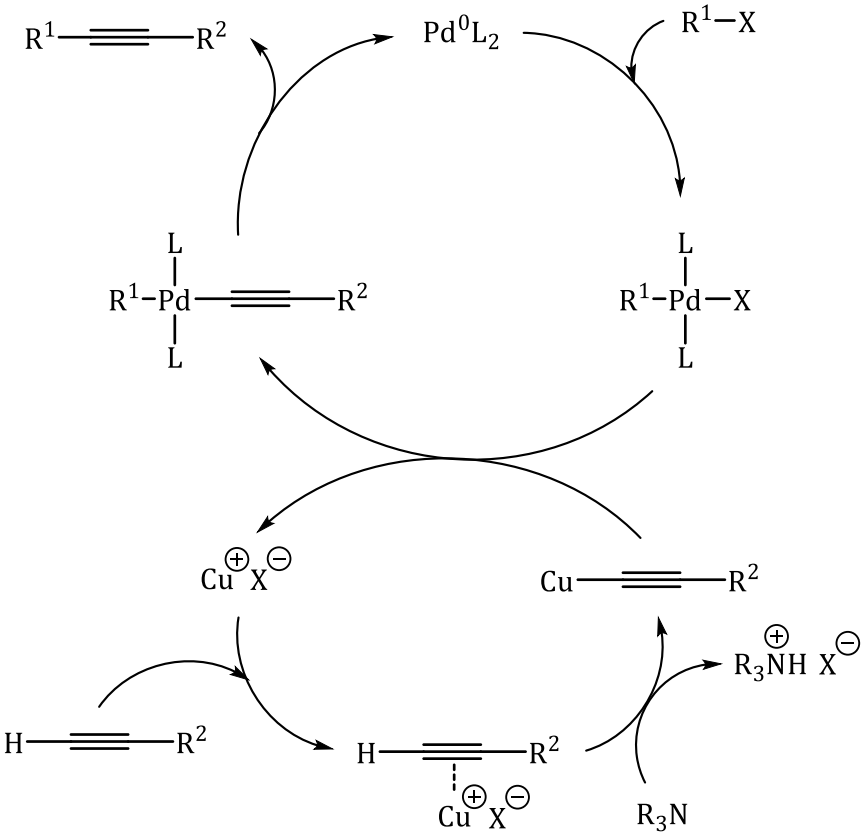

Scheme 11. Sonogashira reaction with independent palladium and copper catalytic cycles. L = ligand.

3.2 Optimisation of a Continuous Flow Sonogashira Reaction

Development of the proposed continuous flow synthesis of 3-propyne-pyridine **3.03** was divided into three process stages: (i) Sonogashira reaction; (ii) work-up; (iii) lithiation-borylation reaction. Each stage was assigned to a different team for optimisation, as is common during process development. Propyne was substituted for 1-hexyne to provide a suitable case study for optimisation of the Sonogashira reaction (Scheme 12). 1-Hexyne was selected as it was the shortest chain terminal alkyne with a boiling point high enough to avoid significant evaporation from the reactant reservoir at room temperature (bp = 71-72 °C). This resulted in a practically simpler process which could be translated to the propyne system once optimised. An automated platform was used throughout this work which utilised on-line HPLC and mass spectrometry for quantification and product identification respectively. Furthermore, a dilution pump (P3) was required to avoid saturation of the HPLC detector. The discrete variables such as catalyst, base and solvents were selected based on preliminary studies.[120]

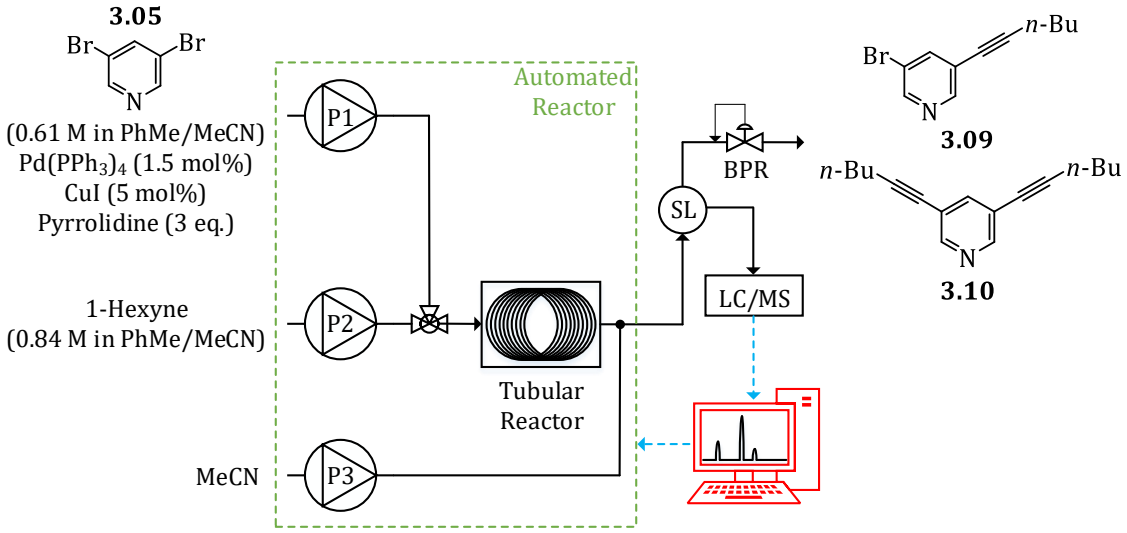

Scheme 12. Schematic of the automated flow reactor used to optimise the Sonogashira reaction case study. P = pump, BPR = back-pressure regulator, SL = sample loop. See experimental for more details.

The primary objective during the optimisation was to maximise the conversion, as 3,5-dibromopyidine **3.05** was difficult to remove during the downstream work-up, and formed additional impurities if present in the subsequent lithiation-borylation stage. Initially, a mixture of starting material **3.05**,

desired mono-alkynylated pyridine **3.09** and undesired bis-alkynylated pyridine **3.10** was obtained by refluxing 3,5-dibromopyridine **3.05** and 1-hexyne in toluene overnight. However, attempts to purify each compound by column chromatography were unsuccessful. Therefore, the mass of each compound in the mixture was determined by quantitative NMR using 1,3,5-trimethoxybenzene (1,3,5-TMB) as an internal standard (Table 7) [Eq (31)]. The calculated purities were used to calibrate the HPLC directly from the post-reaction mixture, enabling on-line quantification of future reactions.

$$p_x = \frac{I_x}{I_{cal}} \times \frac{N_{cal}}{N_x} \times \frac{M_x}{M_{cal}} \times \frac{W_{cal}}{W_x} \times P_{cal} \qquad (31)$$

Table 7. NMR data for the purity assessment of compounds **3.05**, **3.09** and **3.10** in a post-reaction mixture. The nuclei integrated for each compound are circled in red. *I* = integration, *N* = number of nuclei, *M* = molecular mass, *W* = gravimetric weight, *P* = purity.

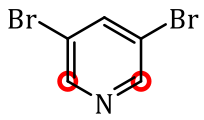

3.05

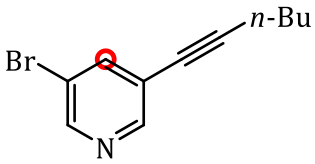

3.09

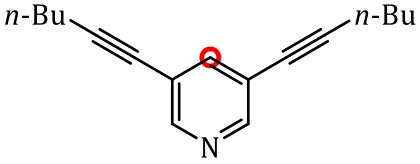

3.10

Compound	***I***	***N***	***M*/g mol^{-1}**	***W*/mg**	***P*/%**
SM **3.05**	2.04	2	236.89	65.25	**28.0**
Mono **3.09**	1.98	1	238.13	65.25	**54.6**
Bis **3.10**	0.26	1	239.36	65.25	**7.2**
1,3,5-TMB	4.40	3	168.19	19.22	97.0

A HPLC method was efficiently developed utilising a systematic design of experiments approach. A 2-level full factorial was conducted with respect to temperature (40-60 °C) and 5-90% gradient time (3-9 min) using a H_2O/MeCN mobile phase with 3% TFA buffer. Mass spectrometry was used post-HPLC to verify the retention times of the reactant and products. Models were fit to the retention times for each compound, which were validated with additional runs. The models for the reactant, products (Figure 34a) and three minor impurities (Figure 34b) showed an excellent predictive ability. Hence, the models were used to identify the conditions corresponding to the optimum resolution between the compounds: 40

°C, 5-90% gradient 9 min. The resolution between bis **3.10** and impurity 3 was further improved by adjusting the pH of the mobile phase (Figure 35). Lower pH values were found to increase the resolution between bis **3.10** and impurity 3 and decrease the resolution between impurities 1 and 2. A satisfactory compromise was obtained using 5% TFA as buffer. As all compounds had eluted after 8 min, the method was adjusted to 5-80% gradient in 8 min to reduce the overall analysis time.

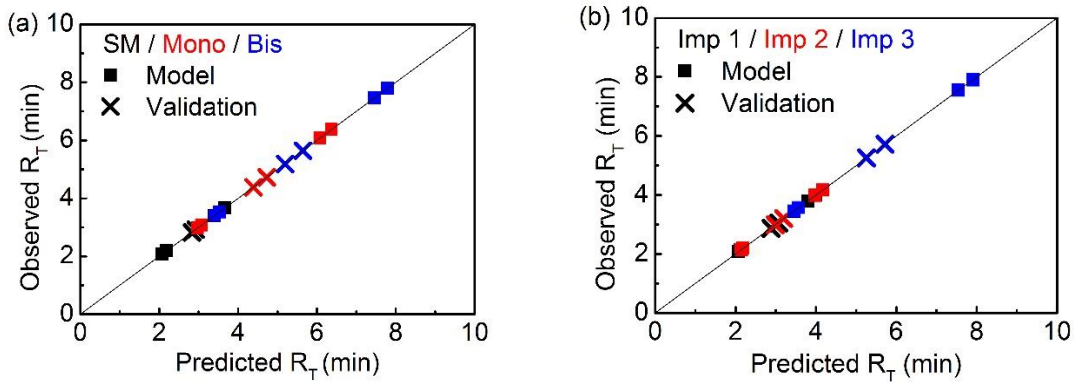

Figure 34. HPLC observed vs. predicted plots for the retention time (R_T) of compounds present in the Sonogashira reaction: (a) SM **3.05**, mono **3.09**, bis **3.10**; (b) three minor impurities. □ = 2-level full factorial, × = additional runs conducted to validate the models: (i) 40 °C, 5-90% gradient in 5.2 min; (ii) 50 °C, 5-90% gradient in 6 min. Imp = impurity.

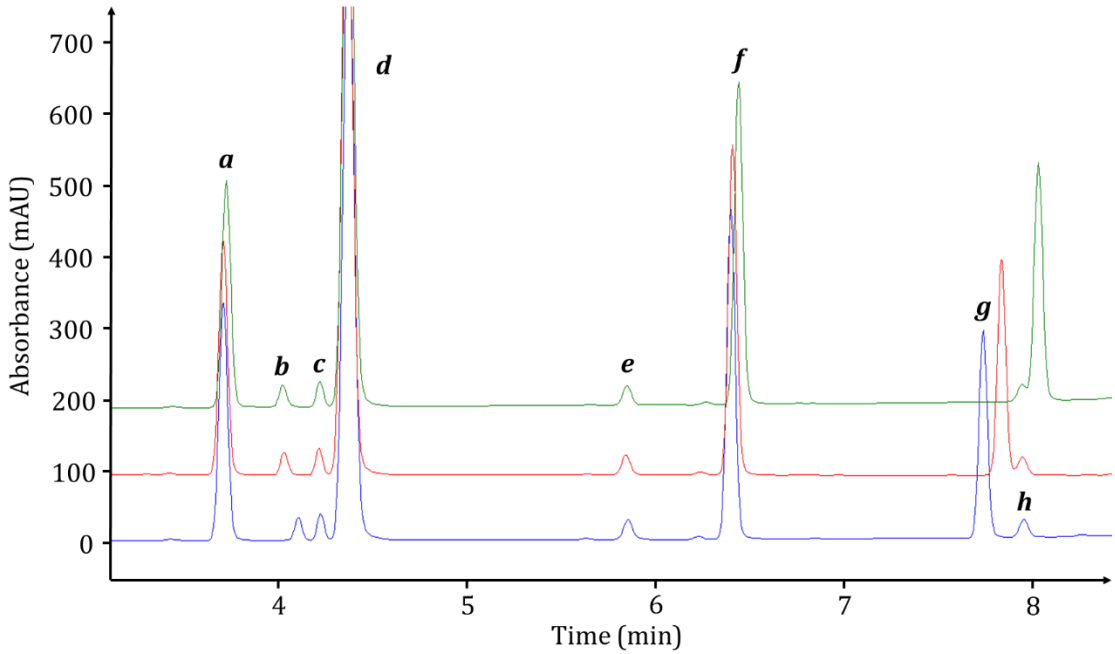

Figure 35. Overlaid HPLC chromatograms for the Sonogashira reaction using different buffers: 5% TFA (—), 3% TFA (—), 5% ammonium acetate (—). *a* = SM **3.05**, *b* = impurity 1, *c* = impurity 2, *d* = toluene, *e* = biphenyl (internal standard), *f* = mono **3.09**, *g* = bis **3.10**, *h* = impurity 3.

Initially, the loading of the copper catalyst and PhMe/MeCN solvent ratio were screened using a 2-level full factorial design. The upper and lower bounds of the variables were 5-10 mol% of CuI and 3.6-5.1:1 PhMe/MeCN solvent ratio. Increasing the PhMe/MeCN ratio above 3:1 resulted in the formation of free-flowing immiscible slugs in the reactor (Figure 36a). It was postulated that these slugs were the pyrrolidine.HBr salt formed during the reaction, which is insoluble in more non-polar solvent mixtures. In-line Raman spectroscopy was integrated downstream of the reactor to ensure steady-state operation was achieved in the two-phase flow (Figure 36b). The spectra showed that the consumption of SM **3.05** and formation of mono **3.09** could be monitored effectively in transient state. For a reaction with a 2 min residence time, the profiles stabilised after 5 min. Therefore, all experiments were left for 3 reactor volumes to reach steady state before analysis.

(a)

(b)

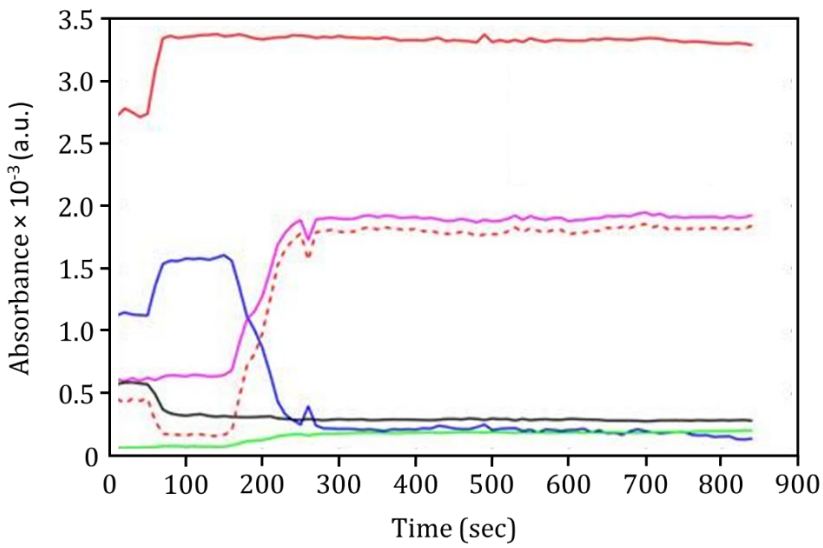

Figure 36. (a) formation of free-flowing slugs during the Sonogashira reaction; (b) Example Raman spectra for a reaction at 120 °C with a 2 min residence time. Toluene (—, 524 cm^{-1}), mono **3.09** (—, 1576 cm^{-1}), mono **3.09** (---, 2232 cm^{-1}), SM **3.05** (—, 281 cm^{-1}), MeCN (—, 378 cm^{-1}), 1-hexyne (—, 2119 cm^{-1}).

Polynomial modelling of the 2-level full factorial with respect to the amount of SM **3.05** remaining revealed the presence of a significant interaction term between the CuI loading and PhMe/MeCN ratio (Figure 37). At PhMe/MeCN ratios above 4.2:1, a higher CuI loading is favoured. In contrast, at PhMe/MeCN ratios below 4.2:1, a lower CuI loading is favoured. Furthermore, increasing the PhMe/MeCN ratio has little effect on the reaction at 5 mol% of CuI, whereas a significant increase in conversion is observed at 10 mol% of CuI. This suggests that a complex relationship between the co-catalytic cycle and the polarity of the solvent exists, which would be difficult to predict from chemical intuition alone.

It was hypothesised that the use of higher CuI loadings at low PhMe/MeCN ratios resulted in a lower conversion due to a potential competing Glaser coupling reaction. The Glaser coupling is a copper catalysed acetylenic coupling reaction which occurs in the presence of oxidants. Hence, Sonogashira reactions conducted under aerobic conditions can lead to the formation of 1,3-diynes.[121] Therefore, it was postulated that the homocoupling of 1-hexyne **3.11** to form 1,3-diyne **3.12** (Scheme 13) was kinetically favoured over the Sonogashira reaction at low PhMe/MeCN ratios. However, it should be noted that 1,3-diyne **3.12** was not observed by LC/MS.

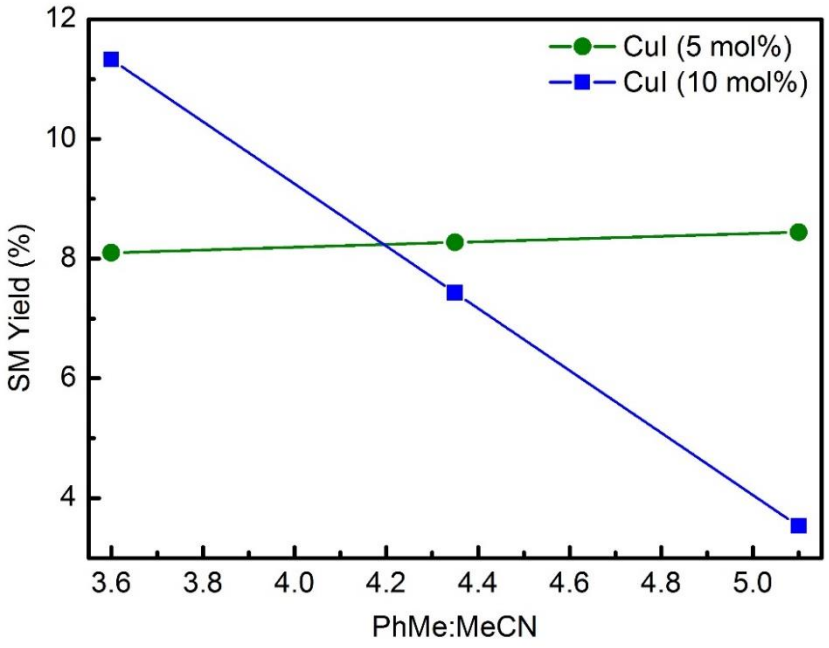

Figure 37. Plot showing the effect of the interaction between CuI mol% and PhMe/MeCN ratio on the amount of SM **3.05** remaining. Reaction conditions: t_{res} = 4.25 min, 1-hexyne equiv. = 1.4, temperature = 135 °C, $Pd(PPh_3)_4$ = 1.5 mol%, pyrrolidine equiv. = 3.0.

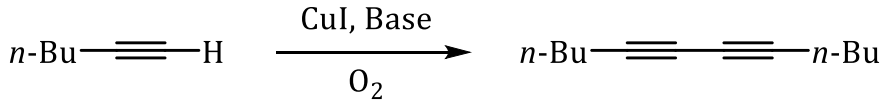

3.11 **3.12**

Scheme 13. Potential Glaser coupling of 1-hexyne **3.11** to form 1,3-diyne **3.12**.

To test the effect of oxygen on the reaction, reservoir solutions were prepared using degassed solvents under an inert atmosphere (Table 8). This resulted in a significant decrease in conversion of SM **3.05** compared to when the reservoirs were left open to air for one hour prior to the reaction (Entry 1 & 2). This suggested that oxygen had a beneficial effect on the Sonogashira reaction, and that the competing Glaser coupling reaction had a negligible effect on the reaction outcome under the previously determined optimum conditions (10 mol% CuI, 5.1:1 PhMe/MeCN). The copper source was changed to $CuCl_2$ to investigate whether oxidation of Cu(I) to Cu(II) was having a positive effect on the reaction (Entry 3). Although the reaction still proceeded in a good yield, a lower conversion was observed, indicating that copper oxidation alone would have a negative effect on the reaction.

Based on these results, it was rationalised that oxygen was playing a role in the palladium catalytic cycle. It is known that PPh_3 readily oxidises in air to form triphenylphosphine oxide. This could result in a shift in the ligand dissociation-association equilibrium from the 18e$^-$ $Pd(PPh_3)_4$ precatalyst **3.13** towards the 14e$^-$ $Pd(PPh_3)_2$ active catalyst **3.14** (Scheme 14). This type of rate-limiting ligand dissociation has previously been observed for oxidative addition of bromoarenes to Pd^0 complexes with hindered phosphine ligands.[122] However, kinetic studies that are beyond the scope of this work would be required to confirm this. Nevertheless, all future experiments were conducted under an aerobic atmosphere.

Table 8. Summary of experiments testing the effect of oxygen on the Sonogashira reaction.

Entry[a]	Cu Source	SM 3.05/%	Mono 3.09/%	Bis 3.10/%
1[b]	CuI	5.7	69.6	24.7
2	CuI	16.5	70.7	12.8
3	$CuCl_2$	21.6	65.8	12.6

[a] 4.25 min, 135 °C, $Pd(PPh_3)_4$ (1.5 mol%), Cu (10 mol%), PhMe/MeCN (5.1:1), pyrrolidine (3 equiv.).

[b] Reactant reservoirs open to air for one hour prior to the reaction.

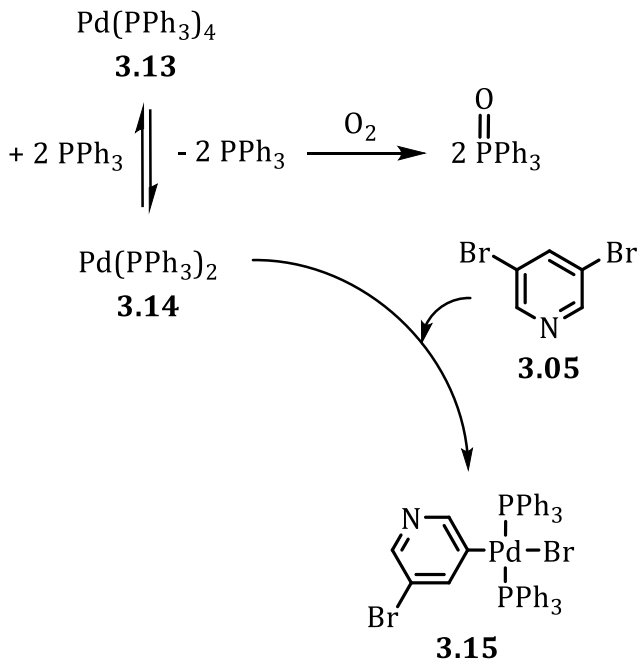

Scheme 14. Proposed effect of oxygen on oxidative addition of bromoarenes to Pd^0. In cases with a rate-limiting ligand dissociation step, removal of PPh_3 ligands by oxidation to PPh_3O drives the equilibrium forward.

The remaining continuous variables were optimised subject to the following variable limits: residence time (3 – 8 min), equivalents of 1-hexyne (1.2 – 1.6) and temperature (120 – 150 °C). A Box-Behnken design was selected which is shown graphically for three factors in Figure 38a. In contrast to central composite designs, a Box-Behnken design always has three levels and conducts experiments at the midpoints of the edges. They benefit from a reduced number of experiments required to identify all first- and second-order coefficients in cases with three or less factors. This makes them particularly well-suited for optimising expensive systems, such as those involving high value catalysts. However, this comes at the expense of a lower predictive ability at the extremes of the experimental space.

The composition of the reaction mixture was determined for each experiment and response surfaces fitted to the SM **3.05**, mono **3.09** and bis **3.10** compounds (Figure 38b). Notably, the residence time was found to be insignificant with respect to all three, indicating that the reaction had stalled after 3 min. This was likely caused by deactivation of the catalyst under the reaction conditions. In addition, the temperature had a relatively small effect on the conversion of SM **3.05**. Increasing the temperature from 120 to 135 °C slightly improved conversion. However, further increasing the temperature from 135 to 150 °C was detrimental to the conversion, suggesting higher temperatures promoted catalyst deactivation. The yield of the

desired mono **3.09** product remained virtually constant with changing 1-hexyne equivalents. In contrast, the consumption of SM **3.05** and formation of bis **3.10** were approximately inversely proportional, indicating equal rates of reactions for the two consecutive steps within the experimental space.

(a)

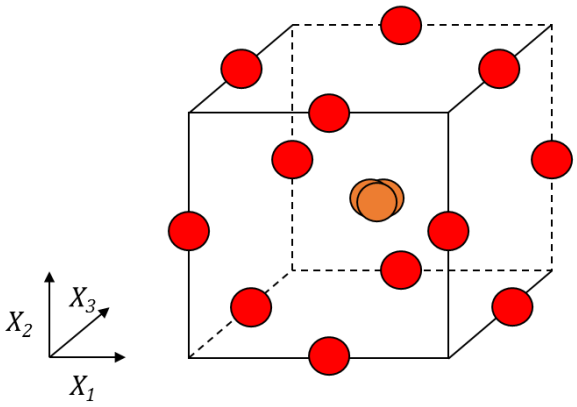

Exp	X_1	X_2	X_3
1	-1	-1	0
2	+1	-1	0
3	-1	+1	0
4	+1	+1	0
5	-1	0	-1
6	+1	0	-1
7	-1	0	+1
8	+1	0	+1
9	0	-1	-1
10	0	+1	-1
11	0	-1	+1
12	0	+1	+1

(b)

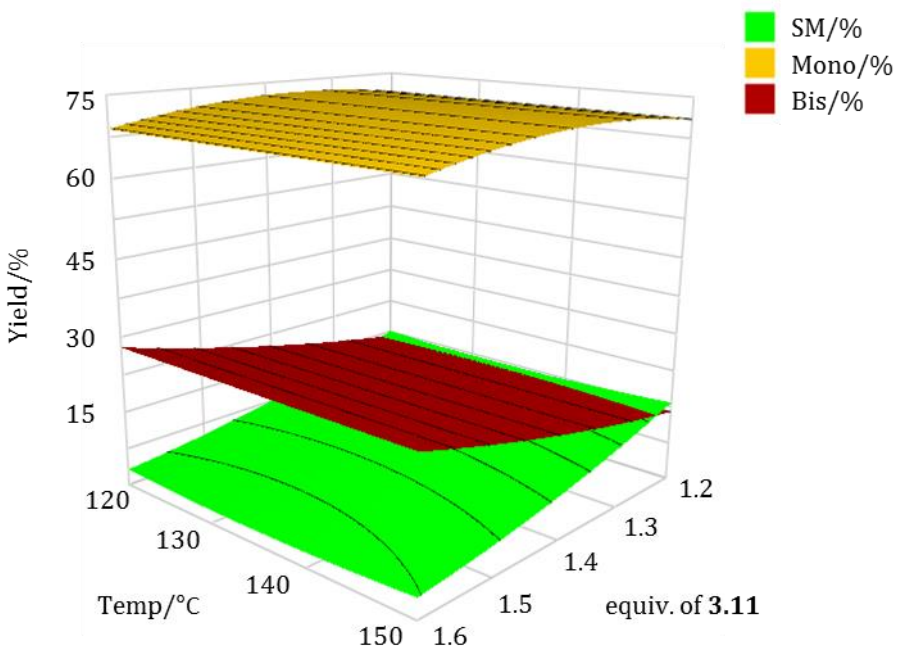

Figure 38. (a) Box-Behnken design for three factors (X_1, X_2, X_3) between limits -1 and +1; (b) response surfaces for SM **3.05**, mono **3.09** and bis **3.10**.

The main aim of the optimisation was to maximise the conversion to prevent SM **3.05** from interfering with downstream steps, whilst still operating under economically favourable conditions. This problem belonged to the class of expensive-to-evaluate problems, as this work had identified the Sonogashira reaction as a complex system involving high value catalysts. Furthermore, strict deadlines applied to the pharmaceutical industry resulted in significant time constraints for the remaining process development to be completed. Therefore, self-optimisation using the previously explored TSEMO algorithm was selected to simultaneously maximise STY and minimise the amount of SM **3.05** remaining [Eq (32)]. Taking into consideration the factor effects identified from the Box-Behnken response surfaces, the lower limit of residence time was reduced to explore potentially more interesting regions of space.

$$minimise[-\ln(STY), \ln(\%\ of\ SM\ \mathbf{3.05})] \quad (32)$$

subject to:

Residence time/min ∈ [1.0, 8.0]

1-hexyne equivalents ∈ [1.2, 1.6]

Temperature/°C ∈ [120, 150]

The optimisation was initialised with 20 LHC experiments, followed by 60 experiments designed by the TSEMO algorithm. The algorithm converged on a Pareto front consisting of 20 non-dominated solutions (Figure 39). The optimal STY was 3198.8 kg m^{-3} h^{-1} with 10.9% SM **3.05** remaining. In contrast, the optimal conversion corresponded to 1.9% SM **3.05** remaining with a STY of 315.4 kg m^{-3} h^{-1}. Hence, the results highlighted the inherent trade-off between conversion and productivity.

The reaction profiles for the % of SM-**3.05** remaining and STY are shown in Figure 40a and 8b respectively. Notably, inspection along the z-axis indicates that varying the temperature between 120 and 150 °C has little effect on either objective. In contrast, reducing the residence time corresponds to a large increase in STY, due to both a reduction in process time and conversion of mono **3.09** to bis **3.10** (Figure 40c). This correlates with a relatively small increase in SM **3.05** remaining. For example, the STY can be increased from 656.9 to 1585.7 kg m^{-3} h^{-1} by reducing the residence time from 4.1 to 1.8 min, whilst only increasing the SM **3.05** remaining from 2.1 to 3.7%. The STY can be further increased at the lower limits of residence

time by reducing the equivalents of 1-hexyne, which reduces conversion of mono **3.09** to bis **3.10**. However, this corresponds to a relatively large increase in % of SM **3.05** remaining. For example, the STY can be increased from 3009.2 to 3198.8 kg m^{-3} h^{-1} by reducing the equivalents of 1-hexyne from 1.60 to 1.46 when t_{res} = 1 min, but this results in an increase in SM **3.05** remaining from 7.4 to 10.9%.

The results from this optimisation followed precise trends and contained no erroneous data points, showcasing the high accuracy of the self-optimising reactor developed throughout this work. Low experimental noise enabled rapid optimisation of the experimental space to meet the time constraints of the project. Furthermore, the multi-objective Pareto front optimisation approach enabled clear visualisation of the trade-off between conversion and productivity. In this case, the best STY could readily be selected under the current work-up limitations with respect to SM **3.05**. Unlike targeted or weighted objective optimisation, the TSEMO algorithm identifies the complete trade-off, such that the data can be re-evaluated without further experimentation if process parameters are altered. This is particularly beneficial in the pharmaceutical industry, where the specifications of the downstream work-up are dynamic during process development. Therefore, with most pharmaceutical processes having competing objectives, the use of such algorithms is clearly a beneficial tool for flexible project scenario planning.

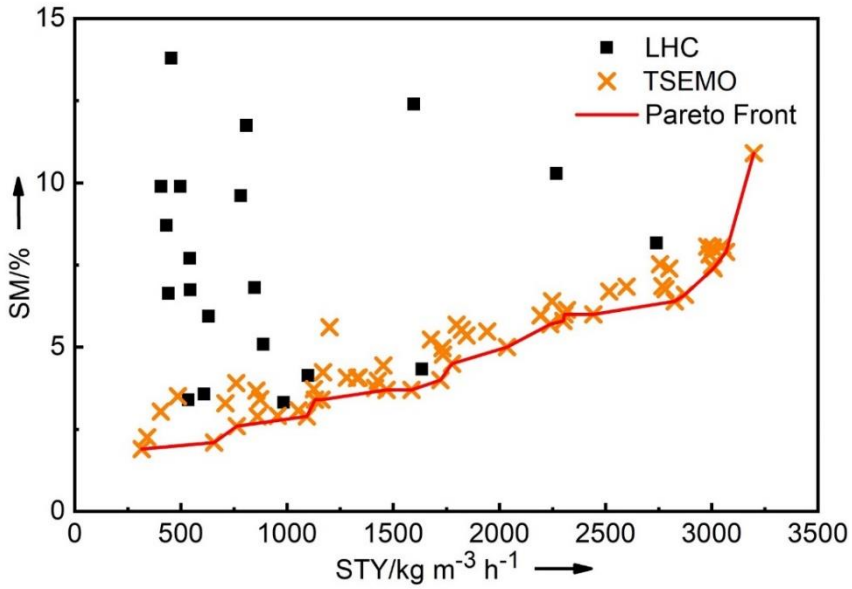

Figure 39. Results for the optimisation of the Sonogashira reaction with respect to STY and SM **3.05** remaining. The initial LHC size was 20. The TSEMO algorithm conducted an additional 60 experiments, 20 of which formed a Pareto front highlighting the trade-off between the objectives.

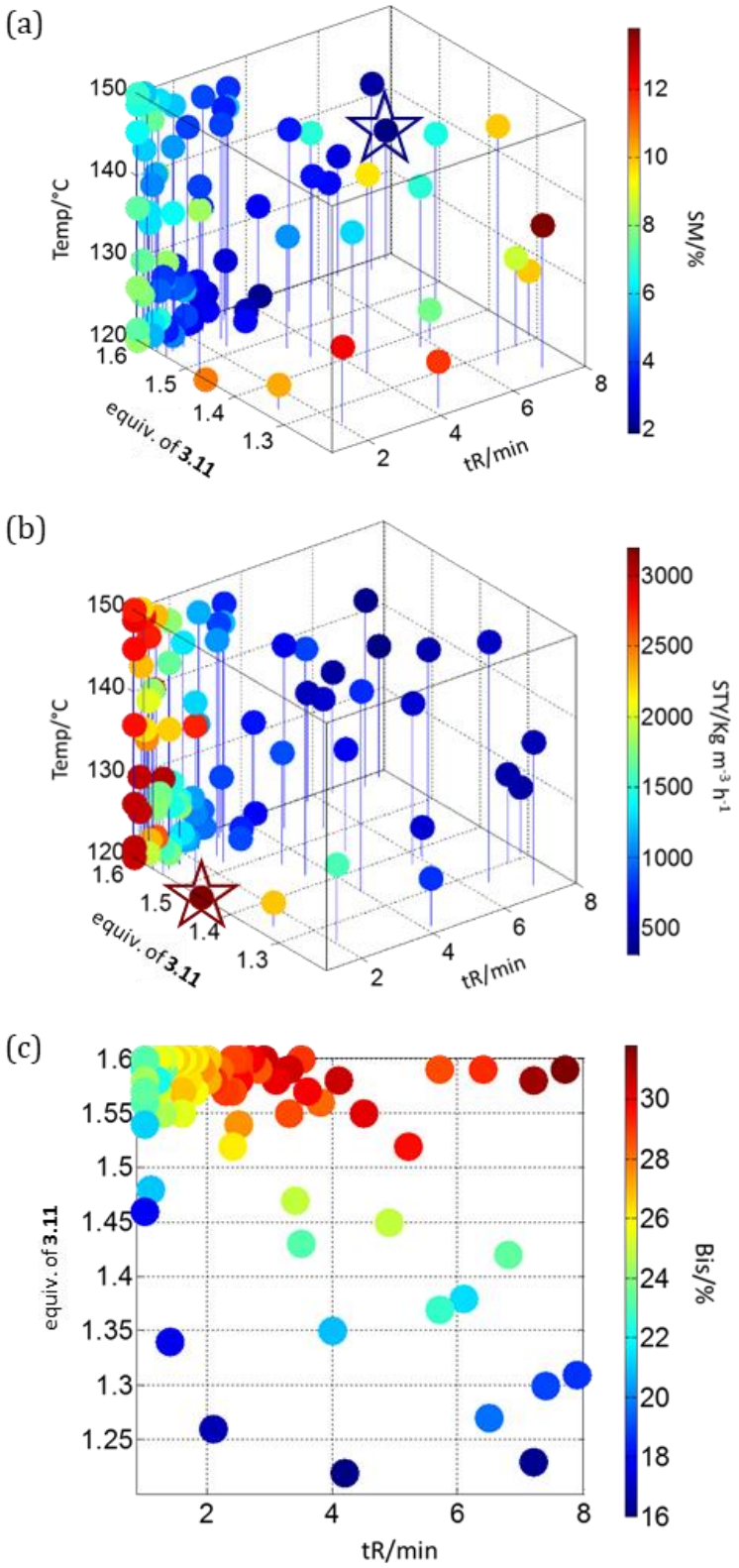

Figure 40. Plots of experiments performed during the optimisation for different responses: (a) % of SM **3.05** remaining; (b) STY with respect to mono **3.09**; (c) % of bis **3.10**, rotated to depict data as viewed along the z-axis. ☆ = optimum.

One of the challenges associated with expensive-to-evaluate optimisation is determining an appropriate termination criterion. Too few experiments can yield inaccurate models, whereas too many experiments are wasteful in terms of time and reagents. For multi-objective problems, the optimisation could be terminated once the hypervolume improvement between experiments falls below a predefined level. Although this method could be easily automated, there is no guarantee that the hypervolume will improve between each experiment. For example, the hypervolume after each TSEMO experiment for the Sonogashira optimisation is displayed in Figure 41a. The hypervolume stabilised between experiments 41 and 47, however a significant increase in hypervolume was observed between experiments 47 and 56. Hence, premature termination would have resulted in the identification of an incomplete trade-off curve. Rather, the progress of the optimisation was monitored via visual inspection of the predicted Pareto front (Figure 41b). This was achieved using NSGA-II to evaluate the hyperparameters of the current GP surrogate models. It was evident that the initial 20 LHC experiments were insufficient for creating a GP model that accurately describes the actual Pareto front. The shape of the Pareto front was improved after initial exploration by the TSEMO algorithm, however the extreme points of the front were not identified until between experiments 40 and 60. The optimisation was terminated after 80 experiments, as there were no significant changes to the GP model between experiments 60 and 80. Although this method required manual evaluation, it avoided using predefined limits and thus reduced the risk of premature termination.

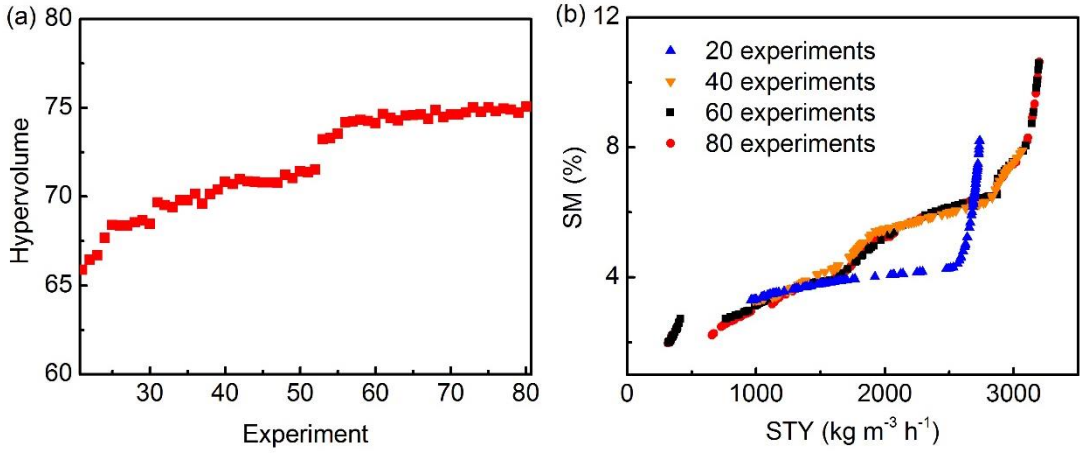

Figure 41. Different approaches for termination of a TSEMO self-optimisation: (a) quantified change in hypervolume between experiments; (b) visual inspection of the Pareto front predicted from the GP models.

3.3 Comparison of Multi-Objective Optimisation Algorithms

Self-optimising systems must be kept up-to-date with the most recent and advanced technologies to ensure maximum efficiency is achieved. Therefore, recently developed multi-objective optimisation algorithms (MOOA) should be compared against their older counterparts with respect to Pareto convergence and diversity. In general, MOOAs are compared using mathematical test functions which represent a wide range of optimisation problems.[123] These have a different number of variables and objectives with varying Pareto front properties. However, the variable and objective space are not specifically designed to mimic real chemical space, for example, high dimensional problems (e.g. DTLZ7a, inputs = 8) with disconnected local Pareto fronts. Hence, a series of chemistry-based test problems have been designed to improve the evaluation of MOOAs for the self-optimisation of chemical reactions. This was achieved by constructing a kinetic-based reaction simulator.

Four reactions with known kinetics (pre-exponential factors and activation energies) were identified in the literature: (i) Van de Vusse reaction;[124] (ii) nucleophilic aromatic substitution between 2,4-difluoronitrobenzene and morpholine;[125] (iii) isomerisation of lactose to lactulose;[126] (iv) Paal-Knorr reaction between 2,5-hexanedione and ethanolamine (Scheme 15).[127] These examples provided a good representation of non-competitive (iv) and competitive reactions, including competing parallel (i, ii & iii) and consecutive pathways (ii & iii). Although reactions (iii) and (iv) contain reversible reactions, the k_{-1} rate constants are negligible and were therefore omitted. Six test problems were formulated using reaction variable limits as constraints and different process metrics as objectives. Details and visual representations of the variable and objective space for each test problem are provided in the experimental section. A summary of the test problems including a description of the Pareto front is provided in Table 9. Each problem was designed to contain between 2-4 variables and 2-3 objectives, as higher dimensional problems are not realistic of current self-optimising chemical platforms. Furthermore, the variable limits and objectives for each problem were selected to ensure a diverse range of Pareto fronts were generated in terms of morphology, uniformity and continuity.

(i)

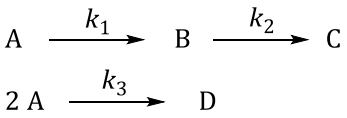

A_1 = 2.1 × 10^{10} min^{-1}, $A2$ = 2.1 × 10^{10} min^{-1}, $A3$ = 1.5 × 10^{8} min^{-1},
$E_{a,1}$ = 81.1 kJ mol^{-1}, $E_{a,2}$ = 81.1 kJ mol^{-1}, $E_{a,3}$ = 71.2 kJ mol^{-1}

(ii)

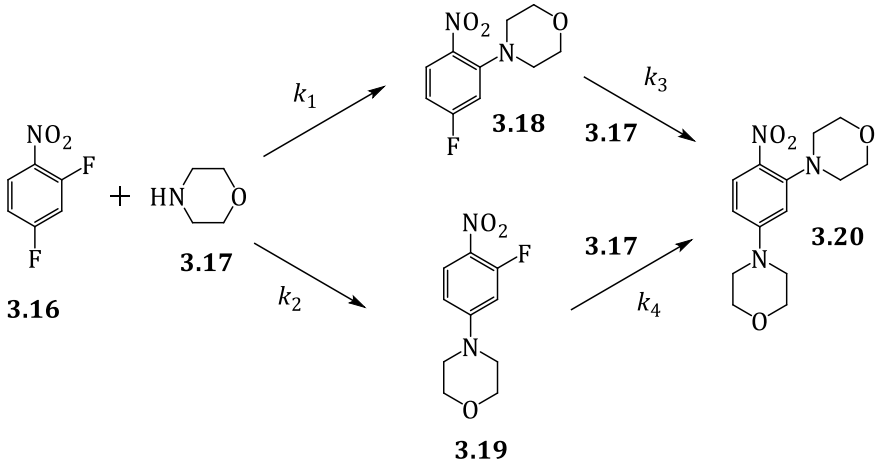

A_1 = 1.6 × 10^{6} M^{-1} min^{-1}, A_2 = 1.4 × 10^{4} M^{-1} min^{-1}, A_3 = 1.0 × 10^{4} M^{-1} min^{-1},
A_4 = 3.7 × 10^{8} M^{-1} min^{-1}, $E_{a,1}$ = 43.2 kJ mol^{-1}, $E_{a,2}$ = 35.3 kJ mol^{-1},
$E_{a,3}$ = 40.8 kJ mol^{-1}, $E_{a,4}$ = 68.9 kJ mol^{-1}

(iii)

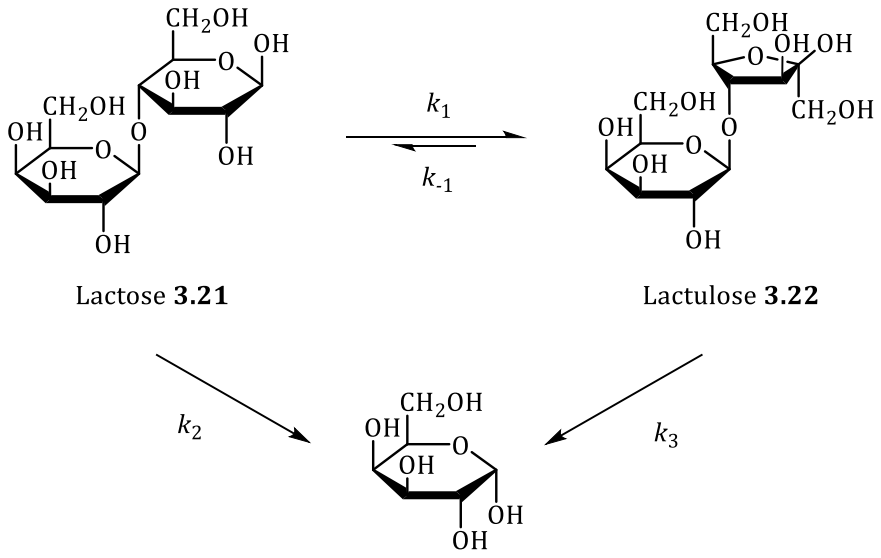

Lactose **3.21**

Lactulose **3.22**

Galactose **3.23**

pH = 11, A_1 = 9.5 × 10^{14} min^{-1}, A_2 = 7.0 × 10^{24} min^{-1}, A_3 = 4.0 × 10^{7} min^{-1},
$E_{a,1}$ = 105.1 kJ mol^{-1}, $E_{a,2}$ = 174.0 kJ mol^{-1}, $E_{a,3}$ = 54.9 kJ mol^{-1}

(iv)

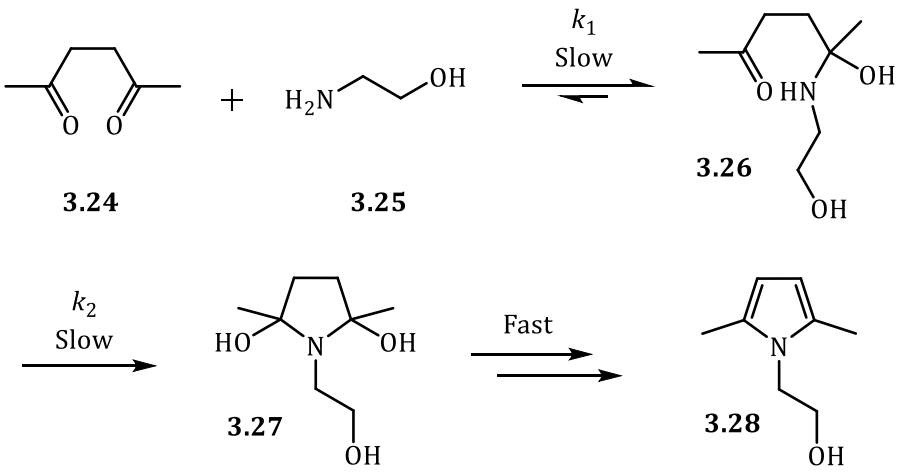

A_1 = 15.4 M^{-1} min^{-1}, A_2 = 405.2 min^{-1}, $E_{a,1}$ = 12.2 kJ mol^{-1}, $E_{a,2}$ = 20.0 kJ mol^{-1}

Scheme 15. Literature reactions and kinetic data used to formulate the chemistry-based multi-objective test problems: (i) Van de Vusse reaction; (ii) nucleophilic aromatic substitution between 2,4-difluoronitrobenzene **3.16** and morpholine **3.17**; (iii) isomerisation of lactose **3.21** to lactulose **3.22**; (iv) Paal-Knorr reaction between 2,5-hexanedione **3.24** and ethanolamine **3.25**. A = pre-exponential factor, E_a = activation energy.

Table 9. Summary of the chemistry-based multi-objective test problems. VdV = Van der Vusse, PK = Paal-Knorr.

Test Problem	Variables	Objectives	Description of Pareto Front
VdV1	2	2	Density of solutions fall away near to the Pareto front, which is non-uniformly distributed between linear and convex regions
S_NAr1	2	3	Optimal solutions follow a convoluted path through objective space with concave regions
S_NAr2	4	3	Convex, non-uniformly distributed Pareto front
Lactose1	2	2	Pareto front is a convex curve with many solutions
PK1	2	2	Pareto front is a convex curve with relatively few solutions
PK2	3	2	Pareto front consists of three discontinuous linear and concave regions

The simulation procedure is outlined below. Firstly, the pre-exponential factors, A, and activation energies, E_a, were used to calculate the rate constants, k, for each reaction step. This was achieved using the temperature dependant Arrhenius equation [Eq (33)], where T = temperature and R = gas constant (8.314 J mol^{-1} K^{-1}). Rate equations with respect to the consumption of each species were written in their differential form. For example, the differential rate equations for the four compounds (A-D) in the Van de Vusse reaction were written according to [Eq (34-(37)] respectively. The concentration of each compound at the outlet of the reactor was determined by evaluating the rate equations using an ordinary differential equation (ODE) solver. The ODE solver is a temporal discretisation method which provides approximate solutions to transient rate problems by calculating the concentrations iteratively in time steps. This process was terminated after four reactor volumes to ensure steady-state was achieved. In this case, the system was modelled for four CSTRs in series by solving simultaneously the coupled ODE equations.[128]

$$k = Ae^{-\frac{E_a}{RT}} \tag{33}$$

$$rate = -\frac{\Delta A}{\Delta t} = k_1[A] + k_3[A]^2 \tag{34}$$

$$rate = -\frac{\Delta B}{\Delta t} = -k_1[A] + k_2[B] \tag{35}$$

$$rate = -\frac{\Delta C}{\Delta t} = -k_2[B] \tag{36}$$

$$rate = -\frac{\Delta D}{\Delta t} = -k_3[A]^2 \tag{37}$$

The yields of each compound were calculated from the outlet concentrations. The error associated with the experimental platform used throughout this work was previously characterised to have a maximum absolute and relative error of 0.25% and 0.5% respectively.[129] Therefore, the yields were adjusted according to [Eq (38)] to better reflect a real chemical system, where Y = yield and $rand$ = random number between 0 and 1. If the adjusted yield, Y_{adj}, was less than 0 or greater than 100, then it was forced onto the nearest boundary. This ensured the successful calculation of alternative objectives of interest such as STY and RME.

$$Y_{adj} = Y + \left(\left(\frac{rand - 0.5}{2} \right) + Y \left(\frac{rand - 0.5}{100} \right) \right) \quad (38)$$

The results were given to a specified MOOA, which generated the next set of reaction conditions based on the previous results. To assess the performance of each MOOA, the hypervolume after every iteration was calculated during post-processing. As calculation of the actual hypervolume is considered to be too computationally expensive, a Monte-Carlo method was used to provide a satisfactory approximation.[130] The estimate was made by calculating the percentage of 100,000 random points in the objective space which were dominated by the current Pareto front.[131, 132] The utopian and anti-utopian point for the objective space of each test problem were selected by creating a superset of the non-dominated solutions from all runs across all algorithms. The reference point for the objective space was then defined as the anti-utopian point shifted by 0.01 of the difference between the utopian and anti-utopian point.[133]

The performance of TSEMO,[96] Pareto efficient global optimisation (ParEGO),[133] NSGA-II[94] and expected improvement matrix efficient global optimisation (EIM-EGO)[134] were compared using the developed approach. Implementations of ParEGO, NSGA-II and EIM-EGO were all available in the platform for evolutionary multi-objective optimisation (PlatEMO) toolbox in MATLAB.[135, 136] The TSEMO algorithm used throughout this work was compared with both one and four points (batch sequential, BS-TSEMO) per iteration. ParEGO and EIM-EGO were chosen as they represent alternative surrogate model-based multi-objective optimisation algorithms, whereas NSGA-II is a commonly used genetic algorithm. The TSEMO, BS-TSEMO, ParEGO and EIM-EGO were initialised using a LHC design of size 20. Each algorithm had a function evaluation budget of 100, and was ran 20 times for each test problem to compare average performance. To account for the function evaluation budget, the NSGA-II population size and total number of generations were changed to 20 and 5 respectively.

Plots showing the average change in hypervolume throughout the optimisations are shown in Figure 42. Furthermore, boxplots of the optimisation results after 60 function evaluations are displayed in Figure 43, which provides a more detailed view at a practical number of experiments. From these results, the following observations and conclusions can be made:

- The NSGA-II algorithm has the lowest hypervolume after any number of function evaluations beyond the initial dataset, apart from the Lactose1 test problem where it has similar performance to ParEGO. Thus, surrogate model-based approaches are more suitable for expensive-to-evaluate problems.
- The TSEMO and BS-TSEMO algorithms have a very similar performance based on the median and interquartile range of the hypervolume after 60 function evaluations. However, a notable difference occurs for the VdV1, S_NAr2 and PK1 test problems, where the increase in hypervolume after the initial dataset is slower for BS-TSEMO. This is due to a reduction in the use of information gathered at run time. Hence, a balance between experiment time and total number of experiments is required.
- ParEGO suffers from a large range of hypervolumes in 3 of the 6 test problems (Lactose1, PK1, PK2), indicating that ParEGO is less robust compared to the other algorithms.
- EIM-EGO outperforms the other algorithms on 4 of the 6 test problems (VdV1, Lactose1, PK1, PK2) based on the median of the hypervolume after 60 function evaluations. Furthermore, the increase in hypervolume is significantly faster after the initial dataset compared to TSEMO for the VdV1 and PK2 test problems. This is likely caused by an increased emphasis on exploitation when using an expected improvement matrix compared to Thompson sampling.

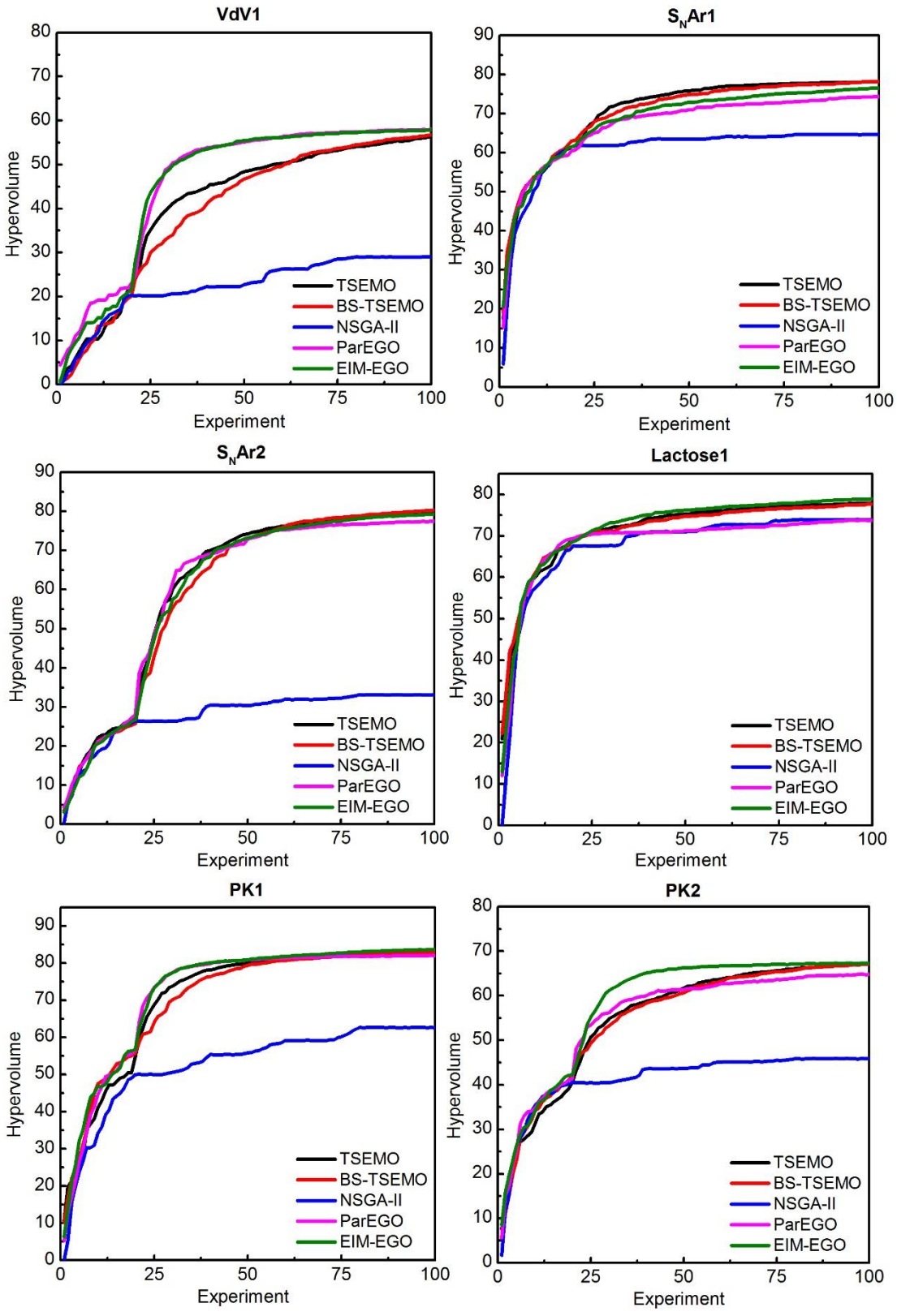

Figure 42. Plots showing the average change in hypervolume across 20 runs with 100 function evaluations each.

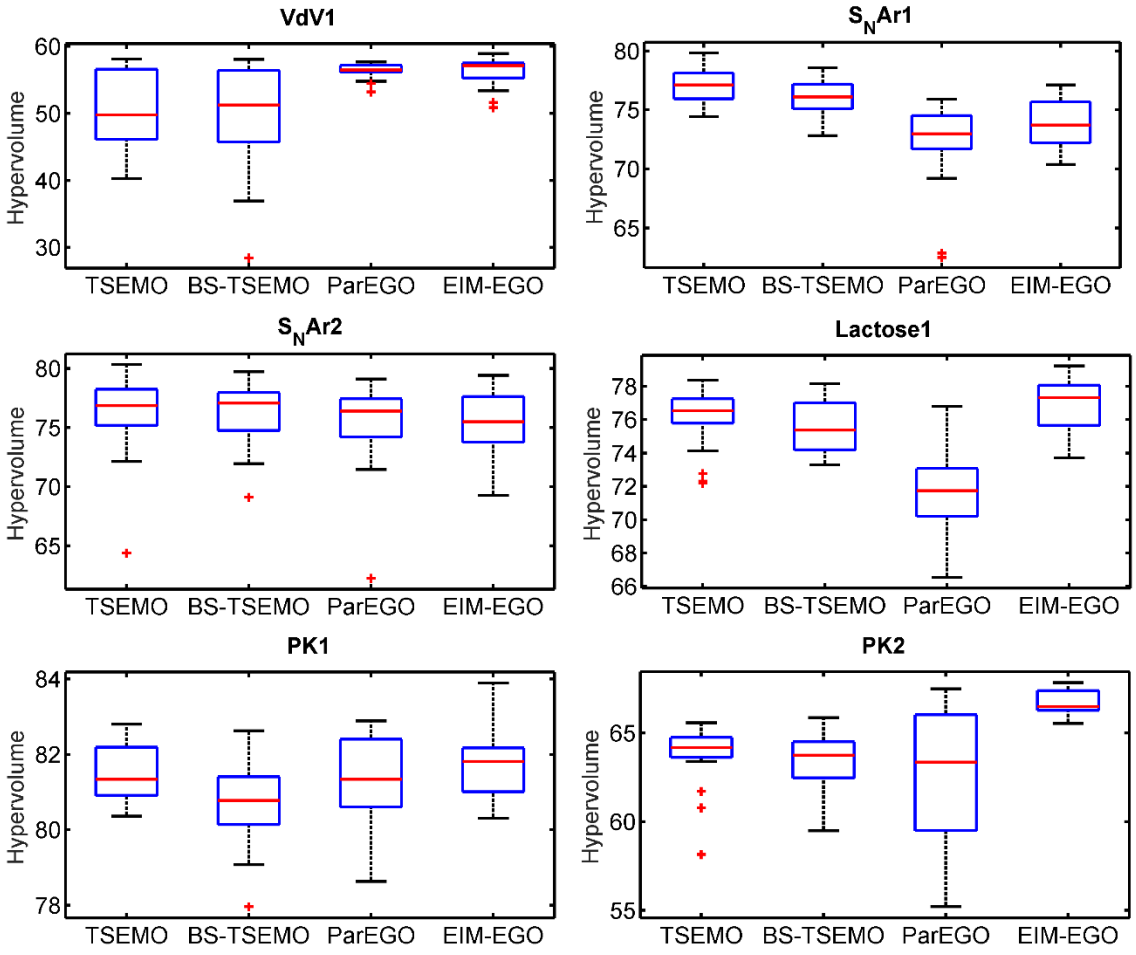

Figure 43. Boxplots of the optimisation results after 20 runs and 60 function evaluations using hypervolume as a performance indicator. The NSGA-II results were omitted for clarity. + = outlier (more than 1.5× the interquartile range away from the upper or lower quartile).

3.4 Conclusions

There has been an increasing shift towards the use of continuous flow chemistry for the synthesis of APIs in recent years.[137] In this work, a Sonogashira reaction used in the synthesis of lanabecestat, a phase III clinical trial drug candidate for the treatment of Alzheimer's disease, was transferred from batch to flow.[113] Initial analytical development resulted in a robust autonomous flow reactor, which was utilised to perform a systematic DoE study. These investigations led to the identification of: (i) unexpected interactions between the solvent and co-catalyst; (ii) a positive correlation between aerobic conditions and conversion; (iii) response surface models for each compound of interest, which guided further optimisation studies.

Despite the advantages associated with feedback-directed optimisation, the use of self-optimisation to develop pharmaceutically relevant steps have been sparsely reported.[46, 48] This is partly due to the focus on single objective optimisation in academia, whereas industry must consider multiple conflicting objectives during process design. Our previously described multi-objective optimisation approach was used to simultaneously optimise conversion and STY of the Sonogashira reaction with respect to three parameters. Identification of the Pareto front enabled the optimum reaction conditions to be re-evaluated with changing downstream work-up specifications in the active learning process. In this way, individual steps could be optimised in parallel and combined to yield a multi-step process in a reduced time frame. Furthermore, optimisation of the Sonogashira reaction required only 35 hours with no human intervention. Hence, this work demonstrated how a standardised workflow of analytical development, automated DoE studies and multi-objective self-optimisation can be utilised to provide all necessary information within the time constraints of a late-stage pharmaceutical development project.

The efficiency of self-optimisation can be directly related to the choice of optimisation algorithm. Therefore, it is important to keep self-optimising systems up-to-date with the latest advances in computer science. This is imperative in the pharmaceutical industry, where reactions involve high-value drug precursors. A method to compare the performance of multi-objective optimisation algorithms for the self-optimisation of chemical reactions was developed using a kinetic-based reaction simulator. Of the algorithms tested, EIM-EGO was found to outperform the TSEMO algorithm used throughout this work, and should therefore be implemented for future multi-objective optimisations.[134]

Chapter 4 A Miniature CSTR Cascade Reactor for Biphasic Continuous Flow Photochemistry

4.1 Introduction

Ultraviolet and visible (UV-Vis) light are parts of the electromagnetic spectrum defined by wavelengths between 10-400 nm and 400-700 nm respectively. The energy from UV-Vis photons can be absorbed by molecules and exploited to achieve many organic transformations, such as: cycloadditions, sigmatropic rearrangements and electrocyclic ring closures.[138] Photoactivation of substrates often removes the need for additional reagents, thus reducing by-product formation. Hence, photons can be described as "traceless and green reagents", making photochemical methods attractive for sustainable process development.[139] A reaction of particular interest to the fine chemical industry is the aerobic oxidation of C-H bonds. This reaction utilises molecular oxygen as a low cost and environmentally friendly oxidant, to provide access to valuable building blocks for further functionalisation. As such, this work will focus on photochemistry in the context of aerobic oxidations.

Absorption of photons by a molecule results in photoexcitation, where an electron is promoted from a lower energy level to a higher energy level. In the case of oxygen, the ground state (Figure 44a) and excited states (Figure 44b & c) differ in the spin and occupancy of the degenerate π* orbitals. Triplet state refers to ground state oxygen ($^3\sum_g^-$) where the two π* electrons occupy different orbitals with the same spin. Singlet state refers to the two excited states of oxygen, where the spin of the two π* electrons are opposite. The configuration where the electrons occupy different orbitals ($^1\sum_g^+$) is 63 kJ mol^{-1} higher in energy compared to when the electrons are paired ($^1\Delta_g$).[140] This results in rapid conversion from $O_2(^1\sum_g^+)$ to $O_2(^1\Delta_g)$, which is a highly reactive and electrophilic species due to a low-lying lowest unoccupied molecular orbital (LUMO). Therefore, $O_2(^1\Delta_g)$ readily reacts with electron-rich substrates such as activated alkenes.[141]

In systems that have poor UV-Vis light absorptivity, a photosensitiser (PS) can be used to induce a chemical reaction. A photosensitiser is defined as a molecule which absorbs radiation and causes a photochemical change in a different molecule, without itself being consumed in the reaction.[142] Photosensitisers absorb light and are promoted from the ground singlet state, S_0, to the excited singlet state, S_1.

Intersystem crossing (ISC) generates the lower energy excited triplet state, T_1, of the photosensitiser, which has a longer lifetime (μs *vs.* ns).[143] This enables the T_1 state of the photosensitiser to instigate aerobic oxidation following either a type I or type II mechanism.[144] The type II mechanism (Figure 44d) is characterised by energy transfer from PS(T_1) to $O_2(^3\sum_g^-)$, resulting in the formation of singlet oxygen.[145] $O_2(^1\Delta_g)$ can then either react with the substrate or return to a lower energy state via non-radiative relaxation.

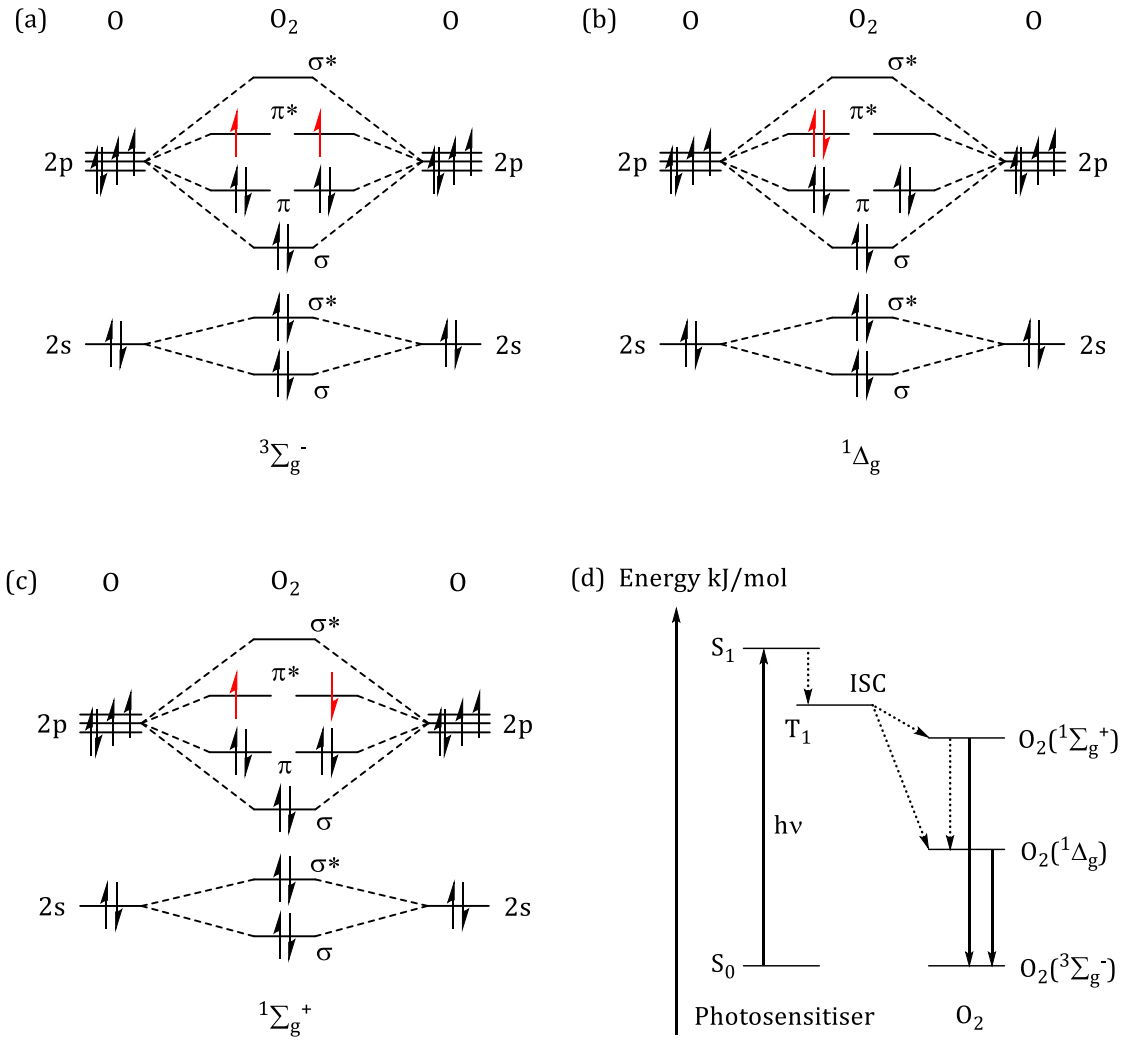

Figure 44. Photoexcitation of oxygen: (a) molecular orbital (MO) diagram for ground state triplet oxygen; (b) MO diagram for excited state singlet oxygen with paired π* electrons; (c) MO diagram for excited state singlet oxygen with unpaired π* electrons; (d) Jablonski diagram showing singlet oxygen production by energy transfer from a photosensitiser (type II mechanism). ISC = intersystem crossing.

Excitation of the photocatalyst results in a high energy electron which can be more easily removed, whilst the low-lying vacant orbital can accept an electron. Thus, the excited photocatalyst can behave as both an oxidant and reductant, where

the redox properties are related to the energy difference between the exited and ground states.[146] In the type I mechanism (Scheme 16), the excited state of the photocatalyst oxidises the substrate to produce a radical cation. The photocatalyst is reoxidised by oxygen, resulting in the formation of superoxide. Loss of a proton from the radical cation produces a substrate radical, which subsequently reacts directly with triplet oxygen, or the superoxide formed during photocatalyst reoxidation. Alternatively, hydrogen abstraction from the radical cation produces a substrate cation, which is quenched by water to form the oxygenated product.[147]

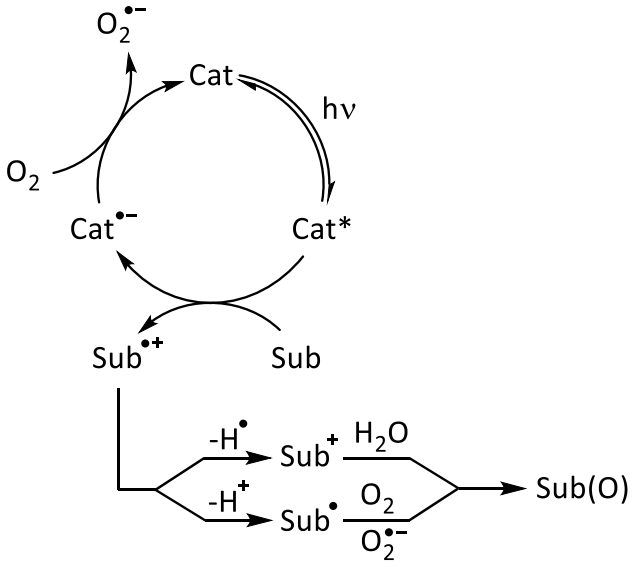

Scheme 16. Type I mechanism for photocatalytic aerobic oxidation. Cat = photocatalyst, Sub = substrate.

Despite the clear advantages of photochemical aerobic oxidations from a sustainability perspective, the uptake of these reactions by the fine chemicals industry has been relatively slow. This is due to difficulties associated with the scale-up of photochemical reactions and the safe use of molecular oxygen in batch. However, recent developments in continuous flow reactor technology have provided a solution to these issues.[148]

The Beer-Lambert law states that there is a logarithmic decrease in the light intensity with increasing path length (Figure 45). Therefore, scaling-up to larger reactors extends the reaction time, causing overirradiation of the reaction mixture. This can result in the formation of significant by-products and impurities, which complicates the subsequent purification steps. In contrast, the narrow channels of continuous flow microreactors provide uniform irradiation of the entire reaction mixture. This significantly reduces reaction times and increases product selectivity,

providing an overall more productive photochemical process.[149] Furthermore, increased productivity can be achieved by running multiple reactors in parallel (numbering-up), rather than increasing the dimensions of the reactor.[150]

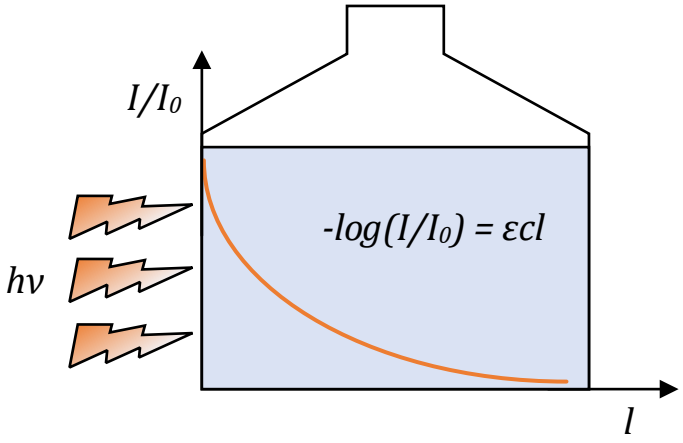

Figure 45. Logarithmic decrease in light intensity with increasing path length, as defined by the Beer-Lambert law. I = light intensity, I_0 = initial light intensity, ε = molar extinction coefficient, c = concentration, l = path length.

One of the challenges associated with aerobic oxidation in batch is achieving good mixing between the gas and liquid phases. This, combined with the poor solubility of O_2 in most organic solvents, results in processes that are often mass transfer limited. Furthermore, the build-up of O_2 in the headspace of the reactor poses a significant explosion risk when used in combination with organic solvents. Therefore, O_2 is generally diluted with N_2 to prevent formation of combustible mixtures. However, this further limits O_2 availability due to competitive dissolution between the gaseous species.[151] The reaction efficiency can be significantly improved in continuous flow microreactors, as the absence of a headspace enables safer use of pure O_2. In addition, the segmented flow observed for biphasic gas-liquid flow in capillary tubing provides a high interfacial area, thus enhancing the rate of mass transfer.[152]

Although microreactors offer more productive photochemical processes on a laboratory-scale, limitations still exist regarding the scale-up of these systems. While numbering-up offers a potential solution, there remains operational challenges in the context of highly regulated manufacturing of pharmaceuticals. Therefore, CSTRs remain the favoured choice of reactor for high productivity applications in the pharmaceutical industry. This led to the development of a 100 mL laser driven CSTR for a kilogram-scale photocatalysed C-N coupling reaction.[153]

The authors utilised a high intensity laser (25 W) to increase the total amount of light absorbed, and thereby overcome the lower surface area to volume ratio.

Miniature CSTR cascades have previously been reported for the laboratory-scale development of multiphasic reactions.[154] Active mixing provided by the CSTRs decouples flow rate and mixing performance, making them more suitable for mass transfer limited reactions with longer residence times.[155] This also enables a low liquid holdup to be maintained, which is essential for minimising material consumption during reaction optimisation. Furthermore, the constant agitation prevents the settling of particulates, thus reducing the risk of reactor fouling compared to microreactors.[156] This is particularly desirable for photodriven reactions, where deposition on the walls of the reactor reduces their performance over time.[157] Herein, this work describes the design, characterisation and application of a LED-based miniature CSTR cascade for biphasic continuous flow photochemistry. The reactor is combined with an automated experimental platform for the development of a photochemical aerobic oxidation reaction, utilising a novel hybrid self-optimisation approach.

4.2 Miniature CSTR Cascade

4.2.1 Reactor Design

A schematic and photo of a single miniature CSTR are shown in Figure 46a. The CSTR was designed with a 2 mL cylindrical reaction chamber, to provide a low liquid holdup for sustainable process development on a laboratory-scale. Active mixing was achieved via magnetic coupling between a PTFE cross stirrer bar (10 mm diameter) and a conventional stirrer plate, both of which are ubiquitous in most chemical laboratories. The magnetic coupling design removed the need for sealing of a motor shaft, which can be challenging on a small-scale.[155] The lid and base of the reactor were constructed from polyacetal and stainless steel respectively. This ensured a good thermal conductivity for high temperature applications, whilst providing high chemical resistance and a low cost of production. Each CSTR had a minimum of two inlet ports for the direct addition of multiple reagents. The reactor was sealed with PTFE gasket and transparent glass cabochon (viewing window), thus enabling visual inspection of the reaction mixture. This simple design allowed

the reactor to be easily cleaned in cases of fouling, providing a more economical alternative to the replacement of blocked microreactors (e.g. chip reactors).

(a)

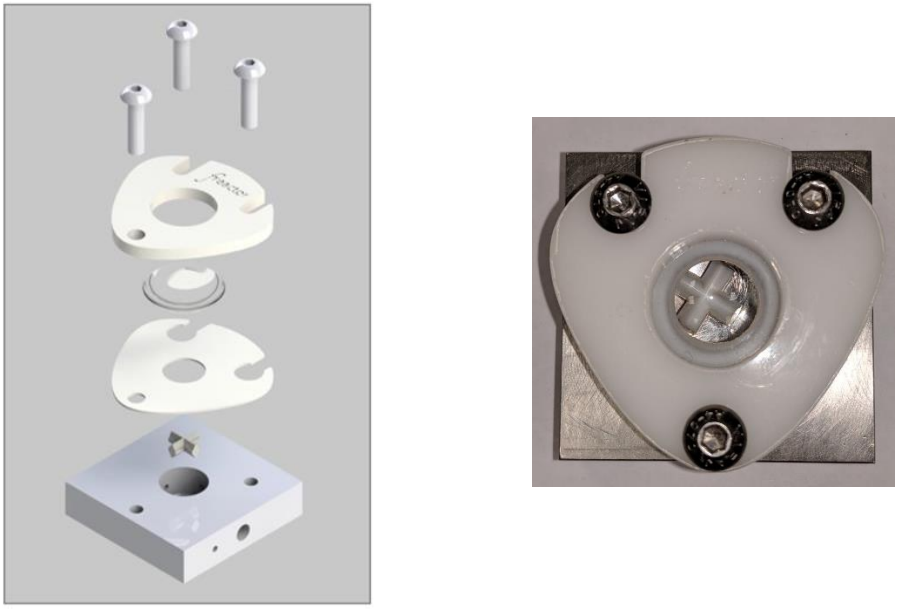

(b)

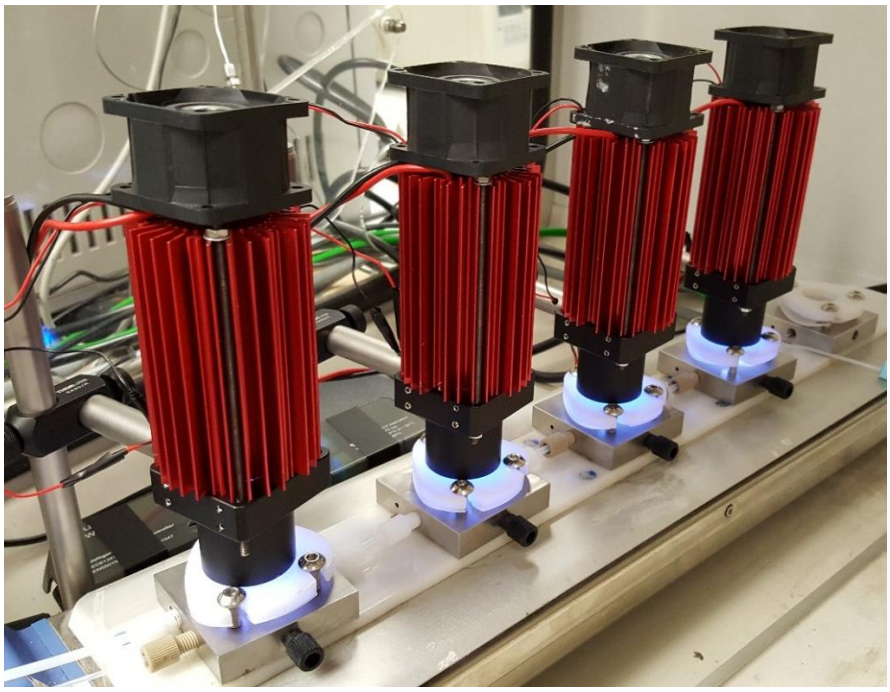

Figure 46. Miniature CSTR cascade design: (a) exploded view CAD drawing of a single miniature CSTR and a top-view photograph of a constructed single miniature CSTR; (b) photograph of four photochemical CSTRs in series.

Irradiation of the reaction mixture was achieved by fitting a light-emitting diode (LED, 365 nm, 2.9 W) above the viewing window of each miniature CSTR (Figure 46b). LEDs offer significant advantages over traditional mercury lamps, including: (i) tailored wavelengths between 365 and 900 nm which provides a wider

range of applications;[158] (ii) narrow emission bands (± 20 nm) which improves selectivity;[148] (iii) high energy efficiency resulting in lower surface temperatures. Advantage (iii) enabled the heat generated from the LEDs to be easily dissipated through a combination of passive and convective cooling, using heat sinks and server square fans respectively. This prevented the heat generated from the LEDs from negatively influencing the reaction. All experiments were conducted at 1000 rpm (highest setting) to maximise the interfacial area between the phases. Furthermore, the modular and versatile design of the reactor enabled the number of CSTRs to easily be changed for different applications. A modified version of this miniature CSTR cascade (fReactor) was made commercially available in 2019 (Asynt), with a view of incorporating photoirradiation in the near future.[159] This provides an affordable plug-and-play continuous flow reactor which is accessible for the general chemist.

4.2.2 Reactor Characterisation

4.2.2.1 Mixing Properties

The mixing properties of the reactor were characterised by determining the residence time distribution (RTD). This was achieved using the pulse method which is outlined below (Figure 47). Initially, the miniature CSTR cascade was pre-filled with water at a flow rate of 4.0 mL min^{-1}. A pulse of 10% (v/v) red food dye was rapidly introduced into the flow stream using a six-port valve, and samples were collected from the outlet of the reactor at regular time intervals. The absorbance of each sample was determined via offline UV-Vis spectroscopy (516 nm). The RTD function $E(t)$ was calculated by dividing the absorbance at each residence time by the total area under the absorbance curve.

The mixing performance was assessed by comparing the experimentally determined RTDs against the CSTRs in series model defined by [Eq (39)].[1] The experimentally determined RTDs were consistent with the CSTRs in series model for n = 1, 3 and 5, where n = number of CSTRs (Figure 48). This suggests that a uniform concentration in each CSTR is achieved, and therefore the agitation provides rapid mixing. As expected, the RTDs become narrower with increasing n, and thus bring the behaviour of the system closer to that of a plug flow reactor (PFR). In addition, the absence of any significant peak tailing indicates that dead volumes

are negligible. As such, the performance of this reactor for a reaction with known kinetics could be predicted using the CSTRs in series model.

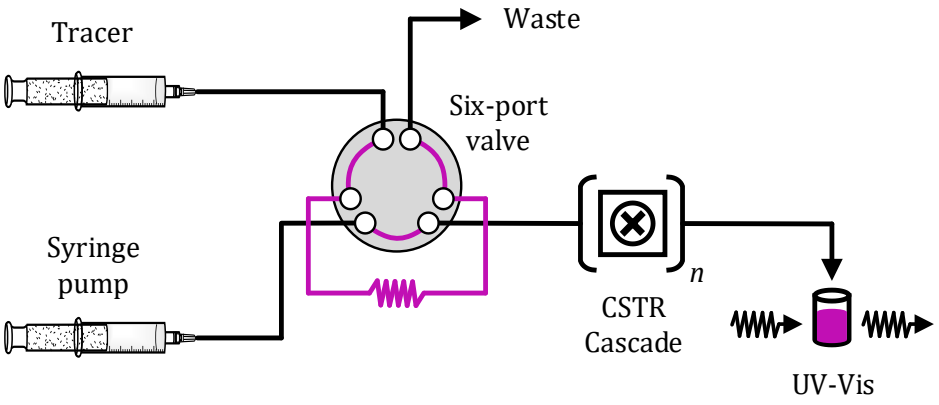

Figure 47. Set-up for determining the RTD of a miniature CSTR cascade using the pulse method.

$$E(t) = \frac{t^{n-1}}{(n-1)!\,\tau_i^n} e^{-t/\tau_i} \tag{39}$$

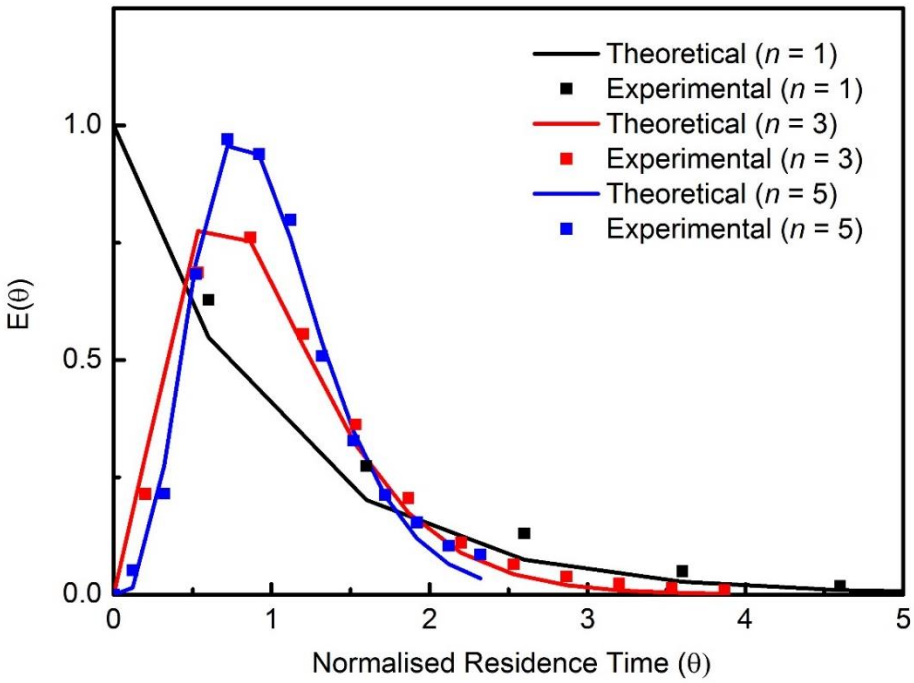

Figure 48. Comparison between theoretical and experimental RTDs for a CSTR cascade with a varying number of stages, *n*. E(θ) = normalised RTD function.

The average residence times (t_m) were determined by calculating the area under the curve for a plot of $tE(t)$ against t [Eq (40)]. The calculated and theoretical values are displayed in Table 10. The relative difference between the calculated and theoretical average residence times increases with decreasing *n*. These

discrepancies are likely due to the impossibility of experimentally injecting a perfect tracer spike. If additional equipment was available, these experimental limitations could be overcome by conducting in-line UV-Vis analysis at the inlet and outlet of the reactor, which would enable deconvolution of the inlet concentration profile and RTD.[156]

$$t_m = \int_0^\infty tE(t)\,dt \tag{40}$$

Table 10. Average calculated and theoretical residence times for 2 mL CSTRs in series at a flow rate of 4 mL min^{-1}.

n	**Theoretical t_m/min**	**Calculated t_m/min**
1	0.50	0.80
3	1.50	1.67
5	2.50	2.52

4.2.2.2 Absorbed Photon Flux Density

The absorbed photon flux density (q_p/V_r) defines the amount of light absorbed per unit of volume per unit of time. Therefore, the higher the absorbed photon flux density of a reactor, the higher the intrinsic rate of reaction for a photochemical process. The absorbed photon flux density can be experimentally determined via chemical actinometry, which uses a photoinduced reaction of a compound with a known quantum yield (ϕ_λ), to measure the incident light intensity (I_0) at a given wavelength. The rate of conversion of the actinometric compound (Act) is defined by [Eq (41)], where *f* is the fraction of light absorbed. The relationship between the rate of conversion of the actinometric compound [Eq (41)], and the rearranged form of the Beer-Lambert law [Eq (42)], can be used to derive [Eq (43)] for the calculation of the incident light intensity.

In this case, the experiments were conducted with a relatively long path length (l = 1 cm) and high concentration of the actinometric compound ([Act] = 0.1 M). Hence, the right-hand term of [Eq (43)] tends towards unity, indicating operation under full absorption (f = 1). Under these conditions, the kinetics of the reaction can be assumed to be zero-order. This simplifies [Eq (43)] to [Eq (44)], where the only unknown is the zeroth-order rate constant (k_0). Notably, the incident light intensity is equivalent to the absorbed photon flux density when f = 1.[160]

$$-\frac{d[Act]}{dt} = \frac{q_p}{V_r}\Phi_\lambda = I_0\Phi_\lambda f = I_0\Phi_\lambda\left(1 - \frac{I}{I_0}\right) \quad (41)$$

$$\frac{I}{I_0} = 10^{-\varepsilon l[Act]} \quad (42)$$

$$I_0 = -\frac{d[Act]}{dt}\left(\frac{1}{\Phi_\lambda}\right)\left(\frac{1}{1 - 10^{-\varepsilon l[Act]}}\right) \quad (43)$$

$$I_0 = \frac{k_0}{\Phi_\lambda} = \frac{q_p}{V_r} \quad (44)$$

o-Nitrobenzaldehyde **4.01** (NBA) is a well characterised chemical actinometer with a known molar extinction coefficient (ε = 260 M^{-1} cm^{-1}) and quantum yield (Φ_{365} = 0.5) at 365 nm.[161] Therefore, the photochemical isomerisation of NBA **4.01** to *o*-nitrosobenzoic acid **4.02** was investigated using an automated continuous flow platform (Scheme 17). In theory, the zeroth-order rate constant is equal to the negative slope of the residence time profile for the photochemical conversion of NBA **4.01** (Figure 49). However, significant curvature was observed as a result of light absorption by the *o*-nitrosobenzoic acid **4.02** product.[160] As such, a second-order polynomial was fit to the data (R^2 = 0.9833), and the initial slope of the curve determined by evaluating the derivative at t_{res} = 0. The resultant zeroth-order rate constant (k_0 = 1.67 μg μL^{-1} min^{-1}) was used to calculate the absorbed photon flux density according to [Eq (44)].

The absorbed photon flux density for the CSTR cascade (q_p/V_r = 0.37 einstein m^{-3} s^{-1}) is an order of magnitude greater than previously reported photochemical batch reactors (q_p/V_r = 0.033 einstein m^{-3} s^{-1}), whilst being only 2x less than a photochemical microreactor chip (q_p/V_r = 0.71 einstein m^{-3} s^{-1}).[162] This can be attributed to the enhanced mixing within the CSTRs, which rapidly transports the reactants and products into and out of the photochemically active region. This overcomes the issue of diminishing light intensity as a function of distance travelled through the reaction medium. Therefore, this design successfully improves productivity compared to batch reactors whilst maintaining the advantages of CSTRs described previously. In addition, as the incident light intensity of this set-up is now known, the quantum yield of reactions can be experimentally determined via kinetic profiling, which provides useful mechanistic insights.[163, 164]

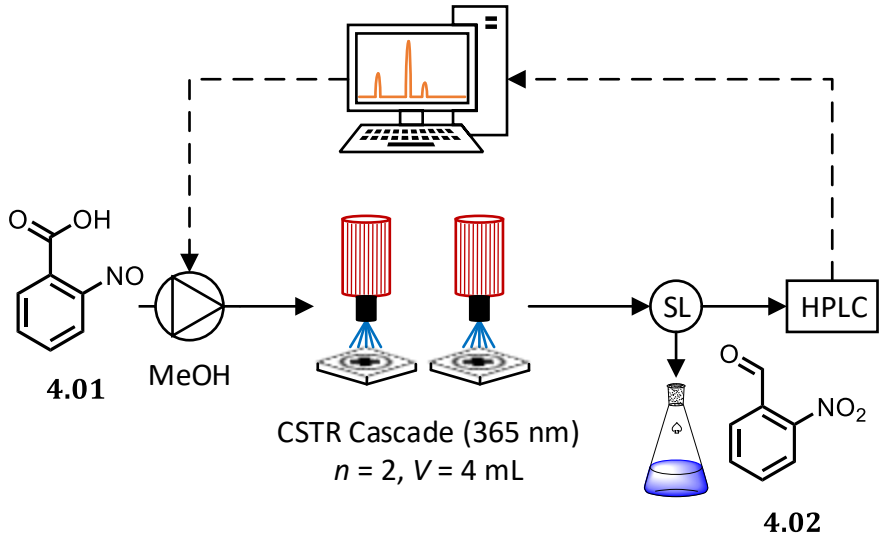

Scheme 17. Automated set-up for the characterisation of absorbed photon flux density using *o*-nitrobenzaldehyde **4.01** as a chemical actinometer.

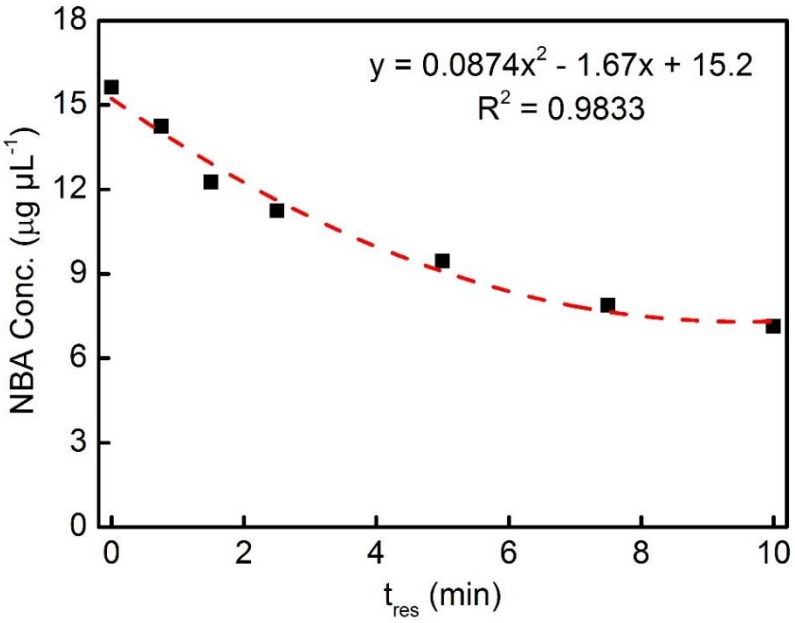

Figure 49. Residence time profile for the conversion of *o*-nitrobenzaldehyde **4.01** (NBA) under irradiation at 365 nm.

4.3 Aerobic Oxidation of C(sp³)-H Bonds

The site-selective oxidation of aliphatic C-H bonds, which are abundant in organic chemistry, provides a strategic tool for the late-stage functionalisation of complex molecules.[165] Despite this, efficient methods for the oxidation of C(sp³)-H bonds are still limited, with most approaches requiring complex transition-metal-based catalytic systems and strong oxidants.[166] Biocatalytic

methods offer significantly milder reaction conditions, but suffer from a very limited substrate scope.[167] An alternative approach involves hydrogen abstraction transfer (HAT), where substrate radicals and generated and trapped by molecular oxygen. This can be achieved electrochemically or photochemically, and thus has a reduced environmental impact.[168, 169]

The decatungstate anion has previously been used as a HAT photocatalyst for the aerobic oxidation of C(sp^3-H) bonds.[170] Notably, Noël *et al.* recently reported an improved continuous flow process, utilising an LED-based microreactor.[171] This enabled the safer use of pure oxygen, whilst overcoming photon penetration and mass transfer limitations. Furthermore, this method had a wide substrate scope for both activated and unactivated C(sp^3)-H bonds. However, the poor solubility of tetra-*n*-butylammonium decatungstate (TBADT) increases the risk of reactor fouling, and limits the solvent selection to acetonitrile, which ranks poorly in terms of waste and life cycle assessment (LCA).[172] In addition, the reaction still requires relatively long residence times (45 mins). Herein, this work focuses on the optimisation of the selective aerobic oxidation of tetralin to α-tetralone (Scheme 18) in continuous flow, utilising the developed LED-based miniature CSTR cascade.

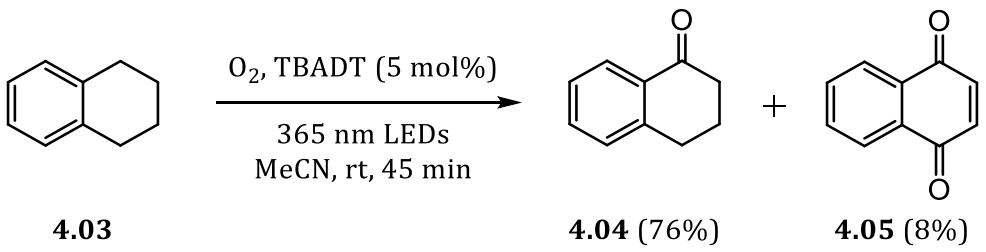

4.03 **4.04** (76%) **4.05** (8%)

Scheme 18. Selective aerobic oxidation of tetralin **4.03** to α-tetralone **4.04**. Overoxidation results in the formation of 1,4-naphthoquinone **4.05**. Reaction conditions and yields are quoted from Noël *et al.*[171]

Although TBADT is commercially available, it is relatively expensive (£296 g^{-1}, Merck).[173] Therefore, TBADT **4.06** was prepared by reaction of sodium tungstate dihydrate with tetrabutylammonium bromide under acidic conditions (Scheme 19).[174] The UV-Vis spectra of the product (Figure 50) showed good agreement with literature, thus confirming the successful synthesis of TBADT **4.06**.[175] Furthermore, the known molar extinction coefficient at 323 nm (ε_{323} = 1.35×10^4 dm^3 mol^{-1} cm^{-1}) was used to calculate a high purity of 92%.[176] However, in contrast to the previously reported yields of 85-95%, only a 47% yield was obtained, indicating poor

reproducibility. Nevertheless, the overall cost was still significantly reduced compared to commercial sources (£1.74 g^{-1} *cf.* £296 g^{-1}).

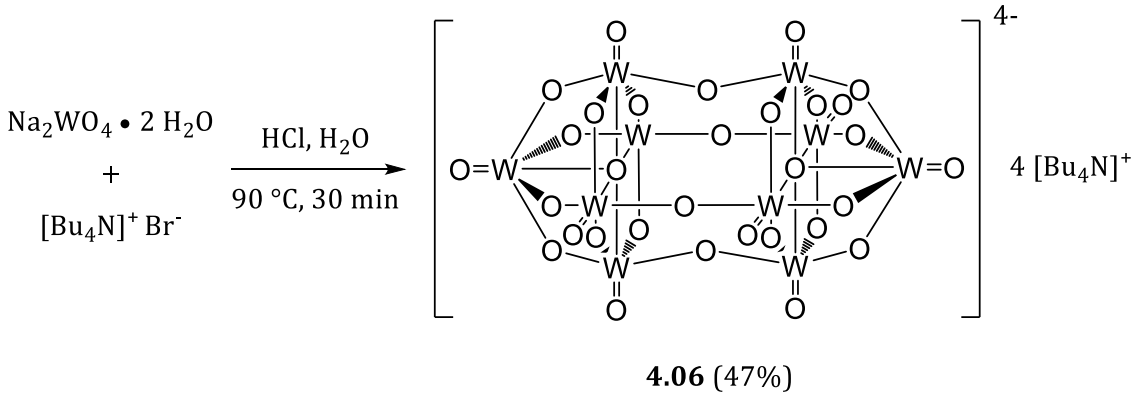

4.06 (47%)

Scheme 19. Synthesis of TBADT **4.06** from sodium tungstate dihydrate and tetrabutylammonium bromide.

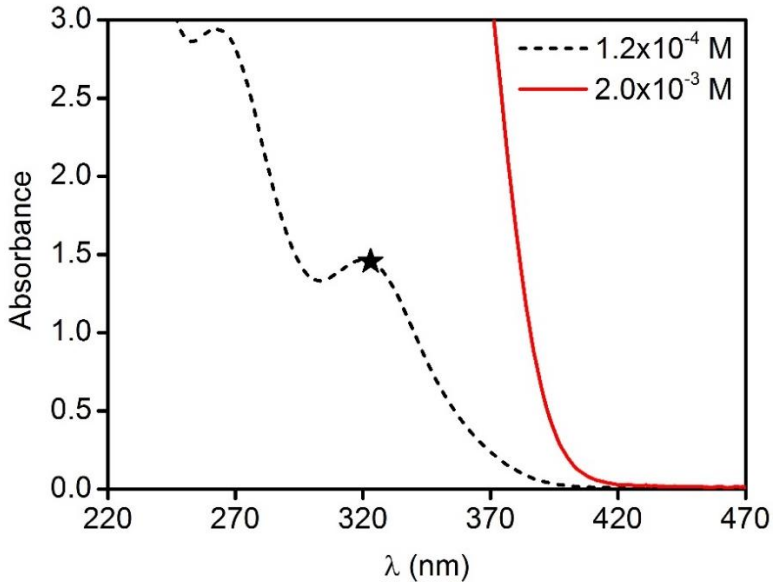

Figure 50. UV-Vis spectrum of prepared TBADT **4.06**. The spectrum is in good agreement with literature, and shows a 92% purity (ε_{323} = 1.24×10^4 dm^3 mol^{-1} cm^{-1}). ★ = absorbance value used to calculate ε_{323}.

The miniature photochemical CSTR cascade was integrated with an automated reactor platform to enable efficient optimisation of the aerobic oxidation of tetralin **4.03** to α-tetralone 4.**04** (Scheme 20). Although the use of pure oxygen is desirable from a process intensification perspective, the headspace in the CSTRs present the same safety risks associated with traditional batch vessels. Therefore, compressed air (21% O_2, 79% N_2) was utilised as a safe source of oxygen for the reaction. The expansion of gas at different temperatures was accounted for using the ideal gas law [Eq (45)], where P = pressure, V = volume, n = number of moles, R = gas constant

(8.314 J K^{-1} mol^{-1}) and T = temperature. This enabled calculation of the fluid and air flow rates required to achieve the desired residence time and oxygen equivalents.

$$PV = nRT \tag{45}$$

One of the challenges associated with multiphasic continuous flow chemistry is achieving reliable autosampling from the phase of interest. In this case, the gas-liquid segmented flow regime, in the tubing between the reactor outlet and sample loop, resulted in sporadic sampling of the undesired gaseous phase. This problem was overcome by the integration of a commercially available inline membrane-based separator (Zaiput).[177, 178] When fitted with a PTFE membrane, the gaseous phase was retained whereas the liquid phase was permeated. This enabled degassing of the reaction mixture at the outlet of the reactor, thus providing reliable autosampling of the liquid phase.

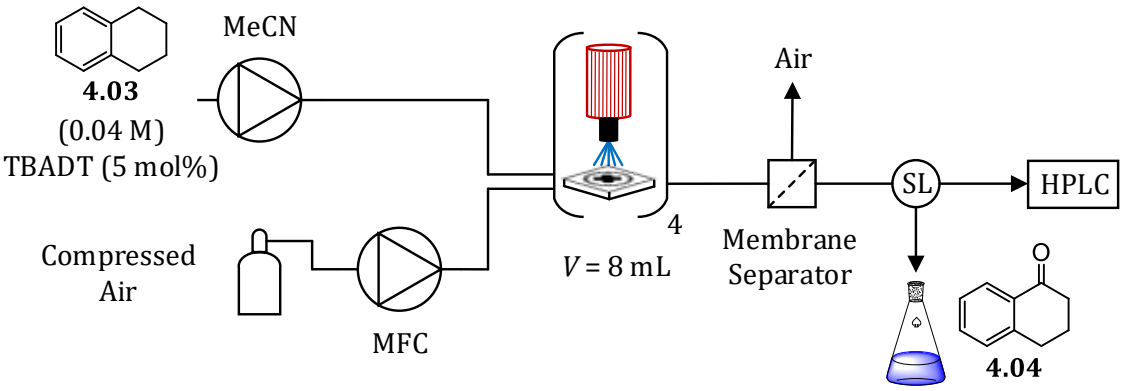

Scheme 20. Automated reactor for the optimisation of the aerobic oxidation of tetralin **4.03** to α-tetralone **4.04**. MFC = mass flow controller.

Initially, a 2-level full factorial DoE was conducted to screen the following variables and experimental space: residence time (5 – 20 min), O_2 equivalents (0.5 – 3) and temperature (29 – 59 °C). Although an increased pressure would increase the amount of dissolved oxygen, use of a BPR resulted in inaccurate gas flow rates. Therefore, all reactions herein were conducted at ambient pressure. The results of the experiments at the lower temperature limit are shown in Table 11.

Table 11. Results of the full factorial experiments at the lower temperature limit.

Entry[a]	t_{res}/min	O_2 equiv.	Conversion/%	Yield/%[b]
1	5	0.5	32	9
2	20	0.5	31	10
3	5	3.0	51	13
4	20	3.0	87	22

[a] TBADT (5 mol%), temperature = 29 °C, MeCN. [b] Yield of α-tetralone **4.04**.

In all cases the conversion was significantly higher than the yield of α-tetralone **4.04**. This indicated the formation of a by-product, which was verified by the presence of a significant impurity peak in the HPLC chromatograms. A sample was collected and the by-product isolated via flash column chromatography. ^{1}H NMR spectroscopy characterised the impurity as an ≈15:1 mixture of tetralin-1,4-dione **4.08** and 1,4-naphthoquinone **4.05**. Reanalysis of this mixture by HPLC showed that 1,4-naphthoquinone **4.05** had formed during purification, and was therefore not a product of the reaction conditions.

A proposed reaction scheme, which is consistent with the above observations, is shown in Scheme 21. Initially, tetralin **4.03** is oxidised to peroxide **4.07**, which subsequently decomposes into α-tetralone **4.04**. Over-oxidation of α-tetralone **4.04** results in the formation of diketone **4.08**. Notably, the potential α-tetralol products were not observed, suggesting that they were either not formed, or were rapidly oxidised under the reaction conditions to their corresponding ketones.[179] The keto-enol tautomerisation between diketone **4.08** and dienol **4.09** results in further oxidation to yield enedione **4.05**. The degradation of diketone **4.08** occurred post-reaction, and thus prevented accurate HPLC calibration. Rather, the yield of **4.08** was estimated based on the expected mass balance.

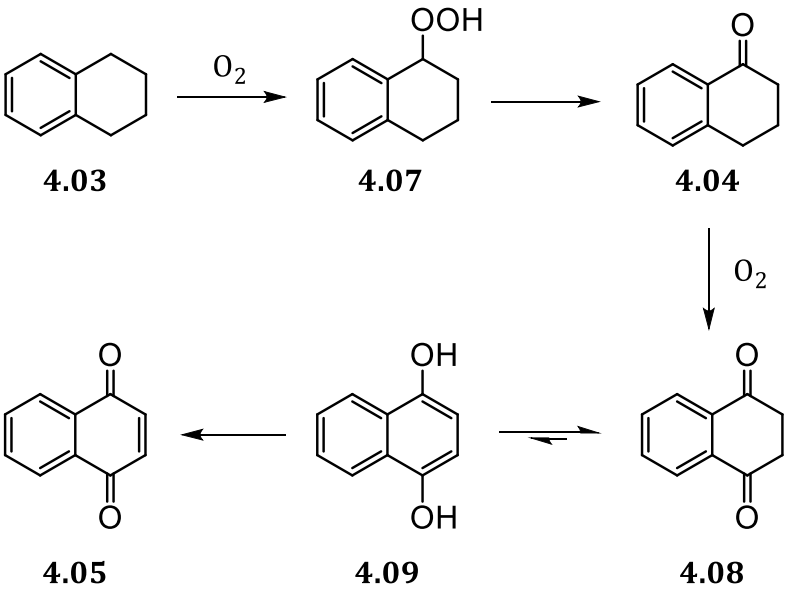

Scheme 21. Proposed reaction scheme for the TBADT photocatalysed aerobic oxidation of tetralin **4.03**.

The composition of the reaction mixture was determined for each experiment and response surfaces fit to the tetralin **4.03**, α-tetralone **4.04** and diketone **4.08** compounds (Figure 51). Notably, temperature was found to have no significant effect on the reaction, suggesting it had a negligible influence on the oxygen solubility and reaction kinetics. Therefore, ambient temperature was used for all future experiments. Conversion of tetralin **4.03** and formation of diketone **4.08** favoured long residence times and high oxygen equivalents. An interaction term between the variables was also identified, which showed residence time to have a greater influence on the reaction at higher equivalents of oxygen. Furthermore, the yield of α-tetralone **4.04** was severely limited as a result of over-oxidation to diketone **4.08** at all points within the experimental space. This indicates that the rate of oxidation of α-tetralone **4.04** is faster than the rate of oxidation of tetralin **4.03**. In addition, a square term was detected for the α-tetralone **4.04** model. Although a full factorial design alone cannot differentiate between square terms, it could be concluded that the yield of tetralone **4.04** favoured either intermediary residence times or oxygen equivalents, which corresponds to a balance between conversion and over-oxidation.

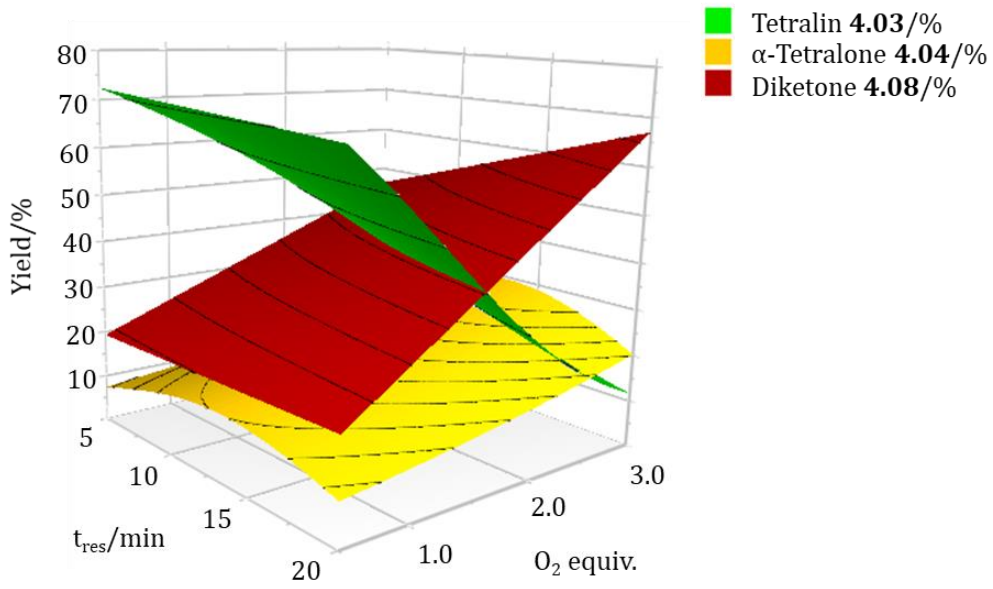

Figure 51. Response surfaces for tetralin **4.03**, α-tetralone **4.04** and diketone **4.08**. The α-tetralone **4.04** model is shown with the t_{res}*t_{res} square term.

It was hypothesised that the experimental space was dominated by over-oxidation due to the high photocatalytic activity of TBADT. Therefore, a batch screening was conducted to identify a more suitable photosensitiser (Table 12, entries 1-3). Benzophenone was selected for further optimisation, as the degree of over-oxidation was significantly reduced. However, α-tetralone **4.04** yields were lower when using benzophenone compared to TBADT in continuous flow, including at higher benzophenone loadings (entries 4-7). One of the advantages of using benzophenone compared to TBADT is an increased solubility in a wide range of organic solvents.[180] This enabled the effect of different solvents on the reaction to be investigated (entries 8-10). Ethyl acetate was found to outperform both acetonitrile and toluene. Notably, entry 10 showed a similar α-tetralone **4.04** yield (25%) and a reduced diketone **4.08** yield (7%) compared to that predicted from the response surface of the previous TBADT system (**4.04** = 27%, **4.08** = 60%). Control experiments under these new conditions confirmed that light was required for the reaction to proceed (entry 11). Furthermore, despite the structural similarities between benzophenone and the product, α-tetralone **4.04** was not an effective photosensitiser for the reaction (entry 12).

The residence time profile for the conversion of tetralin **4.03** to α-tetralone **4.04** and diketone **4.08** was determined under the new reaction conditions (Figure 52a). The yield of α-tetralone **4.04** increases with increasing residence time up to 30 min, where further increasing the residence time has a detrimental effect on the

reaction progress. This can be accounted for by the decomposition of benzophenone (Figure 52b), which resulted in a complex mixture of impurities. This is consistent with previous studies, which identified 15 degradation products as a result of OH-addition, carboxylation and ring opening in the presence of hydroxyl radicals.[181]

Table 12. Screening experiments for the photochemical aerobic oxidation of tetralin **4.03** to α-tetralone **4.04**.

Entry	PS[e]	PS mol%	Solvent	Time/min	4.03/%	4.04/%	4.08/%
1[a]	A	5	MeCN	240	0	0	100
2[a]	B	5	MeCN	240	3	60	37
3[a]	C	5	MeCN	240	10	77	13
4[b]	A	5	MeCN	20	13	22	65
5[b]	C	5	MeCN	20	74	9	17
6[b]	C	10	MeCN	20	71	9	20
7[b]	C	20	MeCN	20	57	17	26
8[b]	C	20	MeCN	10	71	19	10
9[b]	C	20	PhMe	10	93	7	0
10[b]	C	20	EtOAc	10	68	25	7
11[b,c]	C	20	EtOAc	10	> 99	< 1	0
12[b,d]	C	20	EtOAc	10	97	3	0

[a] Batch experiments open to air. [b] Flow experiments with 3.0 equivalents of oxygen. [c] No light. [d] No photosensitiser. Reaction mixture spiked with 20 mol% of α-tetralone. [e] PS = photosensitiser (A = TBADT; B = 2-*tert*-butylanthraquinone; C = benzophenone).

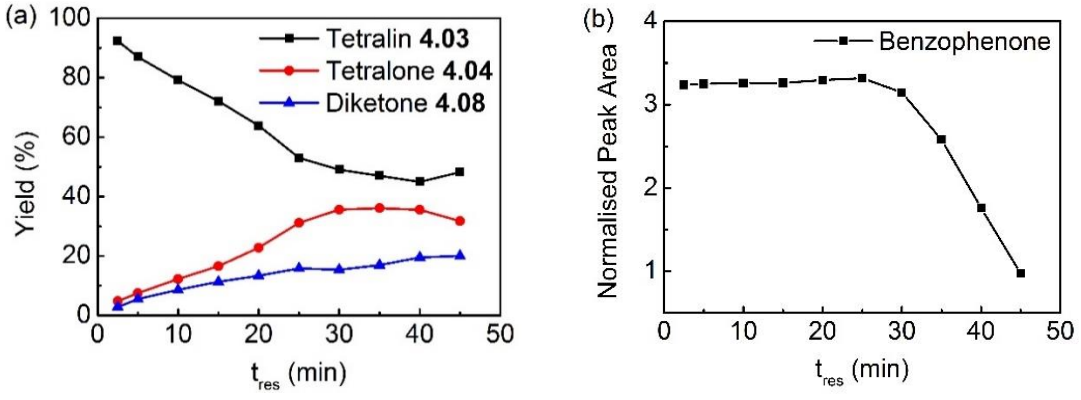

Figure 52. Residence time profiles for the photochemical aerobic oxidation of tetralin **4.03**: (a) conversion of tetralin **4.03** to α-tetralone **4.04** and diketone **4.08**; (b) decomposition of benzophenone. Conditions: benzophenone (20 mol%), O_2 (3 equiv.), EtOAc.

To ensure consistent product quality, it is important to understand how fluctuations in process variables, such as those caused by system drift, affect the response of the system. However, previous self-optimisations of photochemical reactions have solely focused on the identification of optimum conditions, thus overlooking process robustness.[73, 74] Bourne *et al.* described how statistical empirical modelling of data acquired during a global self-optimisation (i.e. SNOBFIT), could be used to predict reaction outcomes within the entire experimental space.[68] Although the models in this work showed good fit to the data, experiments were not specifically directed towards the regions of highest interest. Therefore, a hybrid self-optimisation approach is proposed, which combines global optimisation techniques with local response surface mapping to provide greater understanding of process stability around the optimum conditions.[a]

The hybrid self-optimisation algorithm can be divided into three consecutive stages: optimisation, screening and response surface mapping (Figure 53). Initially, the global optimum of the system is located using the SNOBFIT algorithm described previously. This stage is terminated once the best predicted conditions are the same for three consecutive iterations. Following this, a predefined target region is identified using a series of Plackett-Burman screening designs (fractional factorials, resolution III).[182] This is achieved by constructing a GP surrogate model of the existing data, and optimising for the upper and lower bounds of the target region. The system is then evaluated at the candidate set of experiments, and the process repeated until the target region is experimentally identified within a 20% relative tolerance. In the final stage a CCF design is conducted, which has the upper and lower bounds that were determined during the screening stage. These results are then used to construct a local response surface of the target region around the optimum.

The hybrid self-optimisation approach was used to further optimise the photochemical aerobic oxidation of tetralin **4.03**. The aim of the optimisation was to maximise the yield of α-tetralone **4.04** [Eq (46)], and explore a target region corresponding to a 10% decrease in yield from the optimum. Based on the previous

[a] The remaining work in this chapter was carried out in collaboration with Ph.D. student J. A. Manson. JAM wrote the hybrid self-optimisation algorithm and the Author conducted all experimental work.

results, the upper bounds with respect to residence time and oxygen equivalents were increased. Furthermore, the amount of benzophenone was also increased from 20 to 50 mol%.

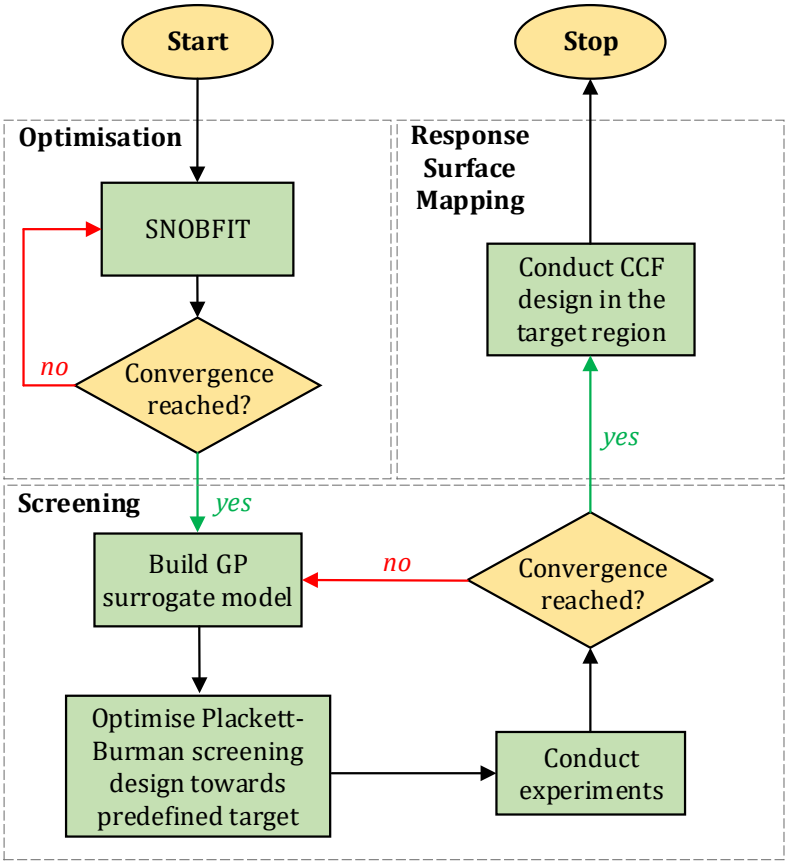

Figure 53. Hybrid self-optimisation algorithm flowchart.

$$maximise[\%\ \text{yield of}\ \mathbf{4.04}], explore[10 \pm 2\ \% < \max] \quad (46)$$

subject to: Residence time/min ∈ [2, 30]

O_2 equivalents ∈ [1.0, 5.0]

The initial SNOBFIT optimisation was terminated after 38 experiments, with an improved α-tetralone **4.04** yield of 65% (Figure 54a). This was achieved at a t_{res} of 18.3 min and O_2 equiv. of 4.69. These conditions corresponded to a sweet spot in the experimental space, balancing the conversion of tetralin **4.03** with over-oxidation i.e. formation of diketone **4.08**. The screening stage required three iterations totalling 12 experiments (Figure 54b). On each successive iteration, the size of the Plackett-Burman design decreased, as the algorithm converged on a point corresponding to a 10 ± 2 % reduction in yield. This point gave an α-tetralone **4.04** yield of 53%, which was observed at a t_{res} of 19.4 min and O_2 equiv. of 3.69.

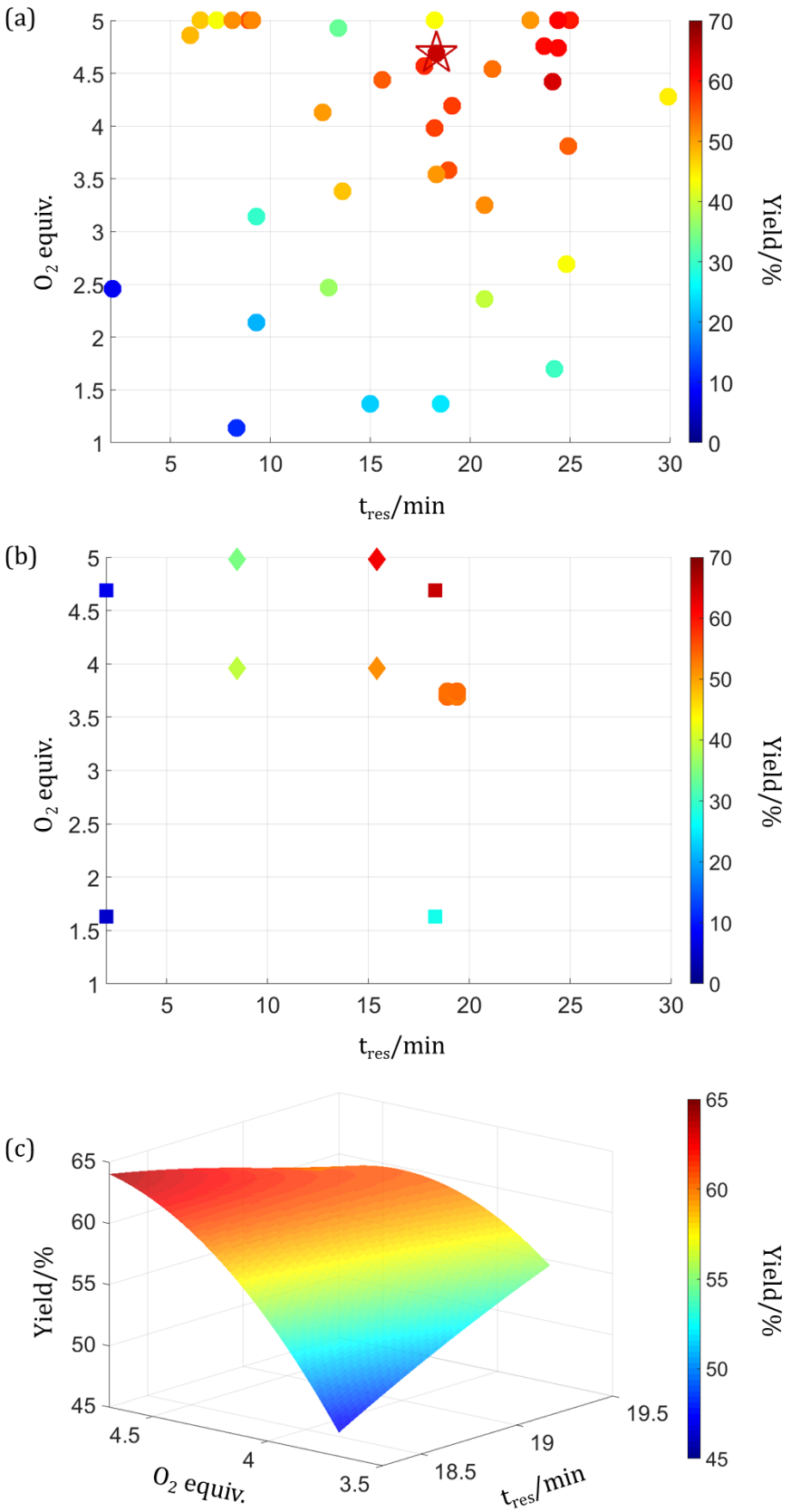

Figure 54. Hybrid self-optimisation results: (a) SNOBFIT optimisation; (b) Plackett-Burman screening designs where ■ = iteration 1, ◆ = iteration 2 and ● = iteration 3; (c) response surface of the target region determined using a CCF DoE. Conditions: benzophenone (50 mol%), EtOAc. ☆ = maximum yield.

The subsequent CCF design was conducted between the upper and lower bounds of the target region determined during screening (t_{res} ∈ [18.3, 19.4]; O_2 equiv. ∈ [3.69, 4.69]), and a response surface fit to the data (Figure 54c). The response surface showed a stronger dependence on oxygen equivalents compared to residence time. In addition, an interaction term between the variables was identified, where increasing residence time at low and high oxygen equivalents had a positive and negative impact on the yield respectively. Although the algorithm was successful in identifying a target region, it failed to explore all areas of interest around the optimum, such as those at longer residence times. This can be attributed to the symmetrical experimental designs used throughout, which have limited flexibility for exploration of experimental space.

Nevertheless, an optimum α-tetralone **4.04** yield of 65% was obtained, which is comparable with previously reported examples (Scheme 22).[171] Notably, the optimised reaction conditions provide an improved process from both an economical and environmental perspective. For example, benzophenone offers a metal-free, cheaper and more readily available alternative to TBADT. Air is also utilised as a non-toxic oxidant, which has minimal risks associated with its storage. The replacement of pure oxygen with air was enabled by the rapid mixing achieved in the miniature CSTRs, which helps to overcome the mass transfer limitations associated with gas-liquid segmented flow in tubular reactors. Furthermore, ethyl acetate is a preferred solvent of choice compared to acetonitrile in terms of LCA, and provides greater solubility for alkanes. This, combined with a significantly reduced residence time, provides an overall more productive process.

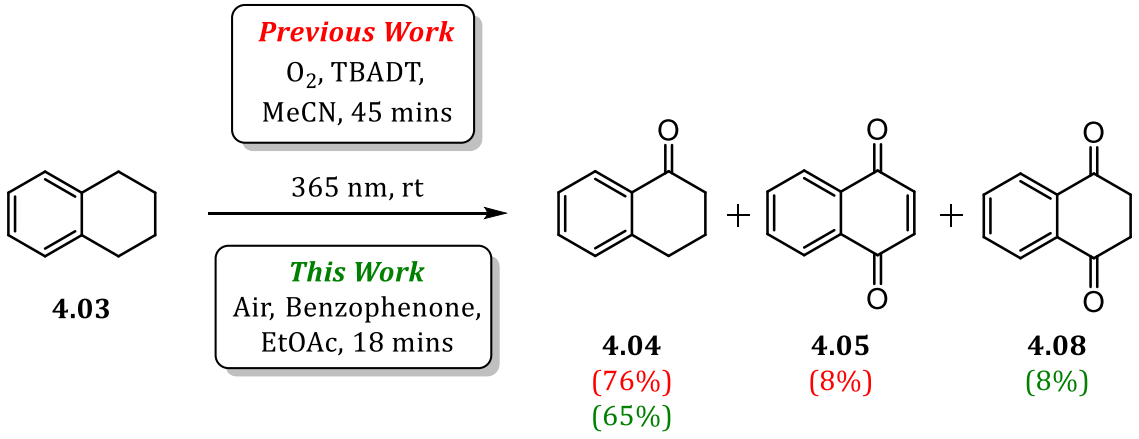

Scheme 22. Comparison of optimised reaction conditions between previous work and this work for the photochemical aerobic oxidation of C(sp^3)-H bonds.

4.4 Conclusions

The development of LED-based continuous flow microreactors has led to a renewed interest in photochemistry in recent years.[148] In this work, a new photochemical miniature CSTR cascade was developed and characterised. The RTD of the reactor showed good agreement with the CSTRs in series model, thus confirming that rapid mixing was achieved. Furthermore, chemical actinometry showed the reactor to have a 10× greater absorbed photon flux density compared to previously reported photochemical batch reactors.[162]

The reactor was used to develop a continuous flow process for the site-selective aerobic oxidation of C(sp^3)-H bonds; a reaction of great utility in the late-stage functionalisation of complex molecules.[147] For this, the oxidation of tetralin to α-tetralone was selected as an appropriate case study. In contrast to previous work, initial DoE studies using TBADT as a photocatalyst led to the identification of tetralin-1,4-dione as the major by-product. Subsequent screening experiments identified benzophenone as a more favourable photosensitiser, however, reaction profiles indicated significant degradation at residence times greater than 30 min.

During process design, it is equally important to gain a detailed understanding of process stability, as it is to identify optimal operating conditions. Therefore, a new hybrid self-optimisation algorithm was developed, which had synergistic aims of identifying the global optimum and mapping a local response surface around it. This approach successfully optimised the formation of α-tetralone in a yield of 65%, and provided a response surface in the target region corresponding to a 10% reduction in yield. This response surface was useful for identifying the relative influence of each variable in close proximity to the optimum. However, this approach is currently limited by rigid symmetrical experimental designs, which fail to locate and fully explore the entire area of interest.

In summary, a new photochemical miniature CSTR cascade reactor was used to provide good yields for the aerobic oxidation of C(sp^3)-H bonds in continuous flow under mild reaction conditions. Notably, pure oxygen was replaced with air as the oxidant, and the residence time of the reaction reduced by a factor of 2.5 compared to previous work.[171] This highlights the efficiency of the developed reactor towards multiphasic reactions on a laboratory-scale. Furthermore, the

decoupling of flow rate and mixing performance greatly broadens the scope of self-optimisations to a wider range of chemistries.

Chapter 5 Self-Optimisation of Multi-Step Continuous Reaction and Extraction Processes

5.1 Introduction

Multi-step reactions are those that involve more than one chemical transformation of the same compound, and are key for the synthesis of complex APIs from readily available starting materials. Traditionally, this has been achieved by iterative step-by-step transformations in batch, where intermediates are purified and isolated between each synthetic step (Figure 55a).[183] However, this process has a very high space-time demand, as large inventories of intermediates must be stored and transported between different manufacturing sites. In contrast, continuous flow offers in-line purification and the addition of reagents at set points in the sequence, thus providing a more productive uninterrupted reaction network (Figure 55b).[184] This minimises the risk of supply chain disruptions, enabling reliable on-demand synthesis of APIs with a reduced ecological footprint. These benefits are especially emphasised in cases where APIs have a short shelf life.[185]

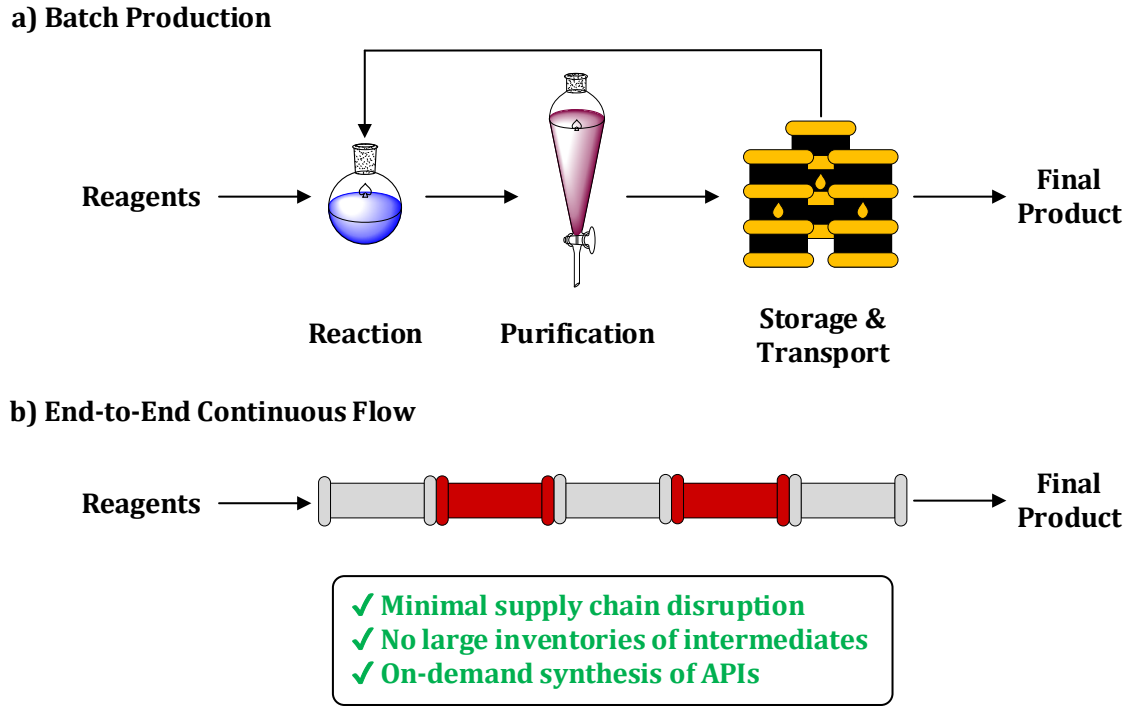

Figure 55. Comparison of multi-step manufacturing: (a) batch production; (b) end-to-end continuous flow.

The end-to-end continuous flow synthesis of APIs is enabled by emerging in-line purification technologies.[186] In-line purification accommodates the use of

excess reagents to drive reactions to completion, and allows reactions with otherwise incompatible conditions to be combined in the same continuous process. One of the most widely used purification techniques is liquid-liquid extraction (LLE), which separates compounds based on their relative solubilities in two immiscible liquids.[187]

An in-line gravity-based LLE system was developed utilising computer vision to automate the process (Scheme 23), where computer vision refers to the ability of computers to interpret digital media.[188] In this case, a camera was used to monitor the biphasic interface in the separation column, and a feedback loop created to dynamically adjust the flow rate of the light-phase outlet, thus keeping the interface at the desired position.[189] This method was shown to be suitable for a number of transformations in DCM, including: hydrazone formation, mCPBA epoxidation of allyl alcohols and dithiane formation. In-line aqueous work-up of the reaction mixtures successfully removed the hydrazine **5.01**, mCPBA by-product **5.02** and dithiol **5.03** impurities, yielding analytically pure hydrazones **5.04**, epoxides **5.05** and dithianes **5.06** respectively. However, gravity-based systems are hindered by slow rates of phase separation for solvents with similar densities.

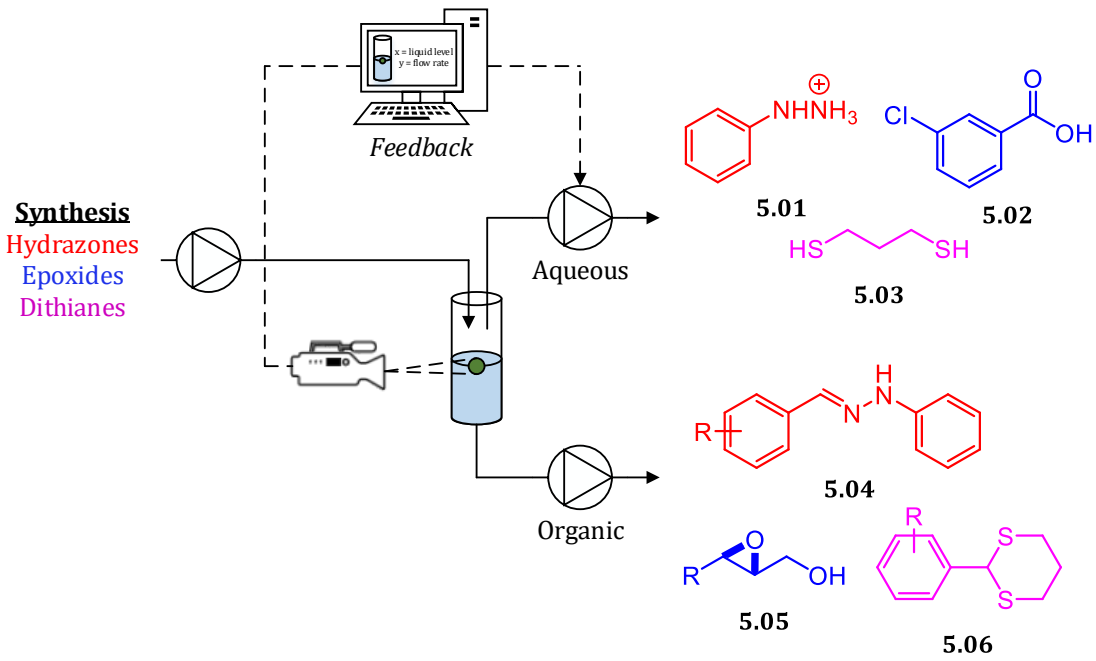

Scheme 23. A computer vision approach for in-line gravity-based liquid-liquid extraction.

Alternatively, membranes can be used for the continuous separation of immiscible organic and aqueous phases. The phase with a higher affinity for the

membrane material (wetting phase) fills the pores, creating a differential pressure across the membrane. For complete separation to occur, the transmembrane pressure must be adjusted to allow permeation of the wetting phase, whilst simultaneously retaining the non-wetting phase.[190] One challenge associated with this includes accounting for variations in pressure as a result of changing operating conditions downstream. This has previously required sophisticated feedback pressure control systems, comprising of adjustable back-pressure regulators at the outlets of the separtor.[191] More recently, a liquid-liquid separator which utilises a diaphragm as an internal pressure controller has been reported (Figure 56).[177] This improved design significantly simplifies in-line membrane-based separation, providing a modular plug-and-play unit (Zaiput) which can be readily integrated into reconfigurable continuous flow systems.[70, 185] As such, this separator has been used for a wide range of applications, including: multi-step syntheses,[192] reaction quenching,[193] solvent switching[194] and multistage counter-current extraction.[195]

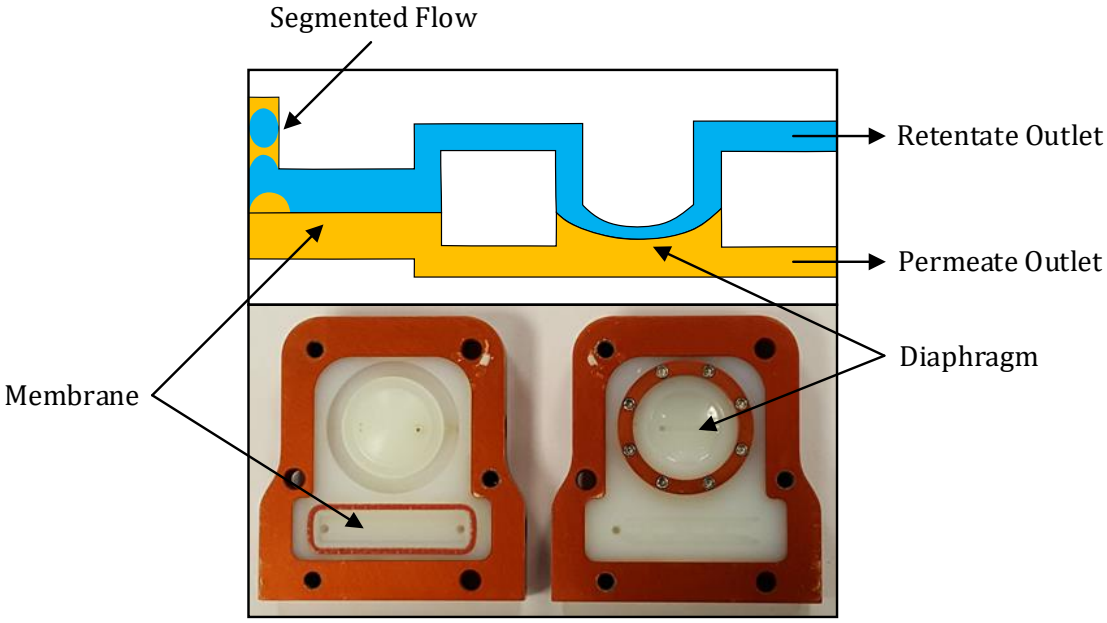

Figure 56. An in-line membrane-based liquid-liquid separator with internal pressure control (diaphragm).

Although significant advances have been made towards the development of in-line LLE equipment, there has been little work regarding the efficient optimisation of extraction steps in multi-step continuous flow processes. Rather, automated optimisation has focused solely on the optimisation of reaction conditions, overlooking the significant effect of downstream purification steps on important process metrics. Jamison *et al.* reported the self-optimisation of a diverse

range of multi-step processes, using a reconfigurable continuous flow system and a black-box algorithm.[70] However, the downstream extraction conditions were fixed, and therefore not included in the optimisation. Herein, this work describes for the first time the self-optimisation of in-line LLEs, and reaction-extraction multi-step continuous flow processes, where both stages are simultaneously optimised.

5.2 In-Line Separation of Structurally Similar Impurities

The presence of structurally similar impurities presents a significant challenge during multi-step continuous flow sequences. These can arise as a result of incomplete reactions and/or limited product selectivity. The ability to control these during the reaction steps is not always possible, therefore rigorous optimisation of the purification steps is required to provide a robust process. In cases where compounds possess acidic or basic functional groups, in-line purification can be achieved via pH-based LLE.[196] However, such systems are generally very sensitive to changes in pH, and thus present a challenging optimisation problem. Herein, the continuous extraction of a 1^{o} and 2^{o} amine mixture is optimised using a self-optimisation approach.

In-line membrane-based separation was achieved using the commercially available Zaiput fitted with a hydrophobic membrane, which could be readily integrated into our existing automated continuous flow system. There are two modes of failure associated with membrane-based separators: (i) breakthrough of the retained (aqueous) phase; (ii) retention of the permeate (organic) phase. Previous studies showed that full separation occurred for both hexane-water and ethyl acetate-water solvent systems when no back pressure was applied.[178] However, this was only tested for total flow rates between 4-16 mL min^{-1}. Therefore, we initially tested the performance of the Zaiput to separate our desired toluene-water solvent system at lower flow rates (Table 13). For toluene-water ratios of 1:1, almost complete separation was achieved at total flow rates between 0.2-2.0 mL min^{-1}. In contrast, small amounts of retention and breakthrough were observed at toluene-water ratios greater than 2:1, and lower than 1:3 respectively. Therefore, to ensure successful separation of the solvent system, toluene-water ratios were maintained between 2:1 and 1:3 throughout optimisation of the LLE.

Table 13. Performance of the Zaiput for the membrane-based liquid-liquid separation of a water-toluene solvent system. R = retention, B = breakthrough.

System	Flow Rate/mL min^{-1}		Failure	
	Organic	Aqueous	% R	% B
Toluene-Water	0.10	0.10	0.0	0.0
	0.25	0.25	0.0	1.2
	0.50	0.50	0.0	0.0
	1.00	1.00	0.0	0.0
	0.80	0.20	2.5	0.0
	0.75	0.25	1.9	0.0
	0.67	0.33	0.1	0.0
	0.33	0.67	0.0	0.1
	0.25	0.75	0.2	0.0
	0.20	0.80	0.0	2.0

A schematic of the automated pH-based extractor is shown in Scheme 24. A mixture of α-methylbenzylamine **5.07** (α-Me-BA) and *N*-benzyl-α-methylbenzylamine **5.08** (*N*-Bn-α-Me-BA) was prepared in toluene, such that the *N*-Bn-α-Me-BA **5.08** represented a minor impurity (≈ 5%). The pH of the aqueous phase was varied by adjusting the dilution of a nitric acid stream, where the lower limit of the pH range corresponded to full protonation of the amine mixture, under the assumption of complete acid dissociation. Emulsification of the two phases, by mixing in a miniature CSTR cascade, enabled efficient extraction prior to liquid-liquid separation. The concentration of each amine in the organic phase was determined via on-line HPLC analysis. The aim of the optimisation was to maximise the % difference of the amines remaining in the organic phase [Eq (47)], which is directly related to the separation efficiency.

$$minimise\left[-\Delta amine_{(org)}\right] \tag{47}$$

subject to: pH ∈ [0.358, 0.873]

Organic:Aqueous Ratio ∈ [0.8, 2.0]

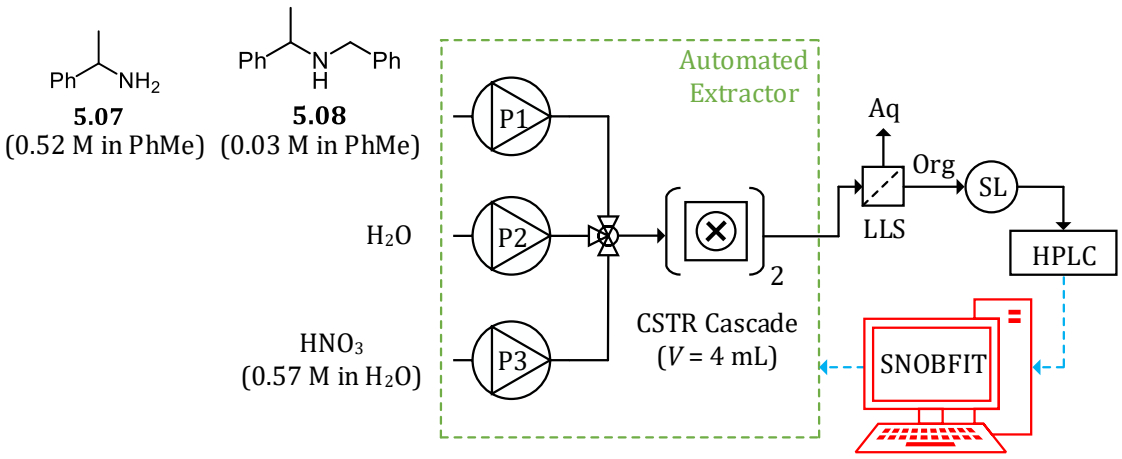

Scheme 24. Schematic of the automated extractor used to optimise the pH-based LLE of an α-Me-BA **5.07** and *N*-Bn-α-Me-BA **5.08** mixture. P = pump, LLS = liquid-liquid separator, Aq = aqueous phase, Org = organic phase. SL = sample loop. See experimental for more details.

Due to the high sensitivity of pH-based LLEs, the SNOBFIT algorithm was selected in preference to simplex, as it is less likely to get stuck in the presence of an erroneous data point. The % of each amine remaining in the organic phase under different conditions is shown in Figure 57. The results showed an increase in the extraction of α-Me-BA **5.07** into the aqueous phase with decreasing pH and organic:aqueous ratio. The preferential extraction of α-Me-BA **5.07** over *N*-Bn-α-Me-BA **5.08** indicates that α-Me-BA **5.07** has a higher pKa. This suggests that the 1° amine cation has increased solvation as a result of less steric hindrance, which outweighs the stabilising effect of additional alkyl chains.

In this case, the optimum was rapidly identified in just 15 experiments, providing a 90% separation at a pH of 0.420 and organic:aqueous ratio of 1.0. The optimisation was run for an additional 46 experiments, where exploration predominantly focused on the region around the optimum, revealing the presence of a cliff edge in the local response surface (Figure 58). This corresponded to a sharp decrease in the % of *N*-Bn-α-Me-BA **5.08** remaining in the organic phase at pHs and organic:aqueous ratios lower than the optimum conditions. At these conditions, both amines were extracted into the aqueous phase, resulting in a poor separation. Therefore, the optimum exists in a region of low process stability, which would need to be accounted for to provide a rigorous plant-scale process.

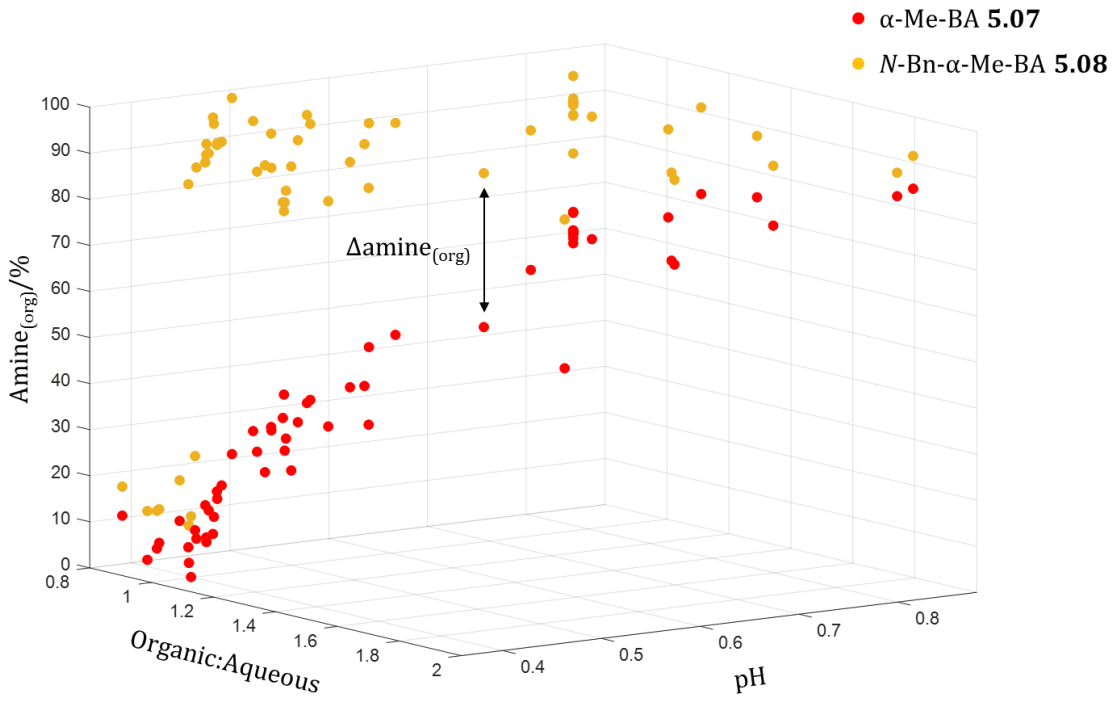

Figure 57. Plot of % amines remaining in the organic phase under different in-line LLE conditions.

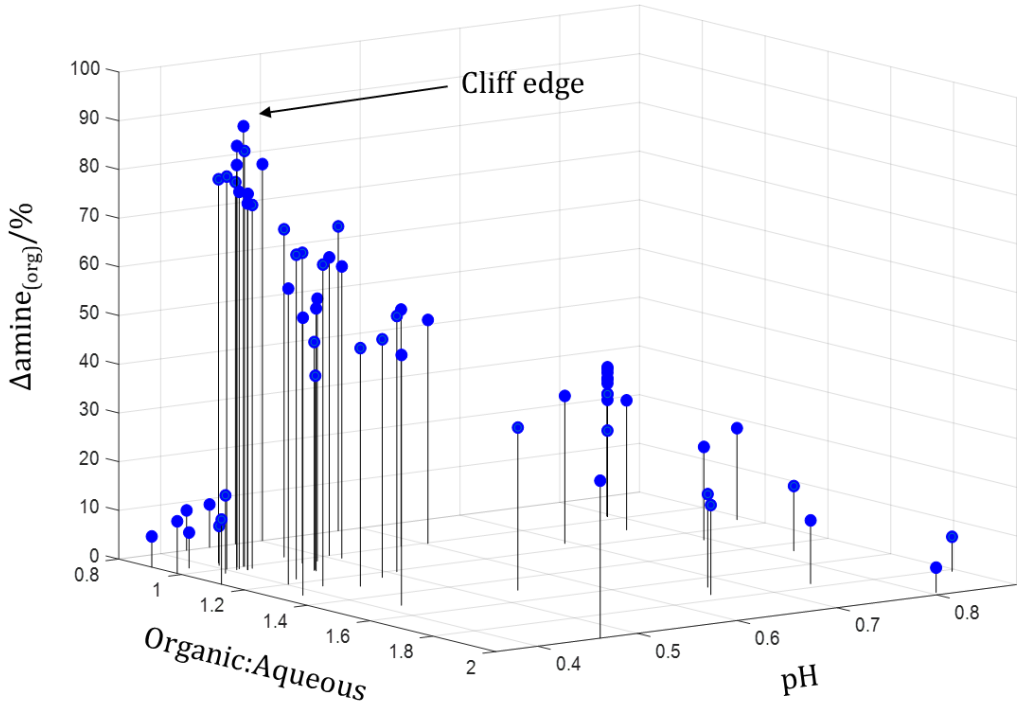

Figure 58. Plot of % difference of amines remaining in the organic phase under different in-line LLE conditions.

Due to the presence of a sharp peak in the response surface, fine-tuning of the extraction conditions was crucial for the optimisation of this system. Hence, automated continuous flow platforms are well suited for the optimisation of LLEs, as they provide precisely adjustable flow rates and effectively remove human error. In addition, this approach is less time-consuming and labour intensive than traditional experimental methods, requiring only 13 hours (i.e. overnight) to identify the optimum with no prior knowledge of the system.

The use of statistical modelling methods, such as DoE, are not appropriate for global optimisation problems with sharp peaks in the response surface. This is due to the poor ability of polynomial models to fit sharp changes in response over a wide variable range.[197] This is shown in Figure 59a, where the global model failed to accurately describe the true nature of the response surface around the optimum. In contrast, the SNOBFIT algorithm fits local polynomial models in subsections of the experimental space. An example of this is shown in Figure 59b, where a local model was fit around the optimum using data in the following region: pH ∈ [0.358, 0.500]; organic:aqueous ratio ∈ [0.8, 1.2]. This provided a model which successfully detected the observed cliff edge. Therefore, it was concluded that SNOBFIT is a well suited algorithm for the self-optimisation of LLEs.

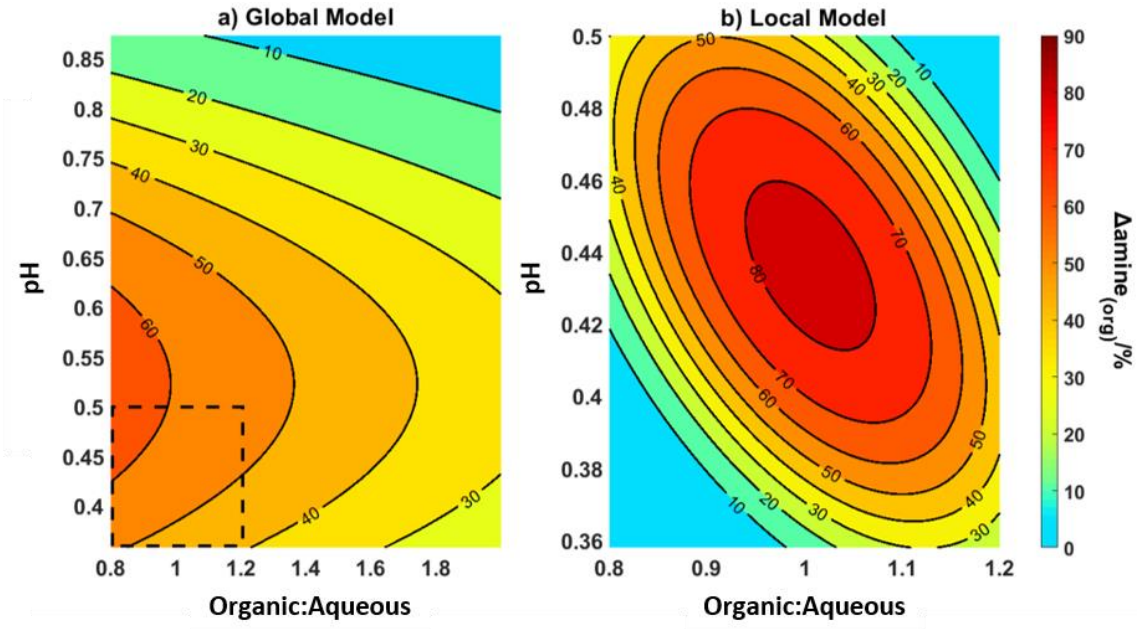

Figure 59. Contour plots showing polynomial models derived from self-optimisation data: (a) global model from all data, dashed box highlights local area around the optimum; (b) local model exclusively from data around the optimum.

5.3 Multi-Step Reaction-Extraction Processes

The production of APIs belongs to the class of complex multi-step processes, which involve multiple transformation and purification steps. For the benefits of end-to-end continuous flow synthesis to be fully exploited, efficient methods to optimise these processes are required. Work in Chapter 3 demonstrated how multi-objective optimisation of individual steps in parallel could theoretically enable the development of a multi-step process in a reduced time frame. An alternative approach would be to optimise the reaction and work-up steps simultaneously on the same experimental platform. Optimising more than one step per optimisation in this way has the potential for significant savings in time and resources, thus streamlining the drug development process. Furthermore, the impact of downstream work-up operations on important process metrics would be automatically considered, thus avoiding the identification of optimum reaction conditions which are later determined to be infeasible. Herein, this work explores the nature of multi-step process optimisation, using two exemplar case studies.

5.3.1 Synthesis of Secondary Amines via Direct *N*-alkylation

With a suitable system for the automated optimisation of LLEs in hand, attention shifted to the self-optimisation of multi-step reaction-extraction processes. For this, the synthesis and purification of *N*-Bn-α-Me-BA **5.08** in continuous flow was investigated. This was achieved by combining the *N*-benzylation of α-Me-BA **5.07** with a downstream aqueous LLE (Scheme 25). The aim of the optimisation was to maximise the purity of *N*-Bn-α-Me-BA **5.08** with respect to all impurities [Eq (48)]. These included unreacted starting materials α-Me-BA **5.07** and benzyl bromide **5.09**, and by-products 3° amine **5.10** and salt **5.11**. Salt **5.11** was formed as a result of the reaction between DIPEA and *in situ* generated hydrobromic acid. Unlike DIPEA, its protonated form **5.11** was detectable by HPLC at 210 nm, and was therefore easily quantified using the same experimental set-up. Aqueous nitric acid was introduced downstream of the reactor for in-line LLE of the amine and salt impurities. Notably, use of purity as the objective function in this case ensured that the optimisation would favour a high yielding reaction step, as well as efficient extraction conditions. Due to the observations in the previous LLE example, SNOBFIT was selected as an appropriate optimisation algorithm.

$$minimise[-\%\ purity\ of\ \mathbf{5.08}] \tag{48}$$

subject to:

t_{res}/min ∈ [6.7, 10.0]

Temperature/°C ∈ [30, 130]

pH ∈ [0.25, 2.26]

Aqueous:Organic Ratio ∈ [0.574, 1.000]

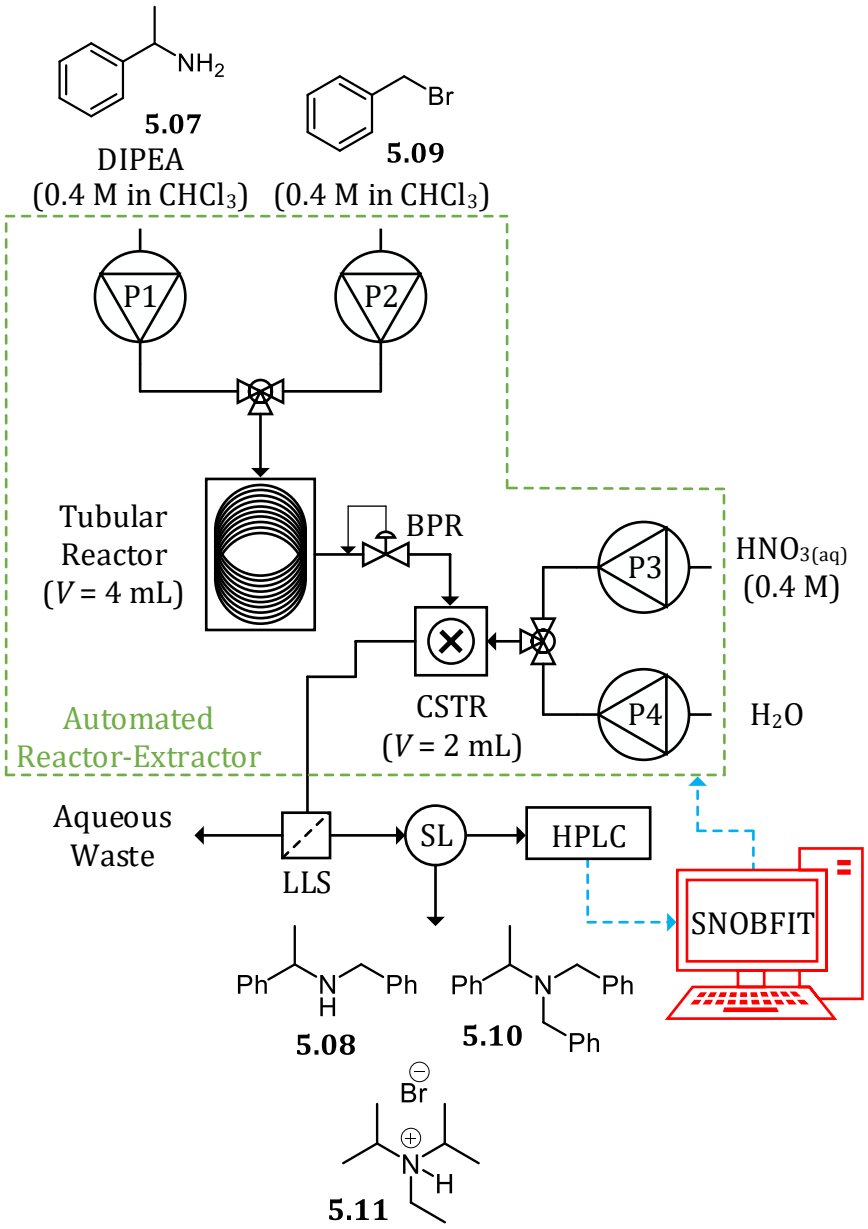

Scheme 25. Schematic of the automated reactor-extractor used to optimise the synthesis and purification of *N*-Bn-α-Me-BA **5.08**. P = pump, BPR = back pressure regulator, LLS = liquid-liquid separator, SL = sample loop. See experimental for more details.

The results of the optimisation are shown in Figure 60. An optimum purity of 71% was identified at the following process conditions: t_{res} = 6.9 min, temperature = 127.2 °C, pH = 0.772 and aqueous:organic ratio = 0.408. In terms of reaction conditions, a high purity was favoured at high temperatures and short residence times. High temperatures were found to drive the reaction to high conversion, where the reduction in unreacted starting materials (Figure 61a & b) outweighed the increase in formation of the 3° amine **5.10** impurity (Figure 61c) with respect to the purity of *N*-Bn-α-Me-BA **5.08**. Although the highest conversions were observed at the longer residence times, this corresponded to an increase in the concentration of salt **5.11** (Figure 61d), which was not efficiently extracted from the organic phase in this region.

Similar to the previous LLE example, there was a noticeable cliff edge around the optimum, where increasing the aqueous:organic ratio from 0.408 to 0.759 corresponded to a decrease in purity from 71% to 16%. This could mainly be attributed to the salt **5.11** impurity, which disfavoured extraction from the organic phase at aqueous:organic ratios greater than 0.5 (Figure 61d). This was likely caused by an increase in ionic strength of the aqueous phase, as a result of other cationic impurities. This could have reduced the solubility of salt **5.11** in the aqueous phase, causing it to favour partitioning in chloroform.[198] Nevertheless, a comparison of the optimum reaction conditions, including and excluding the downstream LLE, showed that the optimised extraction significantly improved the purity of *N*-Bn-α-Me-BA **5.08** (Figure 62). The aqueous acidic work-up reduced the amount of salt **5.11** by 81%, whilst selectively extracting 43% of the unreacted α-Me-BA **5.07** starting material. Therefore, the system was able to successfully optimise both the reaction and extraction steps in just 53 experiments, with no human intervention.

Chloroform was selected as the organic solvent for this reaction as it solubilised the salt by-products formed, thus providing a homogeneous reaction mixture. However, the relatively high dielectric constant of chloroform, compared to other water immiscible solvents, resulted in a challenging extraction. Further improvements in purity could be achieved via multi-stage LLE, where a similar self-optimisation approach could be utilised. Alternatively, purification could be achieved via in-line filtration of a reaction slurry, although the challenges associated with self-optimisation of solid-forming reactions have yet to be fully addressed.

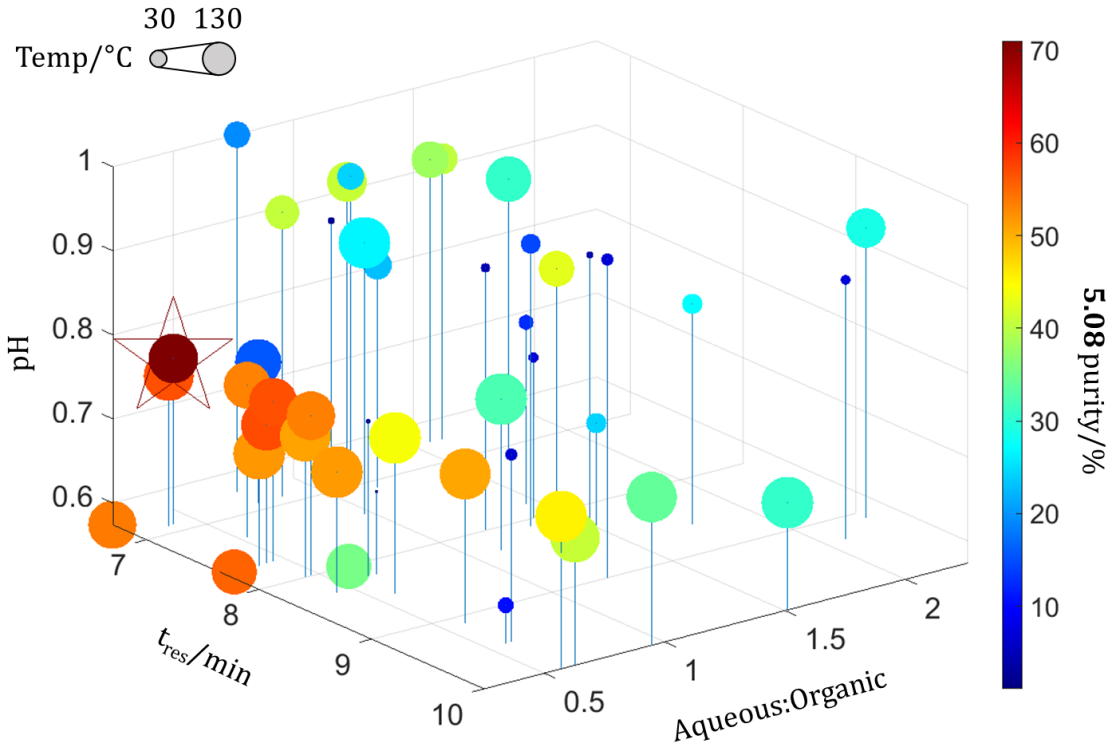

Figure 60. Results for the optimisation of the *N*-benzylation reaction and in-line LLE with respect to purity of the desired product **5.08**. ☆ = maximum % purity.

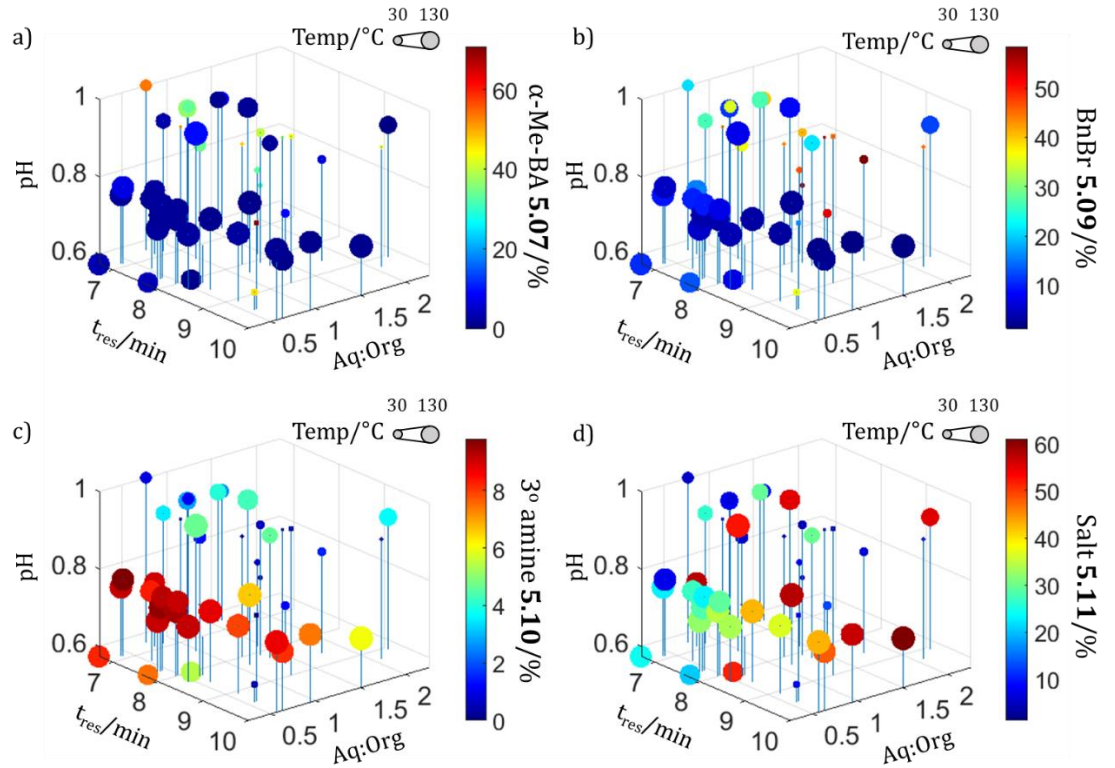

Figure 61. Impurity plots for the *N*-benzylation reaction-extraction process: (a) α-Me-BA **5.07**; (b) benzyl bromide **5.09** (BnBr); (c) 3° amine **5.10**; (d) salt **5.11**.

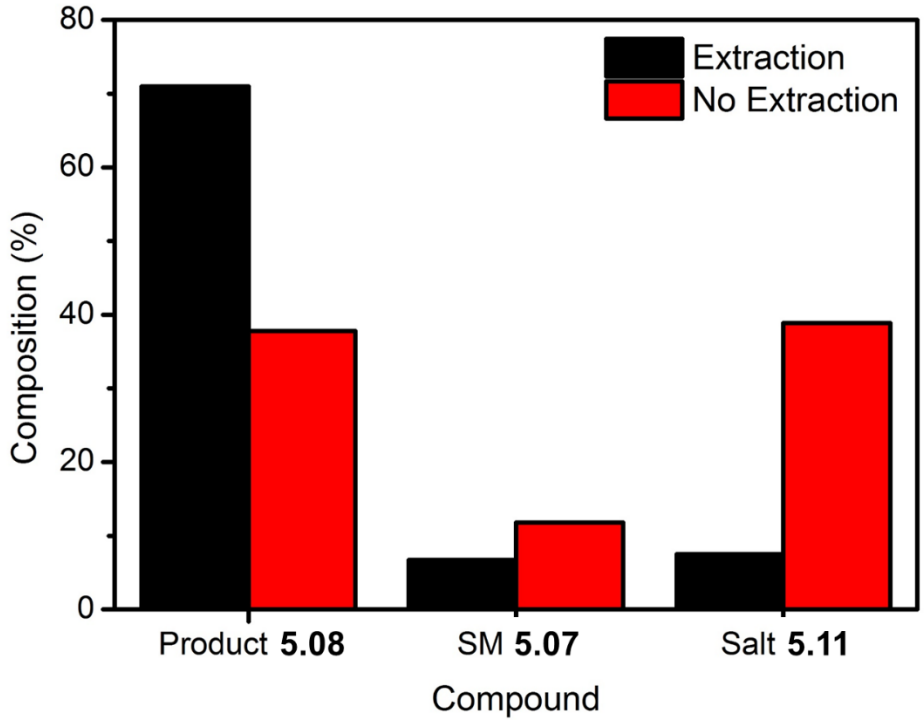

Figure 62. Comparison of the reaction mixture composition at the optimum process conditions, including and excluding the downstream LLE. SM = starting material.

5.3.2 Biphasic Claisen-Schmidt Condensation

Liquid-liquid biphasic reactions are an industrially important class of reaction, which benefit from the use of inexpensive and environmentally benign water soluble inorganic bases. In addition, biphasic solvent systems can solubilise a wide range of polar and non-polar compounds, thus enabling reactions that would otherwise be slurries, to be conducted in continuous flow. In the previous example, LLE of a single phase reaction was achieved by introduction of an aqueous phase downstream of the reactor. In contrast, for liquid-liquid biphasic reactions, partitioning of the starting materials and products between the phases occurs throughout the reaction. Therefore, an automated continuous flow reactor suitable for the self-optimisation of this type of process was developed.

Liquid-liquid biphasic reactions rely on a high interfacial area to overcome mass transfer limitations. Therefore, it was reasoned that the miniature CSTR cascade, described in Chapter 4, would be a suitable choice of reactor. Initially, thermal control of the reactor was established, to broaden the range of chemistries beyond room temperature and photoactivated reactions. A schematic of the design for higher temperature applications is shown in Figure 63a, with a photograph of the resultant reactor displayed in Figure 63b.

An aluminium heating mantle was designed to inset four CSTRs, and maximise the contact area between the reactors and the heat source. The inlet ports of each CSTR were aligned with grooves in the heating mantle, thus enabling the direct addition of reagents. The temperature of the heating mantle was regulated using a feedback loop consisting of: two nickel heating elements, a type K thermocouple and a Eurotherm temperature controller, which was programmed into the control software for the self-optimising system. The design ensured that the cascade was in a compact configuration, which enabled stirring of all four CSTRs to be achieved using a conventional stirrer plate. Type K thermocouples were placed in the additional inlet ports of each CSTR, to directly monitor and record the internal temperature of the reactors using a Pico logger.

(a)

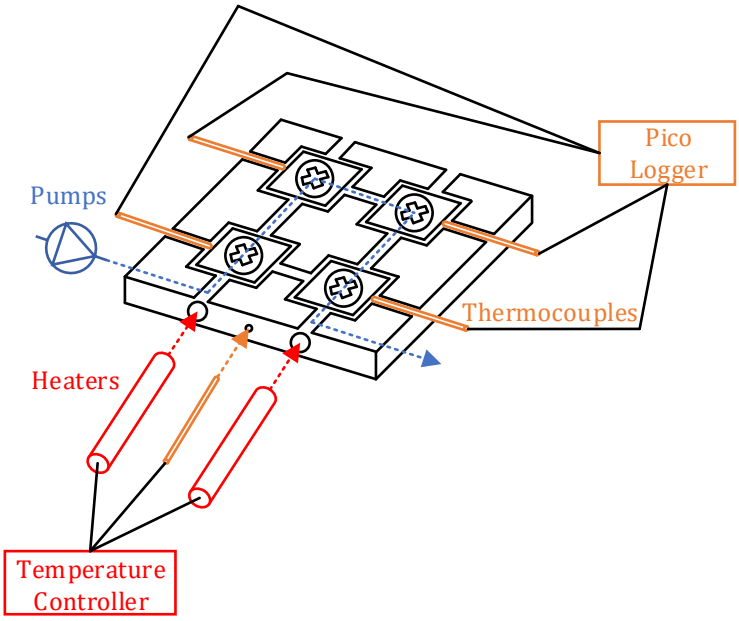

(b)

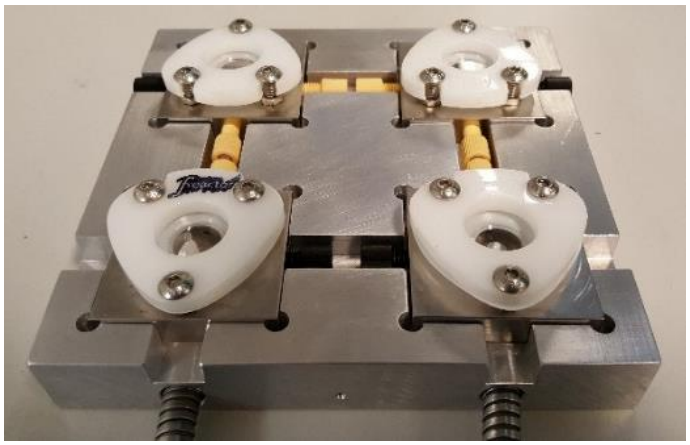

Figure 63. Temperature controlled CSTR cascade using a custom-built heating mantle: (a) schematic; (b) photograph.

The base catalysed aldol condensation remains a widely used C-C bond forming reaction. This involves the nucleophilic addition of an enolate to an aldehyde or ketone, with subsequent dehydration of the resultant β-hydroxy carbonyl yielding α,β-unsaturated carbonyl compounds (enones). The Claisen-Schmidt condensation is a type of crossed-aldol condensation, and refers specifically to the condensation of an aromatic aldehyde with an aliphatic aldehyde or ketone.[199] Enones are useful and versatile synthetic retrons, providing access to greater structural complexity, through transformations such as Michael additions and hetero Diels-Alder reactions.[200, 201] Therefore, the biphasic Claisen-Schmidt condensation between benzaldehyde **5.12** and acetone **5.13** was selected as a relevant case study for this investigation (Scheme 26).

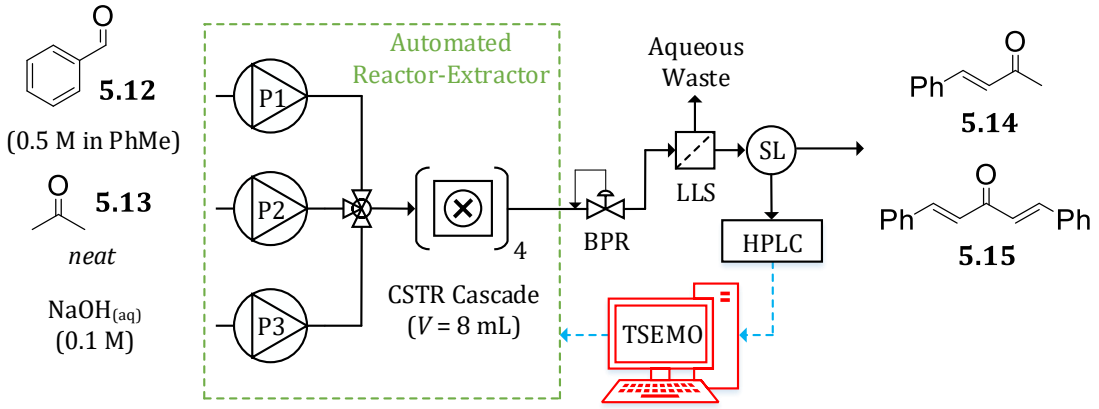

Scheme 26. Schematic of the automated reactor-extractor used to optimise the synthesis and purification of benzylideneacetone **5.14**. P = pump, BPR = back pressure regulator, LLS = liquid-liquid separator, SL = sample loop. See experimental for more details.

Initially, the repeatability of the system was tested by conducting three replicates at the following reaction conditions: t_{res} = 8.0 min, temperature = 80.0 °C, equivalents of acetone **5.13** = 21.5 and NaOH mol% = 30. The yields of the desired benzylideneacetone **5.14** product (32.9%, 39.0% & 40.4%) had a range of 7.5 and a standard deviation of 3.99, indicating low repeatability. It was hypothesised that the heat transfer between the heating mantle and CSTRs was causing a delay in the time taken to achieve steady state.

To test this hypothesis, the internal temperature of each CSTR was monitored as a toluene-water mixture was heated at 20 intervals between 50 and 110 °C (Figure 64). The results indicated that there was a 15 min delay between

stabilisation of the heating mantle temperature and stabilisation of the CSTRs temperature. In addition, there was a further 5 min delay for the temperature of CSTR 1 to stabilise after setting the pumps to their desired flow rates (i.e. increasing the flow rates from dead-time conditions). The data from these experiments showed a very good linear fit between the heating mantle temperature and the average CSTR temperature (R^2 = 0.9999, see experimental). Therefore, the average process temperature (y) could easily be calculated from the set temperature of the heating mantle (x) using the relationship $y = 0.9002x + 2.1477$, for temperatures between 50 and 110 °C.

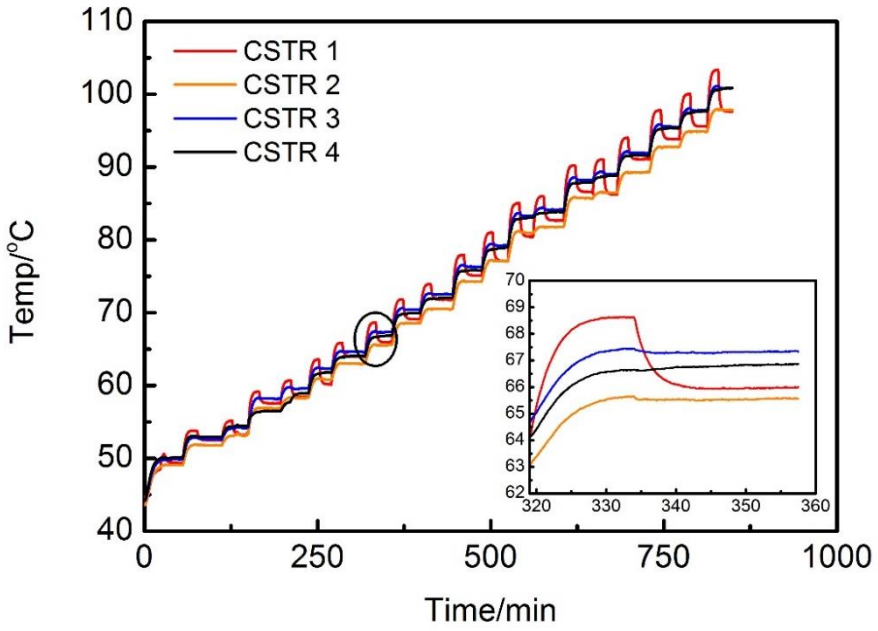

Figure 64. Plot showing the internal temperature profile of each CSTR on heating a toluene-water mixture at 20 intervals between 50 and 110 °C. Inset graph: heating mantle temperature = 71.4 °C.

Based on the observations above, adjustments were made to the self-optimisation procedure (Figure 65). A 15 min wait and 5 min wait were included in the temp stable timer and steady state timer respectively. Three replicates were repeated at the same reaction conditions as previously. In this instance, the yields of benzylideneacetone **5.14** (39.0%, 39.0% & 40.4%) had a range of 1.4 and a standard deviation of 0.808. This highlighted a significant improvement in the repeatability of the system, and confirmed that the changes made to the optimisation program successfully accounted for the heat transfer characteristics of the reactor. However, this increased repeatability came at the cost

of reduced optimisation efficiency, with each experiment taking an additional 20 min longer.

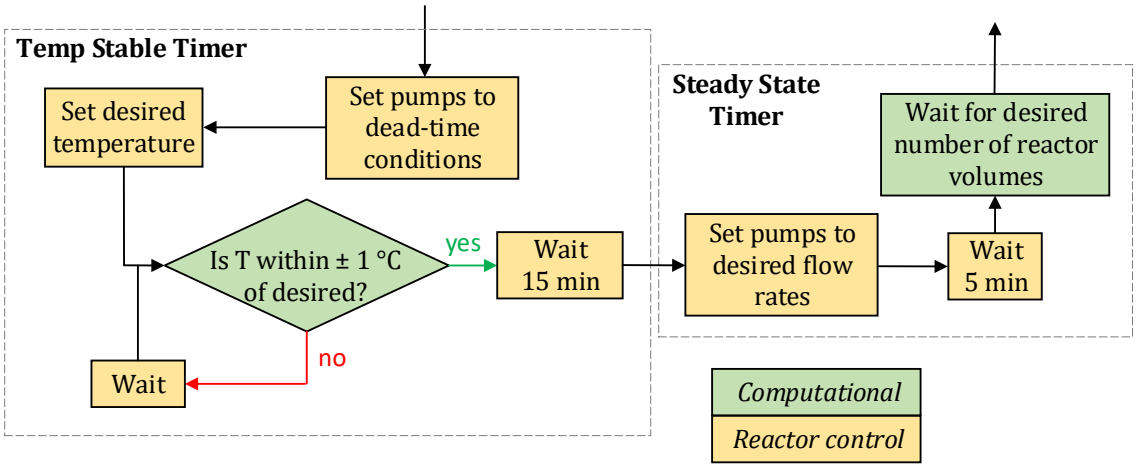

Figure 65. Flow chart of the adjusted self-optimisation procedure.

The reactor set-up for self-optimisation of the Claisen-Schmidt condensation is shown in Scheme 26. In contrast to the previous multi-step optimisation, the multi-objective TSEMO algorithm was selected. As TSEMO utilises GP surrogate models, it was hypothesised that it would be well suited for optimising complex multi-step processes within a relatively small number of experiments. The aim of the optimisation was to simultaneously maximise the purity, STY and RME with respect to benzylideneacetone **5.14** in the organic phase [Eq (49)], thus demonstrating for the first time the tri-objective self-optimisation of a chemical system. The purity of benzylideneacetone **5.14** in the organic phase was determined using on-line HPLC, with respect to unreacted benzaldehyde **5.12** and by-product dibenzylideneacetone **5.15**.

As acetone **5.13** is cheap and readily available, it was used as a neat reagent for the reaction. The miscibility of acetone **5.13** in both toluene and water resulted in a biphasic liquid-liquid reaction medium, where the organic and aqueous phases were toluene-acetone and water-acetone mixtures respectively. The optimisation was conducted with respect to flow rates, flow rate ratios and temperature. Varying the flow rates had an effect on both steps of the process: (i) the reaction in terms of residence time and acetone/sodium hydroxide equivalents; (ii) the extraction in terms of the toluene-acetone-water solvent ratio, and therefore the partitioning of the compounds between the organic and aqueous phases.

$$minimise[-\ln(purity), -\ln(STY), -\ln(RME)] \quad (49)$$

subject to:

$$P1/mL\ min^{-1} \in [0.2, 0.4]$$

$$P2{:}P1 \in [0.5, 1.1]$$

$$Aqueous{:}Organic\ Ratio \in [0.5, 1.2]$$

$$Temperature/°C \in [50, 110]$$

The optimisation was initialised with 20 LHC experiments, followed by a subsequent 89 experiments designed by the TSEMO algorithm. Of the 109 experiments conducted, 18 non-dominated solutions were identified. A comparison of the responses at the optimum for each function identified conflicts between all three objectives (Table 14). In this case, the purity was ≈ 10% lower, the STY was ≈ 2.5× lower and the RME was ≈ 1.5× lower at the optima of the other objectives compared to their own. Inspection of the optimum conditions for each objective showed that they were located at three different corners of the experimental space (see experimental for plots). In general, all of the objectives favoured high temperatures, as formation of the dibenzylideneacetone **5.15** by-product was negligible (< 1%) in the presence of a large excess of acetone **5.13**.[202] Although the optimum conditions for each objective were identified, this method provided limited process knowledge regarding the influence of the variables on each individual step. This was due to confounding between the reaction and work-up steps, caused by monitoring of the multi-step process using a single downstream analytical source. Therefore, systems optimised using this method are best treated as a black-box, where the inputs and outputs are described but without knowledge of how they are related. In cases where a higher degree of process understanding is required, additional PAT should be integrated downstream of each individual step.[29]

Table 14. Comparison of the three optimised functions (row headings) and the purity, STY and RME at these optimised conditions (column headings). Figures in bold are values for the function that has been optimised.

Objective	Purity/%	STY/kg m^{-3} h^{-1}	RME
Purity/%	**87.9**	97.9	4.74
STY/kg m^{-3} h^{-1}	76.1	**259.9**	4.42
RME	78.8	108.3	**7.16**

A surface was fitted to the non-dominated solutions to provide a visual representation of the Pareto front (Figure 66). This successfully highlighted the complete trade-off between all three objectives, which could be used to aid decision making during process design. For example, the Pareto front indicates that a purity of 82.8%, STY of 166.1 kg m^{-3} h^{-1} and RME of 5.66 can be obtained, which represents an approximately equal compromise between all three objectives. Alternatively, a greater importance could be placed on one or more of the objectives, and the process conditions selected accordingly post-optimisation.

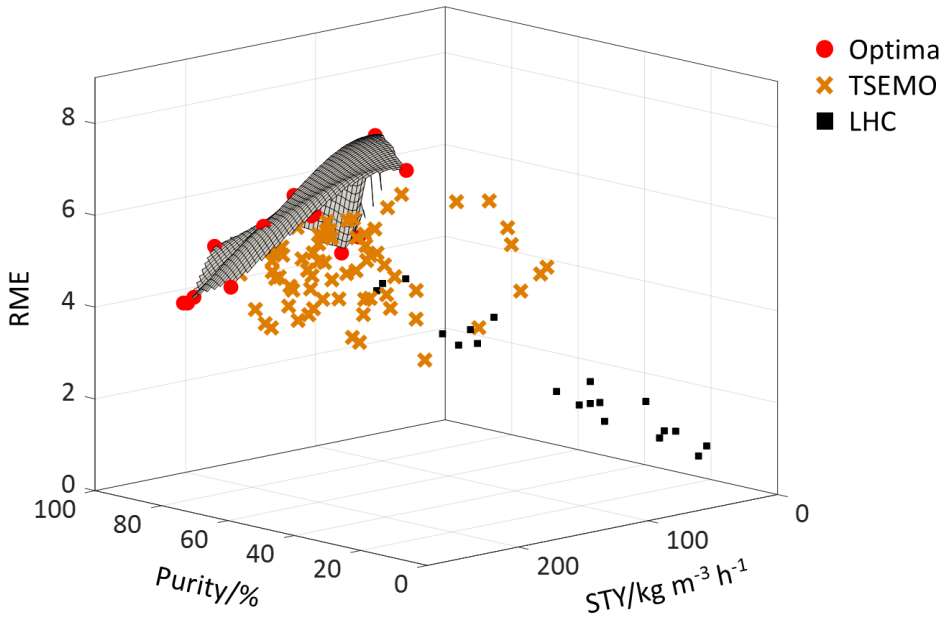

Figure 66. Results for the optimisation of the Claisen-Schmidt condensation reaction and in-line LLE with respect to purity, STY and RME. The initial LHC size was 20. The TSEMO algorithm conducted 89 additional experiments, 18 of which formed a Pareto front highlighting the trade-off between the objectives.

In this case, all reagents were cheap and readily available. Therefore, the termination criteria was based on practical time limitations, and the optimisation was stopped after 65 hours. This corresponds to a significant reduction in the time taken to optimise two steps with respect to three objectives, which would conventionally require six separate optimisations carried out over multiple weeks, and with no guarantee that the trade-off between the objectives would be identified. The major bottleneck with the current system is the heat transfer time between the heating mantle and the CSTR cascade. This could be removed by integrating temperature control into each individual CSTR, which would theoretically reduce the optimisation time further from 65 hours to 29 hours.

5.4 Conclusions

The end-to-end continuous flow synthesis of APIs offers a significantly reduced space-time demand and risk of supply chain disruption compared to traditional batch manufacturing.[185] Furthermore, the development of modular in-line purification technologies has played a key role in enabling multi-step continuous flow processing.[184] However, there has been few reports regarding the efficient optimisation of such systems. In this work, automated methods for the optimisation of in-line liquid-liquid extractions and multi-step reaction-extraction processes were explored.

The removal of structurally similar impurities between reactions is critical to avoid undesired side-reactions. Self-optimisation of a pH-based LLE was investigated for the separation of a 1° and 2° amine mixture. The SNOBFIT algorithm successfully identified an optimum separation of 90% in just 15 experiments, despite its location on a cliff edge in the response surface. The ability of the system to handle sharp changes in response was attributed to a combination of: (i) high precision of the automated continuous flow platform; (ii) fitting of local polynomial models by the SNOBFIT algorithm. In contrast, it was shown that a global polynomial model was unable to detect the sharp change in response over the defined variable range. Therefore, it was concluded that the SNOBFIT algorithm was well suited to the optimisation of LLEs, outperforming more traditional approaches such as DoE. Using this method, a multi-step process for the synthesis and purification of a 2° amine via direct *N*-alkylation and acidic work-up was optimised. An optimum purity of 71% was identified for the desired product, with the single-stage LLE removing 43% of unreacted starting material and 81% of the salt by-product. Notably, self-optimisation of the multi-step process enabled the effect of both the reaction and work-up steps on the purity to be simultaneously considered. This overcomes the challenges associated with sequential optimisation where, for example, an optimised reaction can result in a costly work-up procedure.

During process design, it is equally important to consider the impact of downstream purification on both economic and environmental metrics. Therefore, the ability of the multi-objective TSEMO algorithm to optimise multi-step processes was investigated. For this, a biphasic Claisen-Schmidt condensation reaction-extraction process was selected as an exemplar case study. Initially, a

temperature controlled miniature CSTR cascade was developed and characterised, thus broadening the suitability of the reactor to a wider range of chemistries. The two-step process was then optimised with respect to purity, STY and RME. This method successfully identified the trade-off curve between all three objectives in just 65 hours, thus providing a highly efficient and sustainable approach for the optimisation of multi-step processes. Potential improvements regarding the heating mechanism of the reactor were identified, and could theoretically more than half the current optimisation time. Furthermore, this study revealed that confounding of the reaction and extraction steps can result in limited process knowledge regarding the effect of the variables on each step. This could be overcome by the inclusion of additional PAT throughout the system, albeit at a substantial capital cost.[29] Nevertheless, this self-optimisation approach enabled rapid identification of different process optima for complex multi-step sequences without any human intervention.

Chapter 6 Conclusions and Future Work

The work in this thesis has focused on exploring the nature of existing self-optimising continuous flow systems, and how the technology could be improved to optimise more challenging and industrially relevant problems. The main areas that needed to be addressed were highlighted at the start of this work, and included: (i) application of more data efficient algorithms; (ii) development of suitable laboratory-scale flow reactors; (iii) optimisation of downstream unit operations. This thesis has contributed to each of the areas above, and demonstrated improvements in the form of relevant case studies.

When designing a chemical process, it is important to consider multiple relevant performance criteria. Work in Chapter 2 described the application of TSEMO, a recently developed Bayesian multi-objective optimisation algorithm.[96] Initial work highlighted the *a priori* selection of suitable objectives as a significant challenge. This was overcome by empirical modelling of the initial dataset, which subsequently enabled successful optimisation of two conflicting economic and environmental performance criteria. This approach provided the optimum values for two objectives, and highlighted the complete trade-off curve between them.[69] Therefore, this presents a significantly more data efficient methodology compared to single objective optimisation, and the scalarisation of multiple objectives.[66] Despite this, the amount of material required would still be a significant bottleneck for more expensive-to-evaluate systems, such as those involving APIs. It was hypothesised that the number of experiments could be reduced by predicting the Pareto front from the empirical models of the initial dataset. Although the simulations were in fair agreement with the experimental data, the models were at risk of overfitting in some regions of the variable space. Rather, future work should focus on the development of nanomole-scale high throughput flow equipment, which when combined with multi-objective optimisation, would synergistically increase the efficiency of self-optimising systems.[32]

In Chapter 3, a continuous flow Sonogashira reaction towards the synthesis of API lanabecestat (AZD3293) was self-optimised. Lanabecestat is a BACE1 inhibitor used for the treatment of Alzheimer's disease which entered phase III clinical trials in July 2016, and was developed by AstraZeneca and Eli Lilly & Co.[113] Optimisation of the continuous flow Sonogashira reaction started in April 2019, where results

were due at the time of the interim analysis in June 2019. To achieve this, the multi-objective self-optimisation approach, developed in Chapter 2, was integrated with a traditional design of experiments workflow. The combination of these methods provided all the desired information within the time constraints of a late-stage pharmaceutical development project. Notably, the trade-off between conversion and productivity was identified, which could be re-evaluated with the dynamic downstream work-up specifications in the active learning process. Hence, data obtained from the multi-objective self-optimisation played a key role in the design of a multi-step process.

In this case, the continuous variables (residence time, temperature, equivalents) were included in the self-optimisation, and the discrete variables (catalyst, ligand, solvent) were screened in preliminary work. Ideally, both continuous and discrete variables would be simultaneously optimised to account for any underlying interactions.[49] Therefore, the future development of multi-objective algorithms for mixed-variable optimisations will play a crucial role in the application of self-optimisation to more complex catalytic systems. Furthermore, optimisation of the Sonogashira reaction required 80 experiments carried out over a period of 35 hours. To facilitate a wider uptake of this technology in the pharmaceutical industry, a further reduction in the number of experiments is required, which is directly related to the efficiency of the algorithm. A kinetic-based reaction simulator was developed to assess the performance of multi-objective optimisation algorithms. By assessing new algorithms in this way, it can be ensured that self-optimising platforms are kept up-to-date with the latest advances in computer science. Of the algorithms tested, EIM-EGO was found to outperform TSEMO, and should therefore form the basis of future work in this area.[134]

In Chapter 4, a miniature CSTR cascade was developed to decouple flow rate and mixing performance. This provided a laboratory-scale reactor suitable for mass transfer limited reactions with longer residence times, thus broadening the scope of self-optimisation to a wider range of chemistries. In addition, the design enabled the incorporation of LEDs for photochemical applications, and was found to have a 10× greater absorbed photon flux density compared to photochemical batch reactors.[162] A biphasic continuous flow process for the site-selective aerobic oxidation of C(sp^3)-H bonds was self-optimised using a new hybrid algorithm, which combined global optimisation with local response surface mapping around the optimum. This

successfully located an optimum with milder reaction conditions compared to previous work, and provided important details regarding process stability around the optimum.[171] Further development of the reactor is underway to enable light intensity to be included as a variable during optimisation, which can have a significant impact on processes involving photodecomposition pathways. In this case, the developed reactor was suitable for the self-optimisation of a gas-liquid biphasic reaction. However, there still remains a lack of techniques for sampling and on-line analysis of slurries, which is a challenge that requires future attention to enable the automated optimisation of multiphasic reactions involving solids.

The end-to-end continuous flow synthesis of APIs involves multiple reaction and work-up unit operations, all of which need to be optimised to yield an efficient overall process.[183] Work in Chapter 5 addressed for the first time the self-optimisation of in-line liquid-liquid extractions and multi-step reaction-extraction processes. Initially, a pH-based LLE of structurally similar impurities was optimised, and the SNOBFIT algorithm found to outperform traditional statistical methods for response surfaces containing cliff edges. This approach was then adopted for the optimisation of a multi-step reaction-extraction process, where the effect of both the reaction and work-up steps on the purity were simultaneously considered. The ability of the multi-objective TSEMO algorithm to optimise a multi-step process was also explored. A biphasic Claisen-Schmidt condensation reaction-extraction process was successfully optimised with respect to three objectives, utilising a temperature controlled version of the miniature CSTR cascade described in Chapter 4. The trade-off curve between the three objectives was identified in 65 hours without any human intervention, and thus presents an efficient method for multi-step process optimisation. As such, this work will likely be extended for the optimisation of complete end-to-end syntheses of APIs in the future. However, challenges which will need to addressed include the deconvolution of factor effects on each step, and the individual control of residence time in telescoped reactors.

In summary, self-optimising continuous flow reactors provide an automated method for intelligent exploration of experimental space, thus rapidly identifying optimum conditions.[50] This thesis has focused on improving self-optimisation to further align with the interests of industry, which has been achieved by introducing multi-objective optimisation algorithms and applying them towards the synthesis of

APIs, developing a new multiphasic CSTR cascade reactor with photochemical capabilities and including downstream work-up operations in the optimisation of multi-step processes. During this work, areas of interest for future research in the field of self-optimisation have been identified. These include: (i) saving material by using nanomole-scale high throughput flow equipment; (ii) developing multi-objective algorithms for mixed variable optimisations; (iii) introducing sampling techniques for multiphasic reactions involving solids; (iv) optimisation of end-to-end total syntheses of APIs. Furthermore, as not all reactions are suitable for continuous flow, there would be a significant interest in the application of self-optimising technology to batch systems. As the rise of automation in chemistry continues, the production of commercially available self-optimising platforms is inevitable. Therefore, providing a user-friendly end product, that does not require specialist knowledge to operate, will be crucial for the widespread adoption of these systems by general chemists and synthetic-based laboratories.

Chapter 7 Experimental

7.1 Automated Reactor Platform

A photo of the automated reactor platform is shown in Figure 67. Reagents were pumped using JASCO PU-980 dual piston HPLC pumps and pump streams mixed using Swagelok SS-100-3 tee-pieces. Gas flow was achieved using a Bronkhorst EL-FLOW prestige mass flow controller. The reactor used was dependent on the experiment, and is stated in the corresponding Chapter Procedures. Sampling was achieved using a VICI Valco EUDA-CI4W sample loop (4-port) with 0.06 or 0.5 µL injection volumes. The reactor was maintained under the desired fixed back pressure using an Upchurch Scientific back pressure regulator. Stainless steel and Polyfon PTFE tubing (1/16" OD, 1/32" ID) was used throughout the reactor. Quantitative analysis was performed on an Agilent 1100 series HPLC instrument fitted with a Sigma Ascentis Express C18 reverse phase column (5 cm length, 4.6 mm ID and 2.7 µm particle size).

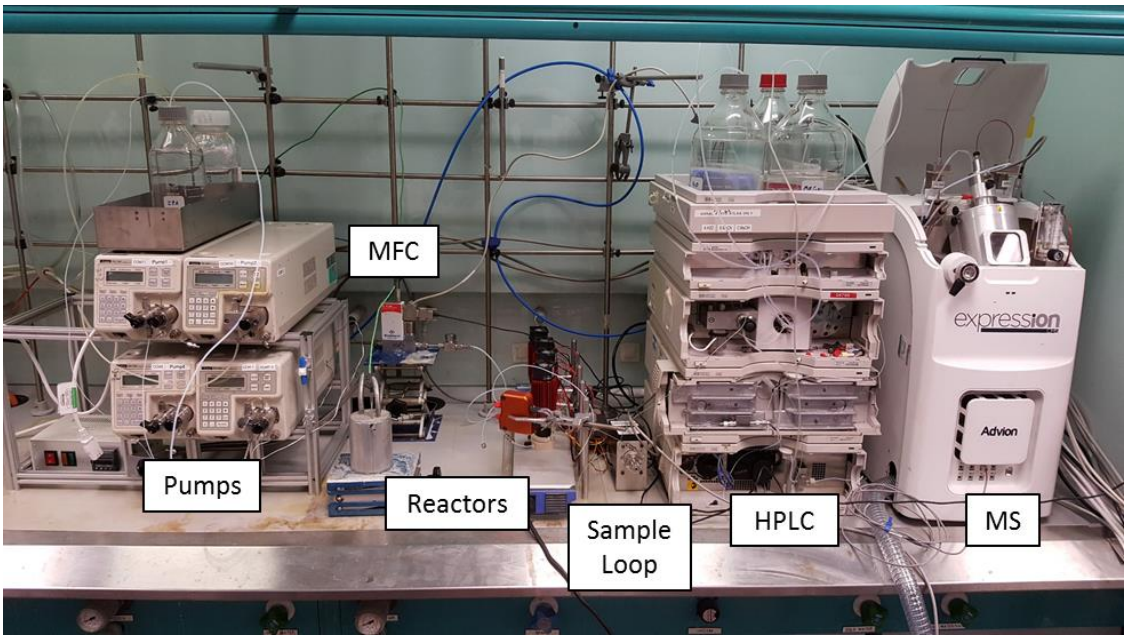

Figure 67. Photograph of the automated continuous flow platform used throughout this work.

An optimisation program was written in MATLAB that; controlled the pump flow rates, reactor temperature and sampling frequency (RS232 control), determined steady state, calculated the responses and controlled the inputs and outputs to and from the optimisation algorithm (Figure 68). Monitoring of the HPLC

was achieved using Agilent ChemStation software, which generated reports in .xls format. Scripts were written to transcribe the data from the reports into MATLAB. The automated reaction and analysis procedure were designed to consume a minimum amount of material during optimisations. Firstly, reactant flow rates were reduced to a minimum during heating/cooling of the reactor. Once the reactor reached the desired operating temperature, the reactant flow rates were set to their desired values. Secondly, experiments in each iteration were sorted in order of increasing temperature. This avoided unnecessary switches between hot and cold reactions. Finally, sequential experiments were started whilst analysis of the previous experiment was running, except during analysis of the final experiment in the iteration. Hence, the amount of time waiting for analysis was minimised. The responses for the objective function(s) were calculated from the HPLC chromatograms at the end of each iteration, and the results input into the optimisation algorithm to generate the next set of conditions.

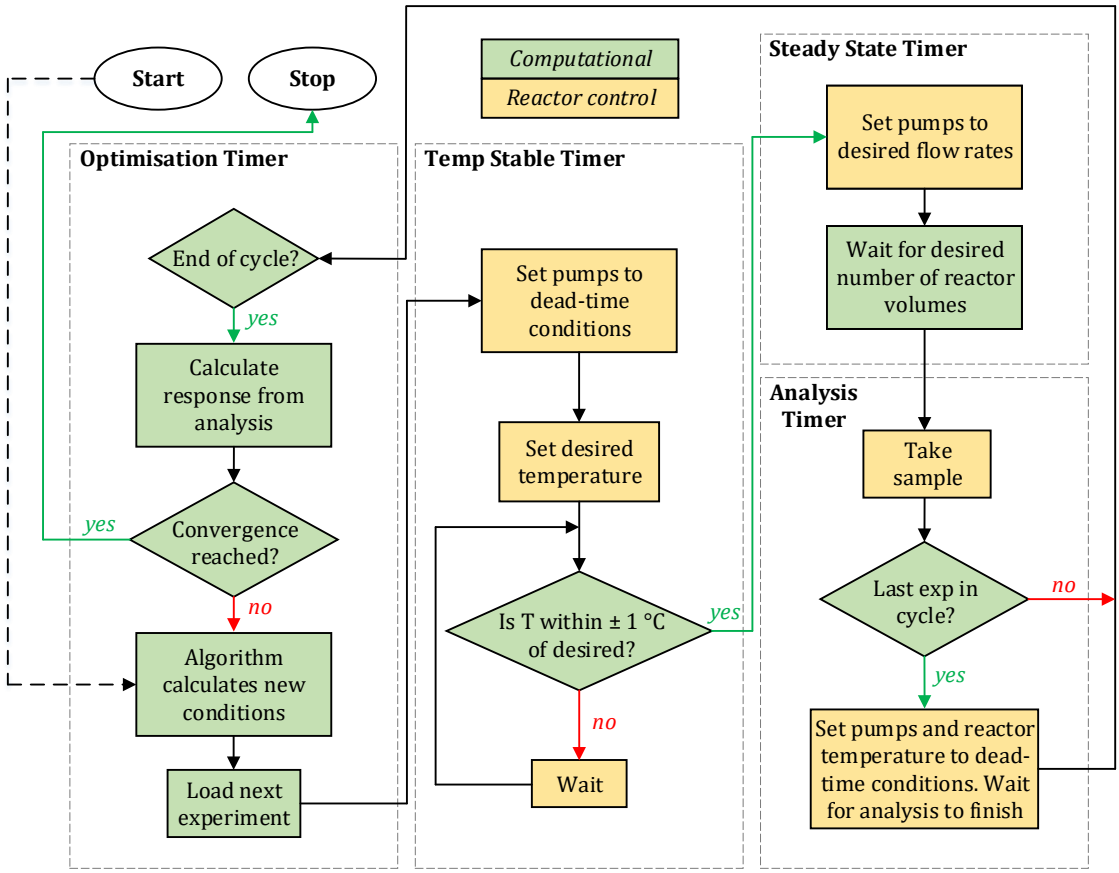

Figure 68. Flow chart of the self-optimisation procedure used throughout this work.

7.2 Offline Analytical Equipment

NMR spectroscopy was performed on a Bruker 500 UltraShield™ NMR Spectrometer (^{1}H NMR at 500 MHz, ^{13}C at 126 MHz) with the appropriate deuterated solvent. Chemical shifts in ^{1}H and ^{13}C NMR spectra are expressed as ppm downfield from TMS, and reported as singlet (s), doublet (d), triplet (t), quartet (q) and combination thereof, or multiplet (m). Coupling constants (*J*) are quoted in Hz and are averaged between coupling partners. LC-MS analysis was performed using an Agilent 1290 series uPLC and a Bruker HCT-Ultra detector with electrospray ionisation in the positive mode. UV-Vis analysis was performed using an Agilent Cary 100 series UV-Vis spectrophotometer.

7.3 Chapter 2 Procedures

7.3.1 Chemicals

α-Methylbenzylamine (99%, Aldrich), diisopropylethylamine (>99%, Fluorochem), benzyl bromide (>99%, Fluorochem), (*R*)-(+)-*N*-benzyl-α-methylbenzylamine (98%, Sigma) and chloroform (HPLC grade, VWR) were purchased from suppliers and used without further purification. A standard of *N*,*N*-dibenzyl-α-methylbenzylamine was synthesised for HPLC calibration.

7.3.2 Synthesis of *N*,*N*-dibenzyl-α-methylbenzylamine

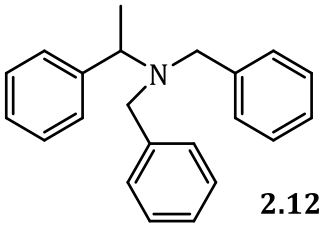

2.12

To a round-bottomed flask, α-methylbenzylamine **2.09** (2.50 g, 20.6 mmol) and diisopropylethylamine (5.33 g, 41.3 mmol) in acetonitrile (150 mL) was added. To this, benzyl bromide **2.10** (10.58 g, 61.9 mmol) was added and the reaction mixture left to stir under reflux for 48 hours. The resultant mixture was concentrated *in vacuo*, then partitioned between an ethyl acetate (100 mL) and water (100 mL) biphasic mixture. The aqueous layer was acidified to pH 1 with HCl (2 M), then separated and basified to pH 12 using NaOH (2.5 M). The aqueous

solution was then extracted with ethyl acetate (2 × 100 mL). The combined organic extracts were concentrated *in vacuo* to yield *N*,*N*-dibenzyl-α-methylbenzylamine **2.12** as an orange solid (1.48 g, 24%).

^{1}H NMR ($CDCl_3$, 500 MHz) δ 7.46 – 7.06 (m, 15H), 3.92 (q, *J* = 6.9 Hz, 1H), 3.61 (d, *J* = 14 Hz, 2H), 3.46 (d, *J* = 14 Hz, 2H), 1.43 (d, *J* = 6.9 Hz, 3H) ppm; ^{13}C NMR ($CDCl_3$, 101 MHz) δ 142.8, 140.5, 128.7, 128.2, 128.1, 128.0, 126.8, 126.7, 56.2, 53.6, 13.8 ppm; *m/z* (ESI$^+$) $C_{22}H_{23}N$ $[M+H]^+$, calculated 302.19, found 302.37; in agreement with published data.[203]

7.3.3 Experimental Set-Up

Reactor: Cambridge Reactor Design Polar Bear Flow Synthesiser, fitted with 4 mL Polyfon PTFE tubing (1/16" OD, 1/32" ID), and maintained under 250 psi back-pressure.

Reservoir solutions were prepared by dissolving the desired reagents in solvent under stirring at ambient conditions. Pump 1: α-methylbenzylamine **2.09** (12.9 mL, 0.10 mol, 0.400 mol L^{-1}), diisopropylethylamine (17.4 mL, 0.10 mol, 0.400 mol L^{-1}) and biphenyl (1.54 g, 10 mmol, 0.040 mol L^{-1}) in chloroform (219.7 mL). Pump 2: benzyl bromide **2.10** (16.6 mL, 0.14 mol, 0.400 mol L^{-1}) in chloroform (333.4 mL). Pump 3: chloroform. Reservoir solutions were replenished when required.

HPLC mobile phases were **A** H_2O (18.2 MΩ), **B** MeCN, both buffered with 0.1% TFA. Method: 10% to 90% **B** 3.5 mins, 90% to 10% **B** 0.5 min, 10% **B** 1 min, flow rate 1.75 mL min^{-1}, column temperature 20 °C.

7.3.4 Empirical Modelling

Polynomial response surface models of the LHC experiments were fitted using Umetrics MODDE (ver 12.1) by including all square and interaction terms then removing terms with a *p*-value less than 0.05. The model for % impurity was transformed logarithmically ($\hat{y}_i = \log(y_i)/(100-y_i)$) to provide a more normal distribution.

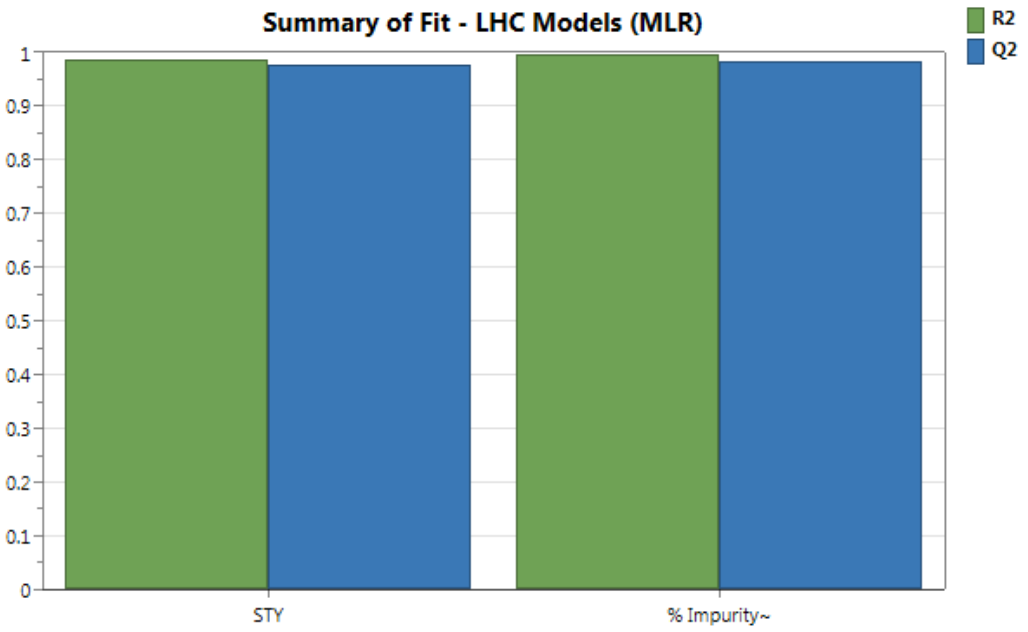

Figure 69. Summary of fit plots for STY and % impurity. STY: $R^2 = 0.988$, $Q^2 = 0.977$. % impurity: $R^2 = 0.996$, $Q^2 = 0.983$.

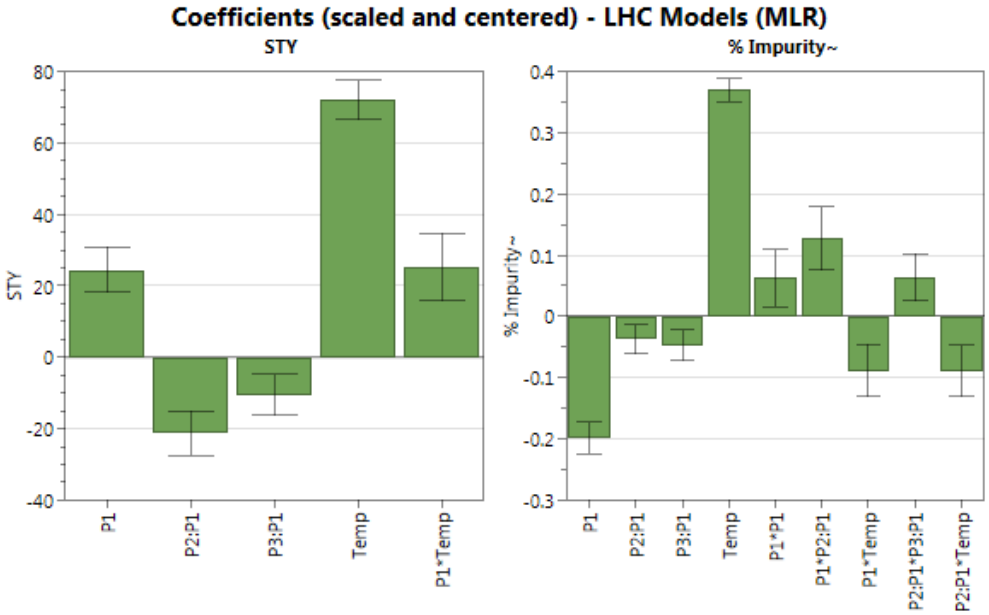

Figure 70. Coefficient plots for the models of STY and % impurity. Insignificant terms (confidence interval crosses 0) were removed from the saturated model one at a time.

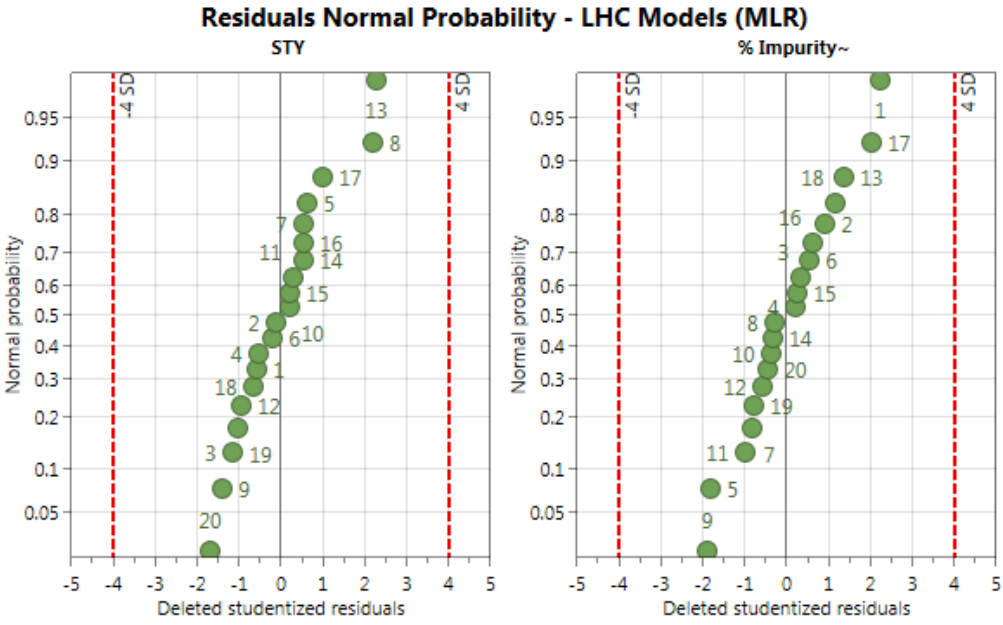

Figure 71. Residuals normal probability plots for STY and % impurity. A straight diagonal line represents a normal distribution. Experiments outside of the 4 standard deviation limits represent outliers.

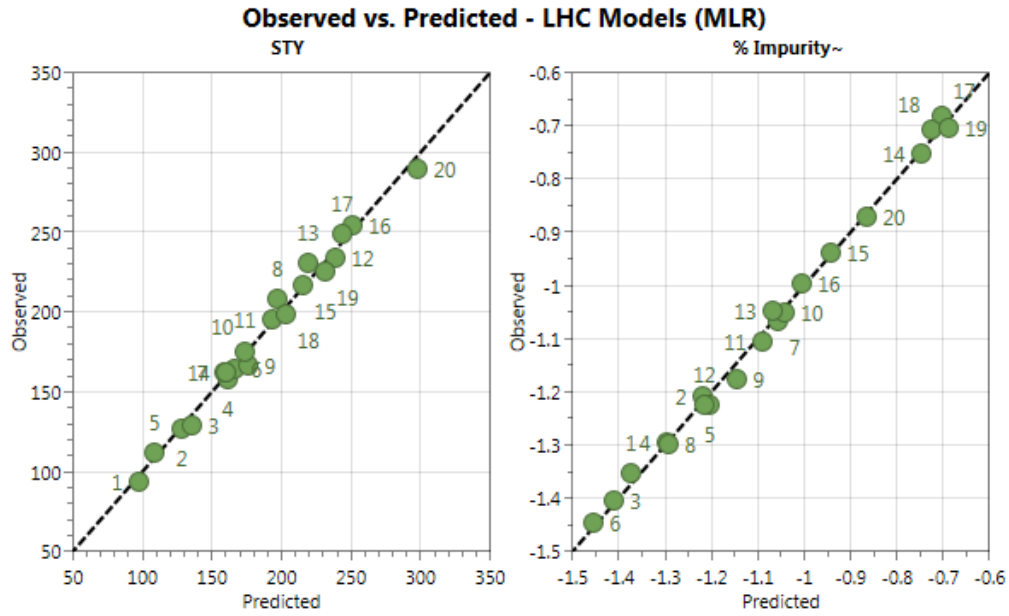

Figure 72. Plots of observed vs. experimental for the models of STY and % impurity. A straight diagonal line indicates the model has a good fit to the experimental data.

7.3.5 Self-Optimisation Results

minimise[-ln(STY), ln(% impurity)]

Table 15. Self-optimisation variables, directly input in terms of flow rates and ratios. P = pump.

	Variables			
Limits	P1/mLmin^{-1}	P2:P1	P3:P1	Temp/°C
Lower	0.20	1.00	0.50	110
Upper	0.40	5.00	1.00	150

Table 16. List of results from the self-optimisation. The first 20 experiments are a LHC design in ascending order of temperature. The non-dominated solutions are highlighted in bold.

Entry	P1/mL min^{-1}	P2:P1	P3:P1	Temp/°C	Impurity/%	STY/kg m^{-3} h^{-1}
1	0.252	4.900	0.694	111.8	4.3	94
2	0.212	2.360	0.785	113.8	5.8	127
3	0.346	2.823	0.661	114.8	3.8	129
4	0.290	1.189	0.704	117.6	4.8	158
5	0.222	4.650	0.953	118.7	5.6	111
6	0.396	2.169	0.883	120.7	3.5	165
7	0.231	1.570	0.861	122.3	7.9	162
8	0.382	1.962	0.613	124.3	4.8	208
9	0.312	3.497	0.629	126.5	6.2	167
10	0.268	3.736	0.528	128.0	8.2	175
11	0.321	4.182	0.500	130.8	7.2	195
12	0.378	1.301	0.802	133.0	5.6	233
13	0.336	2.664	0.930	136.0	8.2	231
14	0.202	3.835	0.975	136.5	15.0	162
15	0.301	4.482	0.577	139.5	10.3	217
16	0.367	3.178	0.737	140.1	9.2	255
17	0.286	2.442	0.575	142.2	17.3	249
18	0.243	4.373	0.763	144.8	16.4	199
19	0.272	3.293	0.835	146.5	16.5	225
20	0.356	1.719	0.905	148.7	11.8	290
21	0.400	1.000	0.987	118.5	3.5	146
22	0.400	1.000	1.000	126.7	3.2	175
23	0.400	1.000	1.000	135.8	4.6	216
24	0.400	1.000	1.000	143.2	5.8	251
25	0.400	5.000	0.500	111.8	3.5	108
26	0.400	1.000	0.757	128.8	4.7	215
27	**0.400**	**1.000**	**0.530**	**130.7**	**5.5**	**259**
28	0.400	1.000	0.520	139.5	7.6	294
29	0.400	5.000	0.660	126.8	4.8	160
30	0.400	4.852	0.549	131.2	4.9	181
31	0.400	1.000	0.799	143.2	7.8	278
32	**0.400**	**1.000**	**0.500**	**150.0**	**10.0**	**331**
33	0.400	2.785	1.000	139.1	6.4	231
34	0.400	2.755	0.978	146.7	9.0	266
35	0.400	1.000	0.615	146.9	9.7	317
36	0.400	5.000	1.000	120.9	3.1	132

37	0.400	1.000	0.500	122.0	4.5	228
38	0.400	1.259	0.505	127.7	5.5	254
39	0.400	1.000	0.500	133.7	6.4	271
40	**0.400**	**1.026**	**0.701**	**110.0**	**2.2**	**142**
41	0.400	2.216	0.992	110.0	2.4	101
42	0.400	1.000	0.500	134.6	6.8	271
43	0.400	1.068	0.500	145.3	9.2	321
44	**0.400**	**1.000**	**0.655**	**110.0**	**2.3**	**147**
45	0.400	5.000	1.000	111.2	2.7	84
46	0.400	1.000	0.907	130.7	4.1	201
47	**0.400**	**1.000**	**0.500**	**140.7**	**7.3**	**298**
48	**0.400**	**1.055**	**0.500**	**119.6**	**3.2**	**205**
49	0.400	1.239	0.500	126.4	5.0	241
50	0.400	1.682	0.500	131.3	6.8	263
51	0.400	1.000	0.569	113.1	2.9	160
52	0.400	1.000	0.569	115.7	3.2	175
53	0.400	1.000	0.568	119.1	3.3	189
54	**0.400**	**1.005**	**0.677**	**150.0**	**8.9**	**326**
55	0.400	1.000	0.549	111.2	2.4	162
56	**0.400**	**1.000**	**0.621**	**132.1**	**4.8**	**243**
57	0.400	1.000	0.549	149.0	9.5	321
58	**0.400**	**1.000**	**0.528**	**150.0**	**8.7**	**325**
59	0.400	1.000	0.500	118.2	3.2	203
60	**0.400**	**1.000**	**0.500**	**123.9**	**3.9**	**226**
61	0.400	1.000	0.870	150.0	8.5	300
62	**0.400**	**1.000**	**0.644**	**150.0**	**8.3**	**314**
63	**0.400**	**1.000**	**0.500**	**110.0**	**2.4**	**166**
64	**0.400**	**1.000**	**0.500**	**115.4**	**2.7**	**181**
65	0.400	1.000	0.500	118.2	3.2	202
66	**0.400**	**1.000**	**0.500**	**134.8**	**6.4**	**279**
67	0.346	1.001	0.756	110.0	2.8	132
68	0.355	1.000	0.500	110.0	2.5	155
69	**0.400**	**1.000**	**0.500**	**133.4**	**6.0**	**269**
70	0.400	1.000	0.500	145.7	9.2	318
71	**0.400**	**1.000**	**0.558**	**126.3**	**4.4**	**231**
72	0.397	1.000	0.558	135.6	6.4	274
73	0.400	1.000	0.558	145.7	8.3	311
74	**0.400**	**1.000**	**0.513**	**150.0**	**9.4**	**326**
75	0.400	1.000	0.500	113.2	3.1	179
76	**0.400**	**1.000**	**0.500**	**131.5**	**5.6**	**263**
77	**0.400**	**1.000**	**0.500**	**137.0**	**6.7**	**282**
78	**0.400**	**1.000**	**0.500**	**141.9**	**7.9**	**303**

7.4 Chapter 3 Procedures

7.4.1 Chemicals

3,5-Dibromobenzene **3.05** (98%, Fluorochem), 1-hexyne **3.11** (97%, Merck), tetrakis(triphenylphosphine)palladium(0) (99%, Merck), copper (I) iodide (99.999%, Merck), pyrrolidine (≥99%, Merck), toluene (HPLC grade, VWR), acetonitrile (HPLC grade, VWR) and biphenyl (≥99%, Merck) were purchased from suppliers and used without further purification. The wt% of mono and bis in a reaction mixture was quantified via ^{1}H NMR and used for HPLC calibration.

7.4.2 Experimental Set-Up

Reactor: Cambridge Reactor Design Polar Bear Flow Synthesiser, fitted with 3 mL Polyfon PTFE tubing (0.1 cm ID), and maintained under 5 bar back-pressure. Changes to the reactor platform: HiTec Zang SyrDos syringe pumps and Knauer AZURA HPLC pumps; Waters Acquity C18 reverse phase column (3 cm length, 4.6 mm ID and 1,7 μm particle size); steady state was monitored using a Kaiser RxN1 785 nm Raman System.

Reservoir solutions were prepared by dissolving the desired reagents in solvent under stirring at ambient conditions. Pump 1: 3,5-dibromopyridine **3.05** (143.55 g, 0.61 mol, 0.61 mol L^{-1}), $Pd(PPh_3)_4$ (10.40 g, 0.009 mol, 0.009 mol L^{-1}), CuI (11.61 g, 0.061 mol, 0.061 mol L^{-1}), pyrrolidine (131.50 g, 1.85 mol, 1.85 mol L^{-1}) and biphenyl (18.80 g, 0.122 mol, 0.122 mol L^{-1}) in PhMe/MeCN (2:1, 1 L); Pump 2: 1-hexyne **3.11** (68.58 g, 0.84 mol, 0.84 mol L^{-1}) in PhMe (1 L); Pump 3 (dilution): MeCN.

HPLC mobile phases were **A** H_2O (18.2 MΩ), **B** MeCN and **C** TFA (1%). The method used was 5% to 80% **B** 8 mins, 80% to 5% **B** 0.1 min, 5% **B** 1 min, flow rate 2 mL min^{-1}, column temperature 40 °C. The method was isocratic with respect to **C** (5%). The dilution pump was set to 5× the combined flow rate of the reagent pumps, to prevent saturation of the HPLC detector by the mono product.

7.4.3 Full Factorial DoE

The 2-level full factorial design was constructed using Umetrics MODDE (ver 12.1). Polynomial response surface models of the experiments were fitted by

including all square and interaction terms then removing terms with a *p*-value less than 0.05.

Table 17. Variables for the full factorial design of experiments.

	Variables	
Limits	**CuI/mol%**	**PhMe:MeCN**
Lower	5	3.6:1
Upper	10	5.1:1

Table 18. List of results from the full factorial design of experiments, including two centre point and upper extreme point replicates.

Entry	CuI/mol%	PhMe:MeCN	SM/%
1	7.5	4.35:1	8.6
2	10	3.6:1	11.2
3	5	5.1:1	8.4
4	7.5	4.35:1	7.5
5	5	3.6:1	8.0
6	10	5.1:1	3.6
7	10	5.1:1	3.4

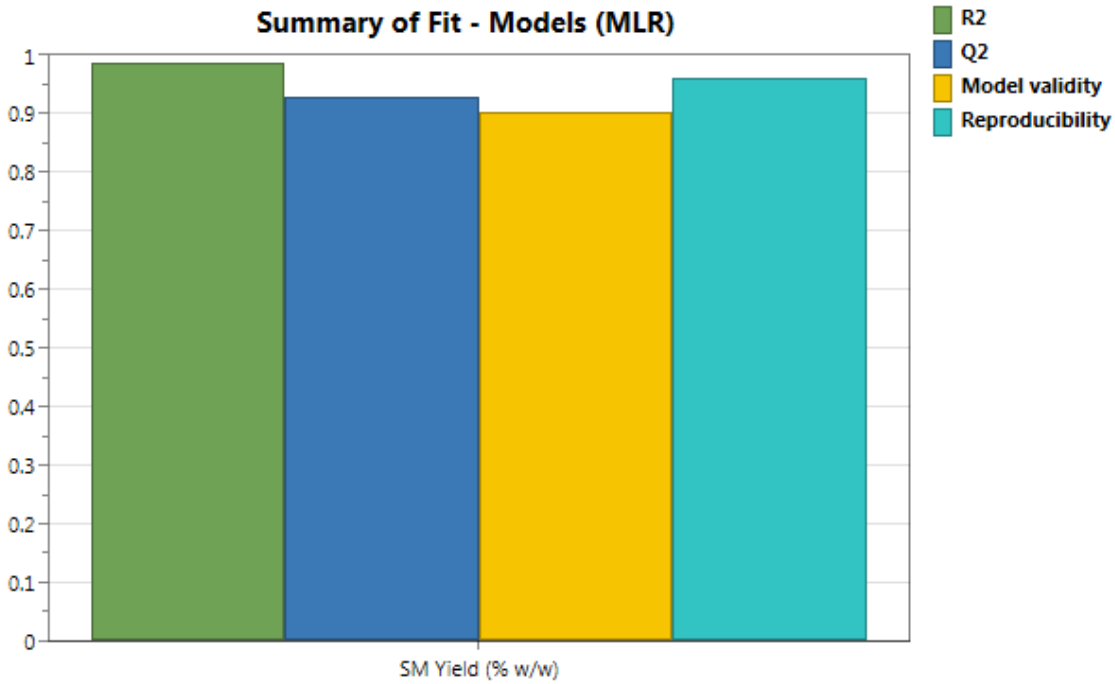

Figure 73. Summary of fit plot for SM. R^2 = 0.986, Q^2 = 0.923. Reproducibility is determined from the replicates, and determines the models sensitivity towards factor effects.

7.4.4 Box-Behnken DoE

The Box-Behnken design was constructed using Umetrics MODDE (ver 12.1). Polynomial response surface models of the experiments were fitted by including all square and interaction terms then removing terms with a *p*-value less than 0.05.

Table 19. Variables for the Box-Behnken design of experiments.

	Variables		
Limits	t_{res}/min	1-hexyne equiv.	Temp/°C
Lower	3.0	1.2	120
Upper	8.0	1.6	150

Table 20. List of results from the Box-Behnken design of experiments, including three centre point replicates.

Entry	t_{res}/min	1-Hexyne equiv.	Temp/°C	SM/%	Mono/%	Bis/%
1	5.5	1.4	135.0	7.5	73.5	19.0
2	5.5	1.4	135.0	5.8	73.3	20.9
3	3.0	1.2	135.0	14.6	71.5	13.9
4	8.0	1.4	150.0	8.9	72.6	18.6
5	3.0	1.4	150.0	8.2	70.7	21.1
6	5.5	1.6	150.0	3.5	68.5	28.0
7	8.0	1.2	135.0	14.2	71.7	14.1
8	3.0	1.4	120.0	6.8	73.3	19.9
9	3.0	1.6	135.0	3.2	68.6	28.2
10	5.5	1.2	150.0	16.0	70.0	14.0
11	5.5	1.6	120.0	2.8	70.4	26.8
12	5.5	1.2	120.0	15.4	70.7	13.9
13	8.0	1.6	135.0	2.9	68.2	28.9
14	8.0	1.4	120.0	8.6	71.9	19.5
15	5.5	1.4	135.0	7.5	72.5	20.1

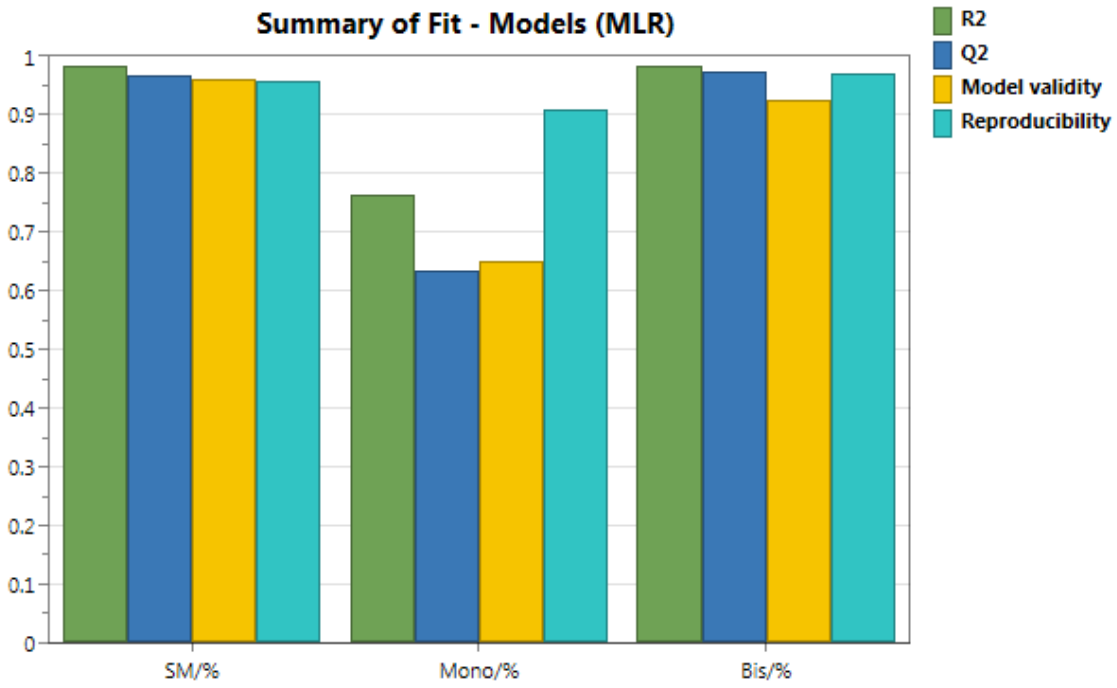

Figure 74. Summary of fit plots for SM, mono and bis. SM: R^2 = 0.985, Q^2 = 0.968. Mono: R^2 = 0.764, Q^2 = 0.634. Bis: R^2 = 0.982, Q^2 = 0.973. Reproducibility is determined from the centre points replicates, and determines the models sensitivity towards factor effects.

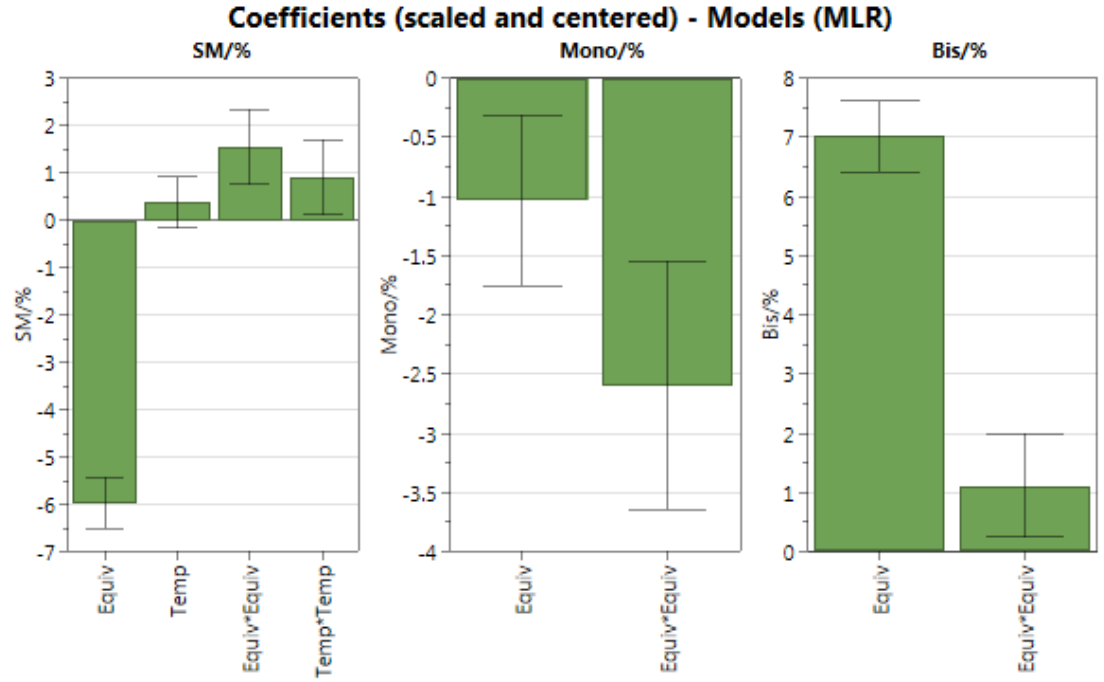

Figure 75. Coefficient plots for the models of SM, mono and bis. Insignificant terms (confidence interval crosses 0) were removed from the saturated model one at a time.

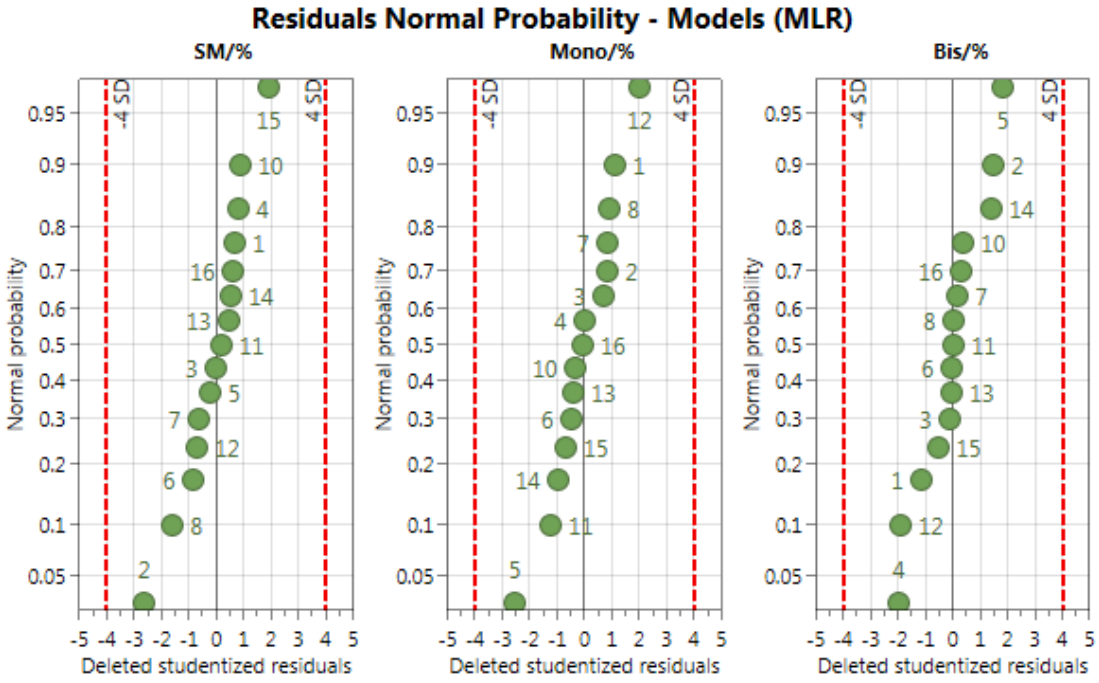

Figure 76. Residuals normal probability plots for SM, mono and bis. A straight diagonal line represents a normal distribution. Experiments outside of the 4 standard deviation limits represent outliers.

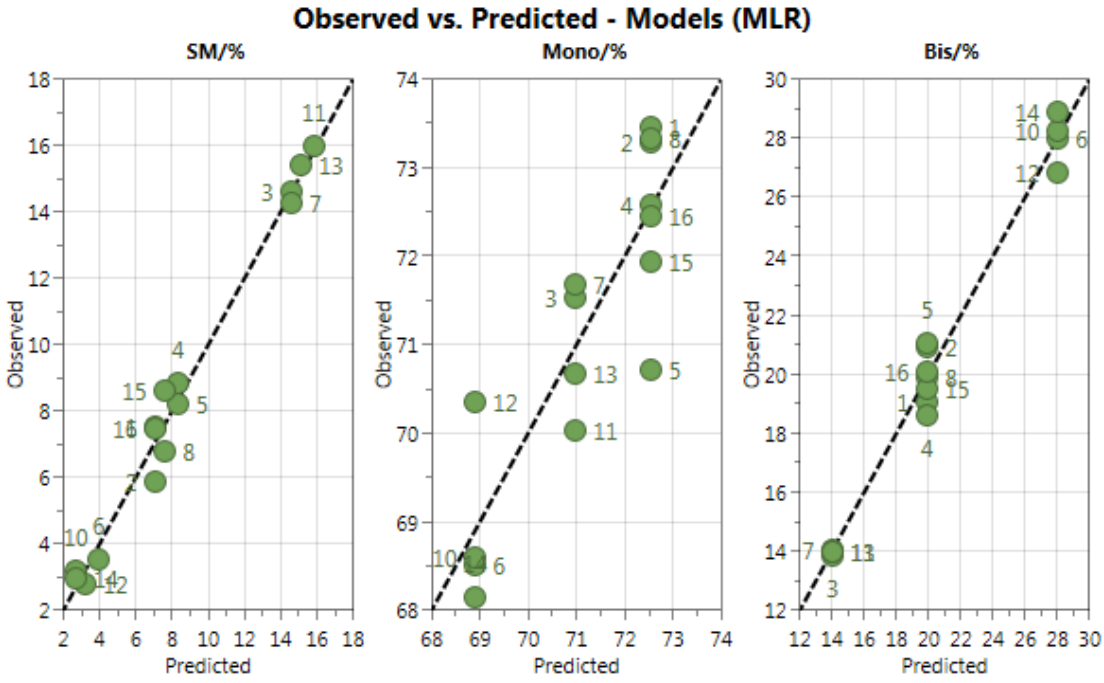

Figure 77. Plots of observed vs. experimental for the models of SM, mono and bis. A straight diagonal line indicates the model has a good fit to the experimental data.

7.4.5 Self-Optimisation Results

minimise[-ln(STY), ln(% of SM **3.05**)]

Table 21. Self-optimisation variables.

	Variables		
Limits	t_{res}/min	1-Hexyne equiv.	Temp/°C
Lower	1.0	1.2	120
Upper	8.0	1.6	150

Table 22. List of results from the self-optimisation. The first 20 experiments are a LHC design in ascending order of temperature. The non-dominated solutions are highlighted in bold.

Entry	t_{res}/min	1-Hexyne equiv.	Temp/°C	STY/kg m^{-3} h^{-1}	SM/%
1	2.8	1.59	121.3	984.2	3.3
2	1.4	1.34	122.9	2268.3	10.3
3	6.1	1.38	123.6	542.2	7.7
4	4.2	1.22	125.7	808.4	11.7
5	1.8	1.57	126.5	1635.3	4.3
6	7.9	1.31	128.0	407.7	9.9
7	2.1	1.26	129.2	1597.3	12.4
8	7.4	1.30	130.7	432.5	8.7
9	4.9	1.45	132.4	631.5	5.9
10	3.4	1.47	133.5	888.7	5.1
11	5.2	1.52	135.6	535.3	3.4
12	7.2	1.23	137.3	455.0	13.8
13	5.7	1.37	139.5	544.6	6.8
14	1.1	1.48	139.9	2740.3	8.2
15	4.5	1.55	142.1	610.0	3.6
16	6.8	1.42	142.6	441.4	6.6
17	4.0	1.35	144.2	782.6	9.6
18	2.5	1.54	146.1	1098.8	4.1
19	3.5	1.43	147.3	848.2	6.8
20	6.5	1.27	149.1	497.7	9.9
21	1.0	1.60	120.0	2979.6	8.1
22	1.0	1.59	125.9	2989.6	7.8
23	1.7	1.60	126.2	1731.1	5.0
24	1.0	1.54	131.6	3049.7	8.1
25	**1.0**	**1.56**	**141.7**	**3067.6**	**7.9**
26	3.1	1.58	145.8	855.9	3.7
27	1.6	1.57	148.7	1797.9	5.7
28	2.4	1.52	149.0	1199.8	5.6
29	2.0	1.58	126.2	1428.0	4.0
30	1.0	1.60	126.5	3004.6	8.0
31	1.3	1.60	135.1	2193.2	6.0
32	2.3	1.57	137.8	1282.5	4.1
33	**2.5**	**1.59**	**125.3**	**1132.1**	**3.4**
34	1.6	1.55	127.0	1822.9	5.5
35	1.0	1.60	136.1	2799.8	7.4
36	1.3	1.55	136.8	2247.8	6.4
37	1.5	1.60	139.5	1845.1	5.4

38	**1.2**	**1.60**	**142.9**	**2300.9**	**5.8**
39	**1.0**	**1.60**	**145.3**	**2826.3**	**6.4**
40	2.4	1.57	148.6	1169.2	4.2
41	2.2	1.59	121.5	1337.2	4.1
42	3.5	1.60	146.9	760.9	3.9
43	1.0	1.57	147.8	2756.5	7.5
44	**1.2**	**1.57**	**150.0**	**2306.7**	**6.0**
45	**1.4**	**1.60**	**138.4**	**2036.3**	**5.0**
46	1.7	1.58	143.2	1676.6	5.2
47	2.1	1.58	145.0	1330.0	4.1
48	**1.0**	**1.60**	**148.7**	**2874.1**	**6.6**
49	1.2	1.58	122.4	2517.3	6.7
50	**1.7**	**1.60**	**126.7**	**1722.7**	**4.0**
51	3.8	1.56	133.5	710.3	3.3
52	6.4	1.59	134.6	405.4	3.0
53	**1.0**	**1.46**	**120.0**	**3198.8**	**10.9**
54	2.0	1.60	120.0	1414.7	3.8
55	3.3	1.59	126.6	861.7	2.9
56	**7.7**	**1.59**	**135.8**	**315.4**	**1.9**
57	**1.8**	**1.60**	**120.0**	**1585.7**	**3.7**
58	**3.6**	**1.57**	**120.7**	**763.3**	**2.6**
59	1.3	1.59	122.0	2317.9	6.1
60	2.9	1.60	122.9	955.8	2.9
61	3.3	1.55	120.6	873.3	3.4
62	**1.9**	**1.59**	**128.1**	**1468.3**	**3.7**
63	1.0	1.59	130.1	3001.4	7.5
64	**1.2**	**1.59**	**134.4**	**2441.9**	**6.0**
65	5.7	1.59	133.2	485.8	3.5
66	2.5	1.58	134.6	1127.4	3.7
67	**1.2**	**1.60**	**149.8**	**2239.8**	**5.7**
68	1.0	1.60	150.0	2767.7	6.9
69	**2.5**	**1.60**	**120.0**	**1093.2**	**2.9**
70	1.7	1.58	120.2	1734.1	4.8
71	**4.1**	**1.58**	**121.4**	**656.9**	**2.1**
72	1.0	1.58	149.8	2783.0	6.8
73	**2.4**	**1.60**	**120.0**	**1162.5**	**3.4**
74	**1.0**	**1.60**	**121.3**	**3009.2**	**7.4**
75	**1.6**	**1.60**	**125.1**	**1776.2**	**4.5**
76	7.2	1.58	142.5	341.3	2.3
77	1.4	1.60	120.0	1942.6	5.5
78	2.7	1.60	122.7	1053.1	3.1
79	1.2	1.57	123.3	2598.4	6.8
80	1.9	1.59	125.3	1454.4	4.4

7.4.6 *In Silico* Multi-Objective Test Problems

7.4.6.1 VdV1 Test Problem

$$minimise[-\ln(\%\,\boldsymbol{B}),\ln(STY)] \tag{50}$$

subject to: Residence time/min ∈ [0.5, 10]

Temperature/°C ∈ [25, 100]

[**A**]/M = 1

(i)

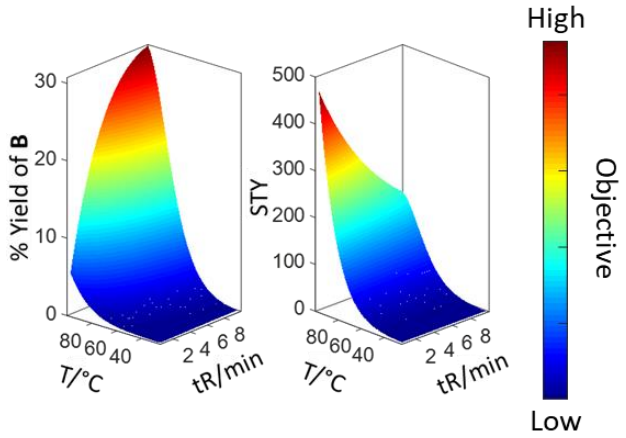

(ii)

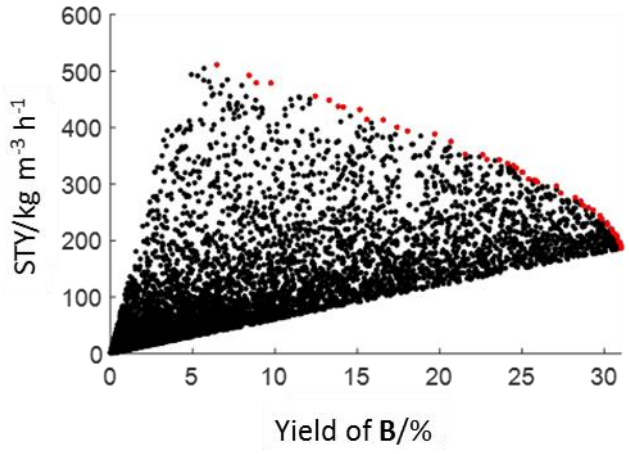

Figure 78. Graphical representations of the VdV1 test problem: (i) variable space; (ii) objective space. Black dots = possible solutions, red dots = non-dominated solutions.

Table 23. List of simulated experiments for the VdV1 test problem, showing changes in average hypervolume (20 runs) with an increasing number of evaluations for 5 different multi-objective algorithms.

	Average Hypervolume				
Experiment	**TSEMO**	**BS-TSEMO**	**NSGA-II**	**ParEGO**	**EIM-EGO**
1	0.874	0.204	0.000	4.440	0.671
2	2.479	0.901	0.977	6.079	3.520
3	3.726	1.481	2.894	7.839	6.631
4	4.263	2.325	3.292	8.739	8.129
5	5.976	4.103	5.816	11.061	9.531
6	7.517	5.754	6.328	11.870	10.678
7	8.914	7.046	8.014	13.785	12.298

8	10.314	7.796	9.328	16.531	13.973
9	10.345	9.337	10.236	18.484	14.005
10	10.333	10.235	10.981	18.633	14.176
11	10.355	13.175	11.734	19.161	15.172
12	11.408	13.413	13.973	19.201	15.164
13	13.330	13.849	14.922	19.218	17.101
14	14.403	13.918	15.745	20.319	17.042
15	15.153	14.284	16.181	20.361	17.750
16	15.271	16.165	16.672	20.487	17.798
17	16.326	17.292	17.087	21.712	19.558
18	19.529	18.772	19.318	21.941	20.255
19	21.605	19.573	20.130	21.956	20.929
20	21.665	20.085	20.212	23.097	21.667
21	24.073	24.317	20.158	24.821	28.110
22	26.096	25.626	20.236	30.520	32.442
23	30.630	26.837	20.149	34.335	37.610
24	33.733	27.528	20.191	36.758	41.595
25	35.127	29.990	20.145	40.273	43.609
26	36.378	30.693	20.158	42.547	44.766
27	37.556	31.532	20.147	44.670	46.124
28	38.691	31.949	20.153	46.401	46.956
29	39.387	32.958	20.271	48.753	48.126
30	40.270	33.569	20.487	49.385	48.883
31	41.178	34.060	20.562	50.406	49.923
32	41.795	35.569	20.611	50.687	50.361
33	42.243	36.289	20.649	51.512	50.915
34	42.852	37.692	20.812	51.983	51.182
35	43.384	38.403	20.796	52.380	51.720
36	43.605	38.691	21.197	52.722	52.122
37	43.744	39.015	21.257	53.282	52.727
38	44.073	39.370	21.659	53.405	52.973
39	44.456	39.860	21.893	53.492	53.326
40	44.804	41.010	22.237	53.840	53.515
41	45.458	41.790	22.210	53.836	53.658
42	45.507	42.512	22.225	54.123	53.953
43	45.718	42.860	22.244	54.196	54.071
44	45.818	42.929	22.253	54.165	54.325
45	46.056	44.087	22.280	54.496	54.398
46	46.762	44.536	22.236	54.526	54.650
47	47.009	44.946	22.278	54.621	54.728
48	47.439	45.447	22.287	54.792	55.264
49	48.010	46.199	22.239	54.992	55.341
50	48.360	46.769	22.756	55.160	55.445
51	48.578	46.998	22.880	55.296	55.561
52	48.736	47.382	23.129	55.408	55.673
53	48.988	47.784	23.284	55.580	55.834
54	49.137	48.006	23.333	55.640	55.855
55	49.307	48.381	23.475	55.723	55.921
56	49.528	48.661	25.106	55.815	56.050
57	49.842	48.749	25.717	55.985	56.021
58	50.100	49.234	25.909	56.027	56.126
59	50.201	49.557	26.025	56.125	56.133
60	50.287	49.532	26.257	56.346	56.178
61	50.332	50.127	26.290	56.453	56.230

62	50.561	50.285	26.363	56.495	56.309
63	50.735	50.968	26.264	56.637	56.429
64	50.873	51.109	26.297	56.781	56.535
65	51.076	52.003	26.339	56.896	56.507
66	51.322	52.213	26.283	56.962	56.677
67	51.704	52.393	26.250	57.044	56.689
68	51.750	52.674	26.960	57.077	56.679
69	52.285	52.764	27.169	57.018	56.890
70	52.620	52.951	27.252	57.067	56.918
71	52.776	53.058	27.472	57.133	56.913
72	52.813	53.133	27.714	57.212	57.022
73	53.000	53.273	27.982	57.215	56.999
74	53.154	53.586	28.302	57.248	57.064
75	53.261	53.671	28.503	57.251	57.091
76	53.427	53.767	28.551	57.405	57.221
77	53.674	53.974	28.615	57.400	57.244
78	53.887	54.032	28.825	57.403	57.281
79	53.969	54.354	28.831	57.416	57.284
80	54.121	54.471	29.014	57.484	57.303
81	54.237	54.533	28.980	57.446	57.339
82	54.244	54.766	28.969	57.468	57.423
83	54.299	54.799	29.034	57.532	57.475
84	54.483	54.898	29.058	57.606	57.421
85	54.537	55.191	29.001	57.627	57.440
86	54.636	55.275	28.984	57.682	57.486
87	54.816	55.364	29.037	57.735	57.589
88	55.024	55.671	28.935	57.823	57.610
89	55.114	55.715	29.011	57.806	57.632
90	55.221	55.840	28.980	57.799	57.596
91	55.401	55.902	29.001	57.813	57.697
92	55.279	55.964	28.972	57.888	57.641
93	55.412	56.027	28.972	57.832	57.663
94	55.466	56.075	28.994	57.893	57.721
95	55.673	56.215	28.973	57.904	57.732
96	55.975	56.218	28.977	57.944	57.750
97	55.959	56.480	28.984	57.914	57.760
98	56.086	56.531	29.006	57.953	57.745
99	56.193	56.651	29.046	57.934	57.812
100	56.368	56.774	29.044	58.051	57.932

Table 24. Statistics describing the performance of 5 multi-objective algorithms for the VdV1 test problem (20 runs). LQ = lower quartile, UQ = upper quartile.

	Hypervolume @ Experiment 60				
Statistic	**TSEMO**	**BS-TSEMO**	**NSGA-II**	**ParEGO**	**EIM-EGO**
Min	40.223	28.469	7.933	53.217	50.874
LQ	46.146	45.753	20.505	56.111	55.289
Median	49.756	51.241	24.799	56.451	57.095
UQ	56.575	56.413	35.305	57.186	57.517
Max	58.110	58.043	43.999	57.656	58.884

7.4.6.2 SNAr1 Test Problem

$$minimise[-\ln(\%\ \mathbf{3.18}), \ln(\%\ \mathbf{3.19}), \ln(\%\ \mathbf{3.20})] \quad (51)$$

subject to:

Residence time/min ∈ [0.5, 20]

Temperature/°C ∈ [60, 140]

[**3.16**]/M = 1

[**3.17**]/M = 3

(i)

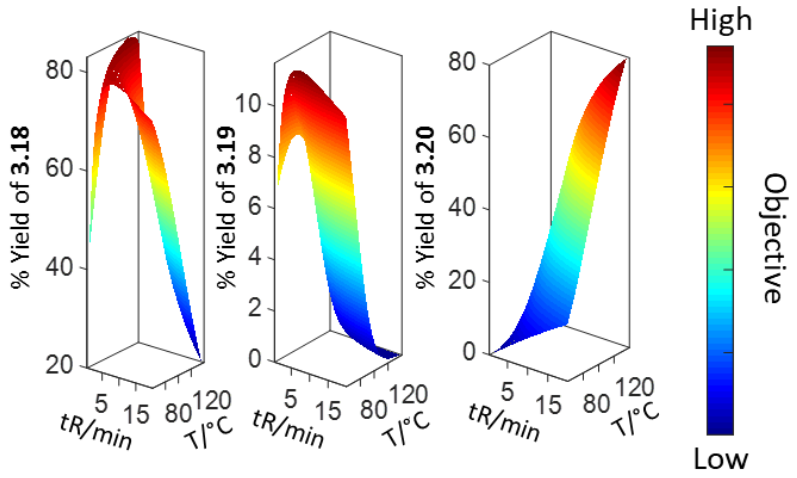

(ii)

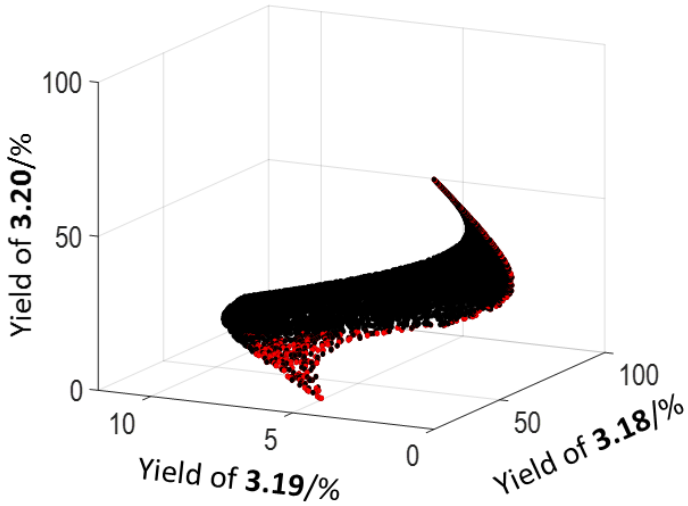

Figure 79. Graphical representations of the SNAr1 test problem: (i) variable space; (ii) objective space. Black dots = possible solutions, red dots = non-dominated solutions.

Table 25. List of simulated experiments for the SNAr1 test problem, showing changes in average hypervolume (20 runs) with an increasing number of evaluations for 5 different multi-objective algorithms.

	Average Hypervolume				
Experiment	**TSEMO**	**BS-TSEMO**	**NSGA-II**	**ParEGO**	**EIM-EGO**
1	17.580	19.124	5.963	15.367	20.616
2	29.510	34.706	21.239	27.993	31.235
3	35.446	39.469	32.507	37.005	36.563
4	41.089	43.924	39.178	43.583	43.101
5	45.645	47.251	42.037	46.166	45.796
6	47.974	50.050	44.185	49.507	46.457
7	49.653	51.596	45.913	51.204	49.450
8	50.410	52.479	47.577	52.672	50.267
9	53.028	53.794	50.246	53.204	52.899
10	53.955	54.267	51.504	53.526	54.830
11	54.724	55.842	54.699	55.689	55.123
12	55.769	56.572	56.064	56.615	56.282
13	56.971	57.281	56.767	57.162	57.467
14	58.113	58.989	58.032	57.924	58.579
15	58.774	59.793	59.086	58.295	58.795
16	59.911	60.525	59.982	58.971	59.170
17	60.493	60.956	60.510	59.238	59.978
18	60.910	62.033	61.106	59.311	61.301
19	61.501	62.955	61.509	60.484	61.486
20	61.796	63.194	61.853	60.688	61.876
21	63.099	64.325	61.833	61.535	63.110
22	64.027	65.477	61.872	63.157	63.888
23	66.316	66.265	61.845	64.233	64.773
24	67.352	66.676	61.815	64.444	65.376
25	67.936	67.942	61.852	65.142	65.975
26	69.577	68.398	61.835	65.268	66.903
27	70.032	68.718	61.861	66.339	67.435
28	70.695	68.887	61.884	66.474	67.895
29	71.741	69.521	61.880	66.929	68.078
30	71.898	69.794	61.857	67.673	68.222
31	72.304	70.485	61.932	68.300	68.307
32	72.690	70.675	62.011	68.515	68.755
33	72.933	71.264	62.012	68.601	69.186
34	72.951	71.598	62.564	68.742	69.295
35	73.170	71.775	62.739	69.189	69.438
36	73.624	71.823	62.771	69.182	70.498
37	73.804	72.411	63.039	69.301	70.587
38	73.920	72.444	63.013	69.469	70.685
39	74.040	72.524	63.292	69.661	71.145
40	74.238	72.770	63.447	69.740	71.313
41	74.417	72.996	63.482	69.852	71.547
42	74.615	73.654	63.559	69.880	71.744
43	74.809	73.736	63.525	69.994	72.147
44	74.905	73.899	63.495	70.194	72.181
45	75.093	74.023	63.509	70.136	72.220
46	75.370	74.216	63.496	70.362	72.291
47	75.539	74.458	63.449	70.502	72.414
48	75.599	74.565	63.497	70.792	72.445

49	75.859	74.752	63.446	70.791	72.833
50	75.915	74.843	63.443	70.984	72.920
51	75.966	74.994	63.470	71.064	72.930
52	76.044	75.020	63.492	71.565	72.951
53	76.064	75.048	63.516	71.581	73.204
54	76.450	75.194	63.500	71.596	73.354
55	76.416	75.223	63.616	71.744	73.413
56	76.556	75.699	63.811	71.714	73.434
57	76.725	75.744	63.802	72.082	73.461
58	76.860	75.837	63.856	72.067	73.560
59	76.991	76.010	64.132	72.119	73.581
60	77.023	76.099	64.159	72.202	73.810
61	77.178	76.365	64.148	72.247	73.866
62	77.158	76.314	64.072	72.315	73.932
63	77.174	76.379	64.160	72.315	74.090
64	77.201	76.387	64.070	72.349	74.076
65	77.264	76.425	64.179	72.530	74.150
66	77.242	76.468	64.092	72.502	74.322
67	77.303	76.510	64.087	72.500	74.576
68	77.357	76.696	64.124	72.508	74.606
69	77.418	76.812	64.118	72.490	74.663
70	77.473	76.847	64.087	72.651	74.764
71	77.548	76.866	64.135	72.668	74.842
72	77.523	76.954	64.196	72.661	74.996
73	77.586	76.918	64.194	72.797	75.027
74	77.640	77.159	64.216	72.789	75.100
75	77.605	77.237	64.328	72.923	75.147
76	77.634	77.286	64.447	73.023	75.240
77	77.728	77.283	64.500	72.965	75.276
78	77.751	77.350	64.641	73.084	75.294
79	77.788	77.472	64.655	73.069	75.332
80	77.750	77.447	64.710	73.202	75.374
81	77.762	77.476	64.641	73.234	75.369
82	77.833	77.490	64.678	73.378	75.358
83	77.875	77.512	64.728	73.424	75.465
84	77.824	77.492	64.679	73.396	75.638
85	77.958	77.593	64.716	73.459	75.696
86	77.921	77.579	64.666	73.449	75.776
87	77.945	77.591	64.672	73.867	75.790
88	77.993	77.588	64.646	73.796	75.883
89	77.981	77.760	64.672	73.849	75.978
90	77.979	77.823	64.704	74.093	76.032
91	78.034	77.873	64.679	74.073	76.173
92	77.987	77.876	64.692	74.140	76.210
93	78.035	77.900	64.703	74.176	76.231
94	77.996	77.990	64.666	74.191	76.285
95	78.042	78.015	64.626	74.198	76.321
96	78.132	78.101	64.701	74.254	76.318
97	78.108	78.111	64.714	74.318	76.396
98	78.194	78.151	64.714	74.264	76.525
99	78.230	78.173	64.720	74.348	76.528
100	78.266	78.237	64.654	74.376	76.555

Table 26. Statistics describing the performance of 5 multi-objective algorithms for the SNAr1 test problem (20 runs). LQ = lower quartile, UQ = upper quartile.

	Hypervolume @ Experiment 60				
Statistic	**TSEMO**	**BS-TSEMO**	**NSGA-II**	**ParEGO**	**EIM-EGO**
Min	74.419	72.810	53.372	62.485	70.382
LQ	75.925	75.119	59.482	71.701	72.191
Median	77.122	76.107	66.405	72.962	73.718
UQ	78.131	77.184	68.150	74.514	75.702
Max	79.845	78.553	73.593	75.923	77.106

7.4.6.3 SNAr2 Test Problem

$$minimise[\ln(\%\,\mathbf{3.19}), -\ln(RME), -\ln(STY)] \quad (52)$$

subject to:

Residence time/min ∈ [0.5, 2]

Temperature/°C ∈ [60, 140]

[**3.16**]/M ∈ [0.1, 2.0]

[**3.17**]/M ∈ [2, 5]

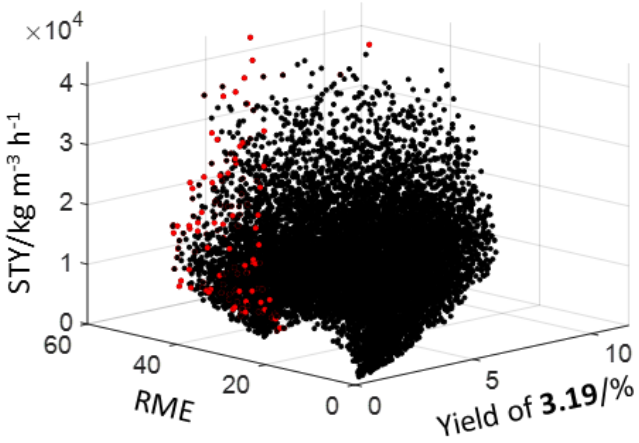

Figure 80. Graphical representations of the objective space for the SNAr2 test problem. Black dots = possible solutions, red dots = non-dominated solutions.

Table 27. List of simulated experiments for the SNAr2 test problem, showing changes in average hypervolume (20 runs) with an increasing number of evaluations for 5 different multi-objective algorithms.

	Average Hypervolume				
Experiment	**TSEMO**	**BS-TSEMO**	**NSGA-II**	**ParEGO**	**EIM-EGO**
1	3.415	3.681	0.501	4.414	3.080
2	6.747	5.550	5.570	6.880	5.072
3	8.856	7.826	7.192	10.095	7.735
4	12.249	11.146	10.968	11.873	9.712
5	13.298	14.773	12.643	14.327	12.083
6	16.167	15.615	13.682	15.522	12.666

7	17.732	16.803	14.190	16.858	14.283
8	18.835	17.260	16.635	18.381	16.393
9	20.734	19.728	17.479	19.627	19.999
10	22.195	21.227	18.570	21.225	20.563
11	22.793	21.937	19.217	21.614	21.081
12	23.019	22.337	19.528	22.456	22.004
13	23.740	22.590	20.567	22.720	22.916
14	24.423	23.379	23.067	23.392	23.623
15	24.555	23.654	24.392	23.871	24.085
16	24.871	23.830	24.709	24.319	24.838
17	25.862	24.545	25.292	25.803	24.919
18	26.353	25.030	25.530	26.218	25.587
19	26.676	25.334	25.845	27.191	26.381
20	26.786	25.744	26.434	28.010	26.781
21	31.823	31.740	26.426	38.698	31.528
22	38.664	36.174	26.398	41.392	35.714
23	41.207	38.023	26.376	42.591	39.799
24	44.662	38.735	26.388	44.345	43.460
25	48.371	42.973	26.458	47.906	47.241
26	51.742	46.077	26.402	51.500	50.590
27	54.729	49.320	26.397	52.105	53.003
28	56.808	50.780	26.366	57.146	54.085
29	57.365	53.692	26.444	58.990	54.558
30	60.055	55.282	26.430	61.617	57.484
31	61.516	56.735	26.469	64.859	58.301
32	62.814	57.260	26.510	64.963	59.997
33	63.184	59.080	26.798	66.607	61.464
34	64.246	60.249	27.027	67.114	63.602
35	65.025	60.797	27.062	67.483	64.122
36	65.520	62.462	27.083	67.692	65.200
37	66.364	63.530	27.321	68.348	65.852
38	68.809	64.487	29.135	68.472	67.602
39	69.786	65.129	30.064	68.821	68.084
40	70.016	65.764	30.458	69.170	68.384
41	70.468	67.696	30.466	69.372	69.758
42	70.727	68.368	30.480	69.500	70.421
43	71.048	68.717	30.403	69.907	70.659
44	71.698	68.945	30.435	70.628	70.941
45	72.196	70.877	30.453	70.751	71.285
46	72.670	71.584	30.479	71.271	71.544
47	73.177	71.936	30.438	71.371	72.298
48	73.671	72.363	30.463	71.598	72.480
49	74.118	72.845	30.448	71.653	72.884
50	74.226	73.239	30.419	72.888	73.169
51	74.538	73.432	30.432	73.228	73.426
52	74.831	73.509	30.722	73.353	73.755
53	74.922	74.094	30.674	73.561	73.986
54	75.135	74.287	30.860	73.975	74.123
55	75.550	74.699	30.977	74.099	74.415
56	75.673	74.784	31.084	74.564	74.747
57	75.742	75.172	31.454	74.970	75.004
58	75.978	75.531	31.485	75.151	75.256
59	76.159	75.780	31.636	75.255	75.496
60	76.216	76.125	31.945	75.315	75.536

61	76.353	76.701	32.011	75.403	75.778
62	76.494	76.757	31.919	75.437	75.859
63	76.571	77.092	32.007	75.723	75.959
64	76.677	77.211	31.982	75.703	76.240
65	77.062	77.415	31.985	75.772	76.312
66	77.356	77.479	31.998	75.832	76.406
67	77.495	77.496	31.938	75.980	76.655
68	77.550	77.724	31.959	76.088	76.679
69	77.597	77.851	32.001	76.203	76.993
70	77.675	77.828	31.995	76.174	76.987
71	77.798	78.150	32.085	76.357	77.150
72	77.887	78.215	32.156	76.546	77.245
73	77.999	78.308	32.188	76.477	77.458
74	78.134	78.398	32.305	76.576	77.468
75	78.151	78.449	32.319	76.628	77.604
76	78.209	78.558	32.487	76.611	77.784
77	78.379	78.671	32.536	76.680	77.895
78	78.507	78.750	32.793	76.724	77.918
79	78.665	78.770	32.903	76.775	78.060
80	78.767	78.885	33.160	76.725	78.116
81	78.978	78.980	33.082	76.760	78.254
82	79.037	79.125	33.194	76.802	78.359
83	79.127	79.213	33.148	76.924	78.437
84	79.141	79.209	33.128	76.971	78.520
85	79.227	79.271	33.129	76.979	78.649
86	79.286	79.389	33.129	77.029	78.624
87	79.339	79.412	33.053	77.081	78.761
88	79.424	79.518	33.090	77.162	78.831
89	79.470	79.605	33.129	77.140	78.790
90	79.550	79.616	33.132	77.233	78.851
91	79.626	79.721	33.156	77.247	78.900
92	79.657	79.829	33.112	77.258	78.934
93	79.692	79.943	33.059	77.338	79.003
94	79.722	79.944	33.034	77.306	79.001
95	79.764	80.016	33.127	77.371	79.080
96	79.775	80.050	33.165	77.366	79.161
97	79.987	80.163	33.098	77.440	79.131
98	80.005	80.182	33.088	77.384	79.253
99	80.015	80.274	33.099	77.437	79.280
100	80.111	80.287	33.138	77.490	79.349

Table 28. Statistics describing the performance of 5 multi-objective algorithms for the S_NAr2 test problem (20 runs). LQ = lower quartile, UQ = upper quartile.

	Hypervolume @ Experiment 60				
Statistic	**TSEMO**	**BS-TSEMO**	**NSGA-II**	**ParEGO**	**EIM-EGO**
Min	64.381	69.104	17.235	62.239	69.264
LQ	75.194	74.750	23.325	74.199	73.751
Median	76.840	77.065	32.032	76.375	75.505
UQ	78.234	77.952	38.557	77.433	77.626
Max	80.343	79.720	47.638	79.114	79.396

7.4.6.4 Lactose1 Test Problem

$$minimise[-\ln(\%\,\mathbf{3.22}), \ln(\%\,\mathbf{3.23})] \quad (53)$$

subject to: Residence time/min ∈ [0.5, 10]

Temperature/°C ∈ [25, 100]

$[\mathbf{3.21}]/\mathrm{M} = 1$

(i)

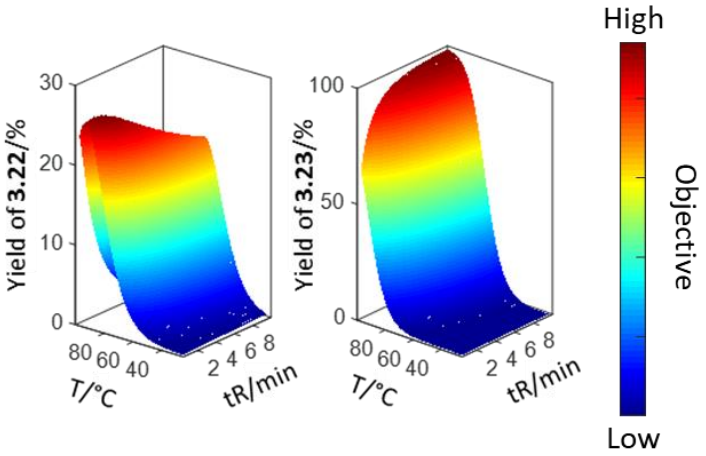

(ii)

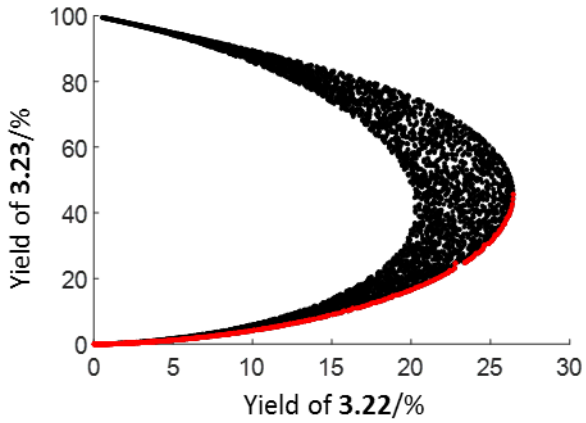

Figure 81. Graphical representations of the Lactose1 test problem: (i) variable space; (ii) objective space. Black dots = possible solutions, red dots = non-dominated solutions.

Table 29. List of simulated experiments for the Lactose1 test problem, showing changes in average hypervolume (20 runs) with an increasing number of evaluations for 5 different multi-objective algorithms.

	Average Hypervolume				
Experiment	**TSEMO**	**BS-TSEMO**	**NSGA-II**	**ParEGO**	**EIM-EGO**
1	20.994	22.299	0.064	12.090	12.911
2	29.239	31.922	11.413	20.616	23.178
3	37.443	42.419	21.925	27.741	32.586
4	43.191	44.265	34.176	40.602	40.128
5	46.848	48.798	44.624	43.800	43.760

6	51.229	52.579	48.717	51.106	53.551
7	54.247	55.145	52.689	55.315	55.948
8	58.335	57.312	54.871	56.390	58.920
9	59.379	59.934	56.668	59.129	59.717
10	60.174	61.304	57.479	60.561	60.529
11	61.440	62.950	58.425	62.315	62.826
12	61.813	64.691	59.693	64.299	63.001
13	62.321	65.073	60.195	64.778	63.844
14	62.890	65.731	61.592	65.668	65.123
15	64.639	66.019	62.104	66.344	66.085
16	66.555	66.627	63.085	67.613	66.445
17	67.156	66.909	64.945	68.370	66.866
18	67.645	67.171	66.415	68.908	67.585
19	68.375	67.764	66.575	69.186	68.231
20	68.700	69.082	67.621	69.407	68.686
21	69.235	69.465	67.564	69.748	68.923
22	69.858	69.751	67.542	70.008	69.613
23	70.068	69.998	67.584	70.199	70.252
24	70.324	70.276	67.486	70.344	70.711
25	70.523	70.456	67.493	70.389	71.307
26	70.763	70.807	67.552	70.476	71.673
27	71.455	71.048	67.498	70.523	71.825
28	71.556	71.055	67.637	70.664	72.412
29	71.646	71.038	67.654	70.686	72.894
30	71.923	71.160	67.727	70.760	73.246
31	72.187	71.207	67.659	70.738	73.275
32	72.241	71.652	67.755	70.766	73.416
33	72.302	72.142	68.123	70.734	73.732
34	72.467	72.229	69.816	70.763	73.936
35	72.598	72.462	69.928	70.806	74.134
36	72.888	72.625	70.049	70.822	74.281
37	73.016	72.789	70.270	70.767	74.566
38	73.440	72.862	70.669	70.816	74.797
39	74.029	73.121	70.705	70.878	74.995
40	74.305	73.501	70.942	70.845	75.113
41	74.277	73.568	70.980	70.791	75.083
42	74.326	73.730	71.019	70.849	75.647
43	74.513	73.740	70.991	70.861	75.680
44	74.677	73.808	71.011	70.893	75.688
45	74.919	73.935	71.075	70.870	75.806
46	74.978	74.231	70.935	70.939	75.864
47	75.013	74.367	71.005	71.042	76.065
48	75.180	74.323	70.999	71.038	76.128
49	75.238	74.635	70.994	71.056	76.115
50	75.321	74.718	71.018	71.237	76.241
51	75.334	74.749	71.037	71.314	76.266
52	75.471	74.807	71.088	71.299	76.367
53	75.558	74.872	71.061	71.388	76.419
54	75.627	74.998	71.504	71.420	76.452
55	75.686	75.037	71.792	71.463	76.515
56	75.794	74.975	72.044	71.621	76.607
57	75.812	75.017	72.337	71.649	76.630
58	75.908	75.211	72.465	71.667	76.770
59	76.016	75.236	72.587	71.723	76.752

60	76.069	75.595	72.770	71.749	76.938
61	76.223	75.691	72.760	71.786	77.063
62	76.329	75.760	72.745	71.793	77.163
63	76.269	75.750	72.782	72.044	77.143
64	76.278	75.817	72.714	72.028	77.202
65	76.495	75.982	72.762	72.058	77.240
66	76.504	76.060	72.720	72.126	77.236
67	76.473	76.085	72.735	72.200	77.337
68	76.564	76.232	72.711	72.192	77.369
69	76.567	76.237	72.736	72.209	77.413
70	76.663	76.351	72.784	72.229	77.449
71	76.776	76.351	72.723	72.196	77.480
72	76.954	76.528	72.905	72.305	77.568
73	77.058	76.545	73.419	72.535	77.690
74	77.074	76.548	73.657	72.591	77.740
75	77.141	76.609	73.652	72.577	77.780
76	77.123	76.652	73.730	72.626	77.876
77	77.211	76.614	73.704	72.542	77.894
78	77.276	76.643	73.754	72.781	77.875
79	77.281	76.795	73.890	72.862	77.958
80	77.293	76.763	73.913	72.882	78.014
81	77.309	76.785	73.942	73.070	78.038
82	77.362	76.924	73.917	73.065	78.174
83	77.436	76.920	73.879	73.070	78.176
84	77.402	76.936	73.903	73.101	78.253
85	77.419	76.924	73.924	73.204	78.249
86	77.458	77.022	73.881	73.289	78.411
87	77.469	77.023	73.900	73.335	78.466
88	77.532	77.052	73.901	73.462	78.536
89	77.558	77.085	73.907	73.419	78.561
90	77.594	77.117	73.918	73.541	78.619
91	77.654	77.289	73.898	73.569	78.615
92	77.722	77.305	73.882	73.608	78.707
93	77.764	77.400	73.905	73.663	78.722
94	77.854	77.402	73.932	73.768	78.755
95	77.864	77.435	73.900	73.790	78.827
96	77.893	77.473	73.982	73.702	78.812
97	77.910	77.509	73.893	73.754	78.877
98	77.947	77.579	73.880	73.775	78.870
99	77.870	77.684	73.883	73.745	78.836
100	77.954	77.744	73.880	73.802	78.948

Table 30. Statistics describing the performance of 5 multi-objective algorithms for the Lactose1 test problem (20 runs). LQ = lower quartile, UQ = upper quartile.

	Hypervolume @ Experiment 60				
Statistic	**TSEMO**	**BS-TSEMO**	**NSGA-II**	**ParEGO**	**EIM-EGO**
Min	72.209	73.297	55.462	66.546	73.708
LQ	75.793	74.201	72.102	70.213	75.663
Median	76.534	75.382	73.492	71.738	77.325
UQ	77.258	77.018	74.874	73.076	78.056
Max	78.365	78.160	78.667	76.795	79.235

7.4.6.5 PK1 Test Problem

$$minimise[-\ln(STY), -\ln(RME)] \quad (54)$$

subject to:

Residence time/min ∈ [0.5, 2]

Equivalents of **3.25** ∈ [1, 10]

Temperature/°C = 50

[**3.24**]/M = 1

(i)

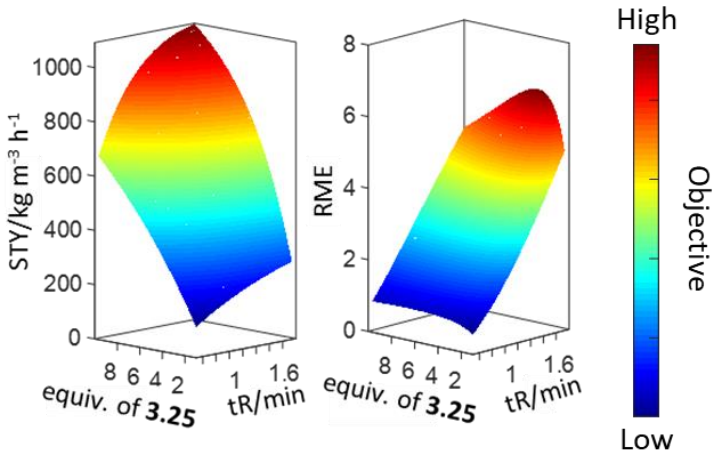

(ii)

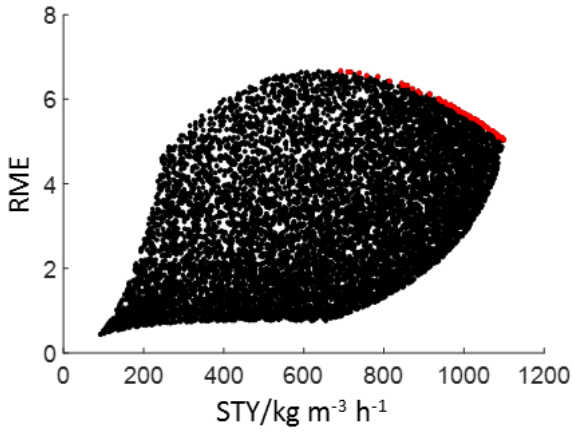

Figure 82. Graphical representations of the PK1 test problem: (i) variable space; (ii) objective space. Black dots = possible solutions, red dots = non-dominated solutions.

Table 31. List of simulated experiments for the PK1 test problem, showing changes in average hypervolume (20 runs) with an increasing number of evaluations for 5 different multi-objective algorithms.

	Average Hypervolume				
Experiment	**TSEMO**	**BS-TSEMO**	**NSGA-II**	**ParEGO**	**EIM-EGO**
1	10.495	10.191	0.000	5.387	6.393
2	19.892	16.785	5.447	13.056	14.002
3	21.360	22.190	15.835	17.445	21.368
4	25.468	24.784	19.783	21.264	25.328
5	26.631	27.343	23.799	26.672	32.199
6	27.973	31.226	26.785	30.144	35.210
7	35.191	35.031	30.277	34.259	39.549
8	36.675	40.252	30.285	39.036	43.893
9	38.159	45.092	30.952	41.393	44.952
10	41.093	47.456	34.141	44.718	46.726
11	42.933	48.249	35.842	46.566	46.798
12	45.572	48.814	39.204	49.496	47.388
13	47.162	49.899	40.400	49.849	48.822
14	47.180	51.324	43.418	50.228	50.427
15	48.101	52.925	44.239	51.055	50.807
16	49.012	53.218	44.952	52.648	51.839
17	49.348	53.977	46.368	54.919	55.008
18	50.556	54.838	48.531	55.310	56.293
19	50.528	54.967	49.103	55.527	56.355
20	54.847	55.735	50.001	56.616	56.754
21	59.819	58.787	50.061	64.176	62.514
22	62.364	60.804	50.025	68.442	65.534
23	65.456	61.124	49.984	70.500	67.986
24	67.184	61.577	50.069	71.827	71.471
25	68.803	64.183	50.024	73.558	73.324
26	70.143	65.642	50.014	74.363	74.287
27	71.879	66.241	50.008	75.064	75.454
28	72.210	67.045	50.164	76.321	76.504
29	73.431	69.492	50.455	77.021	76.824
30	73.840	70.216	50.642	77.503	77.512
31	74.601	70.725	50.849	78.259	77.921
32	75.214	71.155	51.029	78.495	78.506
33	75.485	72.396	51.343	78.713	78.694
34	76.040	73.301	51.880	78.873	78.995
35	76.423	73.808	52.803	79.196	79.178
36	76.972	74.414	53.047	79.295	79.475
37	77.333	75.285	53.259	79.436	79.690
38	77.760	75.669	53.488	79.515	79.780
39	78.128	76.225	54.545	79.716	80.012
40	78.223	76.330	55.367	79.848	80.121
41	78.358	76.760	55.335	80.145	80.181
42	78.750	77.097	55.331	80.183	80.387
43	78.942	77.219	55.299	80.375	80.447
44	79.159	77.421	55.450	80.405	80.556
45	79.315	77.930	55.406	80.562	80.554
46	79.455	78.237	55.347	80.607	80.585
47	79.664	78.498	55.365	80.672	80.642
48	79.720	78.548	55.432	80.688	80.711

49	79.888	79.130	55.580	80.745	80.786
50	80.065	79.377	55.850	80.874	80.851
51	80.202	79.624	55.890	80.886	81.115
52	80.333	79.655	56.346	80.950	81.169
53	80.411	79.767	56.502	81.042	81.323
54	80.578	80.017	56.938	81.122	81.284
55	80.645	80.089	57.257	81.154	81.406
56	80.947	80.257	57.983	81.232	81.490
57	81.072	80.488	58.174	81.302	81.537
58	81.187	80.639	58.283	81.312	81.599
59	81.348	80.678	58.493	81.335	81.728
60	81.507	80.741	59.164	81.364	81.753
61	81.532	80.858	59.181	81.444	81.903
62	81.707	80.935	59.142	81.516	81.913
63	81.800	81.068	59.122	81.487	82.031
64	81.908	81.135	59.115	81.548	82.095
65	81.970	81.106	59.122	81.530	82.136
66	82.020	81.250	59.222	81.570	82.217
67	82.044	81.248	59.111	81.620	82.240
68	82.174	81.329	59.172	81.683	82.288
69	82.225	81.490	59.197	81.670	82.297
70	82.282	81.501	59.152	81.722	82.419
71	82.269	81.577	59.189	81.796	82.465
72	82.308	81.681	59.419	81.749	82.594
73	82.385	81.704	59.415	81.790	82.633
74	82.364	81.709	59.923	81.773	82.683
75	82.469	81.774	60.182	81.791	82.725
76	82.521	82.003	60.648	81.805	82.791
77	82.536	82.062	61.061	81.792	82.858
78	82.608	82.061	61.735	81.812	82.933
79	82.670	82.077	62.255	81.805	83.013
80	82.663	82.110	62.696	81.798	82.988
81	82.694	82.219	62.644	81.793	83.089
82	82.745	82.223	62.651	81.862	83.077
83	82.785	82.281	62.656	81.791	83.194
84	82.778	82.310	62.655	81.826	83.179
85	82.865	82.347	62.667	81.810	83.229
86	82.884	82.382	62.665	81.923	83.303
87	82.975	82.457	62.640	81.876	83.313
88	82.970	82.494	62.698	81.881	83.329
89	82.982	82.518	62.676	81.911	83.381
90	82.986	82.645	62.614	81.926	83.394
91	83.004	82.670	62.615	81.924	83.442
92	83.015	82.703	62.665	81.935	83.532
93	83.034	82.785	62.640	81.962	83.493
94	83.064	82.781	62.716	81.987	83.544
95	83.099	82.806	62.688	81.930	83.512
96	83.141	82.842	62.695	82.005	83.594
97	83.184	82.885	62.672	81.979	83.562
98	83.188	82.862	62.615	81.980	83.601
99	83.172	82.909	62.684	82.037	83.611
100	83.284	82.985	62.641	82.011	83.610

Table 32. Statistics describing the performance of 5 multi-objective algorithms for the PK1 test problem (20 runs). LQ = lower quartile, UQ = upper quartile.

	Hypervolume @ Experiment 60				
Statistic	**TSEMO**	**BS-TSEMO**	**NSGA-II**	**ParEGO**	**EIM-EGO**
Min	80.360	77.958	33.177	78.630	80.302
LQ	80.913	80.140	57.005	80.606	81.005
Median	81.343	80.774	61.587	81.338	81.814
UQ	82.189	81.402	64.755	82.404	82.171
Max	82.805	82.625	74.047	82.890	83.895

7.4.6.6 PK2 Test Problem

$$minimise[\ln(\%\ \mathbf{3.26}), -\ln(STY)] \tag{55}$$

subject to:

Residence time/min ∈ [0.5, 2]

Temperature/°C ∈ [25, 150]

Equivalents of **3.25** ∈ [1, 10]

$[\mathbf{3.24}]/\mathrm{M} = 1$

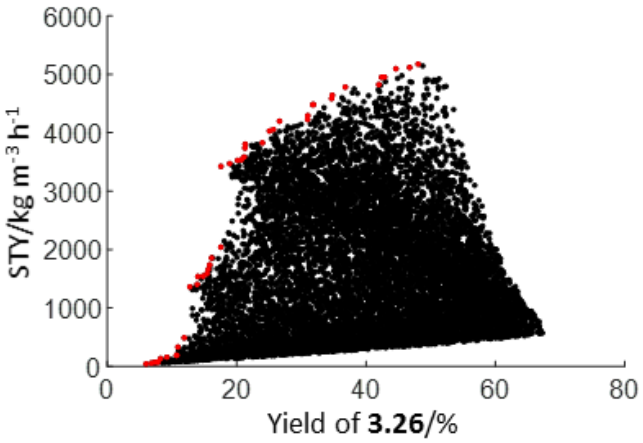

Figure 83. Graphical representations of the objective space for the PK2 test problem. Black dots = possible solutions, red dots = non-dominated solutions.

Table 33. List of simulated experiments for the PK2 test problem, showing changes in average hypervolume (20 runs) with an increasing number of evaluations for 5 different multi-objective algorithms.

	Average Hypervolume				
Experiment	**TSEMO**	**BS-TSEMO**	**NSGA-II**	**ParEGO**	**EIM-EGO**
1	7.647	5.400	1.704	5.686	8.458
2	14.359	11.031	11.656	15.037	15.735
3	19.872	15.286	15.404	17.233	19.619
4	21.979	20.152	23.177	22.321	23.153
5	25.247	23.027	25.703	25.080	26.296
6	27.162	28.071	28.204	31.276	28.931

7	27.739	29.268	29.288	32.925	30.428
8	28.596	30.682	32.199	33.962	30.762
9	29.396	32.079	34.113	34.142	32.527
10	31.256	34.158	35.389	34.705	34.119
11	33.476	34.845	36.332	36.171	35.955
12	33.884	36.224	37.339	36.922	36.504
13	35.067	36.996	37.741	38.083	37.158
14	35.463	37.402	38.087	38.711	38.759
15	36.115	38.452	38.226	38.888	39.145
16	36.729	38.716	39.411	39.411	39.840
17	37.269	39.792	39.729	40.110	40.737
18	38.297	40.068	39.951	40.348	41.806
19	38.966	40.989	40.132	40.968	42.103
20	40.465	41.862	40.457	41.346	42.207
21	43.205	44.712	40.446	48.107	44.690
22	44.919	46.638	40.466	49.502	47.608
23	47.394	47.552	40.491	50.650	50.106
24	49.110	47.838	40.430	52.944	53.462
25	50.716	49.347	40.463	53.471	55.245
26	51.529	50.262	40.379	54.422	56.459
27	52.760	51.124	40.353	54.887	57.814
28	53.272	51.635	40.437	55.830	59.214
29	53.954	52.702	40.437	56.015	60.529
30	54.944	53.322	40.459	56.202	61.278
31	55.302	54.004	40.644	57.035	61.758
32	55.900	54.592	40.800	57.716	62.160
33	56.278	55.729	40.978	58.434	62.720
34	56.565	55.918	41.150	58.844	63.178
35	57.293	56.476	41.282	59.046	63.576
36	57.878	56.807	41.485	59.196	63.967
37	57.985	57.357	41.640	59.479	64.240
38	58.278	57.605	42.108	59.777	64.676
39	58.496	57.852	43.460	59.859	64.868
40	58.779	58.390	43.642	60.064	65.137
41	58.972	58.618	43.665	60.494	65.248
42	59.191	58.903	43.633	60.660	65.489
43	59.583	59.016	43.604	61.127	65.596
44	59.724	59.149	43.630	61.061	65.614
45	60.133	59.469	43.586	61.080	65.796
46	60.580	59.620	43.639	61.288	66.012
47	60.794	59.830	43.661	61.301	66.031
48	60.877	60.144	43.636	61.376	66.049
49	61.336	60.483	43.653	61.339	66.191
50	61.761	60.611	43.663	61.463	66.299
51	62.128	61.047	43.735	61.556	66.282
52	62.214	61.450	43.829	61.644	66.276
53	62.328	62.000	43.853	61.622	66.358
54	62.879	62.188	43.884	61.637	66.429
55	63.106	62.262	44.454	61.673	66.557
56	63.215	62.376	44.438	61.930	66.584
57	63.331	62.590	44.516	62.006	66.596
58	63.568	63.005	44.897	62.240	66.653
59	63.626	63.007	45.120	62.397	66.617
60	63.732	63.315	45.113	62.689	66.750

61	63.923	63.541	45.183	62.769	66.765
62	64.104	63.927	45.202	62.765	66.744
63	64.092	64.089	45.203	62.771	66.805
64	64.446	64.146	45.163	62.864	66.775
65	64.589	64.263	45.208	62.974	66.818
66	64.856	64.297	45.166	62.978	66.848
67	64.891	64.399	45.181	63.130	66.838
68	65.046	64.503	45.125	63.143	66.816
69	65.167	64.537	45.229	63.281	66.884
70	65.264	64.748	45.217	63.205	66.957
71	65.336	64.952	45.190	63.389	66.978
72	65.303	65.057	45.267	63.371	66.939
73	65.384	65.184	45.366	63.409	66.959
74	65.508	65.302	45.370	63.399	67.029
75	65.641	65.389	45.523	63.650	67.072
76	65.656	65.401	45.452	63.576	67.099
77	65.830	65.446	45.534	63.785	67.080
78	66.030	65.586	45.613	63.797	67.019
79	65.981	65.670	45.668	63.978	67.157
80	66.119	65.731	45.867	63.906	67.152
81	66.187	65.980	45.868	64.075	67.118
82	66.256	66.104	45.819	64.125	67.115
83	66.252	66.250	45.878	64.342	67.217
84	66.341	66.266	45.902	64.506	67.235
85	66.357	66.375	45.938	64.503	67.205
86	66.519	66.479	45.900	64.527	67.196
87	66.569	66.458	45.891	64.531	67.238
88	66.593	66.534	45.887	64.568	67.209
89	66.781	66.559	45.837	64.588	67.227
90	66.799	66.639	45.829	64.562	67.247
91	66.871	66.687	45.923	64.535	67.300
92	67.003	66.684	45.868	64.617	67.250
93	67.040	66.714	45.863	64.586	67.282
94	67.129	66.834	45.926	64.704	67.323
95	67.157	66.869	45.887	64.671	67.308
96	67.201	66.968	45.837	64.756	67.270
97	67.221	66.881	45.793	64.771	67.285
98	67.289	67.057	45.944	64.857	67.290
99	67.284	67.057	45.894	64.761	67.296
100	67.346	67.126	45.938	64.803	67.372

Table 34. Statistics describing the performance of 5 multi-objective algorithms for the PK2 test problem (20 runs). LQ = lower quartile, UQ = upper quartile.

	Hypervolume @ Experiment 60				
Statistic	**TSEMO**	**BS-TSEMO**	**NSGA-II**	**ParEGO**	**EIM-EGO**
Min	58.166	59.500	29.748	55.219	65.540
LQ	63.624	62.471	41.815	59.507	66.275
Median	64.191	63.762	45.090	63.362	66.491
UQ	64.752	64.506	49.634	66.042	67.401
Max	65.592	65.869	55.291	67.493	67.843

7.5 Chapter 4 Procedures

7.5.1 Photochemical CSTR Cascade

The miniature CSTR was constructed with a stainless steel base equipped with a polyacetal lid. The reaction chamber was cylindrical with a 2 mL volume, containing a PTFE coated cross stirrer bar (10 mm diameter) to provide mechanical mixing on a conventional stirrer plate. A convex glass lens (viewing window) and PTFE gasket were clamped down between the base and lid using three bolts to form a seal. Three injection ports were drilled into the reaction chamber, offering the choice of one or two flow inlets. The CSTRs were connected using Polyfon PTFE tubing (1/8" OD, 1/16" ID) to form a cascade with a desired number of stages, *n*, and volume, *V*.

Irradiation of the reaction chambers was achieved using Engin LZ4-44UV00-0000 LEDs (365 nm, 2.9 W), clamped and positioned above each glass lens. Heat generated from the LEDs was dissipated through a combination of passive and convective cooling using heat sinks and CPU fans respectively. Stirring was achieved using a long-stage IKA RT 5 stirrer plate.

7.5.2 Chemicals

o-Nitrobenzaldehyde (98%, Aldrich), sodium tungstate dihydrate (≥99.0%, Sigma), tetra-*n*-butylammonium bromide (98%, Alfa Aesar), tetralin (≥97%, Fisher), benzophenone (≥99.0%, Fluka), 2-*tert*-butylanthraquinone (98%, Aldrich), α-tetralone (97%, Aldrich), 1,4-naphthoquinone (97%, Aldrich) and solvents (VWR) were purchased from suppliers and used without further purification. Tetra-*n*-butylammonium decatungstate (TBADT) was synthesised for use as a photocatalyst. Tetralin-1,4-dione was synthesised for characterisation purposes.

7.5.3 Synthesis of Tetra-*n*-butylammonium Decatungstate

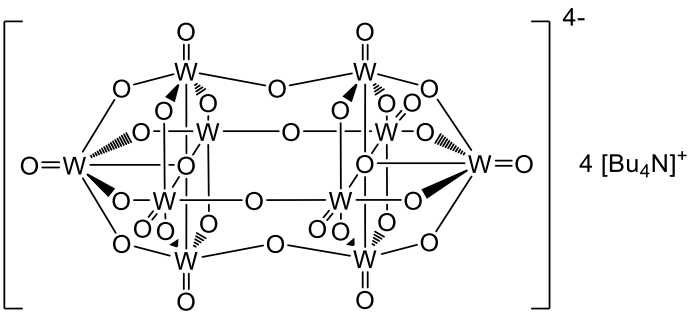

4.06

Tetra-*n*-butylammonium bromide (2.4 g, 7.44 mmol) and sodium tungstate dihydrate (5.0 g, 15.16 mmol) were each dissolved in deionised water (150 mL) in separate 250 mL conical flasks. The solutions were stirred vigorously and heated to 90 °C. Concentrated HCl was added dropwise to both solutions to achieve pH 2, after which the solutions were combined and maintained at 90 °C for 30 minutes. The reaction mixture was cooled to room temperature and the precipitate collected by filtration. The solid was washed with water and dried in an oven at 90 °C for 1.5 hours. After cooling to room temperature, the solid was suspended in DCM (20 mL per gram of solid) and stirred for 2 hours. The solid was then separated from the supernatant solution by filtration to yield TBADT **4.06** (2.66 g, 47%) as a white solid. The purity of the synthesised TBADT **4.06** was 92%, as evaluated by UV spectroscopy ($\varepsilon_{323} = 1.35 \times 10^4$ M^{-1} cm^{-1}). Furthermore, the UV spectrum was in good agreement with published data.[175]

7.5.4 Synthesis of Tetralin-1,4-dione

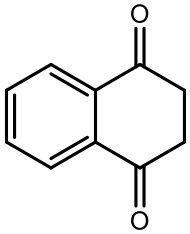

4.08

Tetralin **4.03** (27.5 mg, 0.21 mmol) and TBADT **4.06** (32.6 mg, 9.8×10^{-3} mmol) were dissolved in MeCN (5 mL) in a sample vial. The reaction mixture was irradiated under a 365 nm LED light and left to stir for 4 hours. The reaction mixture was concentrated *in vacuo* and the residue purified by column chromatography

(hexanes:EtOAc, 95:5) to yield an ≈15:1 mixture of tetralin-1,4-dione **4.08** (31.5 mg, 0.20 mmol) and 1,4-naphthoquinone **4.05** (2.1 mg, 0.01 mmol).

^{1}H NMR ($CDCl_3$, 500 MHz) δ 8.07-8.05 (m, 2H), 7.77-7.74 (m, 2H), 3.10 (s, 4H) ppm; in agreement with published data.[204]

7.5.5 Residence Time Distribution

The residence time distribution (RTD) was measured using a 1-. 3- and 5-stage pre-filled reactor with water pumped using a Harvard syringe pump at a flow rate of 4.0 mL min^{-1}. A pulse of 10% (v/v) red food dye was injected into the second inlet of the first CSTR using a six-port valve. Samples were collected from the reactor outlet every 30 seconds and the UV-Vis absorbance (516 nm) was measured using an offline spectrophotometer.

Table 35. Tracer absorbance values at different time points for a 1-, 3- and 5-stage CSTR. The normalised RTD function [$E(\theta)$] was calculated by dividing the absorbance values by the total area under the absorbance curves.

		Normalised RTD Function [$E(\theta)$]		
Entry	t_{res}/min	n = 1	n = 3	n = 5
1	0.3	0.628	0.215	0.052
2	0.8	0.274	0.686	0.215
3	1.3	0.131	0.761	0.683
4	1.8	0.050	0.556	0.971
5	2.3	0.018	0.363	0.939
6	2.8	0.009	0.206	0.799
7	3.3	0.005	0.111	0.509
8	3.8	0.003	0.065	0.328
9	4.3	0.003	0.039	0.213
10	4.8	0.002	0.023	0.154
11	5.3	0.001	0.014	0.104
12	5.8	0.001	0.010	0.086

7.5.6 Chemical Actinometry

The absorbed photon flux density of the reactor was determined using chemical actinometry. A solution of *o*-nitrobenzaldehyde **4.01** (1.56 g, 10.3 mmol, 0.10 mol L^{-1}, ϕ = 0.5) in methanol (100 mL) was pumped through the photochemical CSTR cascade (n = 2, V = 4 mL) at varying residence times, and conversion to *o*-nitrosobenzoic acid **4.02** monitored via on-line HPLC. HPLC mobile phases were **A** H_2O (18.2 MΩ), **B** MeCN, both buffered with 0.1% TFA. The method used was 5% **B** 1 min, 5% to 95% **B** 18 mins, 95% **B** 2 mins, 95% to 5% **B** 0.01 min, 5% **B** 0.99 min, flow rate 1.0 mL min^{-1}, column temperature 20 °C.

Table 36. Time profile for the conversion of *o*-nitrobenzaldehyde **4.01** to *o*-nitrosobenzoic acid **4.02** in the photochemical CSTR cascade.

Entry	t_{res}/min	[*o*-Nitrobenzaldehyde]/M
1	0.0	0.103
2	0.75	0.094
3	1.5	0.081
4	2.5	0.074
5	5.0	0.063
6	7.5	0.052
7	10	0.047

7.5.7 Experimental Set-Up

Reactor: photochemical CSTR cascade (n = 4, V = 8 mL), under ambient pressure. The flow of compressed air into the reactor was controlled using a Bronkhorst EL-FLOW prestige mass flow controller. A Zaiput SEP-10 gas-liquid membrane-based separator was placed downstream of the reactor, and fitted with a PTFE membrane (0.5 µm pore size). The permeate outlet was connected to the sample loop for analysis of the liquid phase.

For the oxidation reactions, the reservoir solutions were prepared by dissolving the desired reagents in solvent under stirring at ambient conditions. Pump 1: substrate (0.04 mol L^{-1}), photosensitiser (5-50 mol%) and biphenyl (0.0025 mol L^{-1}) in the desired solvent.

HPLC mobile phases were **A** H_2O (18.2 MΩ), **B** MeCN, both buffered with 0.1% TFA. The method used was 5% to 95% **B** 5 mins, 95% to 5% **B** 0.1 min, 5% **B** 1 min, flow rate 1.5 mL min^{-1}, column temperature 20 °C.

7.5.8 Full Factorial DoE

The two-level full factorial design was constructed using Umetrics MODDE (ver 12.1). Polynomial response surface models of the experiments were fitted by including all square and interaction terms then removing terms with a p-value less than 0.05. The models for tetralin **4.03** and α-tetralone **4.04** were transformed logarithmically ($\hat{y}_i = \log(y_i)/(100\text{-}y_i)$) to provide a more normal distribution. A square term was detected in the model for α-tetralone yield, therefore t_{res}*t_{res} was included. However, further experimentation would be required to more accurately define the square terms.

Table 37. Variables for the two-level full factorial design of experiments.

	Variables		
Limits	t_{res}/min	O_2 equiv.	Temp/°C
Lower	5	0.5	30
Upper	20	3.0	60

Table 38. List of results from the two-level full factorial design of experiments, including three centre point replicates.

Entry	t_{res}/min	O_2 equiv.	Temp/°C	Tetralin/%	α-Tetralone/%	Diketone/%
1	5.0	3.00	60	26.7	19.3	54.0
2	5.0	0.50	30	68.0	8.7	23.3
3	20.0	3.00	30	12.9	21.8	65.3
4	20.0	3.00	60	11.9	20.5	67.6
5	12.5	1.75	45	43.3	19.9	36.7
6	12.5	1.75	45	36.5	21.4	42.1
7	5.0	0.50	60	79.1	6.9	14.0
8	5.0	3.00	30	49.4	13.1	37.5
9	20.0	0.50	60	72.4	7.6	20.0
10	20.0	0.50	30	69.4	9.7	20.8
11	12.5	1.75	45	38.6	20.5	40.9

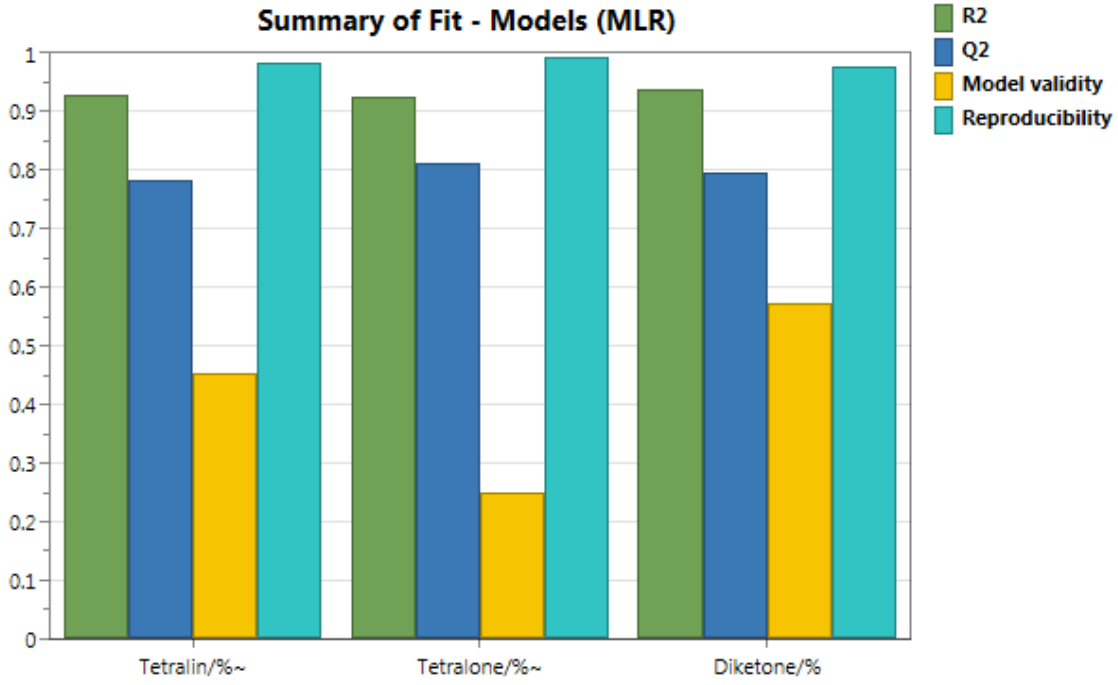

Figure 84. Summary of fit plots for tetralin **4.03**, α-tetralone **4.04** and diketone **4.08**. Tetralin: R^2 = 0.929, Q^2 = 0.784. α-Tetralone yield: R^2 = 0.927, Q^2 = 0.813. Diketone: R^2 = 0.937, Q^2 = 0.796. Reproducibility is determined from the centre points replicates, and determines the models sensitivity towards factor effects.

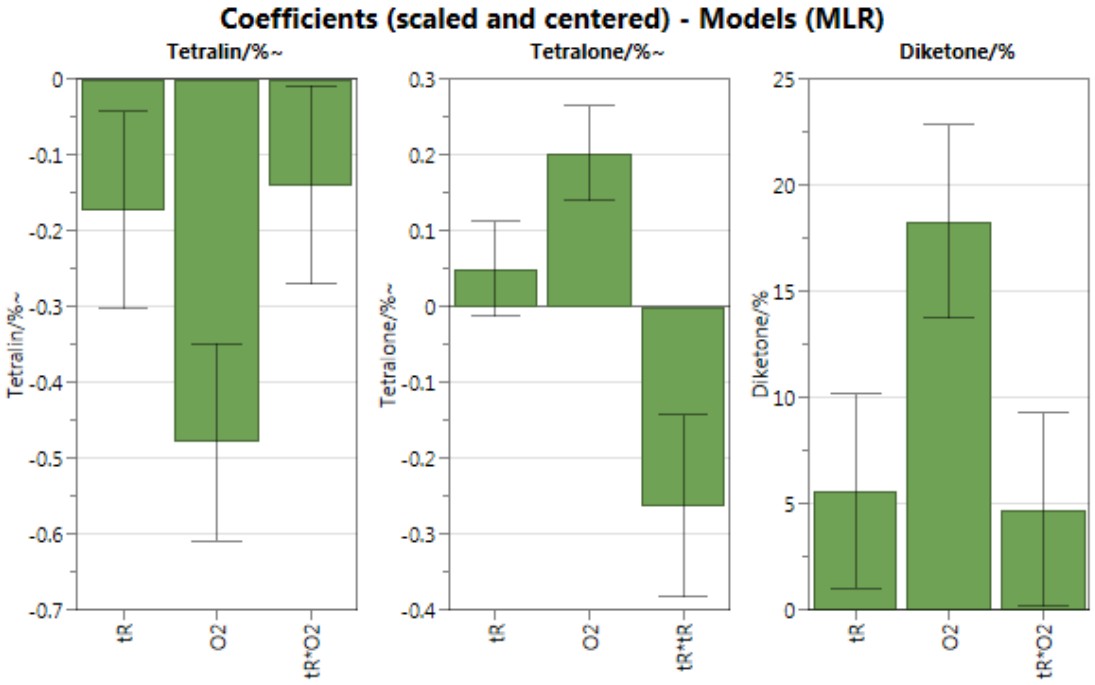

Figure 85. Coefficient plots for the models of tetralin **4.03**, α-tetralone **4.04** and diketone **4.08**. Insignificant terms (confidence interval crosses 0) were removed from the saturated model one at a time.

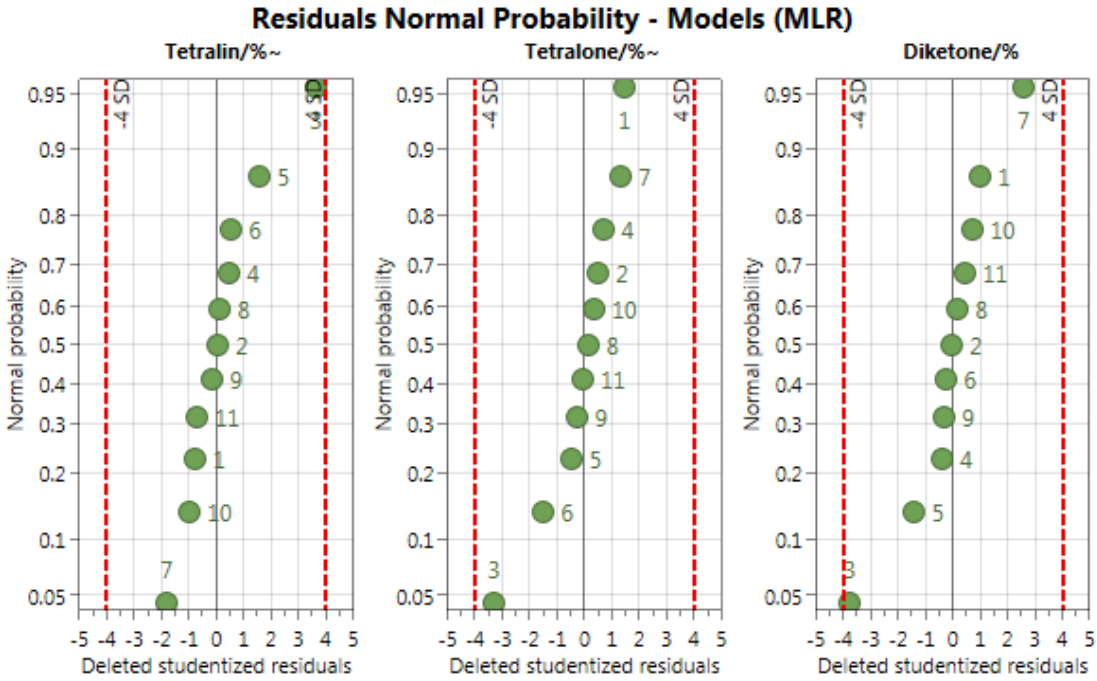

Figure 86. Residuals normal probability plots for tetralin **4.03**, α-tetralone **4.04** and diketone **4.08**. A straight diagonal line represents a normal distribution. Experiments outside of the 4 standard deviation limits represent outliers.

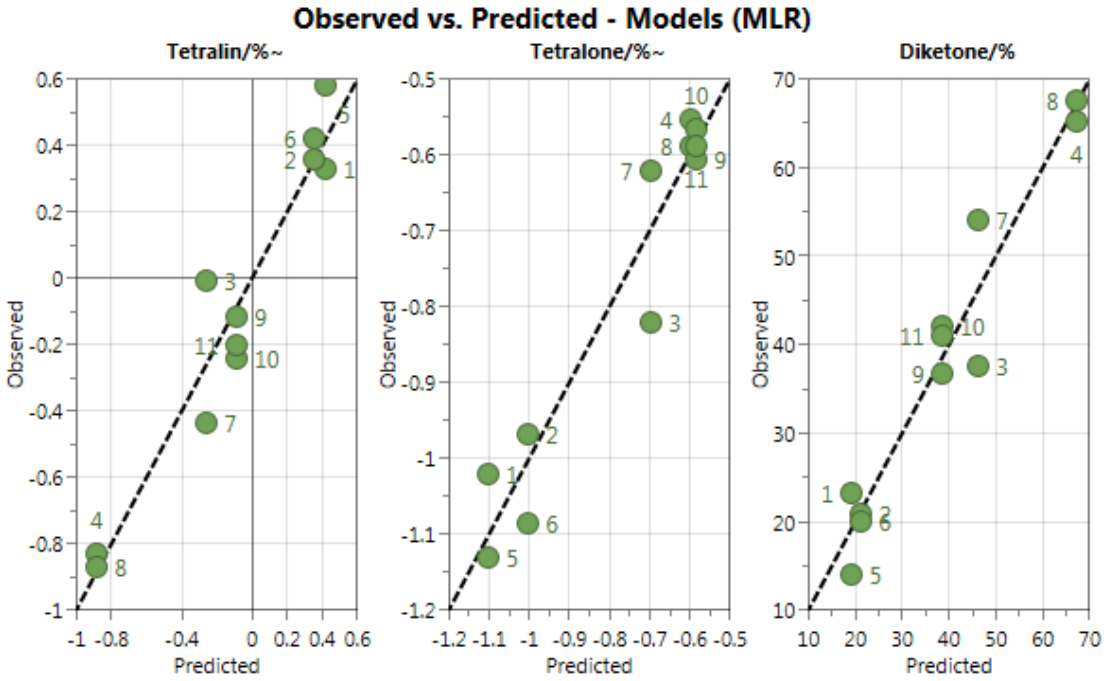

Figure 87. Plots of observed vs. experimental for the models of tetralin **4.03**, α-tetralone **4.04** and diketone **4.08**. A straight diagonal line indicates the model has a good fit to the experimental data.

7.5.9 Self-Optimisation Results

minimise[-(% of α-tetralone **4.04**)]

Table 39. Self-optimisation variables. Fixed parameters: benzophenone loading = 50 mol%, temperature = 25 °C.

	Variables	
Limits	t_{res}/min	O_2 equiv.
Lower	2.0	1.0
Upper	30.0	5.0

Table 40. List of results from the hybrid self-optimisation. SNOBFIT experiments are highlighted in yellow, Plackett-Burman screening experiments are highlighted in purple and CCF experiments are highlighted in orange. The global optimum is highlighted in bold.

Entry	t_{res}/min	O_2 equiv.	Tetralin/%	α-Tetralone/%	Diketone/%
1	24.8	2.69	59.4	43.3	16.2
2	2.1	2.46	8.7	7.7	1.0
3	13.4	4.93	41.5	33.2	8.3
4	8.3	1.14	17.4	11.5	5.9
5	18.5	1.37	37.2	24.6	12.6
6	29.9	4.28	64.7	44.8	19.9
7	6.0	4.86	57.5	48.4	9.1
8	21.1	4.54	62.4	53.5	9.0
9	18.9	3.58	63.7	55.9	7.8
10	25.0	5.00	70.9	59.4	11.6

11	8.9	5.00	63.8	55.1	8.7
12	24.9	3.81	67.6	54.6	13.0
13	20.7	3.25	63.7	51.5	12.2
14	23.7	4.76	71.0	60.5	10.5
15	**18.3**	**4.69**	**72.4**	**64.9**	**7.5**
16	9.1	5.00	60.0	51.7	8.3
17	9.3	3.14	39.7	29.7	10.1
18	15.0	1.37	33.9	22.7	11.2
19	18.2	5.00	55.9	43.3	12.6
20	6.5	5.00	55.4	47.5	7.9
21	23.0	5.00	61.9	50.7	11.2
22	12.9	2.47	45.8	36.7	9.1
23	13.6	3.38	54.1	47.7	6.4
24	18.3	3.54	60.0	50.6	9.5
25	7.3	5.00	52.1	43.2	8.9
26	20.7	2.36	53.3	39.5	13.7
27	19.1	4.19	65.0	57.1	7.9
28	24.4	4.74	73.1	60.8	12.3
29	8.1	5.00	60.7	51.4	9.3
30	9.3	2.14	31.1	20.8	10.2
31	15.6	4.44	59.9	54.9	5.0
32	18.2	3.98	64.5	56.8	7.7
33	24.4	5.00	72.8	61.9	11.0
34	24.2	1.70	50.8	30.2	20.5
35	17.7	4.57	64.9	58.3	6.6
36	24.4	5.00	71.5	61.2	10.3
37	24.1	4.42	74.9	63.9	11.0
38	12.6	4.13	58.2	50.4	7.9
39	2.0	1.63	5.7	5.1	0.6
40	2.0	4.69	10.3	7.3	3.0
41	18.3	1.63	42.9	27.4	15.5
42	18.3	4.69	72.4	64.9	7.5
43	8.5	3.96	48.1	39.2	9.0
44	8.5	4.98	46.5	34.7	11.9
45	15.4	3.96	59.5	51.2	8.3
46	15.4	4.98	66.5	61.9	4.7
47	18.9	3.69	64.4	53.7	10.8
48	18.9	3.74	64.4	53.5	10.9
49	19.4	3.69	63.6	52.9	10.7
50	19.4	3.74	65.6	53.7	11.8
51	18.3	3.69	59.6	45.2	14.5
52	18.3	4.69	68.6	63.1	5.5
53	19.4	3.69	63.1	55.5	7.7
54	19.4	4.69	67.7	61.2	6.5
55	18.3	4.19	67.2	60.4	6.8
56	19.4	4.19	67.3	58.1	9.2
57	18.9	3.69	64.5	53.5	11.0
58	18.9	4.69	68.6	59.7	8.9
59	18.9	4.19	66.6	60.3	6.3

7.6 Chapter 5 Procedures

7.6.1 Temperature Controlled CSTR Cascade

The miniature CSTRs were constructed according to section 7.5.1. Temperature control for automated experiments was achieved using a custom-built aluminium heating mantle, two nickel heating elements and a Eurotherm temperature controller.

The heat transfer to the CSTRs was determined using K-type thermocouple inserts positioned in contact with the fluid inside each reactor. To represent an optimisation process, a toluene/water mixture was pumped through the reactor whilst it was heated at 20 levels between 50 and 110 °C. The temperature of the fluid inside each reactor was continuously monitored (every second) using a PICO logger, and compared to the temperature recorded for the heating mantle. The optimisation procedure was modified for the inclusion of time delays to account for the heat transfer characteristics. A very good linear fit was observed between the average temperature of the CSTRs and the set temperature of the heating mantle, enabling the average process temperature to be easily determined.

Table 41. Thermocouple temperature recordings highlighting the heat transfer characteristics between the heating mantle and the fluid inside the CSTRs.

		Steady State Temp/°C				
Entry	Mantle Temp/°C	CSTR 1	CSTR 2	CSTR 3	CSTR 4	Average
1	52.6	49.4	49.1	49.9	50.1	49.6
2	55.7	52.5	51.8	52.6	52.9	52.4
3	57.2	53.2	53.1	54.1	54.4	53.7
4	61.4	57.5	56.9	58.2	56.5	57.3
5	63.0	58.5	58.3	59.6	58.9	58.8
6	66.0	60.2	60.8	62.3	61.8	61.3
7	68.5	63.9	62.9	64.6	64.0	63.9
8	71.4	66.0	65.5	67.3	66.8	66.4
9	74.8	69.1	68.5	70.5	70.0	69.5
10	77.1	71.8	70.6	72.6	72.0	71.7
11	81.3	75.1	74.2	76.3	75.9	75.4
12	84.5	77.1	77.1	79.3	78.9	78.1
13	88.9	80.4	81.0	83.3	83.1	81.9
14	89.8	82.7	81.8	84.1	83.8	83.1
15	94.3	86.6	85.7	88.2	87.9	87.1
16	95.2	86.2	86.4	89.0	88.8	87.6
17	98.3	91.1	89.2	91.9	91.6	91.0
18	102.3	93.8	92.7	95.5	95.3	94.3
19	104.7	95.6	94.9	97.8	97.7	96.5
20	108.1	97.6	97.9	100.8	100.8	99.3

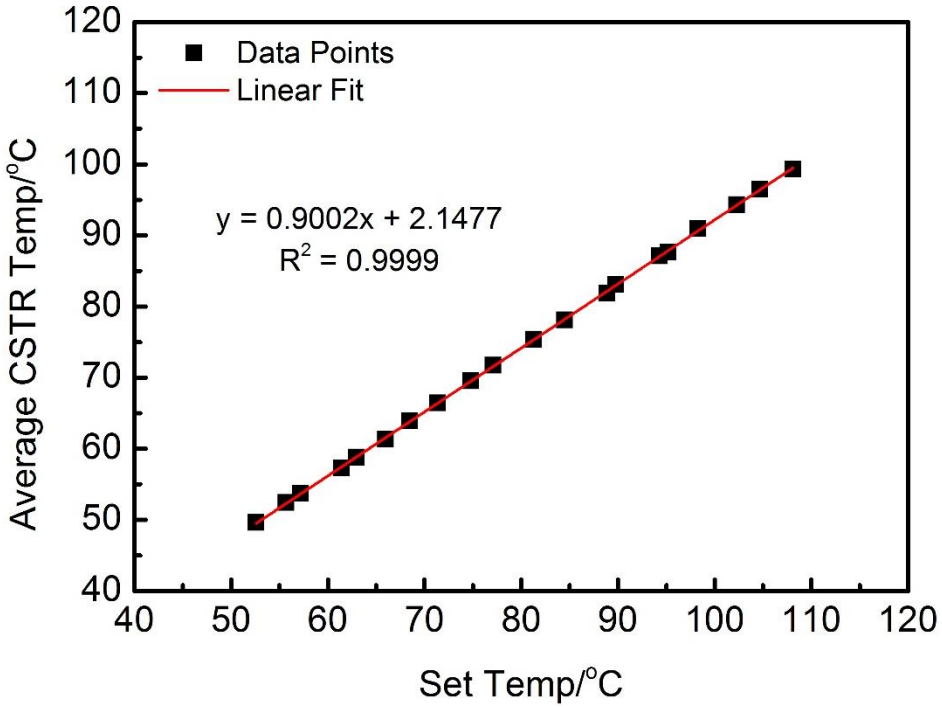

Figure 88. Linear fit between average temperature of the solution inside the CSTRs and the set temperature of the heating mantle.

7.6.2 In-Line Separation of Structurally Similar Impurities

7.6.2.1 Chemicals

α-Methylbenzylamine (99%, Aldrich), (*R*)-(+)-*N*-benzyl-α-methylbenzylamine (98%, Sigma), 70% nitric acid (laboratory grade, Fisher) and toluene (HPLC grade, VWR) were purchased from suppliers and used without further purification.

7.6.2.2 Experimental Set-Up

Reactor: CSTR cascade (n = 2, V = 4 mL), under ambient pressure. A Zaiput SEP-10 liquid-liquid membrane-based separator was placed downstream of the reactor, and fitted with a PTFE membrane (0.5 μm pore size). The permeate outlet was connected to the sample loop for analysis of the organic phase.

Reservoir solutions were prepared by dissolving the desired reagents in solvent under stirring at ambient conditions. Pump 1: nitric acid (70%, 18.1 mL, 0.57 mol L^{-1}) in water (481.9 mL). Pump 2: water. Pump 3: α-methylbenzylamine **5.07** (33.3 mL, 0.26 mol, 0.5158 mol L^{-1}), *N*-benzyl-α-methylbenzylamine **5.08** (3.30 mL, 15.8 mmol, 0.0315 mol L^{-1}) and biphenyl (1.96 g, 12.7 mmol, 0.0254 mol L^{-1}) in toluene (463.5 mL). Reservoir solutions were replenished when required.

HPLC mobile phases were **A** H_2O (18.2 MΩ), **B** MeCN, both buffered with 0.1% TFA. Method: 35% **B** 0.7 min, 35% to 90% **B** 2.5 mins, 90% to 35% **B** 0.1 min, 35% **B** 1 min, flow rate 1.50 mL min^{-1}, column temperature 20 °C.

7.6.2.3 Self-Optimisation Results

$$\text{minimise}[-(\Delta\text{amines}_{(org)})]$$

Table 42. Self-optimisation variables. ν = volumetric flow rate, org = organic, aq = aqueous.

	Variables	
Limits	pH	ν(org):ν(aq)
Lower	0.36	0.80
Upper	0.88	2.00

Table 43. List of results from the SNOBFIT self-optimisation. The identified optimum is highlighted in bold.

Entry	pH	ν(org):ν(aq)	α-Me-$BA_{(org)}$/%	*N*-Bn-α-Me-$BA_{(org)}$/%	Δamine$_{(org)}$/%
1	0.870	1.142	73.1	91.9	18.8
2	0.421	1.025	19.8	94.4	74.6
3	0.806	1.979	87.6	92.7	5.1
4	0.670	1.684	72.5	91.6	19.1
5	0.603	1.006	47.4	93.4	45.9
6	0.537	1.502	58.7	92.1	33.4
7	0.463	1.999	59.6	91.9	32.3
8	0.770	1.108	65.4	92.0	26.6
9	0.873	1.817	84.9	92.0	7.1
10	0.747	1.767	79.4	92.4	13.0
11	0.693	1.156	61.5	91.8	30.3
12	0.824	1.469	78.8	92.1	13.3
13	0.578	1.000	45.3	93.9	48.6
14	0.794	1.278	72.2	91.3	19.1
15	**0.420**	**1.000**	**8.9**	**99.3**	**90.4**
16	0.420	1.253	26.7	92.7	66.0
17	0.420	1.503	40.6	92.0	51.4
18	0.507	1.037	36.3	96.2	59.9
19	0.652	1.751	73.2	91.6	18.4
20	0.421	1.000	12.6	97.9	85.3
21	0.506	1.000	30.9	92.1	61.2
22	0.449	0.800	7.8	16.6	8.8
23	0.794	0.971	63.8	92.2	28.4
24	0.578	0.800	30.0	92.5	62.5
25	0.358	0.986	4.7	15.3	10.7
26	0.358	1.127	3.2	16.4	13.3
27	0.507	1.212	42.1	94.6	52.5
28	0.380	0.954	7.3	14.6	7.3
29	0.794	0.971	62.8	93.1	30.3
30	0.482	1.245	43.0	91.9	48.9
31	0.794	0.971	68.3	92.2	23.9
32	0.358	0.905	13.0	19.3	6.3

33	0.390	1.038	11.1	27.2	16.0
34	0.472	0.964	29.3	96.6	67.3
35	0.764	0.971	61.7	92.3	30.6
36	0.475	0.800	10.5	74.9	74.3
37	0.402	1.004	8.4	89.0	80.6
38	0.459	1.105	39.8	79.6	39.8
39	0.456	1.111	34.9	91.7	46.9
40	0.794	0.971	63.6	81.2	17.6
41	0.456	1.117	27.9	81.8	53.9
42	0.413	0.943	5.3	84.1	78.8
43	0.407	0.964	2.4	10.5	8.1
44	0.483	1.035	28.5	82.3	53.9
45	0.444	1.296	36.3	85.2	48.9
46	0.794	0.971	64.5	89.6	25.1
47	0.407	1.020	8.8	91.9	83.1
48	0.421	1.165	24.9	91.5	66.6
49	0.794	0.971	64.4	91.7	27.3
50	0.411	1.015	14.5	92.0	77.4
51	0.426	0.800	2.4	10.6	8.2
52	0.415	0.995	7.2	93.6	86.4
53	0.794	0.971	68.5	98.0	29.5
54	0.502	0.800	20.9	98.2	77.3
55	0.414	1.033	17.2	94.4	77.2
56	0.382	1.310	37.3	94.3	57.0
57	0.414	1.032	18.8	94.0	75.2
58	0.402	1.200	30.4	91.2	60.7
59	0.794	0.971	64.3	89.4	25.1
60	0.468	1.035	31.4	95.1	63.7
61	0.794	0.971	63.9	92.0	28.1

7.6.3 Synthesis of Secondary Amines via Direct *N*-Alkylation

7.6.3.1 Chemicals

α-Methylbenzylamine (99%, Aldrich), diisopropylethylamine (>99%, Fluorochem), benzyl bromide (>99%, Fluorochem), (*R*)-(+)-*N*-benzyl-α-methylbenzylamine (98%, Sigma), 70% nitric acid (laboratory grade, Fisher), toluene (HPLC grade, VWR) and chloroform (HPLC grade, VWR) were purchased from suppliers and used without further purification. A standard of *N*,*N*-diisopropylethylamine hydrobromide was synthesised for HPLC calibration.

7.6.3.2 Synthesis of *N*,*N*-Diisopropylethylamine Hydrobromide

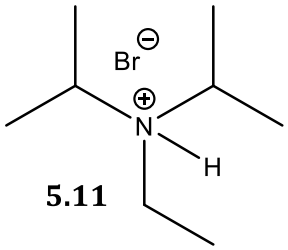

5.11

To a round-bottomed flask, diisopropylethylamine (2.00 g, 15.5 mmol) and hydrobromic acid (48%, 2.60 g) was added in water (40 mL). The reaction mixture was left to stir for 30 minutes at room temperature, then concentrated *in vacuo*. The resultant white solid was dried in an oven at 150 °C over the weekend to yield *N*,*N*-diisopropylethylamine hydrobromide **5.11** (2.17 g, 67%).

^{1}H NMR (D_2O, 500 MHz) δ 3.77 (hept, *J* = 6.7 Hz, 2H), 3.25 (q, *J* = 7.4 Hz, 2H), 1.39 (dd, *J* = 7.0, 2.4 Hz, 15H) ppm; *m/z* (ESI$^+$) $C_8H_{20}N^+$ $[M]^+$, calculated 130.16, found 130.16.

7.6.3.3 Experimental Set-Up

Reactor: Cambridge Reactor Design Polar Bear Flow Synthesiser, fitted with 4 mL Polyfon PTFE tubing (1/16" OD, 1/32" ID), and maintained under 250 psi back-pressure. The reaction mixture was quenched with a stream of $HNO_{3(aq)}$ in a CSTR (*V* = 2 mL). A Zaiput SEP-10 liquid-liquid membrane-based separator was placed downstream of the CSTR, and fitted with a PTFE membrane (0.5 μm pore size). The permeate outlet was connected to the sample loop for analysis of the organic phase.

Reservoir solutions were prepared by dissolving the desired reagents in solvent under stirring at ambient conditions. Pump 1: α-methylbenzylamine **5.07** (12.9 mL, 0.10 mol, 0.400 mol L^{-1}), diisopropylethylamine (17.4 mL, 0.10 mol, 0.400 mol L^{-1}) and biphenyl (1.54 g, 10 mmol, 0.040 mol L^{-1}) in chloroform (219.7 mL). Pump 2: benzyl bromide **5.09** (16.6 mL, 0.14 mol, 0.400 mol L^{-1}) in chloroform (333.4 mL). Pump 3: nitric acid (70%, 12.7 mL, 0.400 mol L^{-1}) in water (487.3 mL). Pump 4: water. Reservoir solutions were replenished when required.

HPLC mobile phases were **A** H_2O (18.2 MΩ), **B** MeCN, both buffered with 0.1% TFA. Method: 10% to 90% **B** 3.5 mins, 90% to 10% **B** 0.5 min, 10% **B** 1 min, flow rate 1.75 $mLmin^{-1}$, column temperature 20 °C.

7.6.3.4 Self-Optimisation Results

minimise[-(purity)]

Table 44. Self-optimisation variables. Fixed parameters: benzyl bromide equivalents = 1, [α-methylbenzylamine] = 0.2 M. ν = volumetric flow rate.

	Variables			
Limits	t_{res}/min	Temp/°C	pH	ν(aq):ν(org)
Lower	6.6	30	0.57	0.25
Upper	10.0	130	1.00	2.26

Table 45. List of results from the SNOBFIT self-optimisation. The identified optimum is highlighted in bold.

Entry	t_{res}/min	Temp/°C	pH	ν(aq):ν(org)	Yield/%	Purity/%
1	8.2	30.0	0.673	0.644	2.3	1.1
2	9.0	63.4	0.953	1.231	13.3	7.1
3	7.1	97.2	0.839	1.163	37.2	22.7
4	7.4	129.9	0.897	0.968	52.2	26.7
5	8.2	38.4	0.759	0.610	3.6	1.8
6	6.7	46.8	0.868	1.156	4.5	2.2
7	8.1	80.4	0.911	1.333	23.7	14.5
8	9.1	113.4	0.919	2.257	45.0	28.7
9	8.0	55.1	0.887	1.190	8.7	4.5
10	9.5	72.0	0.620	0.572	20.1	10.6
11	6.9	105.3	0.912	0.862	44.8	40.6
12	9.5	63.4	0.797	0.597	8.8	6.4
13	6.7	114.1	0.910	1.224	48.8	40.9
14	8.3	46.7	0.898	1.484	5.5	3.3
15	9.3	55.7	0.883	2.078	9.6	7.3
16	7.8	69.8	0.790	1.451	15.0	12.6
17	6.7	92.8	1.000	0.767	29.1	19.3
18	8.3	46.7	0.898	1.484	6.0	3.8
19	6.7	93.4	0.915	1.238	33.1	24.1
20	6.7	101.3	0.908	1.617	42.6	40.4
21	7.1	121.8	0.901	1.705	51.1	30.7
22	9.1	129.1	0.751	0.590	63.3	50.7
23	8.3	46.7	0.898	1.484	6.2	3.2
24	8.6	81.3	0.724	1.369	29.1	24.3
25	8.3	107.9	0.892	1.346	53.0	42.7
26	10.0	130.0	0.702	1.511	58.2	30.6
27	8.3	46.7	0.898	1.484	6.4	3.8
28	8.0	58.3	0.765	1.390	10.4	6.8
29	7.7	121.3	0.574	0.288	63.6	55.3
30	8.0	121.7	0.574	0.621	62.3	35.5
31	10.0	130.0	0.755	0.569	65.0	45.4
32	8.3	46.7	0.898	1.484	6.5	3.5
33	8.6	81.3	0.836	1.771	30.6	27.2
34	6.7	109.7	0.910	1.567	49.3	38.1
35	8.3	130.0	0.718	0.433	65.9	51.5
36	7.7	130.0	0.707	0.392	66.5	51.8
37	8.3	46.7	0.898	1.484	6.8	3.5

38	7.7	125.3	0.765	0.448	65.3	56.6
39	8.0	125.8	0.765	0.465	65.8	53.4
40	8.3	130.0	0.754	1.116	60.6	32.4
41	8.3	46.7	0.898	1.484	6.7	3.4
42	10.0	127.2	0.726	0.628	64.9	40.8
43	6.9	127.7	0.753	0.390	66.5	56.8
44	8.5	130.0	0.759	0.579	66.1	44.2
45	8.3	46.7	0.898	1.484	7.1	4.2
46	6.9	123.0	0.741	0.759	16.2	15.8
47	7.3	123.7	0.755	0.526	65.1	53.0
48	6.7	125.4	0.574	0.250	65.8	53.6
49	10.0	128.4	0.750	0.945	62.1	33.9
50	8.3	46.7	0.898	1.484	6.6	3.8
51	**6.9**	**127.2**	**0.772**	**0.408**	**62.8**	**71.0**
52	7.7	129.2	0.739	0.422	65.9	56.9
53	8.0	129.2	0.742	0.442	66.8	50.8

7.6.4 Biphasic Claisen-Schmidt Condensation

7.6.4.1 Chemicals

Benzaldehyde (>98.0%, Fluorochem), acetone (laboratory grade, VWR), sodium hydroxide pellets (≥97.0%, Fisher), benzylideneacetone (≥98%, Sigma), dibenzylideneacetone (98%, Sigma) and toluene (HPLC grade, VWR) were purchased from suppliers and used without further purification.

7.6.4.2 Experimental Set-Up

Reactor: CSTR cascade (n = 4, V = 8 mL), maintained under 40 psi back-pressure. A Zaiput SEP-10 liquid-liquid membrane-based separator was placed downstream of the BPR, and fitted with a PTFE membrane (0.5 μm pore size). The permeate outlet was connected to the sample loop for analysis of the organic phase.

Reservoir solutions were prepared by dissolving the desired reagents in solvent under stirring at ambient conditions. Pump 1: benzaldehyde **5.12** (25.5 mL, 0.25 mol, 0.50 mol L^{-1}) in toluene (500 mL). Pump 2: acetone **5.13** (neat). Pump 3: sodium hydroxide (4.0 g, 0.10 mol, 0.10 mol L^{-1}) in deionised water (1 L). Reservoir solutions were replenished when required.

HPLC mobile phases were **A** H_2O (18.2 MΩ), **B** MeCN, both buffered with 0.1% TFA. The method used was 10% to 90% **B** 3.5 mins, 90% to 10% **B** 0.5 min, 10% **B** 1 min, flow rate 1.75 mL min^{-1}, column temperature 20 °C.

7.6.4.3 Self-Optimisation Results

minimise[-ln(purity), -ln(STY), -ln(RME)]

Table 46. Self-optimisation variables, directly input in terms of flow rates and ratios. P = pump, v = volumetric flow rate, aq = aqueous, org = organic.

	Variables			
Limits	P1/mL min^{-1}	P2:P1	v(aq):v(org)	Temp/°C
Lower	0.2	0.5	0.5	50.0
Upper	0.4	1.1	1.2	110.0

Table 47. List of results from the TSEMO self-optimisation. The first 20 experiments are a LHC design in ascending order of temperature. The non-dominated solutions are highlighted in bold.

Entry	P1/mL min^{-1}	P2:P1	v(aq):v(org)	T/°C	Purity/%	STY/ kg m^{-3} h^{-1}	RME
1	0.252	1.085	0.772	52.6	38.1	35.73	1.18
2	0.212	0.704	0.900	55.7	22.6	20.66	1.13
3	0.346	0.773	0.725	57.2	15.7	20.69	0.70
4	0.290	0.528	0.785	61.4	14.9	16.43	0.91
5	0.222	1.048	1.134	63.0	40.6	48.88	1.57
6	0.396	0.675	1.036	66.0	19.8	40.23	1.14
7	0.231	0.586	1.005	68.5	27.4	31.31	1.76
8	0.382	0.644	0.658	71.4	21.5	32.23	1.22
9	0.312	0.875	0.680	74.8	37.8	47.55	1.64
10	0.268	0.910	0.540	77.1	38.7	37.83	1.59
11	0.321	0.977	0.500	81.3	45.6	53.56	1.81
12	0.378	0.545	0.923	84.5	33.2	59.31	2.26
13	0.336	0.750	1.102	88.9	49.3	105.04	3.09
14	0.202	0.925	1.165	89.8	62.3	77.11	3.02
15	0.301	1.022	0.607	94.3	64.9	92.02	2.97
16	0.367	0.827	0.832	95.2	55.3	104.24	2.95
17	0.286	0.716	0.605	98.3	57.9	70.27	3.32
18	0.243	1.006	0.868	102.3	78.2	108.60	3.79
19	0.272	0.844	0.969	104.7	73.1	117.19	4.08
20	0.356	0.608	1.066	108.1	61.1	130.10	4.45
21	0.211	0.853	1.200	101.2	72.3	141.73	5.64
22	0.200	1.032	1.157	105.5	81.0	142.82	5.12
23	0.257	0.931	0.690	108.8	74.8	125.84	4.93
24	0.348	1.100	0.669	104.7	67.8	145.56	3.65
25	0.36	0.707	0.938	105.2	54.9	137.90	4.34
26	0.317	1.100	0.646	106.4	78.8	156.99	4.38
27	0.315	1.100	0.801	108.0	71.3	155.49	3.99
28	0.200	0.500	0.742	104.6	60.4	67.49	5.80
29	0.233	0.618	0.892	106.5	49.3	71.75	4.04
30	0.375	0.967	1.161	108.6	66.0	207.84	4.22
31	0.200	0.500	0.973	109.7	53.8	70.30	5.34
32	0.394	1.035	0.823	106.1	66.1	188.46	4.05
33	0.400	1.041	1.050	110.0	70.3	222.47	4.16
34	0.303	0.909	1.123	110.0	76.2	186.25	5.04
35	0.338	0.904	0.872	110.0	57.4	131.62	3.64

36	**0.247**	**1.100**	**1.056**	**108.3**	**84.5**	**170.71**	**4.90**
37	0.303	1.100	1.159	108.3	78.6	212.89	4.74
38	0.255	1.100	0.962	108.4	70.5	133.48	3.89
39	0.332	1.099	1.082	109.7	69.8	148.96	3.14
40	0.200	1.044	0.676	94.6	64.7	64.54	2.95
41	0.288	1.028	1.199	106.6	71.7	176.35	4.32
42	0.297	0.918	1.024	108.4	71.4	170.87	4.90
43	0.312	0.970	1.200	110.0	74.0	194.61	4.65
44	0.220	1.068	1.200	96.7	77.7	150.18	4.65
45	0.263	1.041	1.059	98.8	75.7	172.65	4.89
46	0.395	1.075	1.159	101.6	68.6	214.49	3.74
47	0.380	0.665	1.200	110.0	56.9	155.69	4.32
48	0.204	0.771	1.200	104.6	76.3	115.03	5.20
49	**0.203**	**0.918**	**1.200**	**106.2**	**84.6**	**142.65**	**5.51**
50	**0.200**	**0.918**	**1.200**	**107.1**	**84.1**	**141.74**	**5.56**
51	0.309	0.871	1.167	109.4	76.7	190.44	5.15
52	0.333	0.662	1.197	105.0	64.5	179.95	5.73
53	0.400	0.802	1.200	105.3	66.0	204.67	4.55
54	0.397	0.806	1.176	105.7	66.3	206.09	4.64
55	0.320	0.778	1.157	107.4	71.2	175.54	5.11
56	0.273	1.100	1.043	102.8	79.5	186.00	4.86
57	0.228	0.839	1.189	106.1	78.3	146.61	5.51
58	**0.400**	**1.070**	**1.200**	**107.4**	**76.1**	**259.95**	**4.42**
59	0.334	0.787	1.190	110.0	73.8	197.75	5.38
60	0.206	0.819	1.197	106.1	79.7	127.38	5.40
61	**0.317**	**0.796**	**1.200**	**109.9**	**74.4**	**205.72**	**5.81**
62	0.223	0.962	1.102	110.0	83.9	138.80	4.89
63	**0.277**	**1.085**	**1.200**	**110.0**	**84.1**	**218.61**	**5.29**
64	0.400	0.720	1.128	101.9	58.9	167.44	4.25
65	**0.200**	**1.100**	**1.200**	**105.2**	**86.3**	**165.68**	**5.48**
66	**0.230**	**0.813**	**1.196**	**107.7**	**79.9**	**161.51**	**6.17**
67	0.249	0.842	1.194	107.8	78.0	153.93	5.27
68	0.386	0.615	1.129	101.4	53.8	157.36	4.77
69	0.385	0.589	1.165	102.9	55.1	161.91	5.03
70	0.400	0.663	1.064	103.3	58.7	174.60	4.92
71	0.207	0.889	1.159	110.0	83.4	149.60	5.95
72	0.379	0.751	1.124	101.0	55.1	157.33	4.06
73	0.348	0.736	1.183	101.9	62.8	171.31	4.77
74	0.400	0.707	1.183	102.7	59.6	190.87	4.80
75	0.385	0.823	1.128	110.0	69.3	212.01	4.94
76	0.388	1.064	1.200	99.2	68.3	219.99	3.87
77	**0.400**	**0.910**	**1.200**	**106.6**	**71.1**	**239.33**	**4.73**
78	0.241	0.849	1.199	110.0	71.1	134.60	4.71
79	0.234	0.850	1.200	110.0	70.0	134.57	4.84
80	0.209	0.500	0.916	93.7	54.3	66.06	4.94
81	0.248	0.838	1.172	104.0	75.2	155.22	5.41
82	**0.225**	**0.945**	**1.190**	**104.9**	**82.8**	**166.14**	**5.66**
83	0.371	0.848	1.200	105.2	68.9	210.47	4.79
84	0.317	0.994	1.138	96.3	68.5	175.12	4.14
85	0.363	0.751	1.200	108.1	69.0	185.59	4.83
86	0.204	0.945	1.120	108.1	84.5	127.34	4.94
87	**0.200**	**0.926**	**1.033**	**108.7**	**84.9**	**137.70**	**5.80**
88	0.369	0.993	1.100	98.3	67.4	188.71	3.90
89	0.393	1.030	1.026	98.4	67.8	195.95	3.81

90	0.309	0.922	1.067	103.4	73.3	174.32	4.69
91	0.220	0.885	0.906	105.2	77.5	119.80	5.10
92	0.207	0.970	0.897	102.9	80.2	119.20	4.97
93	**0.209**	**1.094**	**0.754**	**108.3**	**87.4**	**112.25**	**4.48**
94	**0.380**	**1.072**	**1.190**	**110.0**	**79.3**	**246.78**	**4.42**
95	**0.389**	**1.100**	**1.200**	**110.0**	**79.3**	**254.88**	**4.34**
96	0.216	0.500	0.572	97.3	49.8	50.25	4.43
97	0.219	0.560	0.500	98.5	51.1	51.78	4.27
98	0.215	0.583	1.200	105.3	70.7	108.75	6.01
99	0.259	1.002	1.061	110.0	83.7	167.63	4.99
100	0.382	1.018	0.904	88.9	56.4	127.44	2.74
101	0.206	0.500	1.200	98.4	61.9	88.92	5.88
102	**0.241**	**0.500**	**1.200**	**105.0**	**65.6**	**118.13**	**6.67**
103	0.222	0.974	1.132	107.2	84.3	154.40	5.33
104	0.200	1.100	0.500	105.8	85.2	90.41	4.39
105	**0.237**	**0.822**	**1.115**	**108.0**	**83.4**	**159.22**	**6.07**
106	**0.200**	**1.071**	**0.540**	**110.0**	**87.9**	**97.86**	**4.74**
107	**0.206**	**0.500**	**1.200**	**110.0**	**78.8**	**108.34**	**7.16**
108	0.335	1.100	1.200	82.4	61.4	164.96	3.26
109	0.323	0.500	1.200	99.9	61.1	144.17	6.08

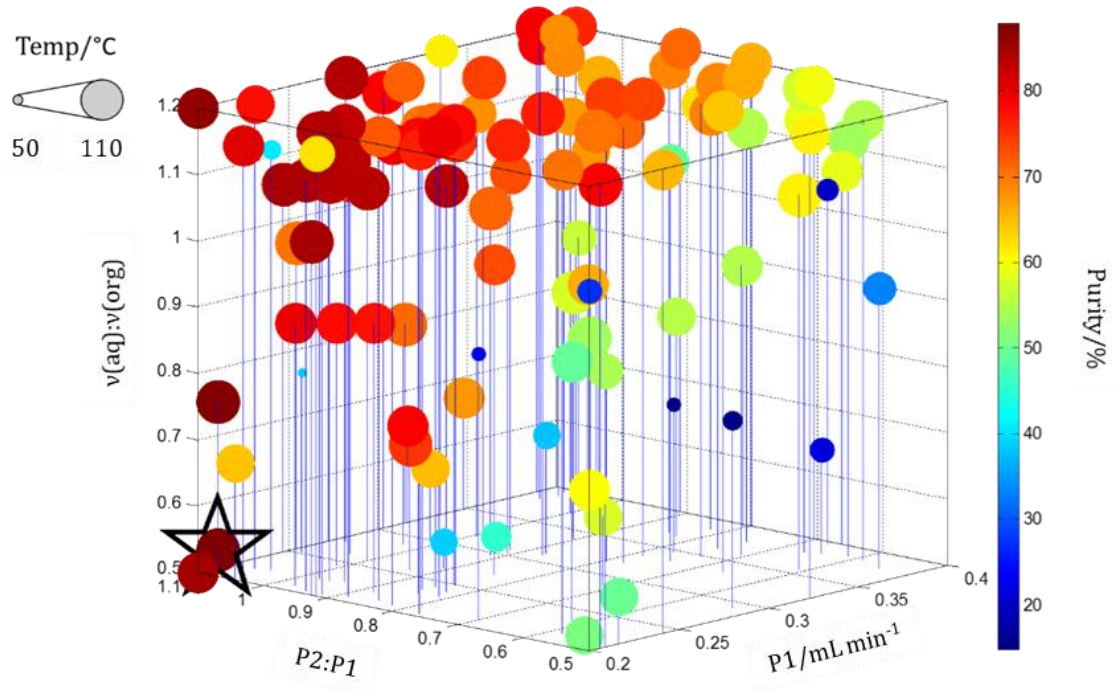

Figure 89. Multi-objective self-optimisation results for purity with respect to benzylideneacetone **5.14**. ☆ = maximum purity.

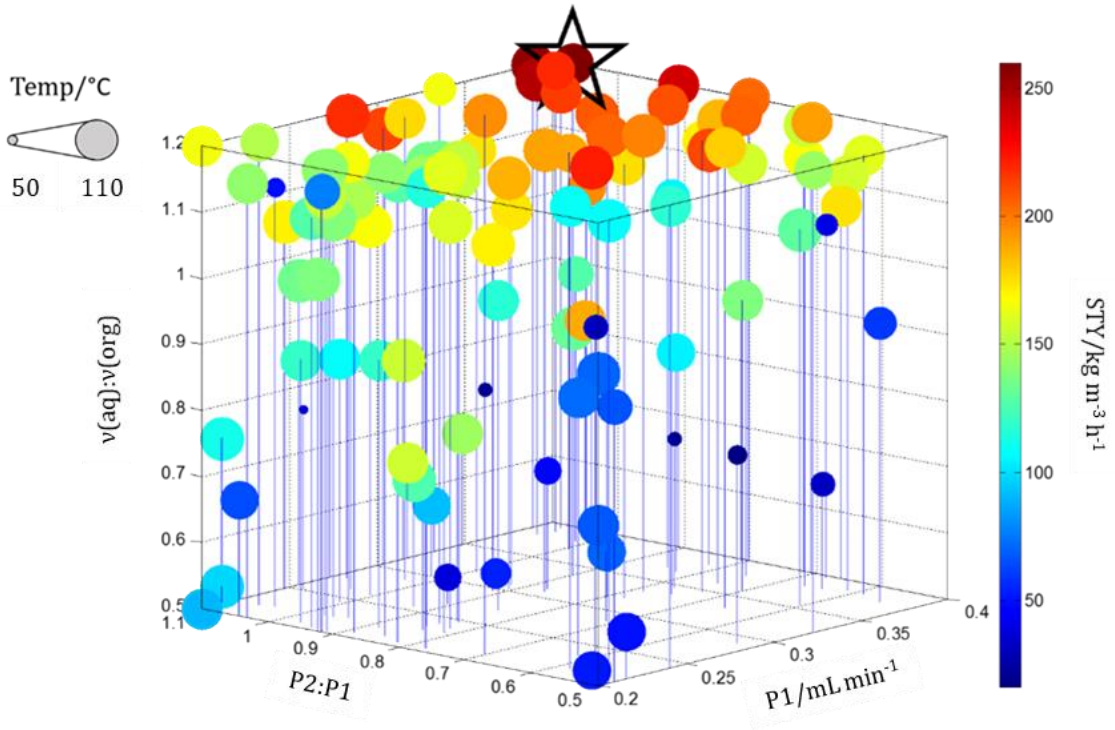

Figure 90. Multi-objective self-optimisation results for STY with respect to benzylideneacetone **5.14**. ☆ = maximum STY.

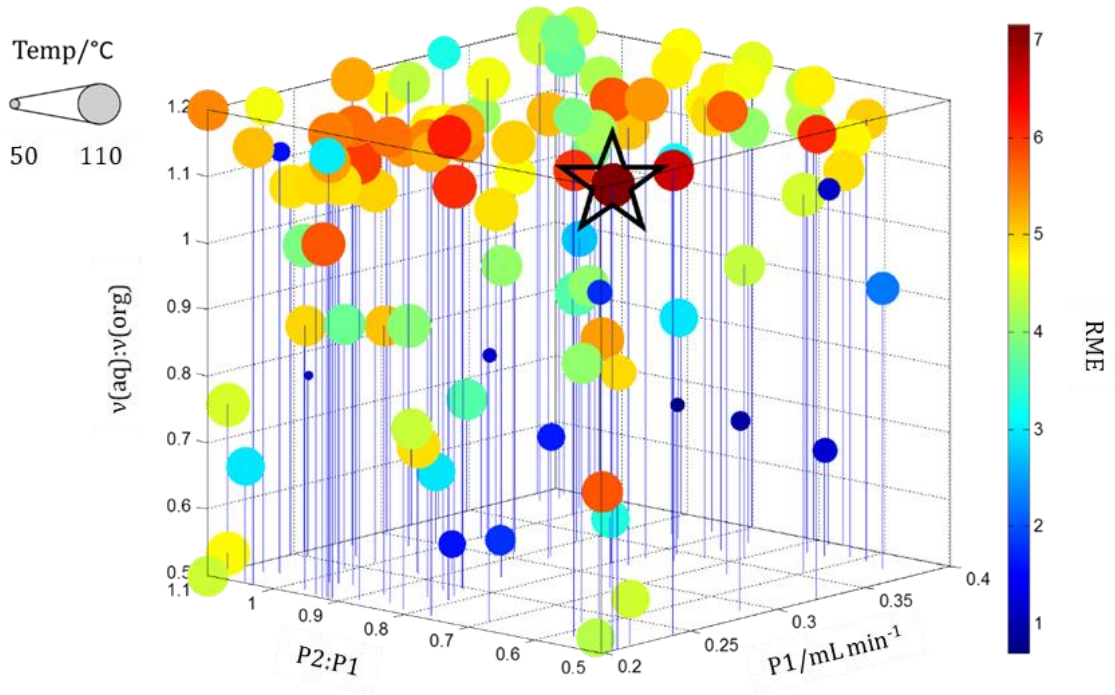

Figure 91. Multi-objective self-optimisation results for RME with respect to benzylideneacetone **5.14**. ☆ = maximum RME.

References

1. O. Levenspiel, *Chemical Reaction Engineering*, John Wiley & Sons, New Delhi, 2004.
2. G. F. Froment, K. B. Bischoff and J. D. Wilde, *Chemical Reactor Analysis and Design*, John Wiley & Sons, New Jersey, 2011.
3. H. S. Fogler, *Elements of Chemical Reaction Engineering*, John Wiley & Sons, New Delhi, 2004.
4. P. V. Danckwerts, *Chem. Eng. Sci.*, 1953, **2**, 1-13.
5. G. Taylor, *Proc. R. Soc. London*, 1953, **219**, 186-203.
6. R. Aris, *Proc. R. Soc. London*, 1955, **235**, 67-77.
7. A. Cholette, J. Blanchet and L. Cloutier, *Can. J. Chem. Eng.*, 1960, **1**, 1-18.
8. J. Coulson and J. F. Richardson, *Coulson and Richardson's Chemical Engineering*, Butterworth-Heinemann, Oxford, 7th edn., 2017.
9. D. J. Lamberto, M. M. Alvarez and F. J. Muzzio, *Chem. Eng. Sci.*, 1999, **54**, 919-942.
10. K. D. Nagy, B. Shen, T. F. Jamison and K. F. Jensen, *Org. Process Res. Dev.*, 2012, **16**, 976-981.
11. P. Rys, *Angew. Chem. Int. Ed.*, 1977, **16**, 807-817.
12. E. L. Paul, V. A. Atiemo-Obeng and S. M. Kresta, *Handbook of Industrial Mixing: Science and Practice*, John Wiley & Sons, New Jersey, 2004.
13. C. Yang, A. R. Teixeira, Y. Shi, S. C. Born, H. Lin, Y. L. Song, B. Martin, B. Schenkel, M. P. Lachegurabi and K. F. Jensen, *Green Chem.*, 2018, **20**, 886-893.
14. M. B. Plutschack, B. Pieber, K. Gilmore and P. H. Seeberger, *Chem. Rev.*, 2017, **117**, 11796-11893.
15. A. Günther, M. Jhunjhunwala, M. Thalmann, M. A. Schmidt and K. F. Jensen, *Langmuir*, 2005, **21**, 1547-1555.
16. T. Gustafsson, H. Sörensen and F. Pontén, *Org. Process Res. Dev.*, 2012, **16**, 925-929.
17. Y. Lu, K. P. Cole, J. W. Fennell, T. D. Maloney, D. Mitchell, R. Subbiah and B. Ramadas, *Org. Process Res. Dev.*, 2018, **22**, 409-419.
18. P. Knapkiewicz, K. Skowerski, D. E. Jaskólska, M. Barbasiewicz and T. K. Olszewski, *Org. Process Res. Dev.*, 2012, **16**, 1430-1435.
19. J.-i. Yoshida, Y. Takahashi and A. Nagaki, *Chem. Commun.*, 2013, **49**, 9896-9904.
20. A. Nagaki, M. Togai, S. Suga, N. Aoki, K. Mae and J.-i. Yoshida, *J. Am. Chem. Soc.*, 2005, **127**, 11666-11675.
21. H. Kim, A. Nagaki and J.-i. Yoshida, *Nat. Commun.*, 2011, **2**.
22. B. Gutmann, *J. Flow Chem.*, 2017, **7**, 1-3.
23. S. G. Newman and K. F. Jensen, *Green Chem.*, 2013, **15**, 1456-1472.

24. B. Gutmann, D. Cantillo and C. O. Kappe, *Angew. Chem. Int. Ed.*, 2015, **54**, 6688-6728.

25. S. G. Newman, L. Gu, C. Lesniak, G. Victor, F. Meschke, L. Abahmane and K. F. Jensen, *Green Chem.*, 2014, **16**, 176-180.

26. B. Gutmann, J.-P. Roduit, D. Roberge and C. O. Kappe, *Angew. Chem. Int. Ed.*, 2010, **49**, 7101-7105.

27. Z. P. Demko and K. B. Sharpless, *J. Org. Chem.*, 2001, **66**, 7945-7950.

28. C. A. Shukla and A. A. Kulkarni, *Beilstein J. Org. Chem.*, 2017, **13**, 960-987.

29. P. Sagmeister, J. D. Williams, C. A. Hone and C. O. Kappe, *React. Chem. Eng.*, 2019, DOI: 10.1039/C9RE00087A.

30. D. L. Browne, S. Wright, B. J. Deadman, S. Dunnage, I. R. Baxendale, R. M. Turner and S. V. Ley, *Rapid Commun. Mass Spectrom.*, 2012, **26**, 1999-2010.

31. A. B. Santanilla, E. L. Regalado, T. Pereira, M. Shevlin, K. Bateman, L.-C. Campeau, J. Schneeweis, S. Berritt, Z.-C. Shi, P. Nantermet, Y. Liu, R. Helmy, C. J. Welch, P. Vachal, I. W. Davies, T. Cernak and S. D. Dreher, *Science*, 2015, **347**, 49-53.

32. D. Perera, J. W. Tucker, S. Brahmbhatt, C. J. Helal, A. Chong, W. Farrell, P. Richardson and N. W. Sach, *Science*, 2018, **359**, 429-434.

33. A. Günther and K. F. Jensen, *Lab Chip*, 2006, **6**, 1487-1503.

34. H. Lange, C. F. Carter, M. D. Hopkin, A. Burke, J. G. Goode, I. R. Baxendale and S. V. Ley, *Chem. Sci.*, 2011, **2**, 765-769.

35. D. X. Hu, M. O'Brien and S. V. Ley, *Org. Lett.*, 2012, **14**, 4246-4249.

36. P. L. Heider, S. C. Born, S. Basak, B. Benyahia, R. Lakerveld, H. Zhang, R. Hogan, L. Buchbinder, A. Wolfe, S. Mascia, J. M. B. Evans, T. F. Jamison and K. F. Jensen, *Org. Process Res. Dev.*, 2014, **18**, 402-409.

37. V. Czitrom, *Am. Stat.*, 1999, **53**, 126-131.

38. A. Sugimoto, T. Fukuyama, T. Rahman and I. Ryu, *Tetrahedron Lett.*, 2009, **50**, 6364-6367.

39. R. Leardi, *Anal. Chim. Acta*, 2009, **652**, 161-172.

40. G. E. P. Box, W. G. Hunter and J. S. Hunter, *Statistics for Experimenters*, Wiley, New York, 1978.

41. D. C. Montgomery, *Design and Analysis of Experiments*, Wiley, Singapore, 8th edn., 2013.

42. S. A. Raw, B. A. Taylor and S. Tomasi, *Org. Process Res. Dev.*, 2011, **15**, 688-692.

43. B. J. Reizman and K. F. Jensen, *Acc. Chem. Res.*, 2016, **49**, 1786-1796.

44. V. Sans and L. Cronin, *Chem. Soc. Rev.*, 2016, **45**, 2032-2043.

45. D. C. Fabry, E. Sugiono and M. Rueping, *React. Chem. Eng.*, 2016, **1**, 129-133.

46. N. Holmes, G. R. Akien, A. J. Blacker, R. L. Woodward, R. E. Meadows and R. A. Bourne, *React. Chem. Eng.*, 2016, **1**, 366-371.

47. D. Cortés-Borda, E. Wimmer, B. Gouilleux, E. Barré, N. Oger, L. Goulamaly, L. Peault, B. Charrier, C. Truchet, P. Giraudeau, M. Rodriguez-Zubiri, E. L. Grognec and F.-X. Felpin, *J. Org. Chem.*, 2018, **83**, 14286-14299.

48. D. E. Fitzpatrick, T. Maujean, A. C. Evans and S. V. Ley, *Angew. Chem. Int. Ed.*, 2018, **57**, 15128-15132.

49. B. J. Reizman, Y.-M. Wang, S. L. Buchwald and K. F. Jensen, *React. Chem. Eng.*, 2016, **1**, 658-666.

50. A. D. Clayton, J. A. Manson, C. J. Taylor, T. W. Chamberlain, B. A. Taylor, G. Clemens and R. A. Bourne, *React. Chem. Eng.*, 2019, DOI: 10.1039/c9re00209j.

51. S. Krishnadasan, R. J. C. Brown, A. J. deMello and J. C. deMello, *Lab Chip*, 2007, **7**, 1434-1441.

52. S. Krishnadasan, A. Yashina, A. J. DeMello and J. C. DeMello, in *Advances in Chemical Engineering*, ed. J. C. Schouten, Academic Press, 2010, pp. 195-231.

53. J. P. McMullen, M. T. Stone, S. L. Buchwald and K. F. Jensen, *Angew. Chem. Int. Ed.*, 2010, **49**, 7076-7080.

54. J. P. McMullen and K. F. Jensen, *Org. Process Res. Dev.*, 2010, **14**, 1169-1176.

55. A. J. Parrott, R. A. Bourne, G. R. Akien, D. J. Irvine and M. Poliakoff, *Angew. Chem. Int. Ed.*, 2011, **50**, 3788-3792.

56. R. A. Bourne, R. A. Skilton, A. J. Parrott, D. J. Irvine and M. Poliakoff, *Org. Process Res. Dev.*, 2011, **15**, 932-938.

57. J. S. Moore and K. F. Jensen, *Org. Process Res. Dev.*, 2012, **16**, 1409-1415.

58. D. N. Jumbam, R. A. Skilton, A. J. Parrott, R. A. Bourne and M. Poliakoff, *J. Flow Chem.*, 2012, **1**, 24-27.

59. R. A. Skilton, A. J. Parrott, M. W. George, M. Poliakoff and R. A. Bourne, *Appl. Spectrosc.*, 2013, **67**, 1127-1131.

60. Z. Amara, E. S. Streng, R. A. Skilton, J. Jin, M. W. George and M. Poliakoff, *Eur. J. Org. Chem.*, 2015, **28**, 6141-6145.

61. V. Sans, L. Porwol, V. Dragone and L. Cronin, *Chem. Sci.*, 2015, **6**, 1258-1264.

62. B. J. Reizman and K. F. Jensen, *Chem. Commun.*, 2015, **51**, 13290-13293.

63. C. Houben, N. Peremezhney, A. Zubov, J. Kosek and A. A. Lapkin, *Org. Process Res. Dev.*, 2015, **19**, 1049-1053.

64. N. Holmes, G. R. Akien, R. J. D. Savage, C. Stanetty, I. R. Baxendale, A. J. Blacker, B. A. Taylor, R. L. Woodward, R. E. Meadows and R. A. Bourne, *React. Chem. Eng.*, 2016, **1**, 96-100.

65. D. Cortés-Borda, K. V. Kutonova, C. Jamet, M. E. Trusova, F. Zammattio, C. Truchet, M. Rodriguez-Zubiri and F.-X. Felpin, *Org. Process Res. Dev.*, 2016, **20**, 1979-1987.

66. D. E. Fitzpatrick, C. Battilocchio and S. V. Ley, *Org. Process Res. Dev.*, 2016, **20**, 386-394.

67. B. E. Walker, J. H. Bannock, A. M. Nightingale and J. C. deMello, *React. Chem. Eng.*, 2017, **2**, 785-798.

68. M. I. Jeraal, N. Holmes, G. R. Akien and R. A. Bourne, *Tetrahedron*, 2018, **74**, 3158-3164.

69. A. M. Schweidtmann, A. D. Clayton, N. Holmes, E. Bradford, R. A. Bourne and A. A. Lapkin, *Chem. Eng. J.*, 2018, **352**, 277-282.

70. A.-C. Bédard, A. Adamo, K. C. Aroh, M. G. Russell, A. A. Bedermann, J. Torosian, B. Yue, K. F. Jensen and T. F. Jamison, *Science*, 2018, **361**, 1220-1225.

71. L. M. Baumgartner, C. W. Coley, B. J. Reizman, K. W. Gao and K. F. Jensen, *React. Chem. Eng.*, 2018, **3**, 301-311.

72. N. Cherkasov, Y. Bai, A. J. Expósito and E. V. Rebrov, *React. Chem. Eng.*, 2018, **3**, 769-780.

73. H.-W. Hsieh, C. W. Coley, L. M. Baumgartner, K. F. Jensen and R. I. Robinson, *Org. Process Res. Dev.*, 2018, **22**, 542-550.

74. K. Poscharny, D. C. Fabry, S. Heddrich, E. Sugiono, M. A. Liauw and M. Rueping, *Tetrahedron*, 2018, **74**, 3171-3175.

75. M. Rubens, J. H. Vrijsen, J. Laun and T. Junkers, *Angew. Chem. Int. Ed.*, 2019, **58**, 3183-3187.

76. W. Spendley, G. R. Hext and F. R. Himsworth, *Technometrics*, 1962, **4**, 441-461.

77. J. A. Nelder and R. Mead, *Comput. J.*, 1965, **7**, 308-313.

78. M. W. Routh, P. A. Swartz and M. B. Denton, *Anal. Chem.*, 1977, **49**, 1422-1428.

79. K. J. Beers, *Numerical Methods for Chemical Engineering: Applications in MATLAB*, Cambridge University Press, New York, 2007.

80. P. Y. Papalambros and D. J. Wilde, *Principles of Optimal Design*, Cambridge University Press, New York, 2000.

81. D. E. Goldberg, *Genetic Algorithms in Search, Optimization and Machine Learning*, Addison-Wesley Pub. Co., Reading, MA, 1989.

82. J. E. Kreutz, A. Shukhaev, W. Du, S. Druskin, O. Daugulis and R. F. Ismagilov, *J. Am. Chem. Soc.*, 2010, **132**, 3128-3132.

83. W. Huyer and A. Neumaier, *ACM Trans. Math. Softw.*, 2008, **35**, 1-25.

84. N. V. Queipo, R. T. Haftka, W. Shyy, T. Goel, R. Vaidyanathan and P. K. Tucker, *Prog. Aerosp. Sci.*, 2005, **41**, 1-28.

85. E. Brochu, V. M. Cora and N. d. Freitas, *pre-print*, 2010, arXiv:1012.2599.

86. C. E. Rasmussen and C. K. I. Williams, *Gaussian Processes for Machine Learning*, MIT Press, Cambridge, Massachusetts, 2006.

87. B. Shahriari, K. Swersky, Z. Wang, R. P. Adams and N. d. Freitas, *Proc. IEEE*, 2016, **104**, 148-175.

88. D. J. Russo, B. Roy, A. Kazerouni, I. Osband and Z. Wen, *Found. Trends Mach. Learn.*, 2018, **11**, 1-96.

89. G. J. Janz and S. C. Wait, *J. Chem. Phys.*, 1955, **23**, 1550-1551.

90. B. M. Trost, *Science*, 1991, **254**, 1471-1477.

91. R. A. Sheldon, *Green Chem.*, 2007, **9**, 1273-1283.

92. D. J. C. Constable, A. D. Curzons and V. L. Cunningham, *Green Chem.*, 2002, **4**, 521-527.

93. A. Konak, D. W. Coit and A. E. Smith, *Reliab. Eng. Syst. Safe.*, 2006, **91**, 992-1007.

94. K. Deb, A. Pratap, S. Agarwal and T. Meyarivan, *IEEE Trans. Evol. Comput.*, 2002, **6**, 182-197.

95. N. Peremezhney, E. Hines, A. Lapkin and C. Connaughton, *Eng. Optimiz.*, 2014, **46**, 1593-1607.

96. E. Bradford, A. M. Schweidtmann and A. Lapkin, *J. Glob. Optim.*, 2018, **71**, 407-438.

97. V. R. Joseph and Y. Hung, *Statistica Sinica*, 2008, **18**, 171-186.

98. A. Auger, J. Bader, D. Brockhoff and E. Zitzler, *Theor. Comput. Sci.*, 2012, **425**, 75-103.

99. J. S. Carey, D. Laffan, C. Thomson and M. T. Williams, *Org. Biomol. Chem.*, 2006, **4**, 2337-2347.

100. R. N. Salvatore, C. H. Yoon and K. W. Jung, *Tetrahedron*, 2001, **57**, 7785-7811.

101. J. L. Moore, S. M. Taylor and V. A. Soloshonok, *Arkivoc*, 2005, **6**, 287-292.

102. D. R. Jones, M. Schonlau and W. J. Welch, *J. Glob. Optim.*, 1998, **13**, 455-492.

103. C. Jiménez-González, P. Poechlauer, Q. B. Broxterman, B.-S. Yang, D. a. Ende, J. Baird, C. Bertsch, R. E. Hannah, P. Dell'Orco, H. Noorman, S. Yee, R. Reintjens, A. Wells, V. Massonneau and J. Manley, *Org. Process Res. Dev.*, 2011, **15**, 900-911.

104. C. C. Carmona-Vargas, L. d. C. Alves, T. J. Brocksom and K. T. d. Oliveira, *React. Chem. Eng.*, 2017, **2**, 366-374.

105. N. C. Neyt and D. L. Riley, *React. Chem. Eng.*, 2018, **3**, 17-24.

106. R. P. Dhanya, A. Herath, D. J. Sheffler and N. D. P. Cosford, *Tetrahedron*, 2018, **74**, 3165-3170.

107. D. R. Snead and T. F. Jamison, *Angew. Chem. Int. Ed.*, 2015, **54**, 983-987.

108. P. R. D. Murray, D. L. Browne, J. C. Pastre, C. Butters, D. Guthrie and S. V. Ley, *Org. Process Res. Dev.*, 2013, **17**, 1192-1208.

109. M. D. Hopkin, I. R. Baxendale and S. V. Ley, *Chem. Commun.*, 2010, **46**, 2450-2452.

110. Alzheimer's-Association, *Alzheimer's Dement.*, 2016, **12**, 459-509.

111. R. Yan and R. Vassar, *Lancet Neurol.*, 2014, **13**, 319-329.

112. D. Oehlrich, H. Prokopcova and H. J. M. Gijsen, *Bioorg. Med. Chem. Lett.*, 2014, **24**, 2033-2045.

113. ALZFORUM, Therapeutics: Lanabecestat, https://www.alzforum.org/therapeutics/azd3293, (accessed 24 May, 2019).

114. S. Eketjäll, J. Janson, K. Kaspersson, A. Bogstedt, F. Jeppsson, J. Fälting, S. B. Haeberlein, A. R. Kugler, R. C. Alexander and G. Cebers, *J. Alzheimer's Dis.*, 2016, **50**, 1109-1123.

115. G. Cebers, R. C. Alexander, S. B. Haeberlein, D. Han, R. Goldwater, L. Ereshefsky, T. Olsson, N. Ye, L. Rosen, M. Russell, J. Maltby, S. Eketjäll and A. R. Kugler, *J. Alzheimer's Dis.*, 2017, **55**, 1039-1053.

116. N. Ye, S. A. Monk, P. Daga, D. M. Bender, L. B. Rosen, J. Mullen, M. C. Minkwitz and A. R. Kugler, *Clin. Pharmacol. Drug Dev.*, 2018, **7**, 233-243.

117. G. Csjernyik, S. Karlstroem, A. Kers, K. Kolmodin, M. Nyloef, L. Oehberg, L. Rakos, L. Sandberg, F. Sehgelmeble, P. Soederman, B.-M. Swahn and B. Von, *WO 2012/087237 A1*, 2012.

118. I. W. Ashworth, A. D. Campbell, J. H. Cherryman, J. Clark, A. Crampton, E. G. B. Eden-Rump, M. Evans, M. F. Jones, S. McKeever-Abbas, R. E. Meadows, K. Skilling, D. T. E. Whittaker, R. L. Woodward and P. A. Inglesby, *Org. Process Res. Dev.*, 2018, **22**, 1801-1808.

119. R. Chinchilla and C. Nájera, *Chem. Rev.*, 2007, **107**, 874-922.

120. D. Znidar, C. A. Hone, P. Inglesby, A. Boyd and C. O. Kappe, *Org. Process Res. Dev.*, 2017, **21**, 878-884.

121. A. John, S. Modak, M. Madasu, M. Katari and P. Ghosh, *Polyhedron*, 2013, **64**, 20-29.

122. F. Barrios-Landeros and J. F. Hartwig, *J. Am. Chem. Soc.*, 2005, **127**, 6944-6945.

123. S. Mirjalili and A. Lewis, *Inf. Sci.*, 2015, **300**, 158-192.

124. J. Vojtesek and P. Dostal, presented in part at the International Conference Cybernetics and Informatics, 2010.

125. J. W. Lee, Z. Horváth, A. G. O'Brien, P. H. Seeberger and A. Seidel-Morgenstern, *Chem. Eng. J.*, 2014, **251**, 355-370.

126. S. A. Hashemi and F. Z. Ashtiani, *Food Bioprod. Process.*, 2010, **88**, 181-187.

127. J. S. Moore and K. F. Jensen, *Angew. Chem. Int. Ed.*, 2014, **53**, 470-473.

128. J. A. Manson, Mathematical Modelling of Titanium Dioxide Nanoparticle Synthesis in a Spinning Disk Reactor, MEng Dissertation, Newcastle University, 2017.

129. C. A. Hone, Evolution of kinetic motifs through rate-based experimental design in flow reactors, Ph.D Thesis, University of Leeds, 2016.

130. K. Bringmann, T. Friedrich, C. Igel and T. Voβ, *Artif. Intell.*, 2013, **204**, 22-29.

131. Simone, MATLAB File Exchange, Hypervolume approximation, https://uk.mathworks.com/matlabcentral/fileexchange/50517-hypervolume-approximation, (accessed 13 June, 2019).

132. Simone, MATLAB File Exchange, Pareto filtering, https://uk.mathworks.com/matlabcentral/fileexchange/50477-pareto-filtering, (accessed 13 June, 2019).

133. J. Knowles, *IEEE Trans. Evol. Comput.*, 2006, **10**, 50-66.

134. D. Zhan, Y. Cheng and J. Liu, *IEEE Trans. Evol. Comput.*, 2017, **21**, 956-975.

135. Y. Tian, R. Cheng, X. Zhang and Y. Jin, *IEEE Comput. Intell. Mag.*, 2017, **12**, 73-87.

136. Y. Tian and S. Peng, GitHub, BIMK/PlatEMO: Evolutionary multi-objective optimization platform, https://github.com/BIMK/PlatEMO, (accessed 13 June, 2019).

137. R. Porta, M. Benaglia and A. Puglisi, *Org. Process Res. Dev.*, 2015, **20**, 2-25.

138. N. Hoffmann, *Chem. Rev.*, 2008, **108**, 1052-1103.

139. N. Hoffmann, *Photochem. Photobiol. Sci.*, 2012, **11**, 1613-1641.

140. C. Schweitzer and R. Schmidt, *Chem. Rev.*, 2003, **103**, 1685-1757.

141. A. A. Ghogare and A. Greer, *Chem. Rev.*, 2016, **116**, 9994-10034.

142. C. Michelin and N. Hoffmann, *ACS Catal.*, 2018, **8**, 12046-12055.

143. M. C. DeRosa and R. J. Crutchley, *Coord. Chem. Rev.*, 2002, **233-234**, 351-371.

144. C. Tanielian, R. Mechin, R. Seghrouchni and C. Schweitzer, *Photochem. Photobiol.*, 2000, **71**, 12-19.

145. S. Lacombe and T. Pigot, *Catal. Sci. Technol.*, 2016, **6**, 1571-1592.

146. V. Balzani, G. Bergamini and P. Ceroni, *Angew. Chem. Int. Ed.*, 2015, **54**, 11320-11337.

147. H. Sterckx, B. Morel and B. U. W. Maes, *Angew. Chem. Int. Ed.*, 2019, **58**, 7946-7970.

148. D. Cambié, C. Bottecchia, N. J. W. Straathof, V. Hessel and T. Noël, *Chem. Rev.*, 2016, **116**, 10276-10341.

149. K. Gilmore and P. H. Seeberger, *Chem. Rec.*, 2014, **14**, 410-418.

150. Y. Su, K. Kuijpers, V. Hessel and T. Noël, *React. Chem. Eng.*, 2016, **1**, 73-81.

151. A. Gavriilidis, A. Constantinou, K. Hellgardt, M. Hii, G. J. Hutchings, G. L. Brett, S. Kuhn and S. P. Marsden, *React. Chem. Eng.*, 2016, **1**, 595-612.

152. C. A. Hone and C. O. Kappe, *Topics Curr. Chem.*, 2019, **377:2**.

153. K. C. Harper, E. G. Moschetta, S. V. Bordawekar and S. J. Wittenberger, *ACS Cent. Sci.*, 2019, **5**, 109-115.

154. M. R. Chapman, M. H. T. Kwan, G. King, K. E. Jolley, M. Hussain, S. Hussain, I. E. Salama, C. G. Niño, L. A. Thompson, M. E. Bayana, A. D. Clayton, B. N. Nguyen, N. J. Turner, N. Kapur and A. J. Blacker, *Org. Process Res. Dev.*, 2017, **21**, 1294-1301.

155. Y. Mo, H. Lin and K. F. Jensen, *Chem. Eng. J.*, 2018, **335**, 936-944.

156. Y. Mo and K. F. Jensen, *React. Chem. Eng.*, 2016, **1**, 501-507.

157. L. D. Elliott, J. P. Knowles, C. S. Stacey, D. J. Klauber and K. I. Booker-Milburn, *React. Chem. Eng.*, 2018, **3**, 86-93.

158. A. Albini and M. Fagnoni, *Handbook of Synthetic Photochemistry*, Wiley-VCH, Weinheim, 2009.

159. Asynt, fReactor Complete Kit, https://www.asynt.com/product/freactor-complete-kit/, (accessed 1 July, 2019).

160. K. L. Willett and R. A. Hites, *J. Chem. Ed.*, 2000, **77**, 900-902.

161. Y. Ji, D. A. DiRocco, C. M. Hong, M. K. Wismer and M. Reibarkh, *Org. Lett.*, 2018, **20**, 2156-2159.

162. T. Aillet, K. Loubiere, O. Dechy-Cabaret and L. Prat, *Int. J. Chem. React. Eng.*, 2014, **12**, 257-269.

163. M. A. Cismesia and T. P. Yoon, *Chem. Sci.*, 2015, **6**, 5426-5434.

164. Y. Su, V. Hessel and T. Noël, *AIChE J.*, 2015, **61**, 2215-2227.

165. M. C. White, *Science*, 2012, **335**, 807-809.

166. R. R. Karimov and J. F. Hartwig, *Angew. Chem. Int. Ed.*, 2017, **57**, 4234-4241.

167. D. Holtmann, M. W. Fraaije, I. W. C. E. Arends, D. J. Opperman and F. Hollmann, *Chem. Commun.*, 2014, **50**, 13180-13200.

168. Y. Kawamata, M. Yan, Z. Liu, D.-H. Bao, J. Chen, J. T. Starr and P. S. Baran, *J. Am. Chem. Soc.*, 2017, **139**, 7448-7451.

169. L. Capaldo and D. Ravelli, *Eur. J. Org. Chem.*, 2017, 2056-2071.

170. M. D. Tzirakis, I. N. Lykakis and M. Orfanopoulos, *Chem. Soc. Rev.*, 2009, **38**, 2609-2621.

171. G. Laudadio, S. Govaerts, Y. Wang, D. Ravelli, H. F. Koolman, M. Fagnoni, S. W. Djuric and T. Noël, *Angew. Chem. Int. Ed.*, 2018, **57**, 4078-4082.

172. R. K. Henderson, C. Jiménez-González, D. J. C. Constable, S. R. Alston, G. G. A. Inglis, G. Fisher, J. Sherwood, S. P. Binks and A. D. Curzons, *Green Chem.*, 2011, **13**, 854-862.

173. Merck, Tetra-*n*-butylammonium decatungstate, https://www.sigmaaldrich.com/catalog/product/aldrich/900432?lang=en&region=GB, (accessed 10 July, 2019).

174. T. Yamase and T. Usami, *J. Chem. Soc., Dalton Trans.*, 1988, 183-190.

175. S. Protti, D. Ravelli, M. Fagnoni and A. Albini, *Chem. Commun.*, 2009, **0**, 7351-7353.

176. A. M. Cardarelli, M. Fagnoni, M. Mella and A. Albini, *J. Org. Chem.*, 2001, **66**, 7320-7327.

177. A. Adamo, P. L. Heider, N. Weeranoppanant and K. F. Jensen, *Ind. Eng. Chem. Res.*, 2013, **52**, 10802-10808.

178. Zaiput Flow Technologies, Liquid-Liquid/Gas-Liquid Separators, https://www.zaiput.com/product/liquid-liquid-gas-separators/, (accessed 11 July, 2019).

179. M. Martan, J. Manassen and D. Vofsi, *Tetrahedron*, 1970, **26**, 3815-3827.

180. D. Dondi, A. M. Cardarelli, M. Fagnoni and A. Albini, *Tetrahedron*, 2006, **62**, 5527-5535.

181. E. Du, J. Li, S. Zhou, M. Li, X. Liu and H. Li, *Water*, 2018, **10**, 1238-1260.

182. R. L. Plackett and J. P. Burman, *Biometrika*, 1946, **33**, 305-325.

183. D. Webb and T. F. Jamison, *Chem. Sci.*, 2010, **1**, 675-680.

184. J. Britton and C. L. Raston, *Chem. Soc. Rev.*, 2017, **46**, 1250-1271.

185. A. Adamo, R. L. Beingessner, M. Behnam, J. Chen, T. F. Jamison, K. F. Jensen, J.-C. M. Monbaliu, A. S. Myerson, E. M. Revalor, D. R. Snead, T. Stelzer, N. Weeranoppanant, S. Y. Wong and P. Zhang, *Science*, 2016, **352**, 61-67.

186. J. Imbrogno, L. Rogers, D. A. Thomas and K. F. Jensen, *Chem. Commun.*, 2018, **54**, 70-73.

187. C. C. Tzschucke, C. Markert, W. Bannwarth, S. Roller, A. Hebel and R. Haag, *Angew. Chem. Int. Ed.*, 2002, **41**, 3964-4000.

188. S. V. Ley, R. J. Ingham, M. O'Brien and D. L. Browne, *Beilstein J. Org. Chem.*, 2013, **9**, 1051-1072.

189. M. O'Brien, P. Koos, D. L. Browne and S. V. Ley, *Org. Biomol. Chem.*, 2012, **10**, 7031-7036.

190. J. G. Kralj, H. R. Sahoo and K. F. Jensen, *Lab Chip*, 2007, **7**, 256-263.

191. A. E. Cervera-Padrell, S. T. Morthensen, D. J. Lewandowski, T. Skovby, S. Kiil and K. V. Gernaey, *Org. Process Res. Dev.*, 2012, **16**, 888-900.

192. R. Lebl, D. Cantillo and C. O. Kappe, *React. Chem. Eng.*, 2019, **4**, 738-746.

193. S. Glöckner, D. N. Tran, R. J. Ingham, S. Fenner, Z. E. Wilson, C. Battilocchio and S. V. Ley, *Org. Biomol. Chem.*, 2015, **13**, 207-214.

194. T. A. Hamlin, G. M. L. Lazarus, C. B. Kelly and N. E. Leadbeater, *Org. Process Res. Dev.*, 2014, **18**, 1253-1258.

195. N. Weeranoppanant, A. Adamo, G. Saparbaiuly, E. Rose, C. Fleury, B. Schenkel and K. F. Jensen, *Ind. Eng. Chem. Res.*, 2017, **56**, 4095-4103.

196. C. Dai, D. R. Snead, P. Zhang and T. F. Jamison, *J. Flow Chem.*, 2015, **5**, 133-138.

197. J. Clegg, J. F. Dawson, S. J. Porter and M. H. Barley, presented in part at the IEEE Congress on Evolutionary Computation, Edinburgh, 2005.

198. A. M. Hyde, S. L. Zultanski, J. H. Waldman, Y.-L. Zhong, M. Shevlin and F. Peng, *Org. Process Res. Dev.*, 2017, **21**, 1355-1370.

199. S. Mandal, S. Mandal, S. K. Ghosh, A. Ghosh, R. Saha, S. Banerjee and B. Saha, *Synth. Commun.*, 2016, **46**, 1327-1342.

200. C. Hui, F. Pu and J. Xu, *Chem. Eur. J.*, 2017, **23**, 4023-4036.

201. M. M. Heravi, T. Ahmadi, M. Ghavidel, B. Heidari and H. Hamidi, *RSC Adv.*, 2015, **5**, 101999-102075.

202. A. F. M. M. Rahman, R. Ali, Y. Jahng and A. A. Kadi, *Molecules*, 2012, **17**, 571-583.

203. Y. Miki, K. Hirano, T. Satoh and M. Miura, *Angew. Chem. Int. Ed.*, 2013, **52**, 10830-10834.

204. Y. Wang, Y. Kuang and Y. Wang, *Chem. Commun.*, 2015, **51**, 5852-5855.